Australian
National
University

Microscopic approach to heavy-ion reactions

A thesis submitted in fulfillment of the requirements for the degree of

Doctor of Philosophy

in the

Department of Nuclear Physics
Research School of Physics and Engineering
Australian National University

Kirsten Vo-Phuoc

March, 2018

Declaration

I confirm that this thesis presented for the degree of Doctor of Philosophy has been composed by myself. The work within was done in collaboration with Associate Professor Cédric Simenel, Dr. Edward Simpson, Professor Mahananda Dasgupta and Professor David Hinde. Part of the work has formed jointly-authored publications which are explicitly indicated on the following pages. Where published work of others has been consulted in this thesis, it has been clearly referenced. I confirm that this thesis has not been submitted for any other degree or professional qualification.

Canberra, March, 2018

Kirsten Vo-Phuoc

Publications

Part of this thesis has been published in the following papers:

1. *Dynamical effects in fusion with exotic nuclei*,
   K. Vo-Phuoc, C. Simenel and E. C. Simpson, Phys. Rev. C **94**, 024612 (2016),
2. *Fusion with exotic nuclei using a microscopic approach*,
   K. Vo-Phuoc, C. Simenel and E. C. Simpson, EPJ Web of Conferences **163**, 00062 (2017),
3. *Nuclear structure effects on heavy-ion reactions with microscopic theory*,
   K. Vo-Phuoc, C. Simenel and E. C. Simpson, EPJ Web of Conferences **123**, 03001 (2016).

Furthermore, contributions have been made to the following publications which have been or will be published:

4. *Nuclear structure dependence of fusion hindrance in heavy element synthesis*,
   J. Khuyagbaatar, H.M. David, D.J. Hinde, I. P. Carter, K. J. Cook, M. Dasgupta, Ch.E. Düllmann, D. Y. Jeung, B. Kindler, B. Lommel, D.H. Luong, E. Prasad, D.C. Rafferty, C. Sengupta, C. Simenel, E.C. Simpson, J.F. Smith, **K. Vo-Phuoc**, J. Walshe, A. Wakhle, E. Williams, and A. Yakushev, Phys. Rev. C **97**, 064618 (2018),
5. *Capture cross sections for the synthesis of new heavy nuclei using radioactive beams*,
   A. Wakhle, K. Hammerton, Z. Kohley, D. J. Morrissey, K. Stiefel, J. Yurkon, J. Walshe, K. J. Cook, M. Dasgupta, D. J. Hinde, D. J. Jeung, E. Prasad, D. C. Rafferty, C. Simenel, E. C. Simpson, **K. Vo-Phuoc**, J. King, W. Loveland, and R. Yanez, Phys. Rev. C **97**, 021602(R) (2018),
6. *Interplay of charge clustering and weak binding in reactions of* ^{8}Li,
   K. J. Cook, I. P. Carter, E. C. Simpson, M. Dasgupta, D. J. Hinde, L. T. Bezzina, Sunil Kalkal, C. Sengupta, C. Simenel, B. M. A. Swinton-Bland, **K. Vo-Phuoc**, and E. Williams, Phys. Rev. C **97**, 021601(R) (2018),
7. *First Elastic Scattering Measurement of* ^{8}Li *on* ^{209}Bi *at the Australian National University*,
   C. Sengupta, I.P. Carter, K.J. Cook, E.C. Simpson, M. Dasgupta, D. J. Hinde, D.Y. Jeung, Sunil Kalkal, **K. Vo-Phuoc**, E. Prasad, D. Rafferty, C. Simenel and E. Williams, EPJ Web of Conferences **163**, 00052 (2017),

8. *Effect of Pauli repulsion and transfer on fusion*,
   C. Simenel, K. Godbey, A.S. Umar, **K. Vo-Phuoc**, M. Dasgupta, D. J. Hinde and E. C. Simpson, EPJ Web of Conferences **163**, 00055 (2017),

9. *Evidence for the Role of Proton Shell Closure in Quasifission Reactions from X-Ray Fluorescence of Mass-Identified Fragments*,
   M. Morjean, D. J. Hinde, C. Simenel, D. Y. Jeung, M. Airiau, K. J. Cook, M. Dasgupta, A. Drouart, D. Jacquet, S. Kalkal, C. S. Palshetkar, E. Prasad, D. Rafferty, E. C. Simpson, L. Tassan-Got, **K. Vo-Phuoc**, and E. Williams, Phys. Rev. Lett. **119**, 222502 (2017),

10. *Time-dependent Hartree-Fock Study of Octupole Vibrations in doubly magic nuclei*,
    C. Simenel, J. Buete and **K. Vo-Phuoc**, EPJ Web of Conferences **123**, 01004 (2016),

11. *Examining the role of transfer coupling in sub-barrier fusion of* $^{46,50}Ti+^{124}Sn$,
    J. F. Liang, J. M. Allmond, C. J. Gross, P. E. Mueller, D. Shapira, R. L. Varner, M. Dasgupta, D. J. Hinde, C. Simenel, E. Williams, **K. Vo-Phuoc**, M. L. Brown, I. P. Carter, M. Evers, D. H. Luong, T. Ebadi, and A. Wakhle, Phys. Rev. C **94**, 024616 (2016),

12. *Multinucleon transfer in* $^{16,18}O,^{19}F+^{208}Pb$ *reactions at energies near the fusion barrier*,
    D. C. Rafferty, M. Dasgupta, D. J. Hinde, C. Simenel, E. C. Simpson, E. Williams, I. P. Carter, K. J. Cook, D. H. Luong, S. D. McNeil, K. Ramachandran, **K. Vo-Phuoc**, and A. Wakhle, Phys. Rev. C **94**, 024607 (2016),

13. *Probing cluster structures through sub-barrier transfer reactions*,
    D. C. Rafferty, M. Dasgupta, D. J. Hinde, C. Simenel, E. C. Simpson, E. Williams, I. P. Carter, K. J. Cook, D. H. Luong, S. D. McNeil, K. Ramachandran, **K. Vo-Phuoc** and A. Wakhle, EPJ Web of Conferences **123**, 03004 (2016),

14. *Nuclear structure effects in quasifission – understanding the formation of the heaviest elements*,
    D. J. Hinde, E. Williams, G. Mohanto, C. Simenel, D. Y. Jeung, M. Dasgupta, E. Prasad, A. Wakhle, **K. Vo-Phuoc**, I. P. Carter, K. J. Cook, D. H. Luong, C. S. Palshetkar, D. C. Rafferty and E. C. Simpson, EPJ Web of Conferences **123**, 03005 (2016),

15. *Asymptotic and near-target direct breakup of* ^{6}Li *and* ^{7}Li,
    Sunil Kalkal, E. C. Simpson, D. H. Luong, K. J. Cook, M. Dasgupta, D. J. Hinde, I. P. Carter, D. Y. Jeung, G. Mohanto, C. S. Palshetkar, E. Prasad, D. C. Rafferty, C.

Simenel, **K. Vo-Phuoc**, E. Williams, L. R. Gasques, P. R. S. Gomes, and R. Linares, Phys. Rev. C **93**, 044605 (2016),

16. *Exploring quasifission characteristics for* $^{34}S+^{232}Th$ *forming* ^{266}Sg,
E. Prasad, A. Wakhle, D. J. Hinde, E. Williams, M. Dasgupta, M. Evers, D. H. Luong, G. Mohanto, C. Simenel, and **K. Vo-Phuoc**, Phys. Rev. C **93**, 024607 (2016).

Acknowledgements

It is my greatest pleasure to acknowledge everyone who has been a part of my PhD. To start with, special thanks are in order for my supervisor, A. Prof. Cédric Simenel. This thesis would not have materialised at all without your expertise and guidance. Thank you for sharing your enthusiasm for physics research and teaching, as well as your endless patience and sense of humour. It has been a pleasure to work with you.

I would like to thank our dynamic group leaders, Prof. Nanda Dasgupta and Prof. David Hinde for including me in the reactions group. Without your generosity in imparting knowledge, experience and passion for physics to everyone in the group I would not have learnt nearly as much during my PhD.

Many thanks go to my supervisor, Dr. Ed Simpson. In addition to your academic help and incredible ability to pull apart any physics problem, thank you for the *constant* moral support and general life advice. You have been a complete sponge to many of my unwarranted complaints.

Thank you to the rest of the reactions group, past and present. It has been great to work amongst and share accelerator shifts with you all. To Dr. Mark Stoyer, for helpful input on parts of this thesis. To the rest of our current team (at time of submission): Dominic Rafferty, Dr. Kaitlin Cook, Dongyun Jeung, Chandrima Sengupta, Lauren Bezzina, Ellen McRae, Dr. Kaushik Banerjee and Dr. Annette Berriman. Thanks also to Liz, Prasad, Joe, Huy, Sunil, Chandani, Gayatri and Ian. My thanks to Ian stretches well beyond work and what I can express on paper.

I extend this to other members of the nuclear phyics department who contibute to its wonderful work environment. Thank you Petra Rickman, for everything you do to keep this place sane and also the chats, lifts and sunday beers. To my friends Jackson, AJ, Ben, Stefan, Boon, and many others for your valuable company over the years. Acknowledgement also goes to our head of department, Prof. Andrew Stuchbery, who is one of the reasons this PhD was seen through to the end and not abandoned halfway.

Thank you to my friends outside of the department for being a necessary portal to the world that isn't nuclear physics.

Finally, I cannot give a big enough thank you to my family. To my parents, your encouragement and support in academic pursuits surely made possible my decision to do postgraduate studies for which I feel fortunate to have done. Thank you all for putting up with my evasion of your questions about the PhD and for continuing to ask how it was going anyway.

The work in this thesis was completed with the support of ANU PhD scholarships as part of the Australian Government Research Training Program. The calculations that constitute a major part of this thesis were performed with the resources of the National Computational Insfrastructure (NCI) which is supported by the Australian Government.

Abstract

Heavy-ion reactions are affected by the nuclear structure of the reactants and many other dynamical processes during the collision. Theoretical studies of such reactions lead to a clearer understanding of prohibitive mechanisms to heavy-ion fusion. One application of this is superheavy element formation, where quasifission is the major competing process to the formation of a compound nucleus in this region of the nuclear chart.

Microscopic approaches that use mean field approximations, such as the time-dependent Hartree-Fock (TDHF) theory, have been increasingly used to study low energy heavy-ion reactions including fusion and quasifission. In addition to reactions, nuclear structure properties can also be studied with microscopic theory. Such approaches do not require empirical knowledge of the nucleus and can be used as a predictive tool for studying structure or reactions involving exotic nuclei. In this thesis, TDHF is used to study nuclear vibrations and heavy-ion reactions at near barrier energies.

The TDHF approach is applied first, in the small amplitude limit, to a systematic study of low-lying octupole and quadrupole vibrational modes of $^{40-54}$Ca isotopes. Then, fusion reactions are calcuated for Ca+Sn systems, using the barrier energy as the main observable. Fusion reactions are first calculated with no couplings (static HF calculations) before including all dynamics that the mean field approximation offers (TDHF calculations). The addition of dynamics often results in a lower fusion barrier compared to the static barrier, with the exception of systems involving the neutron rich projectiles in ^{52,54}Ca+^{116}Sn. The difference in fusion barriers between the static and dynamic calculations is explored by considering couplings to vibrational states and transfer channels. To separate the effects of individual couplings, the coupled-channels approach is used with the HF calculations of the vibrational states as inputs. Such couplings account for most of the reduction of the static barrier. For the most neutron rich systems, coupling to vibrational states does not account for the dynamical barrier increase. Transfer channels, in particular proton pickup, are explored within TDHF and may play a role in this increased barrier energy.

Following from fusion reactions, the factors and dynamics that may hinder fusion in heavier systems are studied in the reactions ^{48}Ca, ^{50}Ti, ^{52}Cr, ^{54}Fe, ^{56,64}Ni, ^{58}Zn+^{208}Pb

at energies ranging from 0% to 30% above the static HF barrier. Although most of these systems fuse at energies within this range, some systems reseparate for which emission of nucleons was apparent at scission point. The contact times were, in most cases, less than 10 zs, and N/Z equilibration of these systems happen on fast time scales (1–2 zs). Larger amounts of mass transfer occur in systems with longer neck times and fewer magic numbers such as ^{34}S+^{232}Th and ^{52,54}Cr+^{198,196}Pt systems that were also calculated for comparison. Further studies are required to better understand the role of shell effects as well as nucleon emission in quasifission reactions, and subsequently reactions leading to superheavy element formation.

Contents

1 Introduction

The heaviest naturally occurring element on earth is uranium.[1] Astrophysical events are responsible for elements between iron ($Z = 26$) and uranium ($Z = 92$) appearing naturally on earth, almost entirely through either of the r- or s-process, respectively rapid and slow neutron capture from a host nucleus, followed by beta decay. Elements that have more protons than uranium, suitably named as transuranic elements, must be synthesised from nuclear reactions in a laboratory. Rapid neutron capture processes on heavy nuclei produce very neutron rich isotopes which then beta decay towards stability and can thus create heavier transuranic nuclei. However, this method can only attain up to about $Z = 100$, successfully discovering $Z = 99, 100$ [63]. Beyond this, the method is limited by spontaneous fission of the unstable product.

Synthesising yet heavier elements necessitates different methods, namely fusion of two lighter nuclei resulting in a $Z > 100$ system. The name superheavy element (SHE) applies to those that have $Z \geq 104$ which are also known as transactinides. There are many challenges to succeed in SHE formation in all respects. In a practical sense, producing the appropriate materials needed for beams and targets as well as the operation time needed from accelerator facilities for SHE synthesis is expensive. To add to this, production cross sections for SHEs are on the order of picobarns. The best combinations of projectile and target as well as beam energy to encourage high enough production cross sections are not necessarily known for such reactions. As far as reaction dynamics is concerned, the major competing process to the formation of a compound nucleus (CN) from heavy-ion reactions is quasifission [6, 173, 207], causing the compound system to reseparate prematurely. The probability of survival of the CN (P_{CN}) relates to the probability of quasifission (P_{QF}) occurring by $P_{\mathrm{CN}} = 1 - P_{\mathrm{QF}}$. For heavy-ion reactions attempting SHE synthesis, $P_{\mathrm{QF}} \sim 1$.

Shifting to a theoretical perspective of nuclear reactions relevant to SHE research, heavy-ion reactions are excellent examples of complex, many-body quantum mechanical systems. At near barrier energies, they foster dynamical couplings more so than reactions of two light nuclei or reactions at very high energies where couplings are less effective. The aim of this thesis is to study the dynamics present in heavy-ion reactions at near

[1] The presence of ^{244}Pu in nature has been experimentally observed in small quantities [85]. However, whether plutonium is considered as naturally occurring is still an open question.

barrier energies, using a microscopic theoretical approach. Not all systems presented in this thesis are realistic to reproduce in experiment, mostly due to the neutron excess, and are studied with a predictive outlook.

Theoretical understanding of heavy-ion reactions runs parallel to experimental programs in its contribution to SHE research. It may help narrow the practical uncertainties mentioned above relating to projectile and target specifications. At the Australian National University, the experimental program of the reaction dynamics group (using the 14UD tandem accelerator and LINAC facilities with the CUBE detector [83]) includes a vast study of quasifission reactions in order to better understand the dominating process curbing CN formation in heavy-ion reactions. Recent works in this area include Refs. [54, 76, 84, 99, 148, 149, 223, 228].

1.1 Status of superheavy element discovery

Creating superheavy elements with increasing Z number is steered towards the search for the next magic proton and neutron number leading to the island of stability. The largest magic numbers known are $Z = 82$ and $N = 126$ corresponding to the ^{208}Pb nucleus. Nuclides close to these magic numbers are more tightly bound and have higher fission barriers than their neighbours in the nuclear chart. In this spirit, superheavy nuclei that have proton and neutron numbers near magicity (within the proposed island of stability) should in principle have longer half-lives enabling even more fruitful research of these nuclei. Macroscopic-microscopic models for nuclear structure are well in agreement of predicting the next magic number for neutrons to be 184 and for protons to be 114 [122, 134, 190]. More modern self-consistent non-relativistic and relativistic mean field theories also predict neutron shell closure at 184 but additionally predict the shell closure $N = 172$, and predict enhanced proton shell closure in the region $Z = 120 - 126$ [13, 42, 107, 156].

The discovery of SHEs has been in progress since the late 1960s (see e.g. Refs. [86, 87, 123, 137] for reviews) from an immense international effort headlined by the Joint Institute of Nuclear Research (JINR, Dubna) in collaboration with the Lawrence Livermore National Laboratory (LLNL, Livermore), GSI Helmholtz Centre for Heavy Ion Research (GSI, Darmstadt), Lawrence Berkeley National Laboratory (LBNL, Berkeley), and the Institute of Physical and Chemical Research (RIKEN, Saitama), not without further collaborations between many other institutions. Observation of a superheavy nucleus is typically from the detection of alpha decay chains from the evaporation residue,

leading to a lighter nucleus that is likely to decay through spontaneous fission. The most recent and heaviest SHE to date is $Z = 118$, first discovered in 2006 [141]. This, as well as $Z = 113, 115, 117$, were recently given names and added to the periodic table [145].

The elements $Z = 104 - 106$ were first synthesised in the 1960s by using light projectiles, ranging from carbon to neon, on actinide targets at both the JINR and LBNL facilities. Beams of ^{22}Ne on Pt and ^{243}Am targets (JINR) and an ^{16}O beam on a ^{248}Cm target as well as ^{12,13}C and ^{15}N beams on a ^{249}Cf target and an ^{18}O beam on ^{249}Cf target (LBNL) were used. It was from this wave of superheavy experiments that the suggestion of "cold fusion" reactions should take place in the search of yet heavier elements [136, 140]. Instead of an actinide target, the cold fusion method uses a stable target near magic shell closure, either ^{208}Pb or ^{209}Bi, which is bombarded with heavier projectiles starting from Cr upwards. This approach is more mass symmetric and leads to a compound nucleus with smaller excitation energy (typically around 10–15 MeV) than compound nuclei produced from actinide targets. The deexcitation of the compound nucleus formed from cold fusion is via $1n$ emission to reach the ground state of the superheavy nucleus.

A summary of the reactions first discovering elements $Z = 107 - 118$, as credited by the International Union of Pure and Applied Chemistry (IUPAC), are listed in Tab. 1.1 along with their accepted chemical symbols, year of discovery and location of the accelerator facility of the relevant experiment. The cold fusion method was successful in discovering the next wave of SHEs for $Z = 107 - 109$ in the early 1980s by the GSI group [124–126], who continued their discovery stretch for $Z = 110 - 112$ in the mid 1990s [88–90]. The RIKEN group were credited as the first to synthesise $Z = 113$, still with the cold fusion method in 2004 [120].

During this time, the Dubna/LLNL collaboration were running experiments in search of superheavy nuclei using the hot fusion method. This method specifically involves using a ^{48}Ca beam on actinide targets ranging from U to Cf, which can create $Z = 112 - 118$. The hot fusion method results in compound systems with high excitation energies, at around 30–35 MeV, and deexcitation of the compound nucleus to the ground state requires $3n$–$4n$ emission. It was from this method that elements $Z = 114 - 118$ were discovered [138, 141–144]. The resurgence of an actinide target provides a more charge asymmetric system with a significantly smaller Coulomb repulsion than from the cold fusion method. It also creates more neutron rich compound nuclei that cannot be reached by cold fusion methods. For example, synthesising the predicted doubly magic nucleus $^{298}_{184}$114 by using the cold fusion method with a ^{208}Pb target would require an unfeasible beam of ^{90}Ge.

In the search beyond $Z = 118$, difficulties in manufacturing targets in higher Z number

than Cf arise, they simply cannot be produced in sufficient quantities to make targets that are thick enough for SHE experiments. If such targets existed they would be very radioactive and decay before high enough cross sections of SHE evaporation residues could be measured. As the limits of radioactive transuranium targets are being reached, beams heavier than ^{48}Ca are needed to synthesise elements $Z \geq 119$.

Eventually, the search for SHEs will end due to an existence of a heaviest element which will complete the nuclear chart in the direction of the Z number. This is because as the Z number of a nucleus increases, the Coulomb repulsion between the protons also increases. For the nucleus with increasing Z to remain bound and stable, it must compensate with a high ratio of neutrons to protons so that the attractive nucleon-nucleon force can counterbalance the Coulomb repulsion. The neutron to proton ratio of a bound nucleus increases with increasing Z. This, as well as quantum shell effects, allows for the existence of superheavy nuclei. However, at some Z value, the Coulomb repulsion will be too overwhelming for the nucleon-nucleon force to counter it with any number of neutrons, and the resulting system will simply be too unstable for a CN to form. It is uncertain how large this Z number is.

Z number	Reaction	Year	Location	Reference
107 (Bh)	^{209}Bi(^{54}Cr, 1n)^{262}107	1981	GSI	[126]
108 (Hs)	^{208}Pb(^{58}Fe, 1n)^{265}108	1982		[125]
109 (Mt)	^{209}Bi(^{58}Fe, 1n)^{266}109	1984		[124]
110 (Ds)	^{208}Pb(^{62}Ni, 1n)^{269}110	1995	GSI	[89]
111 (Rg)	^{209}Bi(^{64}Ni, 1n)^{272}111	1995		[88]
112 (Cn)	^{208}Pb(^{70}Zn, 1n)^{277}112	1996		[90]
113 (Nh)	^{209}Bi(^{70}Zn, 1n)^{278}113	2004	RIKEN	[120]
114 (Fl)	^{244}Pu(^{48}Ca, 3n)^{289}114	1999	JINR	[142]
115 (Mc)	^{243}Am(^{48}Ca, 3n)^{288}115	2004		[144]
116 (Lv)	^{248}Cm(^{48}Ca, 4n)^{292}116	2000		[143]
117 (Ts)	^{249}Bk(^{48}Ca, 4n)^{293}117	2010		[138]
118 (Og)	^{249}Cf(^{48}Ca, 3n)^{294}118	2006		[141]

Tab. 1.1.: Summary of the reactions that were awarded by IUPAC as first discovering the superheavy elements $Z = 107 - 118$.

1.2 Choice of theory

1.2.1 The Coupled-Channels approach

The Coupled-Channels (CC) approach is the conventional choice for studying nuclear reactions [200], including fusion and couplings at near barrier energies [47]. It is a fully quantum mechanical theory where the wavefunction of the total system is formed on the degrees of freedom of the target and projectile. These intrinsic degrees of freedom of the two nuclei are coupled to their relative motion and the Schrödinger equation is solved for the channel wavefunctions using the coupling interaction. Originally, CC calculations were fit to reproduce scattering data. To adjust the CC model for fusion, incoming wave boundary conditions are applied to all channel wavefunctions, creating a short range, imaginary potential accounting for the part of the total wavefunction that leads to capture which includes fusion.

The CC approach has been successful at reproducing many experimental results from heavy-ion reactions at near barrier energies. It is well known that CC does not explain deep subbarrier fusion hindrance in heavy-ion reactions [94]; couplings are understood to increase transmission at just below barrier energies [74] which translates to an over estimation of fusion cross sections at deep subbarrier energies. As such, other models [91, 116, 186] were proposed to understand the experimentally observed deep subbarrier fusion hindrance. It is also familiar that the CC approach is unable to account for above barrier fusion suppression [132]. Fitting CC calculations to above barrier data can be done by changing the surface diffuseness parameter from the value used for near barrier energies [132], though ideally the model would reproduce data of one system at all energy regimes using the same parameter values.

To describe couplings in reactions, CC requires empirical knowledge of the degrees of freedom of the projectile and or target. If this is not available, calculations from other models can be used to supply this input. Although this is not strictly a limitation of the theory, it would be preferable if the model were able to describe heavy-ion reactions without extensive external input or reliance of other models to include the couplings. A true limitation of the CC aproach is that it neglects a proper description of many couplings that play important roles in heavy-ion reactions, for example multinucleon transfer.

1.2.2 Microscopic approach

Another option to study heavy-ion reactions with is a microscopic approach, where the wavefunction of the total system is built on the wavefunctions of each nucleon (a many-body wavefunction). Solving the Schrödinger equation exactly for the many-body problem is impossible. Mean field theory (interchangeably, self-consistent field theory) can be used to approximate and numerically solve the problem. It has drawn some attention over the last few decades in nuclear physics even though it was conceived long before in other branches of physics and chemistry and applied to nuclear reactions as early as the 1970s [27, 41, 58]. Its expanse in application is largely owed to advances in computer and supercomputer technology that can now handle immense calculations the theory demands.

Mean field theory has many properties that lend itself particularly useful for nuclear physics problems. The construction of the many-body wavefunction for a nuclear system uses Hartree–Fock (HF) theory for which mean field theory will be referred to henceforth. The only input needed for HF calculations is a description of the nucleon-nucleon interaction. Unlike the CC approach, couplings are incorporated in HF calculations without any empirical knowledge nor prior calculations from other models on the degrees of freedom of the reactant nuclides. This is especially useful for studying systems with exotic nuclei near the neutron dripline. In principle, if all couplings are properly described within the CC approach then the results produced by CC and HF reaction calculations at above barrier energies should be the same. However, the advantage of the external input for the couplings in CC calculations is that one can decide which couplings to include or neglect in a reaction. With HF theory, couplings are implicit and included all at once in a reaction meaning one cannot choose which to include or leave out.

Aside from its suitability to nuclear physics problems, the accessibility of both a static and time-dependent version of the HF theory is also a nice feature. The time-dependent version is especially novel as calculations of heavy-ion reactions can be observed over zeptosecond timescales which cannot be done from experiment as measured spectra are time integrated over the entire reaction.

Expectedly, there are shortcomings of HF theory for its use in reaction theory. In the time-dependent Hartree–Fock (TDHF) version, the most significant limitation it presents is the inability to describe quantum tunnelling, an essential physical phenomenon of subbarrier heavy-ion fusion. The premise of the TDHF method is that only the average trajectory of the system is calculated meaning only one exit channel for a heavy-ion

reaction can ever be observed. This limitation arises from restricting the wavefunction of the system to be a Slater determinant, which renders the Schrödinger equations nonlinear. Although the theory is microscopic, because of this single trajectory outcome it is not fully quantum mechanical like the CC model. Studying below barrier fusion with TDHF is therefore not possible unless a nucleus-nucleus potential is extracted from the TDHF dynamics itself [211, 225].

Another limitation that arises from HF theory being only an approximation to the many-body problem is that some correlations that are important for reactions are not implicit, the most notable being pairing. Pairing correlations must be either included separately or an extension of the HF theory altogether must be used.

Furthermore, on a practical note fully time-dependent mean field equations are computationally very expensive. A heavy-ion reaction, for example ^{48}Ca+^{208}Pb at one energy, can take up to days on a supercomputer to solve whereas CC calculations with couplings will take minutes on the average laptop.

Early TDHF applications included vibration [19], fission [130], and reaction [27] studies. The developments of three-dimensional TDHF codes [101, 112, 113, 128, 210] that include spin-orbit couplings [218] have made calculations with all dynamics at the mean field level possible. Recent work in structure and reactions using TDHF has covered many areas (see Refs. [127, 129, 176] for reviews) including vibrations [3, 60, 163, 181, 187, 194], fusion [29, 43, 65, 182, 184, 217, 222, 224], transfer [161, 162, 165, 169–171, 174, 175], quasifission [76, 135, 149, 172, 215, 216, 223, 229] and fission [34, 66, 67, 167, 185, 202] studies.

1.3 Material in this thesis

This thesis is structured as a build up of studies of reactions pertaining to SHE applications with the (TD)HF approach. With each chapter involving calculations, there is increasing complexity in dynamics and couplings for the reactions presented.

The work presented starts with a derivation and outline of the main features of HF theory in Chapter 2, both static and time-dependent versions. Included within is the justification of using HF theory to study nuclear reactions. Numerical details of all calculations made in the rest of the thesis are also presented in this chapter. Chapter 3 applies HF theory to vibrations of chains of isotopes. TDHF calculations are performed on single nuclei to study some of their low-lying vibrational modes. This chapter serves two purposes: to check that the theory reproduces known results measured from experiment

to reasonable agreement and also to predict results for unknown nuclei (approaching the neutron dripline). Increasing the complexity of dynamics from here, Chapter 4 applies the theory to reactions mainly of Ca on Sn. Dynamical effects on the fusion barriers for the systems are studied using results of vibrational modes from Chapter 3 as well as exploring transfer channels. Systems in this chapter range from stable projectiles reacting with stable targets through to exotic projectile and target combinations. The final application of the theory is presented in Chapter 5, including yet heavier systems where a fusion barrier may not even exist, but instead undergo quasifission or deep inelastic collisions over a large energy range. Reactions calculated in Chapter 5 involve projectiles ranging from Ca to Zn on a stable Pb target as well as comparison to systems that have been studied experimentally with S+Th and Cr+Pt reactions. All results and discussions of the three applications are summarised in Chapter 6 which includes an outlook for this work.

2 Hartree–Fock theory: formalism and numerical methods

2.1 Overview

Studying nuclear reactions with microscopic approaches means studying the many-body problem. The governing equation underlying all non-relativistic quantum mechanical particles is the Schrödinger equation. For nuclear systems of N particles, the Schrödinger equation (static and time-dependent) is written accordingly,

$$\hat{H}\Psi = E\Psi, \tag{2.1.1}$$

$$\hat{H}\Psi(r,t) = i\hbar\frac{\partial}{\partial t}\Psi(r,t). \tag{2.1.2}$$

In formulating the Hamiltonian of any nuclear system there are two challenges. The first is choosing an interaction term for $\hat{H}$, made a difficult task because of the unknown exact form of the nucleon-nucleon interaction inside nuclei. Another challenge is solving the Schrödinger equation for systems of more than few particles. Self-consistent mean field theory is one approach that is particularly useful to describe structure and dynamics of nuclear systems.

Originally, Hartree theory [77] was used for atomic physics, using the time-independent Schrödinger equation to approximate the potential of a multielectron atom and solving for the eigenfunctions of the electrons. The approximations were that each electron moved independently and contributed to a net potential of the whole system. The Fock exchange term was included in the theory in 1930 [59], it requires using an antisymmetric wavefunction to describe the total system of fermions.

The combination of these two theories brings the Hartree–Fock (HF) theory. Applied to nuclear physics it is particularly useful as unlike atomic physics, where the exact form of the Coulomb interaction is known, the exact form of the nuclear interaction within the nucleus is not well known. In addition, electrons in atoms feel an external potential due to the Coulomb interaction with the nucleus and such external potential is usually absent

in the description of nuclei. Similarly, treating each nucleon as an independent particle within the nucleus, it is assumed that each contributes to a mean field experienced by all the other nucleons.

The time-dependent Hartree–Fock (TDHF) equations were first derived by Dirac in 1930 [49]. In TDHF, the system is restricted to a Slater determinant at all times. This implies that quantum effects requiring a sum of Slater determinants such as tunnelling are not incorporated into the theory, which is a major limitation of the HF theory.

For this chapter, first the HF theory is derived in both static and time-dependent forms. The approaches to the nucleon-nucleon effective interaction and pairing residual interaction are also outlined. Then, computational methods to solve the HF equations are discussed along with the numerical details for calculating the Skyrme and pairing energy density functionals. Computational details are also presented for the frozen HF bare nucleus-nucleus potential and for transfer probabilities in the TDHF method. Finally, initial numerical conditions for all calculations appearing in this thesis are listed.

2.2 Derivation of Hartree–Fock theory

There are several ways to derive the Hartree–Fock equations. For this section, variational calculus is the adopted method for which details are presented in Appendix A and the notation within is the same for the rest of this section. Modern derivations of the theory can be found for example in Ref. [154].

2.2.1 Static Hartree–Fock equations

Consider a time-independent, N-body quantum mechanical system. The action, labelled E by convention, is defined as

$$E[\Phi] = \langle \Phi, \hat{H}\Phi \rangle = \int_{\widetilde{M}} \Phi^* \hat{H} \Phi d\tilde{\mu} \tag{2.2.1}$$

where $\hat{H}$ is the non-relativistic Schrödinger Hamiltonian

$$\hat{H} = \sum_{j=1}^{N} \frac{-\hbar^2}{2m} \nabla_j^2 + \hat{V}.$$

In nuclear systems, $\hat{V}$ must be approximated by a function that can be dealt with, if not analytically, then numerically. The N-body wavefunction is denoted by Φ and for fermionic systems it will be approximated by a Slater determinant $\Phi : \widetilde{M} \to \mathbb{F}$ which is an element of the (odd) Fock space $\mathcal{F}_-(L^2(M, \mu))$ and the single particle wavefunctions

that comprise Φ are elements of $L^2(M,\mu)$ with measure space M and measure μ with the usual L^2 inner product. The functional $E : \mathcal{F}_- \to \mathbb{R}$ takes arguments from the space of Slater determinants $\mathcal{F}_-$.

The inner product in (2.2.1) is the induced inner product of the Fock space from the usual Lebesgue inner products of the single particle L^2 spaces. In evaluating E, the definiteness of the spatial integral comes from computational limitations when the cartesian coordinate space of $\widetilde{M}$ is defined, depending on calculational needs, which are described in a later section of this chapter. For this section the limits of this integral, although necessary, are omitted for brevity.

Instead of taking the cumbersome route of varying E over the N-body wavefunction Φ, it is more ideal to convert this problem into N one-body equations using the orthonormal single particle wavefunctions $\varphi_j \in L^2(M,\mu), j = 1, ..., N$ which Φ is comprised. The Slater determinant wavefunction written in terms of single particle wavefunctions is

$$\Phi(r_1, r_2, ..., r_N) = \frac{1}{\sqrt{N!}} \sum_{\sigma \in S_N} \operatorname{sgn}(\sigma) \varphi_{\sigma(1)}(r_1) \varphi_{\sigma(2)}(r_2) ... \varphi_{\sigma(N)}(r_N),$$

where S_N is the permutation on N letters and the variables $r_j = (\mathbf{r}_j s_j q_j)$, $j = 1, ..., N$ of each single particle wavefunction contain all the spatial coordinates as well as spin and isospin coordinates. It is clear that if $E = E[\Phi]$ then $E = E[\varphi_i], i = 1, 2, ..., N$ as well.

From the single particle wavefunctions, the one-body density matrix for Slater determinants can be determined from

$$\rho(r, r') = \sum_{j=1}^{N} \varphi_j^*(r') \varphi_j(r). \tag{2.2.2}$$

When taking the evolution of ρ instead of individual φ_i, no information from the system is lost for independent particle systems. To proceed with the derivation, instead force $E = E[\rho]$ and vary ρ to find the differential of E,

$$\delta E = \iint \frac{\delta E[\rho]}{\delta \rho(r, r')} \delta \rho(r, r') dr dr'. \tag{2.2.3}$$

The expression for the functional derivative of E with respect to ρ is unknown and the term will remain in that form for the rest of the derivation. The integral notation over dr here where $r = (\mathbf{r} s q)$ is really an abuse of notation that includes a spatial integral over the $\mathbf{r} = (x, y, z)$ coordinates and summation over spin and isospin coordinates s and

q, that is

$$\int dr \equiv \sum_s \sum_q \iiint dxdydz, \tag{2.2.4}$$

as in Appendix A of Ref. [176]. For the rest of this section only, the integral notation on the left hand side of (2.2.4) is used.

Given that $\rho = \rho[\varphi_i, \varphi_i^*], i = 1, ..., N$, equation (2.2.3) can be taken one step further using the chain rule (A.5) and be written as

$$\delta E = \iiint \frac{\delta E[\rho(\varphi_i^*)]}{\delta \rho(r, r')} \frac{\delta \rho(r, r')}{\delta \varphi_i^*(s)} \delta \varphi_i^*(s) ds dr dr'. \tag{2.2.5}$$

Only φ_i^* is used in the integral as φ_i and φ_i^* are not independent variables so it suffices to vary one of them to obtain the expression $\delta\rho$ in (2.2.3). However, for this derivation they are treated as independent variables. In particular, the derivative of a function with respect to its complex conjugate is taken as zero. It is simpler to vary over φ_i^* for $i \in \{1, ..., N\}$ which will be done in full first. Variation over φ_i is needed later to complete the derivation using this independent variable assumption. A particular $i \in \{1, ..., N\}$ is picked to continue with the derivation.

Finding the functional derivative of ρ with respect to φ_i^* is done via converting it to the form (A.6), and using (A.3),

$$\begin{aligned} \frac{\delta \rho(r, r')}{\delta \varphi_i^*(s)} &= \frac{\partial \rho(r, r')}{\partial \varphi_i^*(s)} \\ &= \frac{\partial \left(\sum_{j=1}^N \varphi_j^*(r') \varphi_j(r) \right)}{\partial \varphi_i^*(s)} \\ &= \varphi_j(r) \delta_{ij} \delta(r' - s) \\ &= \varphi_i(r) \delta(r' - s). \end{aligned} \tag{2.2.6}$$

Substituting (2.2.6) into (2.2.5), the differential of E becomes

$$\delta E = \iint \frac{\delta E}{\delta \rho(r, s)} \varphi_i(r) \delta \varphi_i^*(s) dr ds. \tag{2.2.7}$$

If φ_i^* is an extremum for E, it is not enough to just take $\delta E = 0$ here, as there are extra conditions on all φ_i in that the full set of them must be orthonormal as they serve as a basis for the Slater determinants. This gives the conditions $\langle \varphi_j, \varphi_k \rangle = \delta_{jk}$ for all $j, k \in \{1, ..., N\}$, leading to the $N \times N$ constraints

$$G_{jk} := \langle \varphi_j, \varphi_k \rangle = \delta_{jk}.$$

The variational problem is now

$$\delta\left(E-\sum_{j=1}^{N}\sum_{k=1}^{N}\lambda_{kj}G_{jk}\right)=0$$

for Lagrange multipliers $\lambda_{kj}\in\mathbb{C}$ for each G_{jk}. The indices of λ are reversed so that the summation can be written as matrix multiplication $\mathbf{\Lambda G}$ where $\Lambda=(\lambda_{kj})$ and $\mathbf{G}=(G_{jk})$ which will be useful later. Linearity of δ implies

$$\delta E-\sum_{j=1}^{N}\sum_{k=1}^{N}\lambda_{kj}\delta G_{jk}=0. \tag{2.2.8}$$

As $G_{jk}=G_{jk}[\varphi_i]$ is in the form (A.1), the functional derivative of equation G_{jk} with respect to φ_i^* can use (A.3),

$$\begin{aligned}\frac{\delta G_{jk}}{\delta\varphi_i^*(s)}&=\frac{\partial\left(\varphi_j^*(r)\varphi_k(r)\right)}{\partial\varphi_i^*(s)}\\&=\varphi_k(r)\delta_{ij}\delta(r-s)\\&=\varphi_k(s)\delta_{ij}.\end{aligned} \tag{2.2.9}$$

Substituting (2.2.9) into (2.2.8) and using (2.2.7),

$$\begin{aligned}\delta E-\sum_{j=1}^{N}\sum_{k=1}^{N}\lambda_{kj}\delta G_{jk}&=\iint\frac{\delta E}{\delta\rho(r,s)}\varphi_i(r)\delta\varphi_i^*(s)drds-\sum_{j=1}^{N}\sum_{k=1}^{N}\lambda_{kj}\int\varphi_k(s)\delta_{ij}\delta\varphi_i^*(s)ds\\&=\int\left(\int\frac{\delta E}{\delta\rho(r,s)}\varphi_i(r)dr-\sum_{k=1}^{N}\lambda_{ki}\varphi_k(s)\right)\delta\varphi_i^*(s)ds\\&=0.\end{aligned}$$

Since the variation of φ_i^* is arbitrary it is enough to say that the term inside the parentheses is equal to zero,

$$\int\frac{\delta E}{\delta\rho(r,s)}\varphi_i(r)dr-\sum_{k=1}^{N}\lambda_{ki}\varphi_k(s)=0.$$

Now the derivative term can be relabelled to

$$h(s,r):=\frac{\delta E}{\delta\rho(r,s)}$$

and be called the Hartree–Fock single particle Hamiltonian. Rearranging the summand so the indices follow vector and matrix multiplication, and relabelling the summation

index to j, the equation is

$$\int h(s,r)\varphi_i(r)dr = \sum_{j=1}^{N} \varphi_j(s)\lambda_{ji}. \tag{2.2.10}$$

Variation was over φ_i^* for a particular $i \in \{1, ..., N\}$ but the choice of i was arbitrary and so there are in fact N equations of the form (2.2.10). This equation is close to (but not quite) an eigenvalue equation for φ_i. Instead of an operation on φ_i resulting in a scalar multiple of φ_i, the result is a linear combination of all φ_is. This can be dealt with if the properties of the λ_{ji} are known. Re-deriving the equations up until now but with variation over φ_i instead will give very similar equations to (2.2.10) and only the main results are shown:

$$\frac{\delta\rho(r,r')}{\delta\varphi_i(s)} = \varphi_i^*(r')\delta(r-s)\delta\varphi_i(s),$$

$$\delta E = \iint h(r',s)\varphi_i^*(r')\delta\varphi_i(s)dr'ds, \tag{2.2.11}$$

$$\delta G_{jk} = \int \varphi_j^*(s)\delta_{ik}\delta\varphi_i(s)ds. \tag{2.2.12}$$

Substituting (2.2.11) and (2.2.12) into (2.2.8) results in the expression

$$\int \left(\int h(r',s)\varphi_i^*(r')dr' + \sum_{j=1}^{N} \lambda_{ij}\varphi_j^*(s) \right) \delta\varphi_i(s)ds = 0.$$

Similarly, variation over φ_i is arbitrary so these equations become

$$\int h(r,s)\varphi_i^*(r)dr = \sum_{j=1}^{N} \lambda_{ij}\varphi_j^*(s). \tag{2.2.13}$$

Note that the complex conjugate of one-body density matrix

$$\begin{aligned}\rho(r,r')^* &= \left(\sum_{j=1}^{N} \varphi_j^*(r')\varphi_j(r) \right)^* \\ &= \rho(r',r)\end{aligned}$$

and it follows that $h(s,r)^* = h(r,s)$ since evaluation of E is a real number.

Taking variation with respect to φ_i and φ_i^* produces a set of equations that are complex conjugate. Subtracting the conjugate of (2.2.13) from (2.2.10) leaves

$$0 = \sum_{j=1}^{N} \varphi_j(s) \left(\lambda_{ji} - \lambda_{ij}^* \right)$$

since the single particle wavefunctions are linearly independent then it follows that $\lambda_{ij}^* = \lambda_{ji}$, which means that the matrix Λ is hermitian and therefore also normal. Now the finite dimensional spectral theorem can be applied to the matrix Λ. The theorem states that for every normal matrix, there is a unitary matrix U that diagonalises it and the diagonal matrix has real entries. This means the matrix Λ can be written as $\Lambda = UDU^*$ where the matrix U is unitary and D is diagonal.

The N HF equations can be written as vector equations using variations over all the φ_i, where $\boldsymbol{\varphi} = (\varphi_1, \varphi_2, ..., \varphi_N)^\top$,

$$\begin{aligned}\int h(s,r)\boldsymbol{\varphi}(r)^\top dr &= \boldsymbol{\varphi}(s)^\top \Lambda \\ &= \boldsymbol{\varphi}(s)^\top UDU^*.\end{aligned}$$

Multiplying both sides on the right by U,

$$\begin{aligned}\int h(s,r)\boldsymbol{\varphi}(r)^\top drU &= \boldsymbol{\varphi}(s)^\top UD(U^*U) \\ \Rightarrow \int h(s,r)\left(\boldsymbol{\varphi}(r)^\top U\right)dr &= \left(\boldsymbol{\varphi}(s)^\top U\right)D\end{aligned}$$

moving U inside the integral on the LHS for componentwise scalar multiplication. Now let $\tilde{\boldsymbol{\varphi}} = \boldsymbol{\varphi}^\top U$. The new wavefunctions are a unitary transformation of the original single particle wavefuctions so orthonormality of the $\tilde{\varphi}_i$ is retained. Labelling the real diagonal entries of D as $\epsilon_i, i = 1, ..., N$, the stationary Hartree–Fock equations are recovered,

$$\int h(s,r)\tilde{\varphi}_i(r)dr = \epsilon_i \tilde{\varphi}_i(s). \tag{2.2.14}$$

2.2.2 Time-dependent Hartree–Fock equations

Deriving the time-dependent HF (TDHF) equations is very similar to the static version. However, all integrals relating to the first variation of the functional are over a time variable as well as spatial variables through inner products. The extra time variable requires a new action for the whole system $J = J[\Phi]$ which is a definite integral,

$$\begin{aligned}J[\Phi] &= \int_{t_0}^{t_1} \left\langle \Phi, \left(i\hbar\frac{\partial}{\partial t} - \hat{H}\right)\Phi \right\rangle dt \\ &= \int_{t_0}^{t_1} \langle \Phi, i\hbar D_t \Phi\rangle - \langle \Phi, \hat{H}\Phi\rangle dt,\end{aligned}$$

using the notation D_t for partial differentiation by t. Requiring stationarity of the action, $\delta J = 0$, without restricting the variational space of Φ leads to the time-dependent

Schrödinger equation (2.1.2). However, TDHF is obtained by assuming the state of the system to be a Slater determinant, Φ, at all times. This or the single particle wavefunctions are then extremal functions for J. The wavefunctions Φ and $\varphi_j, j = 1, ..., N$ remain the same as the previous section. Variation of J over the conjugate single particle wavefunction for a particular $j \in \{1, ..., N\}$ follows.

To break up different parts of the action, J will be written as $J = J_1 + J_2$ with

$$J_1 = \int_{t_0}^{t_1} \langle \Phi, i\hbar D_t \Phi \rangle dt,$$
$$J_2 = -\int_{t_0}^{t_1} \langle \Phi, \hat{H}\Phi \rangle dt = -\int_{t_0}^{t_1} E[\rho(t)] dt.$$

The $E[\rho]$ appearing in the J_2 term is the same as for the static case except the wavefunctions in the one body density matrix ρ now have a time variable,

$$\rho(t) = \rho(r, r', t) = \sum_{j=1}^{N} \varphi_j^*(r', t)\varphi_j(r, t).$$

First, the conversion of the inner product in J_1 to single particle wavefunctions is done,

$$\begin{aligned}
\langle \Phi, i\hbar D_t \Phi \rangle &= \frac{i\hbar}{N!} \sum_{\sigma \in S_N} \sum_{\tau \in S_N} \mathrm{sgn}(\sigma)\mathrm{sgn}(\tau) \left\langle \varphi_{\sigma(1)}(r_1)...\varphi_{\sigma(N)}(r_N), D_t \left[\varphi_{\tau(1)}(r_1)...\varphi_{\tau(N)}(r_N) \right] \right\rangle \\
&= \frac{i\hbar}{N!} \sum_{\sigma \in S_N} \sum_{\tau \in S_N} \mathrm{sgn}(\sigma\tau) \sum_{j=1}^{N} \Bigg\{ \iint ... \int \varphi_{\sigma(1)}^*(r_1)...\varphi_{\sigma(N)}^*(r_N)\varphi_{\tau(1)}(r_1)... \\
&\qquad ...D_t \left[\varphi_{\tau(j)}(r_j) \right] ...\varphi_{\tau(N)}(r_N) dr_1 dr_2 ... dr_N \Bigg\} \\
&= \frac{i\hbar}{N!} \sum_{\sigma \in S_N} \sum_{\tau \in S_N} \mathrm{sgn}(\sigma\tau) \sum_{j=1}^{N} \Bigg\{ \int \varphi_{\sigma(1)}^*(r_1)\varphi_{\tau(1)}(r_1) dr_1 \times ... \\
&\qquad \times \int \varphi_{\sigma(j)}^*(r_j) D_t \varphi_{\tau(j)}(r_j) dr_j ... \int \varphi_{\sigma(N)}^*(r_N)\varphi_{\tau(N)}(r_N) dr_N \Bigg\}.
\end{aligned}$$

Since the φ_j only depend on one variable each within the set $\{r_1, ..., r_N\}$, the integrals can be rearranged in the last line. The integrals not containing the partial derivative term will all be zero unless $\tau = \sigma$ due to orthonormality. Only one $\tau \in S_N$ will match the σ permutation so $\mathrm{sgn}(\sigma\tau)\big|_{\tau=\sigma} = 1$ for the nonzero integral. The final result when summing over the τ is

$$\langle \Phi, i\hbar \partial_t \Phi \rangle = \frac{i\hbar}{N!} \sum_{\sigma \in S_N} \sum_{j=1}^{N} \left\langle \varphi_{\sigma(j)}, D_t \varphi_{\sigma(j)} \right\rangle.$$

For each $\sigma \in S_N$, the sum over j results in the sum of N inner products over every index,

although each term appearing in different orders for different permutations σ. As there are $N!$ of $\sigma \in S_N$, the expression becomes

$$\langle \Phi, i\hbar D_t \Phi \rangle = i\hbar \sum_{j=1}^{N} \langle \varphi_j, D_t \varphi_j \rangle.$$

The total action is now

$$\begin{aligned} J &= J_1 + J_2 \\ &= \int_{t_0}^{t_1} i\hbar \sum_{j=1}^{N} \langle \varphi_j, D_t \varphi_j \rangle dt - \int_{t_0}^{t_1} E[\rho(t)] dt. \end{aligned}$$

The variation of J over the conjugate single particle wavefunction φ_k^* is now done for a particular $k \in \{1, ..., N\}$. Although J is an action over a time variable, it is also functional of a functional over spatial variables from the inner product as well so they must be included in the computation of the derivatives. However, since the outer integral is over a time variable and there are no constraints to the functions with respect to the time variable, there is no need for Lagrange multipliers in this derivation. The integration limits of all variables are omitted for brevity.

The differential of J_1 is

$$\begin{aligned} \delta J_1 &= \iint \frac{\delta J_1[\varphi_k^*]}{\delta \varphi_k^*(s,t)} \delta \varphi_k^*(s,t) ds dt \\ &= \iint i\hbar \sum_{j=1}^{N} \frac{\partial}{\partial \varphi_k^*(s,t)} \Big\langle \varphi_j(r,t), D_t \varphi_j(r,t) \Big\rangle \delta \varphi_k^*(s,t) ds dt \\ &= \iint i\hbar D_t \varphi_k(s,t) \delta \varphi_k^*(s,t) ds dt. \end{aligned}$$

And for J_2,

$$\begin{aligned} \delta J_2 &= \iint \frac{\delta J_2[\varphi_k^*]}{\delta \varphi_k^*(s,t)} \delta \varphi_k^*(s,t) ds dt \\ &= -\iint \iiint \frac{\delta E[\rho]}{\delta \rho(r,r',t')} \frac{\delta \rho(r,r',t')}{\delta \varphi_k^*(s,t)} dr dr' dt' \ \delta \varphi_k^*(s,t) ds dt \qquad (2.2.15) \\ &= -\iint \int h(s,r,t) \varphi_k(r,t) dr \ \delta \varphi_k^*(s,t) ds dt \qquad (2.2.16) \end{aligned}$$

where line (2.2.15) makes use of (A.5) and line (2.2.16) makes use of (2.2.6) with an

added time variable. The differential for the total action J is

$$\begin{aligned}\delta J &= \delta J_1 + \delta J_2 \\ &= \iint \left(i\hbar D_t \varphi_k(s,t) - \int h(s,r,t)\varphi_k(r,t)dr \right) \delta\varphi_k^*(s,t)dsdt \\ &= 0.\end{aligned}$$

As for the static version, variation of φ_k^* is arbitrary so the term in the parentheses is equal to zero, resulting in the N TDHF equations

$$i\hbar\frac{\partial}{\partial t}\varphi_k(s,t) = \int h(s,r,t)\varphi_k(r,t)dr \tag{2.2.17}$$

for $k = 1, 2, ..., N$.

Checking the variation over φ_k instead can similarly be done and will lead to the differential

$$\begin{aligned}\delta J &= \iint \left(-i\hbar D_t \varphi_k^*(s,t) - \int h(r',s,t)\varphi_k^*(r',t)dr' \right) \delta\varphi_k(s,t)dsdt \\ &= 0\end{aligned}$$

which leads to the complex conjugate equations to (2.2.17).

2.3 Nucleon-nucleon interaction

Up until now there has been no explicit expression of the N-body Hamiltonian, either $\hat{H}$ for the total system or h for single particles. For the static HF case, evaluation of $\langle\hat{H}\rangle$ is not explicitly done but instead the average energy of the system consists of many parts in the forms of integrals over energy density functionals, such as a kinetic term, a Coulomb term, a nuclear term and perhaps more terms depending on the setup of the problem. The single particle Hamiltonian is then derived directly from these EDFs. The Coulomb and nuclear term will be outlined in this section. The nuclear interaction between nucleons will be described with a phenomenological Skyrme effective interaction in this thesis.

2.3.1 Skyrme effective interaction

There are a few models commonly used for the nucleon-nucleon interaction. These include the Skyrme effective interaction [189] as well as the Gogny interaction [68]. More modern approaches now, such as the quark-meson coupling model [72] (a relativistic

mean field model), have been used to parametrise the Skyrme interaction [115]. The Skyrme interaction has been shown to reproduce basic nuclear properties reasonably and because of its zero range nature, it is quicker for computational purposes than the finite ranged Gogny interaction. An important point about Skyrme effective interaction in use with HF methods is that it is used for both a single nucleus and for reactions, for example to extract the ion-ion potential. This means that the underpinning treatment of structure and reactions is the same within the HF and TDHF approach [12, 129, 176].

The Skyrme two-body interaction in a standard form neglecting tensor terms is

$$\begin{aligned}\hat{v}_{\mathrm{Sk}}(r_j, r_k) = t_0\left(1 + x_0\hat{P}_\sigma\right)\hat{\delta} + \frac{t_1}{2}\left(1 + x_1\hat{P}_\sigma\right)\left(\hat{\mathbf{k}}^{*2}\hat{\delta} + \hat{\delta}\hat{\mathbf{k}}^2\right) + t_2\left(1 + x_2\hat{P}_\sigma\right)\left(\hat{\mathbf{k}}^* \cdot \hat{\delta}\hat{\mathbf{k}}\right) \\ + \frac{t_3}{6}\left(1 + x_3\hat{P}_\sigma\right)\rho^\gamma(\hat{\mathbf{R}})\hat{\delta} + iW_0\hat{\boldsymbol{\sigma}} \cdot \left(\hat{\mathbf{k}}^* \times \hat{\delta}\hat{\mathbf{k}}\right), \qquad (2.3.1)\end{aligned}$$

which acts on particles j and k in the N-body system. The variables $r_j = (\mathbf{r}_j s_j q_j)$ include position, spin and isospin coordinates. There are ten parameters for $\hat{v}_{\mathrm{Sk}}$, labelled $t_0, t_1, t_2, t_3, x_0, x_1, x_2, x_3, \gamma$ and W_0. The term containing W_0 is the spin-orbit part of the interaction. Other terms arising in (2.3.1) are defined as

$$\hat{\delta} = \delta(\mathbf{r}_j - \mathbf{r}_k), \qquad \hat{\boldsymbol{\sigma}} = \left(\hat{\boldsymbol{\sigma}}^j + \hat{\boldsymbol{\sigma}}^k\right)\begin{bmatrix} s_j \\ s_k \end{bmatrix},$$

$$\hat{\mathbf{R}} = \frac{1}{2}\left(\mathbf{r}_j - \mathbf{r}_k\right), \qquad \hat{\boldsymbol{\sigma}}^j = \sum_{i=1}^{3}\sigma_i^j\mathbf{e}_i,$$

$$\hat{\mathbf{k}} = \frac{1}{2i}\left(\nabla_j - \nabla_k\right), \qquad \hat{P}_\sigma = \frac{1}{2}\left(\hat{1} + \hat{\boldsymbol{\sigma}}^j\hat{\boldsymbol{\sigma}}^k\right)\begin{bmatrix} s_j \\ s_k \end{bmatrix},$$

where $\sigma_i, i = 1, 2, 3$ are the Pauli spin matrices and $\hat{P}_\sigma$ is the Pauli operator that swaps the spin coordinates (s_j and s_k) of particles j and k.

Because of the appearance of $\hat{\delta}$ in (2.3.1), the Skyrme effective interaction is a contact force that is apparent when two particles are at the same point in coordinate space. As well as being a contact force, the Skyrme interaction is also density dependent from the ρ^γ term and velocity dependent from the appearance of $\hat{\mathbf{k}}$ terms.

The Skyrme energy density functional can be found by

$$\mathcal{E}_{\mathrm{Sk}} = \frac{1}{2}\sum_{j,k=1}^{N}\langle\Phi, \hat{v}_{\mathrm{Sk}}(r_j, r_k)\Phi\rangle, \qquad (2.3.2)$$

for the HF total wavefunction Φ. In practice, $\mathcal{E}_{\mathrm{Sk}}$ is found using local densities, writing

in notation of Ref. [24],

$$\mathcal{E}_{\rm Sk} = b_0\rho^2 + b_1\rho\tau - b_2\rho\Delta\rho + b_3\rho^{\gamma+2} \tag{2.3.3}$$

$$- \sum_q \left(B_0\rho_q^2 + B_1\rho_q\tau_q - B_2\rho_q\Delta\rho_q + B_3\rho^\gamma\rho_q^2 \right) \tag{2.3.4}$$

$$- b_4\rho\nabla\cdot\mathbf{J} - b_5\mathbf{J}^2 - \sum_q \left(B_4\rho_q\nabla\cdot\mathbf{J}_q - B_5\mathbf{J}_q^2 \right) \tag{2.3.5}$$

$$- b_1\mathbf{j}^2 + b_6\mathbf{S}^2 + b_7\rho^\gamma\mathbf{S}^2 + \sum_q \left(-B_1\mathbf{j}_q^2 - B_6\mathbf{S}_q^2 - B_7\rho^\gamma\mathbf{S}_q^2 \right) \tag{2.3.6}$$

$$+ b_4\mathbf{j}\cdot\nabla\times\mathbf{S} + \sum_q B_4\mathbf{j}_q\cdot\nabla\times\mathbf{S}_q. \tag{2.3.7}$$

The terms that are symmetric under time reversal (time even) are in lines (2.3.3), (2.3.4) and (2.3.5). The time odd terms are lines (2.3.6) and (2.3.7). The Skyrme EDF can also include more time odd terms that may be used in TDHF calculations [114, 212]. The spin-orbit part of the interaction are contained in the terms in lines (2.3.5) and (2.3.7). The relationship between parameters $(x_i, t_i, W_0, \gamma), i = 0, ..., 3$ and $(b_j, B_j), j = 1, ..., 7$ are listed in Appendix B.1. When $q = p$ or n the local densities appearing in the expression for $\mathcal{E}_{\rm Sk}$ are defined as

$$\rho_q = \sum_j \sum_s |\varphi_j|^2 \tag{2.3.8}$$

$$\tau_q = \sum_j \sum_s |\nabla\varphi_j|^2 \tag{2.3.9}$$

$$\mathbf{j}_q = \frac{1}{2i} \sum_j \sum_s \left[\varphi_j^*\nabla\varphi_j - \varphi_j(\nabla\varphi_j)^* \right] \tag{2.3.10}$$

$$\mathbf{J}_q = \frac{1}{2i} \sum_j \sum_{ss'} \left[\varphi_j^*(\mathbf{r}s'q)\nabla\times\hat{\boldsymbol{\sigma}}_{s's}\varphi_j(\mathbf{r}sq) - (\nabla\times\hat{\boldsymbol{\sigma}}_{s's}\varphi_j(\mathbf{r}s'q))^*\varphi_j(\mathbf{r}sq) \right] \tag{2.3.11}$$

$$\mathbf{S}_q = \sum_j \sum_{ss'} \varphi_j^*(\mathbf{r}s'q)\varphi_j(\mathbf{r}sq)\hat{\boldsymbol{\sigma}}_{s's} \tag{2.3.12}$$

and $\hat{\boldsymbol{\sigma}}_{s's} = \hat{\boldsymbol{\sigma}}(s', s)^\top$. When there is no q subscript, the resulting density is the sum over $q = p, n$.

The Skyrme energy is then given by (with the usual 3D volume integral)

$$E_{\rm Sk} = \int \mathcal{E}_{\rm Sk}(\mathbf{r}) d^3r. \tag{2.3.13}$$

2.3.2 Coulomb interaction

As the Skyrme EDF describes only the nucleon-nucleon interaction, the Coulomb interaction must be included for protons. The total Coulomb energy is split into a direct term

and an exchange term [131]. The direct term is

$$E^d_{\text{Coul}} = \frac{e^2}{2} \iint \frac{\rho_p(\mathbf{r})\rho_p(\mathbf{r}')}{|\mathbf{r}-\mathbf{r}'|} d^3r' d^3r.$$

This can be simplified when using the fact that the Coulomb potential satisfies Poisson's electrostatic equation

$$V_C(\mathbf{r}) = e^2 \int \frac{\rho_p(\mathbf{r}')}{|\mathbf{r}-\mathbf{r}'|} d^3r',$$

so

$$E^d_{\text{Coul}} = \frac{1}{2} \int \rho_p(\mathbf{r}) V_C(\mathbf{r}) d^3r.$$

The exchange term, using the Slater approximation [64, 70], is

$$E^e_{\text{Coul}} = -\frac{3e^2}{4} \left(\frac{3}{\pi}\right)^{\frac{1}{3}} \int \rho_p(\mathbf{r})^{\frac{4}{3}} d^3r.$$

The total Coulomb energy in the HF method is given by the sum of the two terms,

$$E_{\text{Coul}} = E^d_{\text{Coul}} + E^e_{\text{Coul}}, \tag{2.3.14}$$

and the resulting Coulomb EDF is

$$\mathcal{E}_{\text{Coul}} = \frac{1}{2}\rho_p V_C - \frac{3}{4}e^2 \left(\frac{3}{\pi}\right)^{\frac{1}{3}} \rho_p^{\frac{4}{3}}. \tag{2.3.15}$$

2.3.3 Single particle Hamiltonian

The HF single particle Hamiltonian h_q for protons or neutrons is derived from taking functional derivatives of $\mathcal{E} = \mathcal{E}_{\text{kin}} + \mathcal{E}_{\text{Sk}} + \mathcal{E}_{\text{Coul}}$ with respect to different local densities [24, 154] with $\mathcal{E}_{\text{Sk}}$ given in (2.3.3)–(2.3.7) and $\mathcal{E}_{\text{Coul}}$ given in (2.3.15). The EDF for kinetic energy of the system is given by

$$\mathcal{E}_{\text{kin}} = \frac{\hbar^2}{2m}\tau. \tag{2.3.16}$$

The expression for the single particle Hamiltonian ($q = p, n$) is

$$h_q = -\nabla \cdot \frac{\delta \mathcal{E}}{\delta \tau_q} \nabla + \frac{\delta \mathcal{E}}{\delta \rho_q} - i \frac{\delta \mathcal{E}}{\delta \mathbf{J}_q} \cdot \nabla \times \hat{\boldsymbol{\sigma}} + \frac{1}{2i} \left\{ \frac{\delta \mathcal{E}}{\delta \mathbf{j}_q}, \nabla \right\} + \frac{\delta \mathcal{E}}{\delta \mathbf{S}_q} \cdot \hat{\boldsymbol{\sigma}}. \tag{2.3.17}$$

When h acts on a single particle wavefunction $\varphi_j(\mathbf{r}sq)$ with isospin q then

$$h_q\varphi_j(\mathbf{r}sq) = \sum_{s'}\Bigg(-\nabla\cdot\frac{\delta\mathcal{E}}{\delta\tau_q}\nabla\delta_{s's} + \frac{\delta\mathcal{E}}{\delta\rho_q}\delta_{s's} - i\frac{\delta\mathcal{E}}{\delta\mathbf{J}_q}\cdot\nabla\times\hat{\boldsymbol{\sigma}}_{s's} + \frac{1}{2i}\left\{\frac{\delta\mathcal{E}}{\delta\mathbf{j}_q},\nabla\right\}\delta_{s's} + \frac{\delta\mathcal{E}}{\delta\mathbf{S}_q}\cdot\hat{\boldsymbol{\sigma}}_{s's}\Bigg)\varphi_j(\mathbf{r}s'q). \tag{2.3.18}$$

The explicit forms of the derivatives with respect to the $(b_i, B_i), i = 1, ..., 7$ parameters are also presented in Appendix B.1.

2.4 Pairing correlations

Mean field theory starts with the assumption of independent particles. The downside of this is that correlations within an N-body system must be added separately. The single particle HF Hamiltonian (2.3.17) is density dependent which implicitly incorporates some correlations. However, to describe a more realistic nuclear system, the pairing two-body correlations must be included additionally. The Bardeen–Cooper–Schrieffer (BCS) theory [8] can be used within HF to account for pairing. A generalised marriage of these two theories is the Hartree–Fock–Bogoliubov (HFB) theory, where instead of the system comprising independent particles, the latter are independent quasiparticles. The mean field and pairing field are both self consistent in this framework.

A simplification of HFB theory is to use what is called HF+BCS where the pairing field is just an additional interaction term separate to the nucleon-nucleon interactions described in section 2.3 and the single particle wavefunctions take on the BCS occupation numbers. In this thesis, pairing correlations in nuclei are accounted for only in the ground state using the HF+BCS theory [14]. HF+BCS is a good approximation for well bound nuclei, but full HFB equations are recommended for drip line or weakly bound nuclei [12].

The BCS wavefunction of an N-body system for paired particles k and $\bar{k}$ (in the canonical basis for single particles) is

$$|\Psi_{\mathrm{BCS}}\rangle = \prod_{k>0}(u_k + v_k a_k^\dagger a_{\bar{k}}^\dagger)|-\rangle, \tag{2.4.1}$$

where v_k^2 is the occupation number of particle k and is related to u_k by $|u_k|^2 + |v_k|^2 = 1$. The occupation numbers also satisfy

$$2\sum_{k>0} v_k^2 = N.$$

For a system with spherical symmetry, the particle $\bar{k}$ has the same quantum numbers $n\ell j$ as particle k but with a reversed sign in magnetic quantum number, m.

A density-dependent delta pairing force [13, 106] is used to describe the pairing interaction between nucleons. It is in the form

$$\hat{v}_{\text{pair}}(\mathbf{r}_j, \mathbf{r}_k) = \tilde{t_0}\delta\left(\mathbf{r}_j - \mathbf{r}_k\right)\left(1 - \alpha\frac{\rho(\mathbf{R})}{\tilde{\rho}_0}\right), \tag{2.4.2}$$

where $\mathbf{R} = \frac{1}{2}(\mathbf{r}_j + \mathbf{r}_k)$. The pairing energy density functional is defined as

$$\mathcal{E}_{\text{pair}} = \sum_{k>0}\sum_{j>0}\langle\Phi, \hat{v}_{\text{pair}}\Phi\rangle f_j u_j v_j f_k u_k v_k,$$

with the factors

$$f_k = \left(1 + \exp\left(\frac{\epsilon_k - \lambda - \Delta\varepsilon}{\mu}\right)\right)^{-\frac{1}{2}}, \tag{2.4.3}$$

where ϵ_k is the single particle energy of particle k, $\Delta\varepsilon$ is a specified energy above the Fermi energy of particle k for the cutoff of the Fermi function f_k so that pairing is still apparent on single particle states at or just above (within $\Delta\varepsilon$) the Fermi energy, and μ is a fixed energy. The parameter λ is a Lagrange multiplier for the variation

$$\delta\langle\Psi_{\text{BCS}}, (\hat{H} - \lambda\hat{N})\Psi_{\text{BCS}}\rangle = 0,$$

for the HF Hamiltonian $\hat{H}$ and particle number operator $\hat{N}$, it can be constrained by the equations

$$N = 2\sum_{k>0} v_k^2 = \sum_k \left[1 - \frac{\epsilon_k - \lambda}{\sqrt{(\epsilon_k - \lambda)^2 + f_k\Delta_{k\bar{k}}^2}}\right]. \tag{2.4.4}$$

An explanation and derivation of the BCS equations can be found in Ref. [154], as well as the solution for v_k above. The pairing gap factor is given by

$$\Delta_{k\bar{k}} = \sum_{m>0} f_m u_m v_m \langle\Phi, \hat{v}_{km}\Phi\rangle.$$

When incorporating BCS pairing into HF theory, the local density terms (2.3.8)–(2.3.12) should now sum over paired states $\{k, \bar{k}\}$ instead of each independent particle j and the summands should be multiplied by the occupation number v_k^2.

The pairing energy is defined as

$$E_{\text{pair}} = \int \mathcal{E}_{\text{pair}}(\mathbf{r}) d^3r. \tag{2.4.5}$$

2.5 Computational methods

2.5.1 Static HF calculations

All static HF ground state calculations in this thesis are made with the EV8 code [25]. This solves the static HF equations (2.2.14) on a 3D cartesian grid and the resulting single particle wavefunction solutions are discretised over the grid. A more recent edition of this code exists [157] with improvements in numerical accuracy such as using Lagrange functions for derivatives instead of finite differences formula such as used in Ref. [25] amongst other things.

In solving the static HF equations, there are three spatial planes of symmetry ($x = 0$, $y = 0$ and $z = 0$) and also a time reversal symmetry assumed. The spatial symmetries mean only an eighth of a nucleus need be calculated. There are no further spatial restrictions for the solutions in this 8th of a box so the nucleus may be triaxial. The time reversal symmetry applies to the total wavefunction (only time even terms in $\mathcal{E}_{\text{Sk}}$ are needed) and so degeneracy in single particle wavefunctions with the same eigenvalue as per Kramer's rule applies. Because of this, only even-even nuclei should be calculated with EV8 [25].

Algorithm for ground state

An outline of the procedure solving HF equations as done by EV8 follows, the imaginary time method, replacing time t by $-it$, is used to iterate static wavefunction solutions of single particle orbitals [48] to achieve convergence. Starting with iteration number $n = 0$, the guess for the mean field potential and single particle wavefunctions of a nucleus with A nucleons are the Nilsson potential and the initial wavefunctions arising from this [25]. Using these wavefunctions, with the superscript indicating the iteration number:

1. An initial set of single particle wavefunctions is chosen, denoted by $\{\varphi_j^{(n)}\}, j = 1, ..., A$, and the density matrix $\rho^{(n)}$ (2.3.8) is obtained.

2. The HF Hamiltonian for the iteration is calculated with $h^{(n)} = h[\rho^{(n)}]$ (2.3.17).

3. A new set of wavefunctions is generated via

$$\psi_j^{(n+1)} = \exp\left(-\frac{\Delta t}{\hbar} h\right) \varphi_j^{(n)},$$

with (2.3.18) (the first order Taylor expansion of the exponential operator is used in the code).

4. The new wavefunctions are reorthonormalised. Because the imaginary time method is employed, the exponential operator in step 3 is no longer unitary so the resulting $\psi_j^{(n+1)}$ are not orthonormal. Orthonormalisation must be restored and can be achieved for example with the Gram–Schmidt method.

5. The occupation numbers v_k (2.4.4) are now solved using the single particle energies $\langle \varphi_k, h\varphi_k \rangle$.

These steps are repeated using the wavefunctions from the previous iteration to begin with until convergence in the φ_j is seen.

Binding energy

The total binding energy (BE) for a HF ground state nucleus is given by

$$\mathrm{BE} = E_{\mathrm{kin}} + E_{\mathrm{Sk}} + E_{\mathrm{Coul}} + E_{\mathrm{pair}}. \tag{2.5.1}$$

Each energy term is an integral over its corresponding energy density functional,

$$E_i = \int \mathcal{E}_i(\mathbf{r}) d^3 r. \tag{2.5.2}$$

Expressions for $E_{\mathrm{Sk}}, E_{\mathrm{Coul}}$ and E_{pair} are given in (2.3.13), (2.3.14) and (2.4.5) respectively. The kinetic energy term is given by applying (2.5.2) to the corresponding EDF in (2.3.16).

Frozen HF potential

The frozen HF method is used to compute nucleus-nucleus bare potentials, it assumes that the two nuclei are frozen in their HF ground state at all points of the reaction. The frozen HF potential [180, 225] between them, $V(\mathbf{r})$, is calculated. For the nuclear part of the potential, the form involves the energy of the total system minus the energies of the separate systems, where each energy is an integral of an energy density functional [33],

using Skyrme EDF. The frozen HF nuclear potential is given by

$$V_N(\mathbf{r}) = E_{\mathrm{Sk}}(\mathbf{r}) - E_{\mathrm{Sk}}[\rho_1] - E_{\mathrm{Sk}}[\rho_2] \tag{2.5.3}$$

where the energy for the total system is,

$$E_{\mathrm{Sk}}(\mathbf{r}) = \int \mathcal{E}_{\mathrm{Sk}}[\rho_1(\mathbf{r}') + \rho_2(\mathbf{r} - \mathbf{r}')]d^3r', \tag{2.5.4}$$

and for each separate nucleus,

$$E_{\mathrm{Sk}}[\rho_j] = \int \mathcal{E}_{\mathrm{Sk}}[\rho_j(\mathbf{r})]d^3r. \tag{2.5.5}$$

The total frozen HF bare potential will also include the Coulomb part, which is calculated in a similar way using the Coulomb EDF in (2.3.15),

$$V_C(\mathbf{r}) = E_{\mathrm{Coul}}(\mathbf{r}) - E_{\mathrm{Coul}}[\rho_1] - E_{\mathrm{Coul}}[\rho_2].$$

Using the proton densities only,

$$E_{\mathrm{Coul}}(\mathbf{r}) = \int \mathcal{E}_{\mathrm{Coul}}[\rho_{1p}(\mathbf{r}') + \rho_{2p}(\mathbf{r} - \mathbf{r}')]d^3r'.$$

The total bare potential is then

$$V(\mathbf{r}) = V_C(\mathbf{r}) + V_N(\mathbf{r}). \tag{2.5.6}$$

The coordinate $\mathbf{r}$ is the vector between the centres of the two nuclei so impact parameter or angular momentum become irrelevant in frozen HF calculations. This approach does not include Pauli repulsion which can be important inside the barrier [186].

2.5.2 TDHF calculations

Algorithm for evolving MF

To solve the TDHF equations on a discretised cartesian 3D grid and also with discretised time steps, the TDHF3D code [101] uses the predictor-corrector method to calculate the HF Hamiltonian and wavefunctions at the midpoint of the small time interval $[t_n, t_{n+1}]$. Conservation of energy means that the HF single particle Hamiltonian is symmetric with respect to time translation (and reversal) over the small time interval $[t_n, t_{n+1}] = [t_n, t_n + \Delta t]$.

Unlike for the static codes, the TDHF3D code includes all time even and time odd terms from the Skyrme EDF (except for terms with $\mathbf{J}^2$), so the only symmetries existing are spatial and there is no Kramer degeneracy in wavefunctions from time reversal symmetry.

The predictor corrector method for each time iteration n for the time dependent case starting from $n = 0$ [58, 176] is

1. An initial set of wavefunctions for the system $\varphi_j^{(n)}$ is used to calculate the density matrix $\rho(t_n) = \rho^{(n)}$.

2. The Hamiltonian at t_n is given by $h[\rho^{(n)}]$.

3. A new set of wavefunctions is predicted for the next time step

$$\tilde{\varphi}_j^{(n+1)} = \exp\left(\frac{-i\Delta t}{\hbar} h^{(n)}\right) \varphi_j^{(n)}.$$

   These wavefunctions are used to calculate the predicted density matrix $\tilde{\rho}^{(n+1)}$.

4. The corrected density matrix for the midpoint of the time interval is given by

$$\rho\left(t_n + \frac{\Delta t}{2}\right) = \frac{\rho^{(n)} + \tilde{\rho}^{(n+1)}}{2},$$

   which is then used to calculate the corrected Hamiltonian at $t_n + \frac{\Delta t}{2}$.

5. The corrected set of wavefunctions for time t_{n+1} is now given by

$$\varphi_j^{(n+1)} = \exp\left(\frac{-i\Delta t}{\hbar} h\left(t_n + \frac{\Delta t}{2}\right)\right) \varphi_j^{(n)}.$$

The steps are repeated until final time t_{final}.

Transfer probabilities

In Chapter 4, transfer channels within the TDHF approach are explored which involves calculating transfer probabilities. Transfer probabilities are calculated using the particle number projection method, presented in Ref. [174].

In order to produce probabilities, first the particle counting operator is needed. For particles with isospin q,

$$\hat{N}_R^q = \sum_s \int_U \hat{a}^\dagger(\mathbf{r}sq)\hat{a}(\mathbf{r}sq)H(x - x_0)d^3r,$$

where U is the entire calculation box and R is the region defined by the Heaviside function within the integral, taken as a region to the right of a plane oriented in the yz directions. In principle, R can be defined in more complicated ways. This operator will count all the particles in the region defined by $H(x-x_0)$ using the creation and annihilation operators at every point within R.

In second quantization, the creation and annihilation operators at the point $(\mathbf{r}sq)$ can be written as the sum involving single particle states with the same coordinates

$$\hat{a}^\dagger(\mathbf{r}sq) = \sum_{i=1}^{N} \varphi_i^*(\mathbf{r}sq)\hat{a}_i^\dagger, \qquad\qquad \hat{a}(\mathbf{r}sq) = \sum_{i=1}^{N} \varphi_i(\mathbf{r}sq)\hat{a}_i.$$

The creation and annihilation operators for a single particle state $\hat{a}_i^\dagger$ and $\hat{a}_i$ are now not dependent on coordinates. Rewriting $\hat{N}_R^q$,

$$\begin{aligned}
\hat{N}_R^q &= \sum_s \int_U \left(\sum_{i=1}^{N} \varphi_i^*(\mathbf{r}sq)\hat{a}_i^\dagger\right)\left(\sum_{j=1}^{N} \varphi_j(\mathbf{r}sq)\hat{a}_j\right) H(x-x_0)d^3r \\
&= \sum_s \sum_{i=1}^{N} \int_U \varphi_i^*(\mathbf{r}sq)\hat{a}_i^\dagger \sum_{j=1}^{N} \varphi_j(\mathbf{r}sq)\hat{a}_j H(x-x_0)d^3r \\
&= \sum_s \sum_{i=1}^{N}\sum_{j=1}^{N} \int_U \varphi_i^*(\mathbf{r}sq)\varphi_j(\mathbf{r}sq)H(x-x_0)d^3r\ \hat{a}_i^\dagger\hat{a}_j \\
&= \sum_{i=1}^{N}\sum_{j=1}^{N} \langle i,j\rangle_R^q \hat{a}_i^\dagger\hat{a}_j
\end{aligned}$$

using the definition

$$\langle i,j\rangle_R^q := \sum_s \int_U \varphi_i^*(\mathbf{r}sq)\varphi_j(\mathbf{r}sq)H(x-x_0)d^3r.$$

The expectation value of $\hat{N}_R^q$ is

$$\begin{aligned}
\langle \hat{N}_R^q \rangle &= \left\langle \sum_{i=1}^{N}\sum_{j=1}^{N} \langle i,j\rangle_R^q \hat{a}_i^\dagger\hat{a}_j \right\rangle \\
&= \sum_{i=1}^{N}\sum_{j=1}^{N} \langle i,j\rangle_R^q \langle \hat{a}_i^\dagger\hat{a}_j\rangle \\
&= \sum_{i=1}^{N}\sum_{j=1}^{N} \langle i,j\rangle_R^q v_i^2\delta_{ij} \\
&= \sum_{i=1}^{N} \langle i,i\rangle_R^q v_i^2.
\end{aligned}$$

using the definition of $\langle \hat{a}_i^\dagger\hat{a}_j\rangle = v_i^2\delta_{ij}$.

To find the probability of a region of the box having $\mathcal{N}$ particles, the particle number projection operator is used. This projects the system's HF wavefunction onto a particle number $\mathcal{N}$. When $q = p$ or n and now dropping this label,

$$\hat{P}_R^{\mathcal{N}} = \frac{1}{2\pi}\int_0^{2\pi} \exp\left(i\theta(\hat{N}_R - \hat{1}\mathcal{N})\right) d\theta.$$

The projector acting on a HF wavefunction will extract the part of the wavefunction with $\mathcal{N}$ particles. Since $\hat{1}\mathcal{N}$ commutes with $\hat{N}_R$ then the exponential term can be split. The expectation value of the projector is

$$\langle \hat{P}_R^{\mathcal{N}} \rangle = \frac{1}{2\pi}\int_0^{2\pi} e^{-i\theta\mathcal{N}} \langle \Phi, e^{i\theta\hat{N}_R}\Phi\rangle d\theta,$$

where the inner product is the determinant of the matrix (full derivation in e.g. Ref. [170]) that has components

$$\begin{aligned} F_{ij} &= \sum_s \int_U \varphi_j^*(\mathbf{r}sq)\varphi_k(\mathbf{r}sq)e^{i\theta H(x-x_0)}d^3r \\ &= \sum_s \int_U \left(\varphi_j^*(\mathbf{r}sq)\varphi_k(\mathbf{r}sq)e^{i\theta}H(x-x_0) + \varphi_j^*(\mathbf{r}sq)\varphi_k(\mathbf{r}sq) - \varphi_j^*(\mathbf{r}sq)\varphi_k(\mathbf{r}sq)H(x-x_0)\right) d^3r \\ &= (e^{i\theta}-1)\langle i,j\rangle_R + \delta_{ij}. \end{aligned}$$

The BCS wavefunction (2.4.1) can be written as sums over different numbers of pairs of particles and does not conserve particle number [154]. Because of this, this particle number projection method will not project the wavefunction on to a good particle number for paired systems as it is formulated on the fact that Φ is a Slater determinant (an eigenvalue of the particle number operator). In the event where systems have no pairing mean field, that is to say magic in neutron or proton number, then the projection can be applied.

For systems with violation in particle number (paired systems), a double projection technique may be applied [162, 170, 171] to rectify this. In this thesis, only single projection technique is used so transfer probabilities are only taken for systems that are magic in protons or neutrons.

2.5.3 Skyrme EDF parametrisation

Only time even parts of the Skyrme EDF are of use in static HF calculations, and all even and odd parts (except for terms with $\mathbf{J}^2$) are used for TDHF calculations in this thesis. There is an overwhelming number of parametrisations for the Skyrme two-body

interaction (2.3.1) to choose from. Fits of the parameters should reproduce several nuclear properties observed experimentally, some examples including binding energy, compressibility and saturation properties. To constrain the parameters, experimental data of the properties for doubly magic nuclei such as ^{48,48}Ca, ^{132}Sn and ^{208}Pb are used.

In this thesis, two parametrisations are chosen to use in TDHF calculations. They are the SLy4d [101] and UNEDF1 [104] parametrisations. Initially all calculations were done with SLy4d, however, it was necessary to check that the results from reactions or vibrations calculations were not interaction dependent. Modern parametrisations of the Skyrme interaction, such as UNEDF1, generalise the spin-orbit part of the Skyrme EDF [152], using two parameters W_0 and W_0' corresponding to b_4 and B_4 in (2.3.5) and (2.3.7) to describe the spin-orbit contribution. For SLy4d and older parametrisations, $W_0 = W_0'$. Neither the SLy4d nor the UNEDF1 parametrisation uses time even spin-orbit $\mathbf{J}^2$ term in (2.3.5).

Many parametrisations incorporate centre of mass corrections for the HF ground state. When calculating the HF ground state, the centre of the nucleus is fixed at some central position $\mathbf{r} = \mathbf{0}$ in the box. As it is a static calculation, the expectation value for momentum is also zero, $\langle \hat{\mathbf{p}} \rangle = 0$, although fluctuations are still existing in the form $\langle \hat{\mathbf{p}}^2 \rangle \neq 0$.

For a nucleus of mass A,

$$\hat{\mathbf{p}} = \sum_{j=1}^{A} \hat{\mathbf{p}}_j = \sum_{j=1}^{A} (-i\hbar\nabla_j)$$

meaning

$$\begin{aligned} \hat{\mathbf{p}}^2 &= \left(\sum_{j=1}^{A} \hat{\mathbf{p}}_j \right)^2 \\ &= \sum_{j=1}^{A} \hat{\mathbf{p}}_j^2 + \sum_{1 \leq i < j \leq A} \hat{\mathbf{p}}_i \cdot \hat{\mathbf{p}}_j, \end{aligned}$$

broken up into one-body and two-body terms. Often the two-body term is ignored (depending on the Skyrme parametrisation) and the centre of mass correction for a HF calculation of a nucleus with mass A maps the total kinetic energy term of the

Hamiltonian of the whole system to

$$\begin{aligned}\hat{T} &\mapsto \hat{T} - \frac{\hat{\mathbf{p}}^2}{2Am} \\ &\simeq \hat{T} - \sum_{j=1}^{A} \frac{\hat{\mathbf{p}}_j^2}{2Am},\end{aligned}$$

ignoring the two-body part of $\hat{\mathbf{p}}^2$. With this correction, the $\hat{\mathbf{p}}^2$ term produces an energy correction term that becomes present in the binding energy (2.5.1) labelled as E_{corr}.

For reactions calculations involving nuclei of different masses, the centre of mass correction would not be appropriate due to the use of different A values for the two colliding partners [104, 176]. It was for this reason that SLy4d and UNEDF1 were used as parametrisations as neither contain centre of mass corrections so they are suitable for reactions. For vibrations calculations on a single nucleus, the centre of mass correction can be included. However for consistency between vibrations and reactions calculations, SLy4d and UNEDF1 are used for both reactions and vibrations calculations in this thesis. As a result there is no E_{corr} term in the HF binding energy.

In addition to Sly4d and UNEDF1, three other parametrisations (all of SLy [37, 38] type) were used for parts of this thesis. One extra in Chapter 3, and two in fusion for static frozen HF calculations. The SLy4 [38] parametrisation is obtained with the same fitting procedure as SLy4d but it includes the centre of mass correction. This was used in vibrations calculations where centre of mass correction is not an issue. Even by just removing centre of mass correction from SLy4 to SLy4d, vibrational spectra of the same nucleus produce rather different results. This is discussed in Chapter 3 (along with results with UNEDF1).

Two more SLy4 type fittings [179] were tested labelled as asym28 and asym36, denoting symmetry energies of 28 MeV and 36 MeV (usually symmetry energy is set at 32 MeV). Other than this, the fitting procedure is the same as for Sly4d and their $(x_i, t_i, W_0, W_0', \gamma)$ parameter values can be found in Appendix B.2. Presented in Fig. 2.1 are the frozen HF potential barriers for $^{40-54}$Ca+^{116}Sn with the Skyrme parametrisations SLy4d (circles), UNEDF1 (open squares), asym28 (diamonds) and asym36 (triangles). The potential barriers for these systems obtained by using the Akyüz–Winther potential [31] (crosses) are also shown as a comparison. In general, symmetry energy in a system decreases when proton and neutron numbers are more similar, and is compensated by an increase in Coulomb energy. For the same system with a decrease in symmetry energy, the resulting frozen HF potential barrier (maximum value of (2.5.6) which depends on Coulomb energy),

increases as seen by the points calculated with asym28, and vice versa. These two extra parametrisations are not included in the main body of this thesis.

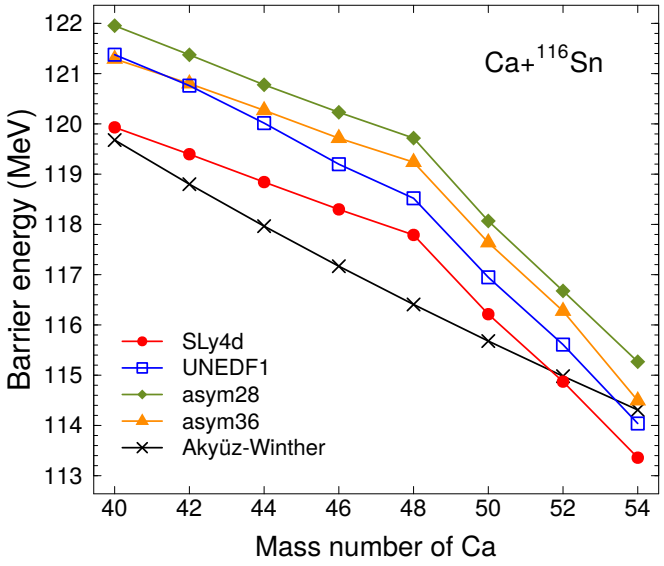

Fig. 2.1.: Frozen HF potential barriers for the systems $^{40-54}$Ca+^{116}Sn including all Skyrme parametrisations used in this thesis.

2.5.4 BCS pairing parameters

The first HF calculations with a Skyrme EDF that were done with an added BCS pairing functional was in Ref. [26]. For nuclei approaching the dripline, it is recommended that full HFB calculations should be done to treat pairing properly [12]. However, the SLy parametrisations are fit to be suitable for nuclei near the dripline [38] when used for a HF+BCS calculation.

Incorporating time-dependent pairing for TDHF calculations is difficult. Full TDHFB equations require a lot of computation time [2, 194] as it does not include time reversal symmetry and the pairing and mean field interact, unlike in the BCS approximation [12]. Using TDHF with the BCS approximation of pairing where the occupation numbers from the HF+BCS calculation are frozen for a time dependent calculation (frozen occupation approximation) is a good approximation to use instead of the full TDHFB theory [55, 164] and is used in this thesis. Recently, time-dependent BCS pairing has been incorporated into TDHF calculations which are less computationally demanding than TDHFB calculations [167].

As for the values of the parameters in the Fermi function f_k (2.4.3), they are inputs to the EV8 code and are kept at $\mu = 0.5$ MeV and $\Delta\varepsilon = 5$ MeV. The pairing density dependent interaction (2.4.2) has parameter values $\tilde{t}_0 = 1000$ MeV fm^3, $\tilde{\rho}_0 = 0.16$ fm^{-3} and $\alpha = 1$. The different values of α indicate if the pairing is surface pairing ($\alpha = 1$),

volume pairing ($\alpha = 0$) or "mixed" pairing contribution ($\alpha = 0.5$) which can have different effects on neutron halos of nuclei near the dripline [51, 52].

2.6 Initial conditions for HF calculations

Finally, the different initial conditions to set up the calculation space for each type of HF or TDHF calculation are detailed.

Box sizes are in fm and the mesh grid size is $\Delta x = 0.8$ fm. Box sizes are listed in $x - y - z$ direction with the collision axis (if relevant) being in the x direction. All time dependent calculations have a plane of symmetry at $z = 0$ to reduce calculation time.

1. For all HF ground state nuclei, which are calculated as an eighth of the nucleus (as per EV8), there are 14 points from the centre of the nucleus to the edge of the box, corresponding to a size of 11.2^3 fm^3.

2. For vibrations calculations in Chapter 3 that are fully time dependent calculations, the box size must be at least as large as holding half of a nucleus, corresponding to a box size of $22.4 \times 22.4 \times 11.2$ fm^3.

3. For both static and dynamic reactions appearing in Chapter 4 and central collisions in Chapter 5, the box size is $67.4 \times 22.4 \times 11.2$ fm^3. This setup gives two nuclei an initial separation distance between the centres of mass of 44.8 fm. This separation distance is chosen at such a large distance so that Coulomb excitation between the colliding partners are negligible at initial time.

4. For non-central collisions appearing in Chapter 5, the box size is increased in the y direction by a factor of two making a final box size of $67.4 \times 44.8 \times 11.2$ fm^3. The initial separation distance between collision partners is again 44.8 fm.

When discretising both sides of the time-dependent Schrödinger equation (2.1.2) for the HF Hamiltonian $\hat{H}$, the spatial mesh size is related to time step size by

$$\frac{1}{(\Delta x)^2} \propto \frac{1}{\Delta t},$$

considering just one spatial dimension. In order to optimise the number of points on which to solve the wavefunctions versus computational time, the values $\Delta x = 0.8$ fm and $\Delta t = 1.5 \times 10^{-24}$ s are a good compromise [25, 101, 176]. Because of the square relation from the spatial dimension, if the spatial mesh is decreased by for example 0.2 fm in order to have more points in the wavefunction solution, then the time mesh must be

decreased from 1.5×10^{-24} s to 1.0×10^{-24} s to compensate. Reduced time and spatial meshes increase computational time significantly.

For dynamic reaction calculations the initial centre of mass energy for the system can be set at a particular value. From this input, initial momentum is applied to each nucleon via a Galilean boost on the wavefunction

$$\varphi_j(t_0) = \exp\left(i\mathbf{k}_a \cdot \hat{\mathbf{r}}\right)\varphi_j^{\text{g.s.}},\ j = 1, ..., A,$$

acting on the ground state HF single particle wavefunctions $\varphi_j^{\text{g.s.}}$ in nucleus a with mass number A.

Vibrations 3

3.1 Overview

Studying collective vibrations of nuclei is interesting because it sheds light on the structure of the individual nucleus itself and also because collective vibrations play important roles in reaction studies, which will be explored in the following chapter. Many vibrational modes of nuclei across the chart have been observed experimentally. Those modes that are low in excitation energy (low-lying) are of particular interest as they play a more important role in reactions [74] compared to modes with high excitation energy or giant resonances.

To start discussions of vibrations, consider first the basic nuclear property of ground state spin, J, and parity, π. This property cannot be predicted by macroscopic models such as the liquid drop model (LDM). Models such as LDM only consider the bulk nature of a nucleus and consequently do not account for any physical phenomena arising from quantum shell effects. Microscopic approaches provide more insight into properties that arise from nuclear shell structure. Fully independent particle models, for example the shell model, can indeed explain experimentally observed ground states J^π both for odd mass nuclei and also even-even nuclei for which the ground state is always 0^+. For some excited states observed experimentally, pure independent particle states are not sufficient to describe them. A collective model, built upon the idea of coherent superposition of independent particle states, extends independent particle models and can account for collective motion in a nucleus.

A large portion of collective motion in nuclei can be generalised into two main categories of vibrations and rotations. Rotational motion refers to a nucleus that is statically deformed in its ground state, for example any of the actinides, and will naturally have rotational degrees of freedom when excited. This type of collective motion is not considered in this chapter. Instead, vibrations of nuclei are explored and are based on the assumption that the nucleus is spherical or near spherical in its ground state shape and that vibrational motion is not coupled to any degrees of rotational freedom. This applies to nuclides with magic shell closure. Collective vibrational motion of nuclei result in oscillations of electromagnetic multipole moment.

A standard way to study collective vibrations with a microscopic approach is with the

random phase approximation (RPA) method, first appearing in application to oscillations in electron gases [22] and then applied to nuclear physics [57]. It introduces a time-dependent external field or potential to the Hamiltonian of the many-body system, and the response of the particles to this is analysed. The response includes single particle excitations and also two-body correlations within the ground state. The time-dependent Hartree–Fock (TDHF) method with linear response theory [210] is also used to study collective vibrations. In the small amplitude limit, the TDHF equations are the same as the RPA equations [154]. Collective vibrations within this approach come from the attractive residual interaction in the mean field potential. For linear responses, the residual interaction of one-particle one-hole type is taken into account by TDHF and can be observed with one-body operators. Residual interactions describing higher order collisions are not included in the mean field approximation.

In this chapter, TDHF with linear response theory is used to calculate vibrational states of a chain of calcium nuclides. The systematics of one phonon octupole and quadrupole vibrations are studied focussing on the low-lying modes. This application of TDHF is a precursor to the application of TDHF to reaction studies as it involves just one nucleus at a time. Ground states of nuclei are calculated from the static HF method (outlined in section 2.5) which are then used to start a TDHF calculation that introduces a time dependent external potential that includes a vibrational one body operator on top of the usual HF Hamiltonian. The response of the nucleus to this external potential is used to obtain information such as excitation energies and transition strengths of particular multipole excitations.

Expressions of multipole moments on spherical nuclei arising from the electric field induced by a nucleus is outlined first, followed by details of linear response theory. Physical quantities from the calculated multipole moments are then presented. Finally, the single particle excitations contributing to the vibrations, using the single particle levels from HF ground state, are discussed.

3.2 Multipole moments

The multipole expansion for a nucleus is a general decomposition of its shape. A change in shape of a nucleus can arise from the interaction between the nucleus and an external system [23]. An example for this setup is exciting a nucleus via a Coulomb electric field. The external system will be taken as the scalar Coulomb electric field and the nucleus will be written as a continuous charge density distribution, ρ. The multipole expansion comes

from expanding the electric potential, φ, at any point external to the nuclear density, within some region Ω. The 3D volume integral over Ω for this is

$$\varphi(\mathbf{r}) = k_e \int_\Omega \frac{\rho(\mathbf{r}')}{|\mathbf{r} - \mathbf{r}'|} dV', \tag{3.2.1}$$

where the electrostatic constant $k_e = (4\pi\varepsilon_0)^{-1}$. Leaving out the charge density and expanding the rest of the integrand,

$$\begin{aligned} \frac{1}{|\mathbf{r} - \mathbf{r}'|} &= \frac{1}{(r^2 + r'^2 - 2rr'\cos\alpha)^{\frac{1}{2}}} \\ &= \frac{1}{r}\left(1 + \left(\frac{r'}{r}\right)^2 - \frac{2r'}{r}\cos\alpha\right)^{-\frac{1}{2}}, \end{aligned} \tag{3.2.2}$$

where α is the angle between the two vectors $\mathbf{r}$ and $\mathbf{r}'$. Recalling the Taylor expansion of the Legendre polynomials P_λ, the expression (3.2.2) can also be written as

$$\frac{1}{|\mathbf{r} - \mathbf{r}'|} = \frac{1}{r}\sum_{\lambda=0}^{\infty} \frac{r'^\lambda}{r^\lambda} P_\lambda(\cos\alpha). \tag{3.2.3}$$

Substituting (3.2.3) back into the electrostatic potential (3.2.1) and expanding the first few terms of the Legendre polynomials,

$$\begin{aligned} \varphi(\mathbf{r}) &= \frac{k_e}{r}\int_\Omega \rho(\mathbf{r}') \sum_{\lambda=0}^{\infty} \frac{r'^\lambda}{r^\lambda} P_\lambda(\cos\alpha) dV' \qquad (3.2.4) \\ &= \frac{k_e}{r}\int_\Omega \rho(\mathbf{r}') \left(1 + \frac{r'}{r}\cos\alpha + \frac{r'^2}{r^2}\left(\frac{3}{2}\cos^2\alpha - \frac{1}{2}\right) + \frac{r'^3}{r^3}\left(\frac{5}{2}\cos^3\alpha - \frac{3}{2}\cos\alpha\right) + ...\right) dV'. \end{aligned}$$

Multipole moments are already seen just in this initial expansion. The first term (zeroth power of r'/r) in the sum corresponds to the monopole moment, the second corresponds to the dipole, the third to the quadrupole and so on. However, the angle α between the vectors is not a "good" coordinate to use for the multipole expansions since many pairs of vectors in many orientations can have the same angle α between them. Spherical polar coordinates (r, θ, ϕ) are preferred instead. To convert the Legendre expansion into spherical polar coordinates, $\cos\alpha$ must first be expressed into spherical polar coordinates via the spherical cosine law (reducing the vectors $\mathbf{r}$ and $\mathbf{r}'$ to unit vectors $\hat{\mathbf{r}}, \hat{\mathbf{r}}'$),

$$\cos\alpha = \cos\theta\cos\theta' + \sin\theta\sin\theta'\cos(\phi - \phi'). \tag{3.2.5}$$

Since $\cos\alpha = \hat{\mathbf{r}} \cdot \hat{\mathbf{r}}'$ also, the spherical harmonic addition theorem along with (3.2.5) allows the Legendre polynomials in terms of $\cos\alpha$ to be expressed as

$$P_\lambda(\cos\alpha) = \frac{4\pi}{2\lambda+1} \sum_{\mu=-\lambda}^{\lambda} Y_{\lambda\mu}(\theta,\phi) Y^*_{\lambda\mu}(\theta',\phi') \tag{3.2.6}$$

where $Y_{\lambda\mu}(\theta,\phi)$ are the spherical harmonic functions of degree λ. Substituting (3.2.6) into (3.2.4), the electric potential in spherical polar coordinates becomes

$$\varphi(\mathbf{r}) = \frac{k_e}{r} \sum_{\lambda=0}^{\infty} \frac{1}{r^\lambda} \left(\frac{4\pi}{2\lambda+1} \right) \sum_{\mu=-\lambda}^{\lambda} Y_{\lambda\mu}(\theta,\phi) \int_\Omega \rho(\mathbf{r}') r'^\lambda Y^*_{\lambda\mu}(\theta',\phi') dV'.$$

The multipole moment, $Q_{\lambda\mu}$, is defined as

$$Q_{\lambda\mu} := \int_\Omega \rho(\mathbf{r}) r^\lambda Y^*_{\lambda\mu}(\theta,\phi) dV.$$

When nuclei are spherical to begin with, there is no dependence on the azimuthal angle, ϕ, and the only non-zero term for multipole moments are when $\mu = 0$. In this case, spherical harmonic functions are real and multipole moments are simply labelled with one index,

$$Q_\lambda = \int \rho(\mathbf{r}) r^\lambda Y_{\lambda 0}(\theta,\phi) dV. \tag{3.2.7}$$

From this, a one-body multipole operator on a system with A particles can be defined as

$$\hat{Q}_\lambda = \sum_{i=1}^{A} r^\lambda Y_{\lambda 0}(\hat{\mathbf{r}}), \tag{3.2.8}$$

where $\hat{\mathbf{r}}$ is now the position operator of the coordinates of $Y_{\lambda 0}$ and not the unit length vector.

3.3 Linear response theory with time-dependent Hartree–Fock

The evolution of a nucleus wavefunction in response to an external potential of multipole type will be solved (a modern derivation of the linear response theory formalism within the TDHF framework is outlined in e.g. Ref. [210]). The time-dependent wavefunction of the nucleus, Φ, will be written in terms of its excited states, Ψ_ν, which are eigenstates

of the static Schrödinger Hamiltonian

$$\hat{H}_0\Psi_\nu = E_\nu\Psi_\nu.$$

The energy and wavefunction of the ground state corresponds to $\nu = 0$.

The time-dependent wavefunction of the nucleus satisfies the non-relativistic time-dependent Schrödinger equation

$$\hat{H}(t)\Phi(t) = i\hbar\frac{\partial\Phi}{\partial t}(t), \tag{3.3.1}$$

where the total Hamiltonian for the system is split into two parts,

$$\hat{H}(t) = \hat{H}_0 + \hat{H}_e(t).$$

The external potential, denoted by $\hat{H}_e$, is in the form

$$\hat{H}_e(t) = \varepsilon\hat{Q}_\lambda f(t),$$

for a real scalar ε, real-valued time function f and multipole operator $\hat{Q}_\lambda$ in the form of (3.2.8). Since ε and f are real-valued, the three components in $\hat{H}_e$ are commutative.

For now it will be written $\hbar = 1$ to avoid cumbersome notation. As the total Hamiltonian is time-dependent, the unitary evolution operator for (3.3.1) includes the time ordering operator,

$$\begin{aligned} U(t,0) &= \mathcal{T}\left[\exp\left(-i\int_0^t \hat{H}(s)ds\right)\right] \\ &= \mathcal{T}\left[\exp\left(-i\int_0^t \hat{H}_0 + \hat{H}_e(s)ds\right)\right]. \end{aligned}$$

To simplify $U(t,0)$, the evolution operator will be considered over a small time interval $[t_{j-1}, t_j] \subseteq [0,t]$ such that $t_j - t_{j-1} = \Delta t$. The evolution operator over this interval is

$$U(t_j, t_{j-1}) = \mathcal{T}\left[\exp\left(-i\int_{t_{j-1}}^{t_j} \hat{H}_0 + \hat{H}_e(s)ds\right)\right],$$

which can be decomposed to first order (in Δt) as [197]

$$U(t_j, t_{j-1}) = \exp\left(-i\Delta t\hat{H}_0\right)\exp\left(-i\Delta t\hat{H}_e(t_j)\right). \tag{3.3.2}$$

To write the evolution operator over the entire time, first $[0,t]$ is partitioned into n

subintervals $[t_{j-1}, t_j]$ for $j = 1, ..., n$ such that $0 = t_0 < t_1 < ... < t_n = t$ and $t_j - t_{j-1} = \Delta t$. Using the composition property of evolution operators and (3.3.2), the solution for the nucleus wavefunction at time t for sufficiently large n is then

$$\begin{aligned}\Phi(t) &= U(t,0)\Phi(0) \\ &= U(t_n, t_{n-1})...U(t_2,t_1)U(t_1,t_0)\Phi(0) \\ &= e^{-i\Delta t\hat{H}_0}e^{-i\Delta t\hat{H}_e(t_n)}...e^{-i\Delta t\hat{H}_0}e^{-i\Delta t\hat{H}_e(t_1)}e^{-i\Delta t\hat{H}_0}e^{-i\Delta t\hat{H}_e(t_0)}\Phi(0).\end{aligned}$$

To proceed with solving for $\Phi(t)$, the definition of transition probabilities,

$$q_\nu := \langle \Psi_\nu, \hat{Q}_\lambda \Psi_0 \rangle, \tag{3.3.3}$$

is needed. For convenience, q_0 is set to be equal to 0. Additionally, the resolution of identity

$$\hat{\mathbf{1}} = \sum_\nu \Psi_\nu \langle \Psi_\nu, \cdot \, \rangle, \tag{3.3.4}$$

(equivalent to $\sum_\nu |\Psi_\nu\rangle\langle\Psi_\nu|$ in bra–ket notation) is used.

The wavefunction at t_1 will now be solved by approximating exponential operators to their first order Taylor expansion so that only linear terms of ε appear in expanding $\hat{H}_e$,

$$\begin{aligned}\Phi(t_1) &= U(t_1,0)\Phi(0) \\ &= e^{-i\Delta t\hat{H}_0}e^{-i\hat{H}_e(t_1)\Delta t}\Psi_0 \\ &= e^{-i\Delta t\hat{H}_0}\left[\hat{1} - i\Delta t\hat{H}_e(t_1)\right]\Psi_0 + O\left(\varepsilon^2\right) \\ &\simeq e^{-i\Delta t\hat{H}_0}\left[\Psi_0 - i\Delta t\varepsilon\hat{Q}_\lambda f(t_1)\Psi_0\right] \\ &= e^{-i\Delta t\hat{H}_0}\left[\Psi_0 - i\Delta t\varepsilon f(t_1)\sum_\nu \Psi_\nu\langle\Psi_\nu, \hat{Q}\Psi_0\rangle\right] \qquad (3.3.5) \\ &= e^{-i\Delta t\hat{H}_0}\left[\Psi_0 - i\Delta t\varepsilon f(t_1)\sum_\nu q_\nu\Psi_\nu\right] \qquad (3.3.6) \\ &\simeq e^{-iE_0\Delta t}\Psi_0 - i\Delta t\varepsilon f(t_1)\sum_\nu q_\nu e^{-iE_\nu\Delta t}\Psi_\nu,\end{aligned}$$

substituting (3.3.4) in (3.3.5) and (3.3.3) in (3.3.6). By induction or otherwise, the wavefunction at time t_n is

$$\Phi(t_n) = e^{-iE_0 n\Delta t}\left[\Psi_0 - i\varepsilon\sum_\nu q_\nu\Psi_\nu\left(\sum_{j=1}^{n} f(t_j)e^{-i(E_\nu - E_0)(n-j+1)}\Delta t\right)\right].$$

As $n\Delta t = t_n = t$, taking the limit as $n \to \infty$ gives

$$\Phi(t) = e^{-iE_0 t}\left[\Psi_0 - i\varepsilon \sum_\nu q_\nu \Psi_\nu e^{-i(E_\nu - E_0)t}\int_0^t f(s)e^{i(E_\nu - E_0)s}ds\right]. \tag{3.3.7}$$

Now the expectation value of the multipole moment operator $\hat{Q}_\lambda$ can be found using the wavefunction (3.3.7). Taking only the linear expansion in terms of ε again, then

$$\begin{aligned}
\langle \hat{Q}_\lambda \rangle &= \langle \Phi(t), \hat{Q}_\lambda \Phi(t) \rangle \\
&= i\varepsilon \sum_\nu \left[q_\nu^* e^{i(E_\nu - E_0)t}\int_0^t f(s)e^{-i(E_\nu - E_0)s}ds \langle \Psi_\nu, \hat{Q}_\lambda \Psi_0 \rangle\right] \\
&\quad - i\varepsilon \sum_\nu \left[q_\nu e^{-i(E_\nu - E_0)t}\int_0^t f(s)e^{i(E_\nu - E_0)s}ds \langle \Psi_0, \hat{Q}_\lambda \Psi_\nu \rangle\right] + O(\varepsilon^2) \\
&\simeq i\varepsilon \sum_\nu |q_\nu|^2 \left[e^{i(E_\nu - E_0)t}\int_0^t f(s)e^{-i(E_\nu - E_0)s}ds - e^{-i(E_\nu - E_0)t}\int_0^t f(s)e^{i(E_\nu - E_0)s}ds\right].
\end{aligned} \tag{3.3.8}$$

Expressions for the time-dependent wavefunction of a nucleus under an external time-dependent potential and the expectation value of the multipole operator have been obtained so far. The time function f appears within integrals for both Φ and $\langle \hat{Q}_\lambda \rangle$ and to proceed further with simplifying (3.3.8), a specific f will be chosen. Any sensible time function can be chosen although a very liberal interpretation of "sensible" is about to ensue.

The choice of time function used in this chapter is guided by the most ideal but least realistic way for the external function to be activated in the system. This would be for the external potential to be active at initial or zero time, and then be equal to zero for the remaining time. Differently said, this means a boost in the form $\exp(-i\varepsilon\hat{Q}_\lambda)$ is applied to the ground state wavefunction at initial time only. This can be simulated by using the Dirac delta function in place of $f(s)$ in (3.3.8). The liberty to take the Dirac delta function is justified by its appearance only in integrals where it can be made sense of. An example of a well behaved function with continuity in t to use instead would be a sharply peaked gaussian function centred at $t = 0$.

Substituting in the Dirac delta function and ignoring higher order terms of ε into

(3.3.8),

$$\begin{aligned}\langle\hat{Q}_\lambda\rangle &= i\varepsilon\sum_\nu |q_\nu|^2\left(e^{i(E_\nu-E_0)t}\int_0^t \delta(s)e^{-i(E_\nu-E_0)s}ds - e^{-i(E_\nu-E_0)t}\int_0^t \delta(s)e^{i(E\nu-E_0)s}ds\right)\\ &= i\varepsilon\sum_\nu |q_\nu|^2\frac{1}{2}\left(e^{i(E_\nu-E_0)t}-e^{-i(E_\nu-E_0)t}\right)\\ &= -\varepsilon\sum_\nu |q_\nu|^2\sin\left((E_\nu-E_0)t\right). \end{aligned} \tag{3.3.9}$$

From here, the strength function of the multipole moment can be extracted. The strength function resolves the multipole moment in terms of its energy spectrum which will reveal which frequencies are strongly or weakly present in the function $\langle\hat{Q}_\lambda\rangle$. It is defined as

$$Q_\lambda(E) := \lim_{\varepsilon\to 0}\frac{1}{\pi\hbar\varepsilon}\mathfrak{Im}\mathcal{F}[\langle\hat{Q}_\lambda\rangle(t)](E/\hbar), \tag{3.3.10}$$

where $E/\hbar = \frac{2\pi}{t}$, including $\hbar$ back into expressions.

First, the imaginary part of the Fourier transform of (3.3.9) is

$$\begin{aligned}\mathfrak{Im}\mathcal{F}[\langle\hat{Q}_\lambda\rangle(t)](E/\hbar) &= \mathfrak{Im}\int_{-\infty}^{+\infty}\langle\hat{Q}_\lambda\rangle(t)e^{-i\frac{E}{\hbar}t}dt\\ &= -\varepsilon\sum_\nu |q_\nu|^2\mathfrak{Im}\left\{\int_{-\infty}^{+\infty}\sin\left(\frac{E_\nu-E_0}{\hbar}t\right)e^{-i\frac{E}{\hbar}t}dt\right\}\\ &= -\varepsilon\sum_\nu |q_\nu|^2\mathfrak{Im}\left\{\frac{1}{2i}\int_{-\infty}^{+\infty}e^{-i\left(\frac{E-(E_\nu-E_0)}{\hbar}\right)t}-e^{-i\left(\frac{E+(E_\nu-E_0)}{\hbar}\right)t}dt\right\}\\ &= -\varepsilon\sum_\nu |q_\nu|^2\mathfrak{Im}\left\{\frac{1}{2i}2\pi\hbar\left[\delta(E-(E_\nu-E_0))-\delta(E+(E_\nu-E_0))\right]\right\}\\ &= \pi\hbar\varepsilon\sum_\nu |q_\nu|^2\delta(E-(E_\nu-E_0))\end{aligned}$$

since both $E>0$ and $E_\nu - E_0 > 0$. This uses the fact that the Fourier transform of the constant function 1 is the delta function. Substitution into the strength function gives

$$Q_\lambda(E) = \sum_\nu |q_\nu|^2\delta(E-(E_\nu-E_0)).$$

Expressions for both $\langle\hat{Q}_\lambda\rangle(t)$ and $Q_\lambda(E)$ with a particular f have been found, and will be used in TDHF calculations on calcium and tin isotopes.

3.4 Calculations on calcium and tin isotopes

3.4.1 Numerical details

Multipole operator

The vibrational modes considered in this chapter are those generated by small amplitude octupole and quadrupole vibrations of spherical or near spherical nuclei. The corresponding multipole operators used are (using cartesian coordinates of spherical harmonics)

$$\hat{Q}_2 = \sqrt{\frac{5}{16\pi}} \sum_{j=1}^{A} \left[2\hat{x}^2 - \hat{y}^2 - \hat{z}^2 \right], \tag{3.4.1}$$

$$\hat{Q}_3 = \sqrt{\frac{7}{16\pi}} \sum_{j=1}^{A} \left[2\hat{x}^3 - 3\hat{x} \left(\hat{y}^2 + \hat{z}^2 \right) \right]. \tag{3.4.2}$$

To find a reasonable value of ε, the value of the first turning point of $\langle \hat{Q}_\lambda \rangle$ is calculated for a range of ε. If the turning points linearly increase or decrease within this ε range, then the final chosen ε can be any value within this range (otherwise known as the linear regime of $\langle \hat{Q}_\lambda \rangle$). For octupole vibrations, $\varepsilon = 1 \times 10^{-8}$ fm^{-3} and for quadrupole vibrations, $\varepsilon = 1 \times 10^{-4}$ fm^{-2}.

HF calculations

TDHF calculations of the multipole moments for nuclei were calculated over the box size encompassing half the HF ground state with dimensions $22.4 \times 22.4 \times 11.2$ fm^3 in the $x - y - z$ directions with a plane of symmetry at $z = 0$.

The calculations were run for a response time of 15 zs. As the calculation time is not infinite, before extracting the strength function, the moment function $\langle \hat{Q}_\lambda \rangle$ needs to be damped by a suitable function to replicate a hypothetical calculation over infinite time. Undamped, the strength function will contain many small, spurious peaks. Damping the moment function will smooth this out and a suitable damping function to use is the half Gaussian

$$g(t) = \exp\left(-\frac{t^2}{\left(\frac{T}{2}\right)^2} \right),$$

for total calculation time $T = 15$ zs. This was multiplied to $\langle \hat{Q}_\lambda \rangle$ in the expression for $Q_\lambda(E)$ in equation (3.3.10).

As these are single nucleus calculations, it does not matter whether the Skyrme energy

density functional (EDF) parametrisation has a centre of mass correction. In the following chapter where the roles of vibrations in reactions are explored, the same parametrisation between reactions and vibrations calculations should be used for consistency. In this chapter, mostly the SLy4d parametrisation [101] is used and presented although calculations with SLy4 [38] and UNEDF1 [104] were also done for comparison.

Surface pairing is included in the ground state at the BCS level. The form of the pairing function is detailed in section 2.4 and for the time-dependent calculation, the frozen occupation approximation [55, 164] was used.

3.4.2 Moment and strength functions

Octupole and quadrupole moments, using the operators $\hat{Q}_\lambda$ in equations (3.4.2) and (3.4.1) respectively, were calculated for the $^{40-54}$Ca and $^{124-136}$Sn isotopes. Examples of $\langle\hat{Q}_\lambda\rangle(t)$ are presented in Fig. 3.1 for ^{40}Ca and ^{124}Sn. These moment functions are a coherent superposition of many octupole (3^-) or quadrupole (2^+) states.

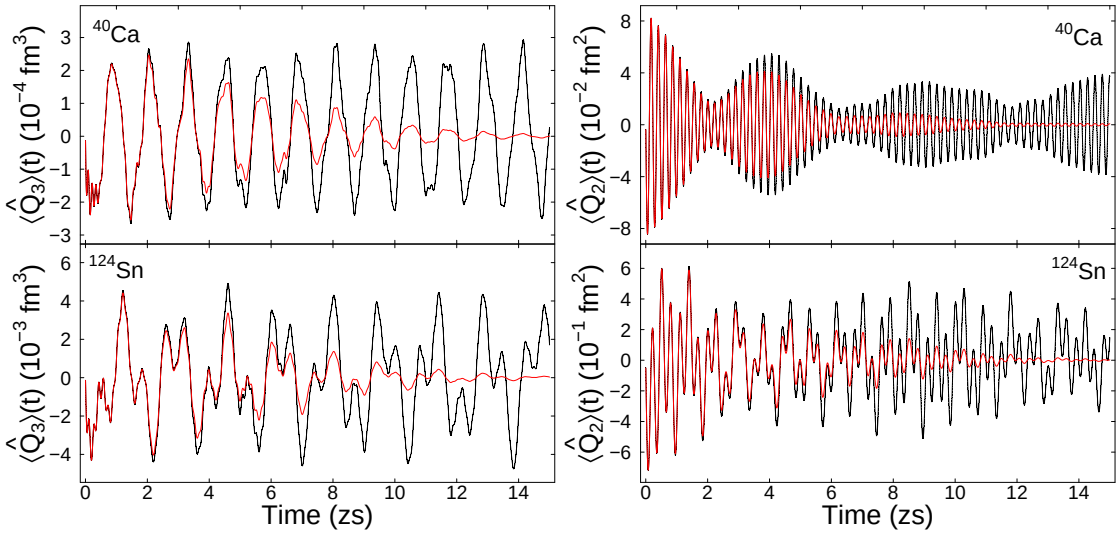

Fig. 3.1.: Left: octupole moment functions and right: quadrupole moment functions for ^{40}Ca (top panels) and ^{124}Sn (bottom panels). Both original (black) and damped (red) functions are shown. All calculations were done with the SLy4d [101] parametrisation of the Skyrme energy density functional.

Both ^{40}Ca and ^{132}Sn have moment functions that are a jagged, sinusoidal type function. This is most clearly seen for the octupole moment of ^{40}Ca. Coarsely, its looks as though the main oscillation in this function is associated with one frequency. When the corresponding strength function for ^{40}Ca is resolved into energy (related to frequency, $E = \hbar\omega_\lambda$), presented in Fig. 3.2 (top left panel for ^{40}Ca), the resulting function is mostly zero but with sharp peaks at particular frequencies that occur in its quasi-sinusoidal moment function, $\langle\hat{Q}_3\rangle$.

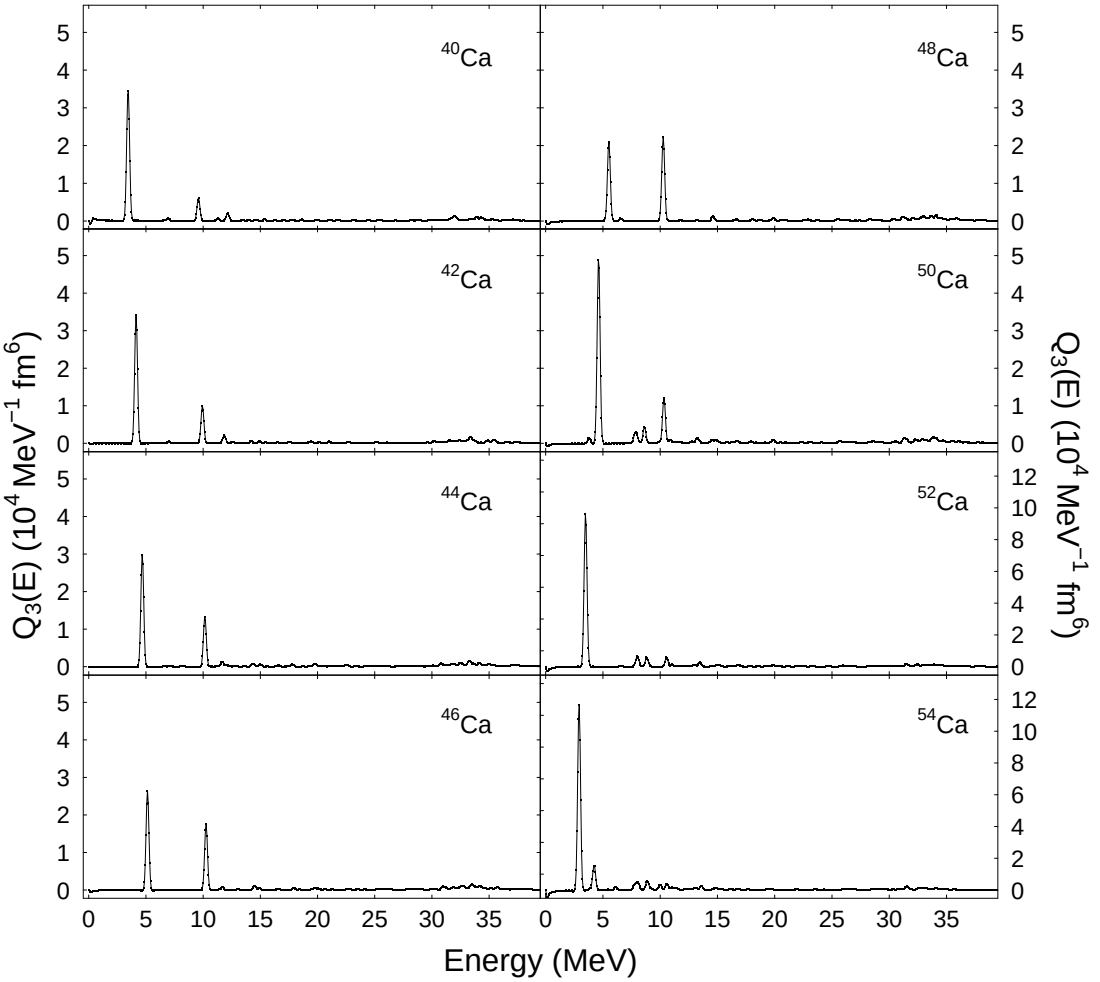

Fig. 3.2.: Octupole strength functions for $^{40-54}$Ca.

The octupole strength functions for all other calcium isotopes are also included in Fig. 3.2. Along the chain of calciums, there is a strong peak between approximately 3–5 MeV. An intensive peak is associated with collective nature and the one with the lowest energy is interpreted as the first excited 3_1^- state. There is a second peak for $^{40-50}$Ca at approximately 10 MeV which increases in relative intensity with respect to the first peak for $^{40-48}$Ca as the neutron number increases to 28, then decreases for ^{50}Ca when $N = 30$. For ^{52,54}Ca (even with a change of scale) this peak is not pronounced and instead various smaller peaks emerge over energies spread between 8–11 MeV. There is also a spread of small peaks between 30–35 MeV consistent for every calcium isotope shown. These are associated with the high energy octupole resonance [188]. This is in agreement with the experimentally observed high energy octupole resonance for ^{40}Ca in particular which was found to have an excitation energy of approximately $110A^{-\frac{1}{3}}$ [35].

The quadrupole strength functions for $^{40-54}$Ca isotopes are presented in Fig. 3.3. There is a consistent strong peak at approximately 18 MeV which is associated with the giant quadrupole resonance (GQR). There are no low-lying peaks for ^{40}Ca but for

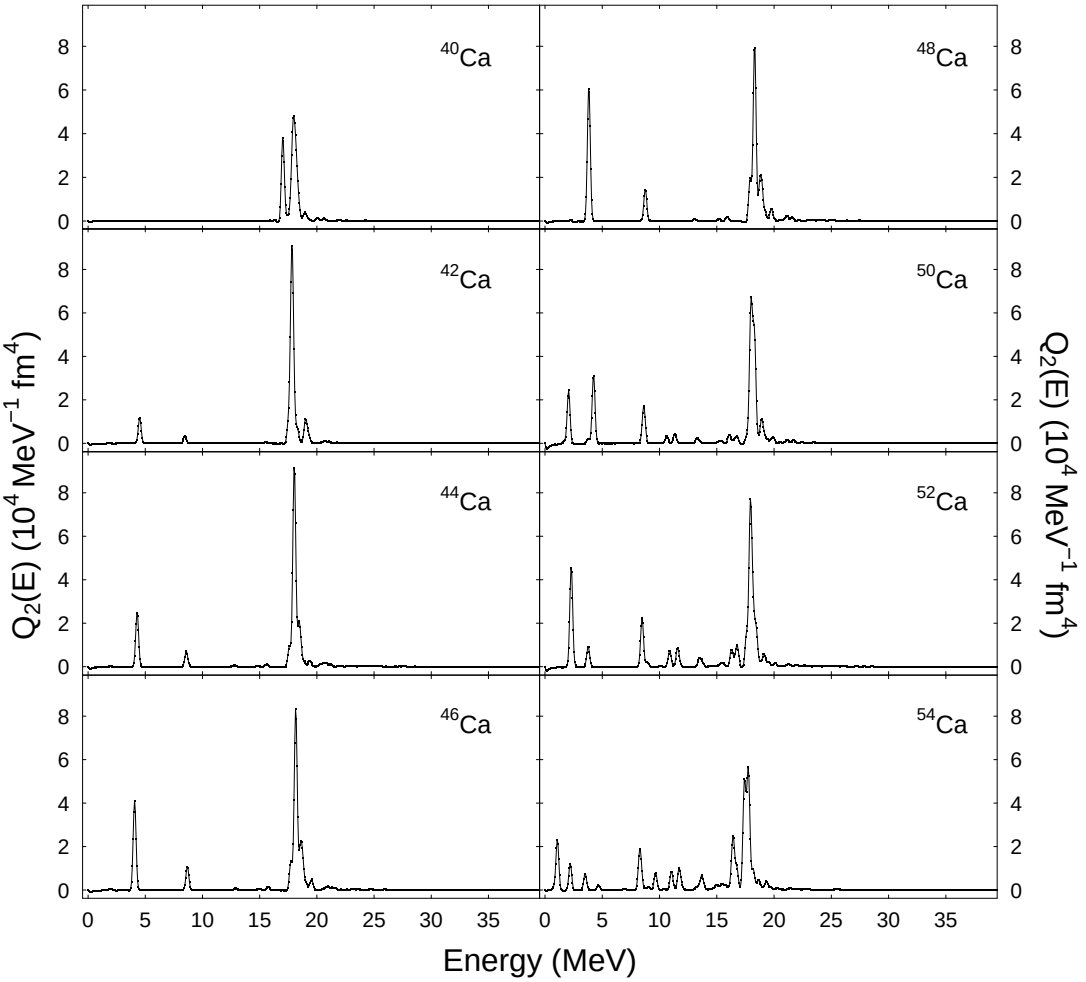

Fig. 3.3.: Quadrupole strength functions for $^{40-54}$Ca.

$^{42-48}$Ca there are peaks at approximately 4 MeV (stronger) and 8 MeV (weaker). As the neutron number increases for these isotopes, both these peaks increase in strength. The isotopes $^{50-54}$Ca have a more varied low energy spectrum with the appearance of several peaks below 10 MeV.

Strength functions for octupole and quadrupole moments of $^{124-136}$Sn isotopes are provided in Appendix C.

3.4.3 Excitation energy and transition strength

An excited state of a nucleus has an associated excitation energy and deformation parameter which can be deduced from experimental measurements. These quantities can also be extracted from strength functions produced from the TDHF vibration calculations. It was already mentioned in the previous section that the first intensive peak in the octupole strength functions for calcium isotopes (Fig. 3.2) is associated with the 3^-_1 state. By contrast, the low-lying intensive peak at ∼4 MeV in the quadrupole strength functions (Fig. 3.3) cannot in general be associated with the first 2^+_1 state. This is because for

many even-even nuclei, 2_1^+ states have been observed experimentally at a lower energy, typically less than 2 MeV. The exception to this is for magic nuclei, where nucleons have to cross a magic shell gap. Because of this, the first collective peak seen for ^{48}Ca in Fig. 3.3 is the true first 2_1^+ state. Discussion on why the low-lying 2_1^+ states are not reproduced by TDHF appear in the next section.

Using the strength functions, the excitation energy of the collective state is simply the position (or the centroid of a gaussian fit) of the peak. The area under a peak, denoted by $|q_\nu|^2$, can be used to calculate the deformation parameter [182]

$$\beta_\lambda = \frac{4\pi|q_\nu|}{3AR_A^\lambda},$$

where R_A is a radius parameter for the nucleus. For calculations of β_λ, the radius parameter was taken to be the HF ground state half saturation density radius of the relevant nucleus.

The deformation parameter can be used to extract the transition probability from the ground state to the excited state, ν, by [74]

$$B(E\lambda) = \left(\frac{3\beta_\lambda Z R_A^\lambda e}{4\pi}\right)^2 = \left(\frac{|q_\nu|Ze}{A}\right)^2.$$

Furthermore, the collectivity of an excited state can be estimated using the Weisskopf estimate for single particle transition strength from ground state [18],

$$B(E\lambda)_\mathcal{W} = \frac{\left(1.20A^{1/3}\right)^{2\lambda}}{4\pi}\left(\frac{3}{3+\lambda}\right)^2 e^2\mathrm{fm}^{2\lambda},$$

and taking the ratio $B(E\lambda)/B(E\lambda)_\mathcal{W}$. When this ratio is close to 1 the state is not considered to be collective.

The systematic results of these quantities for $^{40-54}$Ca are presented in Tab. 3.1 for the 3_1^- state and in Tab. 3.2 for the first 2^+ state calculated by TDHF. For the 3_1^- state, the transition strength in Weisskopf units indicate that it is collective over all isotopes, the least collective being in the ^{48}Ca nucleus. By contrast, the 2^+ state has much lower ratios closer to 1, indicating that TDHF is not calculating this state to be very collective. Experimental low-lying collective 2_1^+ states observed for many even-even nuclei at energies below 2 MeV typically have $B(E2)/B(E2)_\mathcal{W}$ several orders of magnitude higher.

Using different parametrisations of the Skyrme EDF will produce rather varied excitation energy of the first collective peak. This can be seen in Fig. 3.4 on the left with

A (Ca)	$E_x(3_1^-)$ MeV	$E_x(3_1^-)$ MeV (exp.)	β_3	β_3 (exp.)	$B(E3)$ (10^3 fm$^6e^2$)	$B(E3)/B(E3)_{\mathcal{W}}$ (W. u.)
40	3.44	3.74	0.224	0.30-0.41	2.76	29.0
42	4.14	3.45	0.195	0.26	2.37	22.6
44	4.68	3.31	0.165	0.23-0.26	1.89	16.4
46	5.14	3.61	0.141	0.16	1.52	12.1
48	5.52	4.51	0.109	0.17-0.25	1.00	7.31
50	4.63	–	0.168	–	2.47	16.6
52	3.48	–	0.221	–	4.44	27.6
54	2.92	–	0.226	–	4.89	28.2

Tab. 3.1.: Excitation energies, deformation parameters and transition strength for the 3_1^- state of $^{40-54}$Ca isotopes as calculated by TDHF using the SLy4d parametrisation. Experimental values for $E_x(3_1^-)$ and β_3 are taken from Ref. [100].

A (Ca)	$E_x(2^+)$ MeV	$E_x(2_1^+)$ MeV (exp.)	β_2	β_2 (exp.)	$B(E2)$ (fm$^4e^2$)	$B(E2)/B(E2)_{\mathcal{W}}$ (W. u.)
40	–	3.90	–	0.123	–	–
42	4.51	1.53	0.043	0.247	8.23	1.01
44	4.29	1.16	0.058	0.253	16.1	1.86
46	4.07	1.35	0.069	0.153	24.3	2.64
48	3.83	3.83	0.078	0.106	33.2	3.39
50	2.06	–	0.047	–	12.3	1.19
52	2.29	–	0.061	–	21.3	1.95
54	1.08	–	0.041	–	9.97	0.86

Tab. 3.2.: Same as Tab. 3.1 but for the first 2^+ state seen in $^{40-54}$Ca isotopes. Experimental values for for $E_x(2_1^+)$ and β_2 are taken from Ref. [151].

the SLy4d (red circles), SLy4 (green triangles) and UNEDF1 (blue squares) parametrisations. The experimental values (crosses) for $^{40-48}$Ca are also shown for comparison. Between the different parametrisations, the largest variation of $E_x(3_1^-)$ for one nucleus is approximately 1.2 MeV. The largest difference between an experimental and calculated value is approximately 1.7 MeV. It is not the goal nor imperative for this study that the calculations reproduce experimental data to high accuracy as the focus is on the systematics of (low-lying) vibrational modes. However, results from TDHF are within some reasonable agreement with experimental results, particularly for the 3_1^- excitation energy of the doubly magic nuclides ^{40,48}Ca.

The comparison of calculations and experimental values of the deformation parameter is shown in the right panel of Fig. 3.4. The results from TDHF calculations underestimate the values deduced from experimental measurements (the vertical black lines indicate the range of experimental values). Notwithstanding, the agreement between TDHF and experiment is within reason.

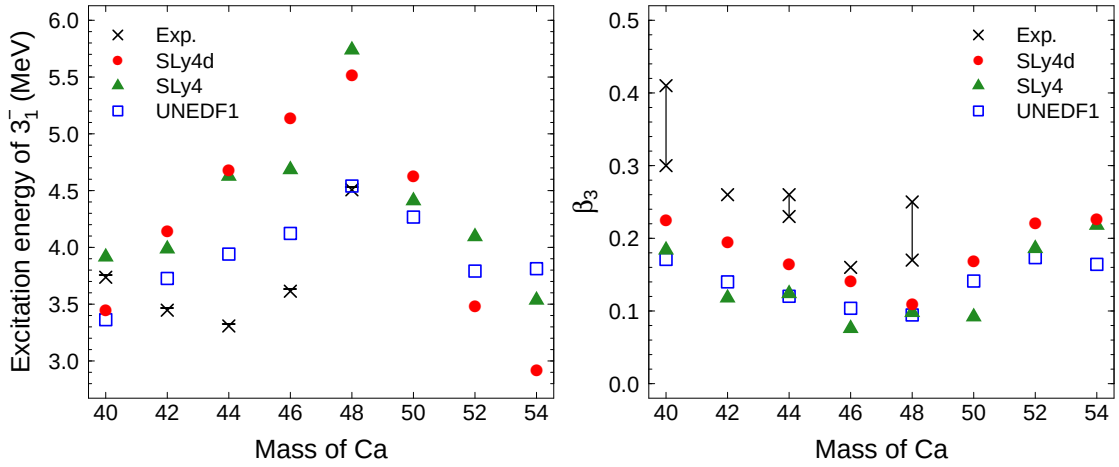

Fig. 3.4.: Comparison of the excitation energy (left) and deformation parameter (right) of the 3_1^- state from HF calculations with the SLy4d [101], SLy4 [38], UNEDF1 [104] parametrisations. Experimental values [100] are also shown for comparison.

3.5 Single particle excitations

In the collective model for vibrations, wavefunctions describing vibrational modes of nuclei are a quantum superposition of all possible single particle excitations and can be represented (using second quantization) as

$$|\nu\rangle = \sum_{fi} A_{fi}\hat{a}^\dagger(f)\hat{a}(i)|0\rangle, \tag{3.5.1}$$

where $|0\rangle$ is the ground state, and A_{fi} are complex-valued weights. The indices i and f decribe all quantum numbers, for example $n\ell jm$, of a particular nucleon. The weights cannot be determined from the TDHF approach to vibrations in a straightforward manner. As such, discussions on contributions from single particle excitations to octupole and quadrupole vibrations in $^{40-54}$Ca remain on a qualitative level. However, the single particle excitations that are valid for a vibrational state can be deduced and are characteristic of that mode.

Excited states of nuclei are often labelled as J^π. For single phonon vibrations of spherical nuclei, J denotes the units of angular momentum in the vibration, (which is equal to λ in (3.2.7)), and the parity ($\pi = (-1)^\lambda$). Octupole (quadrupole) vibrations from a single phonon are hence labelled as 3^- (2^+) states. Nuclides with these octupole (quadrupole) vibrational states, described by wavefunctions of the form (3.5.1), must comprise single particle excitations between shells of opposite (same) parity, exchanging 3 (2) units of angular momentum. The units of angular momentum exchanged from a

nucleon excited from initial shell level $n_i\ell_i j_i$ to final shell level $n_f\ell_f j_f$ lie in the range

$$|j_i - j_i| \leq \lambda \leq |j_f + j_f|, \tag{3.5.2}$$

taking on integer values. This criterium, along with the parity of a single particle shell $(-1)^\ell$, determines which single particle excitations are valid for a particular type of vibrational state.

In this section, first the HF calculations of the ground state shell configuration for $^{40-54}$Ca isotopes are presented. Then, single particle excitations possible for contributing to octupole and quadrupole vibrational modes in these nuclides are discussed qualitatively.

3.5.1 Shell configuration

The single particle shell configuration of a nucleus is taken directly from static HF ground state calculations. Each calcium isotope is calculated separately, but the schematic for the neutron shell configuration for the ^{54}Ca nucleus is shown in Fig. 3.5, and the levels appear in the same order between all isotopes. Only bound levels are shown with the $n\ell j$ labelling included, as well as the magic gaps that are indicated by dashed lines and with the total number of neutrons below the gap.

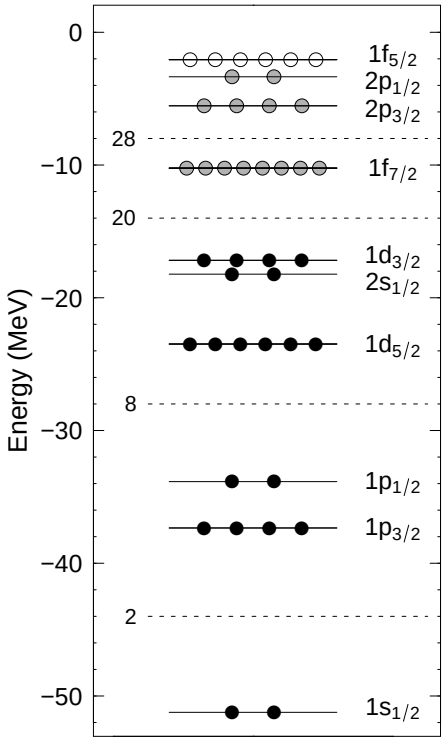

Fig. 3.5.: The neutron shell configuration for calcium as taken from the calculation of ^{54}Ca. The fully shaded circles are completely occupied states for all isotopes, the partially shaded circles shows the range from $N = 20$ to 34 and the open circles is the last bound neutron shell as calculated by HF (with the SLy4d parametrisation). In the heaviest isotopes there will be partial occupation in this shell.

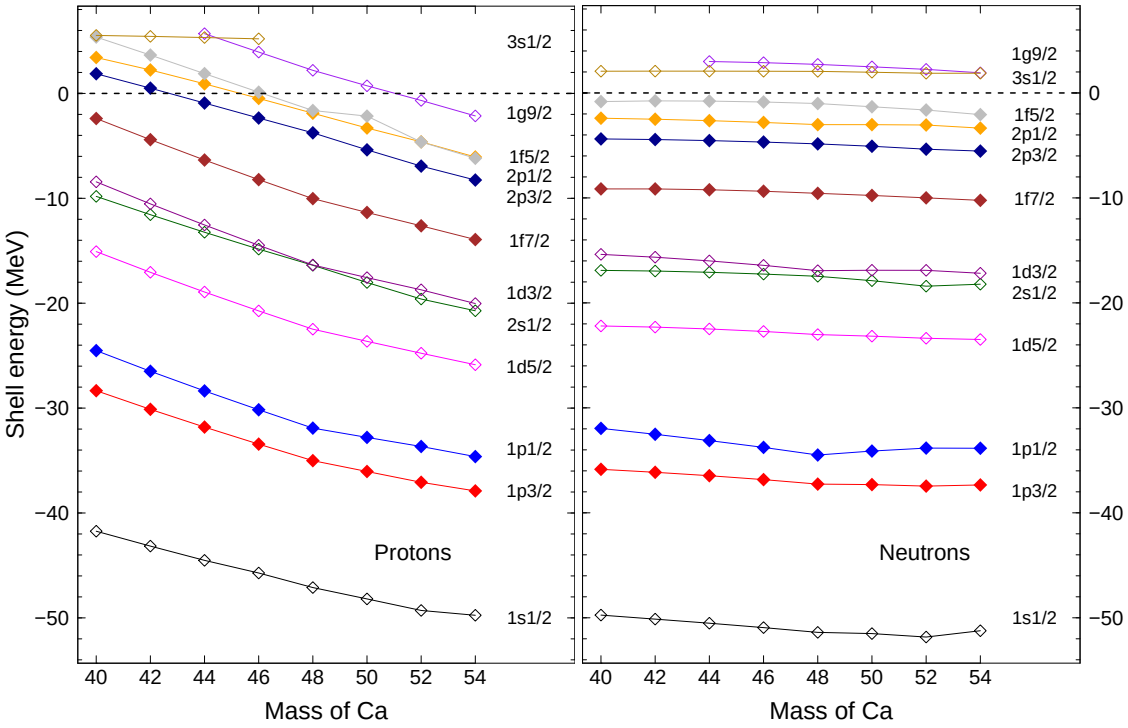

Fig. 3.6.: The energies of the proton (left) and neutron (right) shells for $^{40-54}$Ca. Open diamonds indicate a level with even parity and solid diamonds are odd parity. Calculations were done with the SLy4d parametrisation.

The proton shell ordering for calcium isotopes is the same as for the neutrons in Fig. 3.5 but the energies of the levels are different and the $1d_{3/2}$ shell is the last filled shell. A break down of shell energies for all of $^{40-54}$Ca is presented in Fig. 3.6 for both protons (left) and neutrons (right). It includes shells with zero occupation, for example any proton shells above the $1d_{3/2}$ shell. The proton single particle energies are decreasing with increasing neutron number. This is due to the increasing attraction with the increasing number of neutrons.

In Fig. 3.6, all levels with even parity are shown by open diamond symbols and those with odd parity are shown with solid diamonds. For octupole vibrations, single particle excitations that contribute to the vibrational state should be of nucleons moving between shells that are of opposite symbols (solid to open or vice versa) and that satisfy (3.5.2) for $\lambda = 3$. For a quadrupole vibration, nucleons should move between shells represented by the same diamond symbols and satisfying (3.5.2) for $\lambda = 2$.

Some of the levels included in Fig. 3.6 are unbound, such as the neutron $1g_{9/2}$ and $3s_{1/2}$ shells. Although single particle excitations to these levels contribute to the multipole moment and strength function in TDHF calculations, they should not be included in discussions on collective vibrations as the continuum is not treated properly in the TDHF calculations appearing in this chapter. As such, excitations to unbound shells in such

calculations can lead to a spurious nucleon gas [50, 52]. A small box size relative to the nuclear radius, hard boundary conditions and the frozen approximation of BCS pairing all contribute to this improper treatement.

Hard boundary conditions cause excitation spectra to be discretised and, if the calculation box is small, may reflect emitted nucleons back to the original nucleus leading to unphysical results in the response function [128, 153]. To improve this description, absorbing boundary conditions are often used in place of hard boundary conditions. Implementing this for responses in the linear regime has the same effect as substantially increasing the box size with hard boundary conditions [146], the latter compromising in computational time. Alternatively (or in addition), in the linear regime, the application of the time damping function in generating response functions also mitigates the hard boundary effects [153].

As for the HF ground state calculation on its own, imposing zero BCS occupation numbers for unbound levels [50, 52] could also be done. Excitations to the continuum are more significant for weakly bound nuclei or those that are near the dripline, that is, nuclei with a Fermi energy very close to 0 MeV. This is likely to lead to the pairing cutoff (see section 2.4 and subsection 2.5.4) above 0 MeV. In this chapter, this is only a concern for the nucleus ^{54}Ca. Extensions to the continuum with the BCS equations [159] with HF calculations [108] are available. It is also recommended that the Hartree–Fock–Bogoliubov (HFB) theory should be applied to nuclei near the dripline.

3.5.2 Octupole vibrations

Low-lying octupole vibrations for calcium isotopes are expected to be collective from experimental results and also in the TDHF calculations by the $B(E3)/B(E3)_{\mathcal{W}}$ ratios in Tab. 3.1. Single particle excitations that are valid for single phonon octupole vibrations are presented in Tab. 3.3. Initial and final shells are arranged into columns and an arrow from an initial to a final shell indicates that this excitation satisfies the conditions of angular momentum coupling and parity change. There may be more than one possibility of a final shell for nucleons in a particular initial shell and vice versa.

Proton excitations are the same for all $^{40-54}$Ca isotopes and are indicated on the diagram, there are fewer of these possibilities than for neutrons simply because there are fewer protons than neutrons in $^{42-54}$Ca. As calcium is magic in proton number, proton shells can be considered in a good approximation as either fully occupied or completely vacant. The protons fully occupy up to the $1d_{3/2}$ shell so only proton excitations from the *sd* shells to the fp shells are considered. Higher odd parity shells than these fp shells

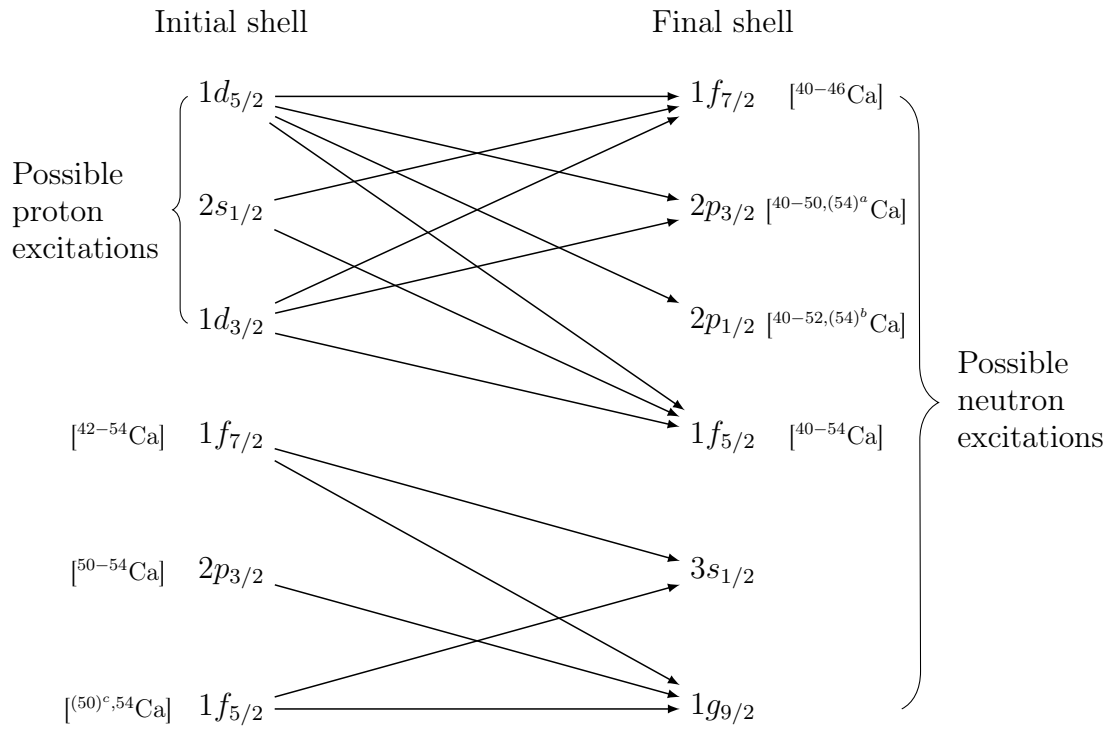

Tab. 3.3.: Possible single particle excitations for the 3^- state in calcium isotopes. [a] ^{54}Ca has 97% occupation in the final $2p_{3/2}$ shell. [b] ^{54}Ca has 61.3% occupation in the final $2p_{1/2}$ shell. [c] ^{50}Ca has 1% occupation in the $1f_{5/2}$ shell.

are unbound, requiring large excitation energies of more than 20 MeV.

In most of the HF ground states for $^{40-54}$Ca, there are partially filled neutron shells near the Fermi energy. The only nucleus that was not magic in neutron number but did have complete occupation in the highest shell level was ^{52}Ca, with no partial occupations for shells at or above $2p_{3/2}$. The nuclides for which the neutron excitations shown in Tab. 3.3 are valid for are indicated in square brackets to the right of the final shell column (where the occupation is relevant in the final shell) or to the left of the initial shell column if there is partial occupation in these levels. For example, neutrons in any of the *sd* shells exciting to the $1f_{7/2}$ shell can only happen for $^{40-46}$Ca since $^{48-54}$Ca has full occupation in this shell. Neutron shells with less than 1% occupation in the initial shell or more than 99% occupation in the final shell have not been considered as possible excitations and are therefore not included in the diagram.

Considering the single particle excitations in Tab. 3.3, an example wavefunction for the 3^-_1 state for ^{40}Ca could be written as (using (3.5.1))

$$\begin{aligned}|3^-_1\rangle = \Big[&A_1\hat{a}^\dagger(1f_{7/2})_\pi\hat{a}(1d_{3/2})_\pi + A_2\hat{a}^\dagger(1f_{7/2})_\nu\hat{a}(1d_{3/2})_\nu \\ &+ A_3\hat{a}^\dagger(1f_{7/2})_\pi\hat{a}(2s_{1/2})_\pi + A_4\hat{a}^\dagger(1f_{7/2})_\nu\hat{a}(2s_{1/2})_\nu + ...\Big]|0\rangle \end{aligned} \tag{3.5.3}$$

where A_{fi} are now just written as $A_k, k = 1, 2, ...$ for simplicity. The wavefunction can be written similarly for all other calcium isotopes however the weights would be different and the excitations attached to them would change as well, according to which ones are possible or appear in Tab. 3.3 for each isotope.

The corresponding excitation energies to the possibilities shown in Tab. 3.3 are seen in Fig. 3.7. Included in Fig. 3.7 are the excitation energies of the 3^-_1 state (crosses) and of the peak at ∼10 MeV (plus signs) appearing in Fig. 3.2. From this plot, it can be surmised that the 3^- states are calculated as mixed states by TDHF. This is because none of the single particle excitation energies are very close to the energy of the first and second collective 3^- peaks due to the residual interaction.

The relative strengths of the 3^- peaks from Fig. 3.2 can be attributed to occupation of relevant proton or neutron shells. The decrease in strength of the 3^-_1 peak of the $^{40-48}$Ca isotopes is interpreted by the increasing neutron number of the calciums leaving fewer vacancies in the $1f_{7/2}$ shell as N increases from 20 to 26, and completely occupied when $N = 28$. When $N = 30$, there are more possibilities for neutron excitations (although to the unbound levels) from $1f_{5/2}$ to $3s_{1/2}$ or $1g_{9/2}$ and also from $2p_{3/2}$ to $1g_{9/2}$.

Conversely, there is an increase in relative strength of the 3^- peak at 10 MeV for the $^{40-48}$Ca isotopes. This can also be interpreted by increasing neutrons available in the $1f_{7/2}$ shell that can be excited to the unbound shells.

3.5.3 Quadrupole vibrations

Many of the same arguments as for the octupole vibrations can be used for quadrupole vibrations, but altered to a non-changing parity between single particle shells with an exchange of 2 units of angular momentum. The possible single particle excitations corresponding to quadrupole vibrations are presented in Tab. 3.4 which is to be read in the same way as for Tab. 3.3. Angular momentum recoupling with the same shell (for example $\hat{a}^\dagger(1f_{7/2})_\nu \hat{a}(1f_{7/2})_\nu$) is not shown as it is not present in TDHF calculations. The labelled arrows with nuclei in square brackets indicate which nuclei that particular excitation is possible for and unlabelled arrows are possible for all $^{40-54}$Ca isotopes. Note there are fewer possibilities for single particle excitations as compared to the octupole vibrations, at least up to the $1g_{9/2}$ shell. The corresponding plots for energies are seen in Fig. 3.8.

Unlike for octupole vibrations, the TDHF calculations for $B(E2)/B(E2)_\mathcal{W}$ indicated that the first observed 2^+ peak seen in Fig. 3.3 for $^{40-54}$Ca is non-collective. As ^{40}Ca is magic in both Z and N the excitations for both protons and neutrons must cross a

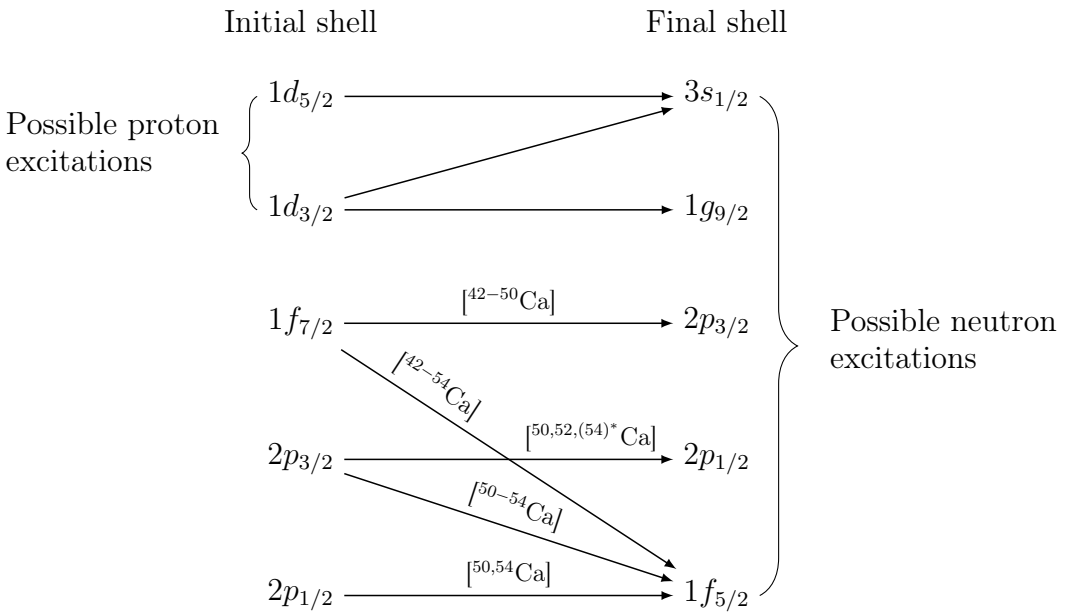

Tab. 3.4.: Possible single particle excitations for the 2^+ state in Ca isotopes. ^{*54}Ca has only 61.3% occupation in the final $2p_{1/2}$ shell.

magic gap requiring larger excitation energies so there is no low-lying 2^+ peak at all in its strength function. The experimental low-lying 2^+_1 state (at energies less than 2 MeV) is a highly collective state and is not reproduced by the TDHF calculations as it essentially corresponds to angular momentum coupling within the same shell.

In Fig. 3.8, the energies of the "first" 2^+ state (labelled as 2^+_{low}, crosses), the peak occurring at ∼8 MeV (pluses), and the GQR peak (asterisks) are included amongst those from the single particle excitations listed in Tab. 3.4. The energies of the two low-lying peaks seen in Fig. 3.3 are very close to specific neutron single particle excitation energies, compatible with the predicted non-collectivity from the reduced transition probabilities. The energy of the low 2^+ peak seen is close to the energy of the neutron excitation from $1f_{7/2}$ to $2p_{3/2}$ for $^{42-50}$Ca and the energies of neutron excitations from $2p_{3/2}$ to $2p_{1/2}$, $2p_{1/2}$ to $1f_{5/2}$ and $2p_{3/2}$ to $1f_{5/2}$ in $^{50-54}$Ca. For the peak occurring at ∼8 MeV appearing for $^{42-54}$Ca, its energy is close to that of the $1f_{7/2}$ to $1f_{5/2}$ neutron excitation.

Unusually, the energy of the GQR peak is also close to the energy from the neutron excitation energy from $1d_{3/2}$ to $3s_{1/2}$ shell, but as this state is indeed collective it should be a coherent superposition of all possible quadrupole excitations.

In terms of relative peak strengths in Fig. 3.3, the low 2^+ peak increases in strength from $^{40-48}$Ca from the additions of neutrons to excite from the $1f_{7/2}$ shell. Similarly, the ∼8 MeV peak increases in strength up to ^{48}Ca then remains almost constant after, where the $1f_{7/2}$ has reached its full capacity to eight neutrons.

The magic number of protons leads to excitations requiring high energies of more than 15 MeV. This is because the next shell with the same parity as the last occupied ($1d_{3/2}$) is above the fp shells altogether. For neutrons, as they fill the fp shells from $N = 22$ and upwards, there are more possibilities for excitations of neutrons within this entire group of shells, hence the opening of more possibilities shown in both Tab. 3.4 and Fig. 3.8. With these extra possibilities for neutron excitations, the corresponding low-lying peak in Fig. 3.3 for these three nuclei is not stronger but instead splits into two (^{50,52}Ca) or three (^{54}Ca) peaks below 5 MeV.

The goal of this chapter was to focus on low-lying vibrational modes, which affect fusion reactions. It is clear that the collective 2^+_1 states are not calculated properly by TDHF, which directly translates to an improper treatment of 2^+_1 states in reaction calculations. Although the consistency of how low-lying 2^+ states are considered by TDHF is there between vibrations and reactions calculations, it means that the effect of the 2^+_1 state on fusion reactions cannot be studied well with this approach, except with some doubly magic nuclei.

As collectivity of vibrations in TDHF arises from the residual interaction, one method to confirm whether the 2^+ states really are non-collective would be to remove the residual interaction by freezing the initial mean field [2, 176] in the TDHF calculation and comparing the response to the unfrozen TDHF calculation. If the same vibrational spectra (as in Fig. 3.3) results from this modification, then the 2^+ states seen are definitely not collective. Low-lying 2^+ states in spherical nuclei can be reproduced to better agreement with experimental results in quasiparticle-RPA (QRPA) calculations [78, 203] which is the linearised version of TDHFB. It may also be that beyond mean field descriptions, for example the second RPA approach [1, 201, 234], are necessary to describe the 2^+_1 state for more exotic nuclei.

3.6 Summary

In this chapter, vibrations were studied using linear response theory in the TDHF framework. The focus of the study was on single phonon octupole and quadrupole vibrations in $^{40-54}$Ca isotopes. The low-lying octupole vibration was calculated as a collective state by TDHF. The resulting excitation energies and deformation parameters found from the strength function for the 3^-_1 state are within reasonable agreement with experimental values for the isotopes they are known for. For quadrupole vibrations, TDHF calculations do not reproduce excitation energy nor the deformation parameter of

the collective 2_1^+ state observed experimentally in many even-even nuclei. The lowest 2^+ states in most nuclei that were calculated by TDHF were not found to be very collective in their nature.

To explain the nature of the peaks seen in the strength functions, single particle excitations with energies corresponding to the HF ground state shell levels were considered. The comparison of the single particle excitation energies to the octupole vibrations excitation energies was compatible with the collectivity of the 3^- states. The low-lying 2^+ states had excitation energies that were very close to specific single particle excitations, further suggesting their non-collective nature.

A better description of these 2^+ states is necessary for further studies of low-lying quadrupole vibrations, as well as their effects on fusion reactions, and may require beyond mean field approaches. Other future work in this area could also include calculating vibrational spectra of protons or neutrons separately. This could help decompose the strength functions and resulting vibrational modes seen from the excitation of the whole nucleus.

The unbound states in the HF ground state should also be dealt with properly by incorporating pairing modifications to the continuum either through modifications of the BCS approximation by setting occupation numbers of unbound states to zero [50, 52] or by using the HFB theory for exotic nuclei. Alternatively, using more suitable boundary conditions [128, 153] for the time-dependent calculations could also improve the description of excitations to unbound levels.

Additionally, to only concentrate on low-lying vibrations of excitation energies up to about 10 MeV, using an appropriate time filtering function in the linear response theory that removes the contribution from the giant resonances could also be done [184].

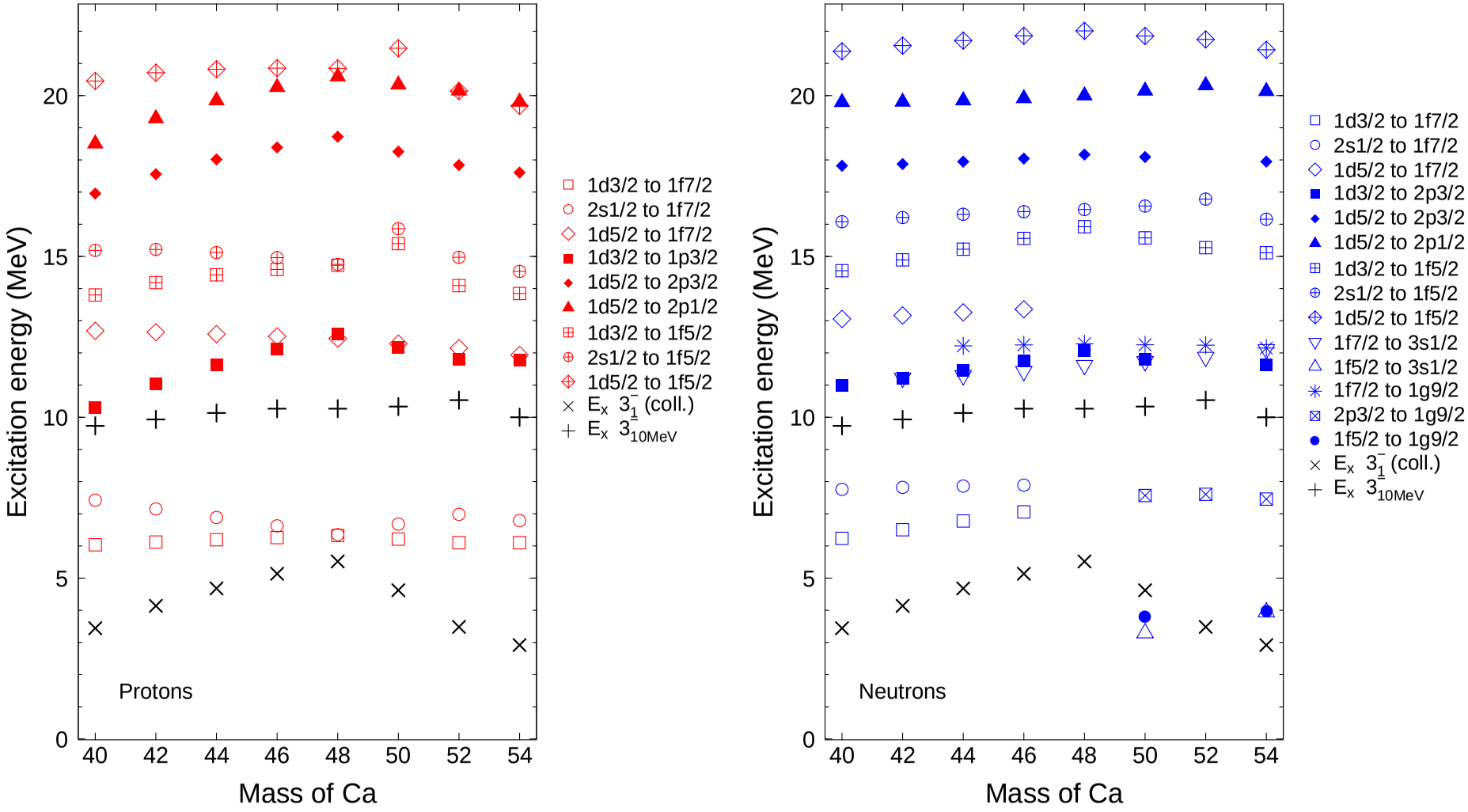

Fig. 3.7.: Energies of proton (left) and neutron (right) single particle excitations for calcium octupole vibrations.

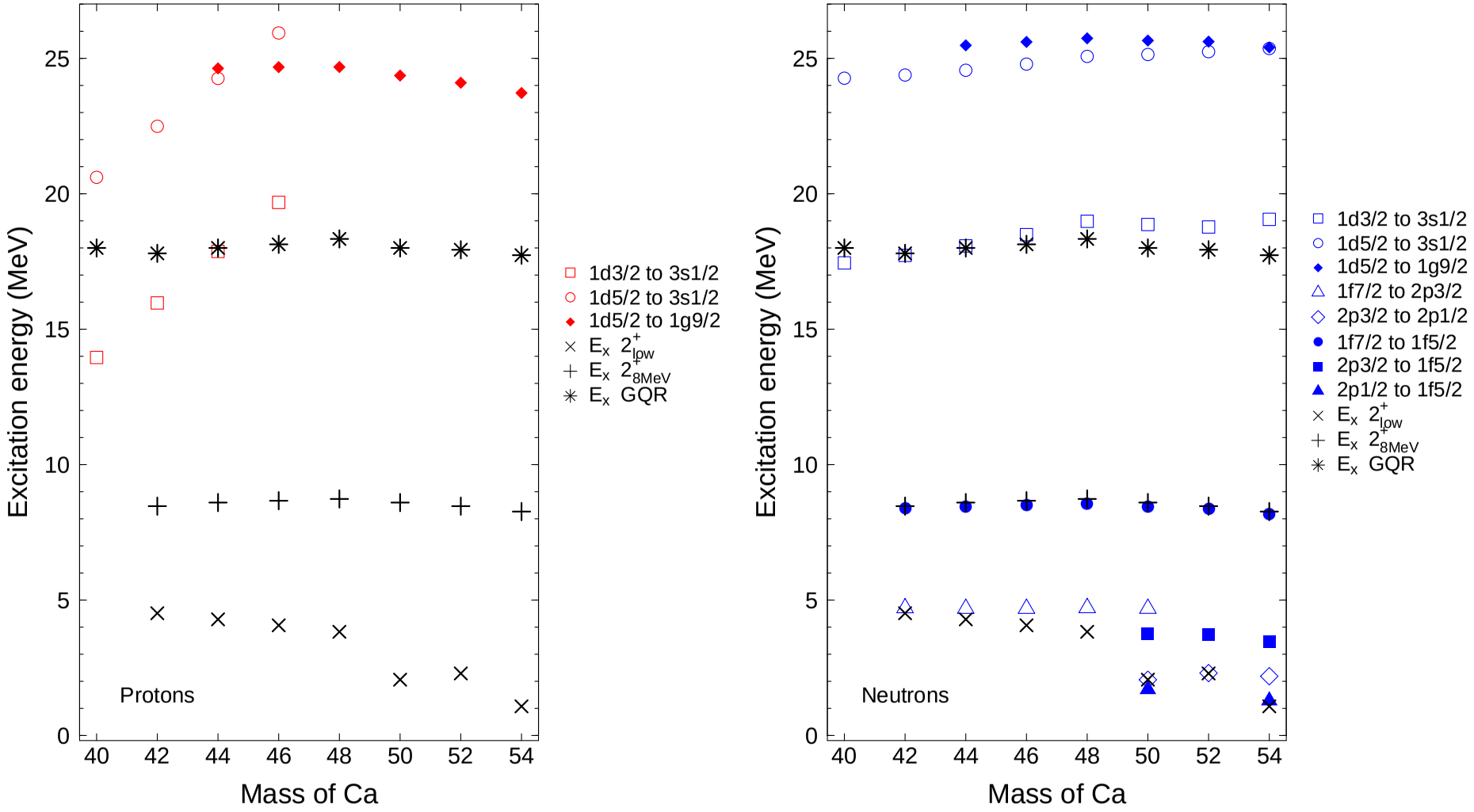

Fig. 3.8.: Energies of proton (left) and neutron (right) single particle excitations for calcium quadrupole vibrations.

Fusion reactions 4

4.1 Overview

In this chapter the Hartree–Fock (HF) method is applied to fusion reactions to follow on the previous chapter that applied HF to single nucleus evolutions. Many fusion reactions across various mass regions of the nuclear chart have been experimentally studied, particularly for reactions with stable beams and targets but also more recently for reactions with unstable nuclei. Conventionally, theoretical modelling of such fusion reactions has been done with the coupled channels approach (CC). However, many well studied reactions with stable beams are still not fully understood, such as the doubly magic system ^{16}O+^{208}Pb [45, 121, 235].

The goal of this chapter is to investigate what a microscopic approach can offer to understanding fusion reactions. The coupled-channels approach requires a prior knowledge of the projectile and target structure and also some assumption about their interaction potential. Microscopic methods, such as HF, self-consistently predict all of this. This is particularly important for reactions involving nuclei far from the valley of beta stability to see if reaction processes change for exotic nuclei.

In studying fusion reactions with the HF method, the main quantity used to compare different systems is the fusion barrier energy. How to obtain this and other relevant quantities is explained in the appropriate sections in this chapter. The barrier energy is a characteristic quantity of a fusion reaction. In a classical single barrier picture, the barrier energy (or height) defines whether or not fusion can occur. Below the barrier energy, quantum mechanical tunnelling can happen. It is now known that fusion dictated by a single barrier energy is an oversimplification and does not explain measured fusion cross sections. It has been shown that the single barrier is effectively replaced by a distribution of barriers, which results from coupling effects. An experimental barrier distribution can be extracted from measured fusion cross sections [46, 155].

Material presented in this chapter concentrates on the energy region at and just above or below the barrier energy. The reason for this is that these energies are where dynamical processes such as vibrations and transfer are likely to have the largest influence on fusion. Far below the barrier, the nuclei do not reach close enough to interact and have the possibility of internal excitations. Far above the barrier, fusion cross sections are

insensitive to the specifics of couplings. Other processes that can occur in this energy region, for example particle emission, are explored in the next chapter.

To study fusion reactions using HF in a systematic way, considered first are the static properties of the individual nuclei and the effect of these on fusion and the barrier energy. To isolate static effects, the frozen HF method is used. Static properties that are expected to influence fusion reactions at near barrier energies are neutron skin effects [61] and deformation [110, 195, 231] and are discussed first. Then, dynamic effects are introduced using the time-dependent HF (TDHF) method.

4.2 Static picture of fusion

Studies of fusion reactions can begin with the simplest picture by forcibly restricting the nuclei to have no internal freedoms, removing the possibility of internal excitations and other dynamical processes known to play a role in fusion. During a collision, excitations that can occur are due to the Coulomb interaction and, when separation distances between the nuclei are close enough, via the nuclear potential. These internal excitations release the nuclei from their ground state.

The following sections present calculations based on the frozen Hartree–Fock technique, outlined in subsection 2.5.1, whereby the nuclei are frozen in their initial ground state and are brought close together by reducing their separation distance.

The systems appearing in this chapter are:

I. $^{40-54}$Ca+^{116}Sn,

II. $^{36-58}$Ca+^{132}Sn,

III. ^{40}Ca+$^{124-136}$Sn.

These chains were chosen because they are of mid-mass range, calcium and tin both are magic in proton number so the effect of additional neutrons in fusion reactions can be explored, and two of the chains (groups I and III) start with stable isotopes and move towards reactions involving nuclei approaching the neutron dripline. Experiments in this mass region including some of the ones in the chains exist already, such as ^{40}Ca+^{124}Sn [102, 168] and ^{48}Ca+^{132}Sn [102].

4.2.1 Nucleus-nucleus potential from phenomenology

As two nuclei approach each other they undergo repulsion from the long range Coulomb potential and attraction from the short ranged nuclear force. The general form of the

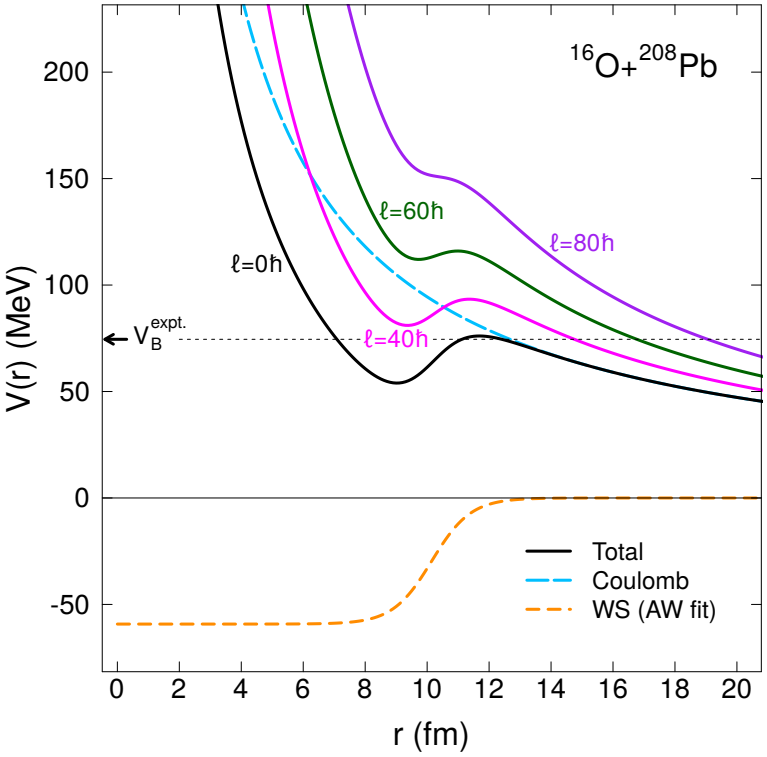

Fig. 4.1.: A nucleus-nucleus potential for the system ^{16}O+^{208}Pb and its components. The total potential (solid line) is shown for four different values of ℓ.

one dimensional nucleus-nucleus potential, as a function of separation distance r, can be written as

$$\begin{aligned} V(r) &= V_N(r) + V_C(r) + V_\ell(r) \\ &= V_N(r) + \frac{Z_1 Z_2 e^2}{r} + \frac{\ell(\ell+1)\hbar^2}{2\mu r^2}. \end{aligned} \tag{4.2.1}$$

The exact form of the Coulomb potential (V_C) and the centrifugal potental (V_ℓ) is known but remains unknown for the nuclear potential (V_N). A popular form used for the nuclear potential is the Woods–Saxon (WS) potential [233]

$$V_N(r) = \frac{-V_0}{1 + \exp\left(\frac{r-R_0}{a}\right)}, \tag{4.2.2}$$

which has three parameters V_0, R_0 and a. An example of a total nucleus-nucleus potential for $\ell = 0\hbar$ (black) for the system ^{16}O+^{208}Pb is shown in Fig. 4.1 using the Akyüz–Winther (AW) potential fit [31] for the WS parameters, $V_0 = 59.22$ MeV, $R_0 = 10.15$ fm and $a = 0.63$ fm (see Appendix D for more details on this fit). The Coulomb (blue, long dashed) and WS nuclear (orange, dashed) components are also shown in Fig. 4.1. The total potential for different values of ℓ are also shown by the solid coloured lines. As ℓ

increases, the "pocket" left of the peak of $V(r)$ (at around $r = 9$ fm in this case) becomes shallower and eventually disappears for a high enough value of ℓ. In this case $\ell = 80\hbar$ is sufficient for this to occur.

4.2.2 Nucleus-nucleus potential from Hartree–Fock

The HF method to calculate the bare nucleus-nucleus potential is outlined in subsection 2.5.1. It was mentioned that

- The Coulomb contribution is not taken as a point Coulomb potential as done for the V_C term in equation (4.2.1), rather it is calculated from the Coulomb field of the two nuclei which has a direct and exchange term (calculated with the Slater approximation [64, 70]),
- The nuclear contribution is an integral over the energy density functional, (dependent on the two densities of the nuclei) which is taken to be the Skyrme EDF,
- The potential is always calculated as a function of $\mathbf{r}$, the vector between the centre of masses of the two nuclei. By construction, the HF nucleus-nucleus potential is independent of angular momentum and has no centrifugal potential contribution.

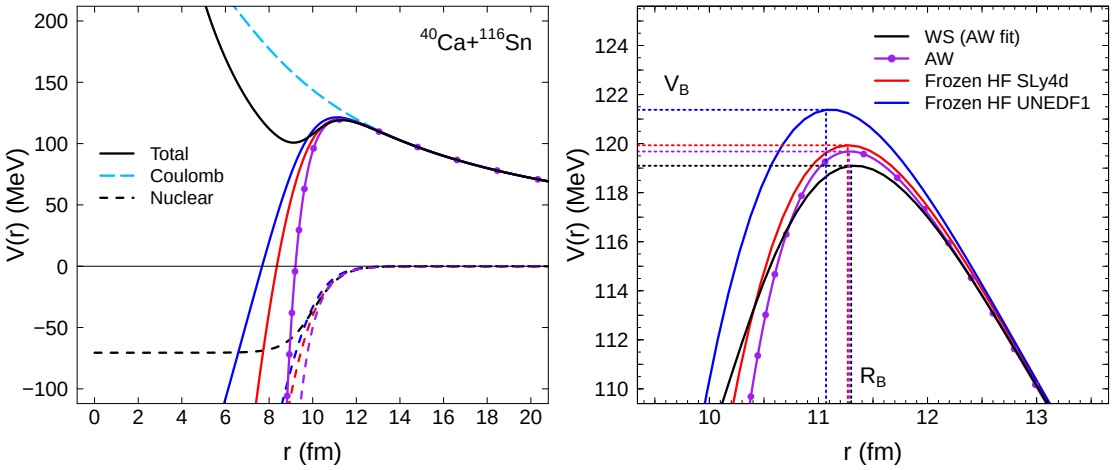

Fig. 4.2.: Left: Total nucleus-nucleus potentials (solid lines) for ^{40}Ca+^{116}Sn calculated with frozen HF, WS and AW potentials. The Coulomb potential (long-dashed) and the nuclear potentials (short-dashed) are also shown. Right: a zoom in of the barrier region.

An example of the total nucleus-nucleus potential (solid lines) for the system ^{40}Ca+^{116}Sn is given in Fig. 4.2, for frozen HF with two Skyrme parametrisations (blue and red), WS with AW fits (black), and the AW form for the nuclear contribution to the potential [31] (purple). The form for the AW nuclear potential is in Appendix D. On the left is the decomposition of the total potential into the Coulomb potential (long dashed) and the

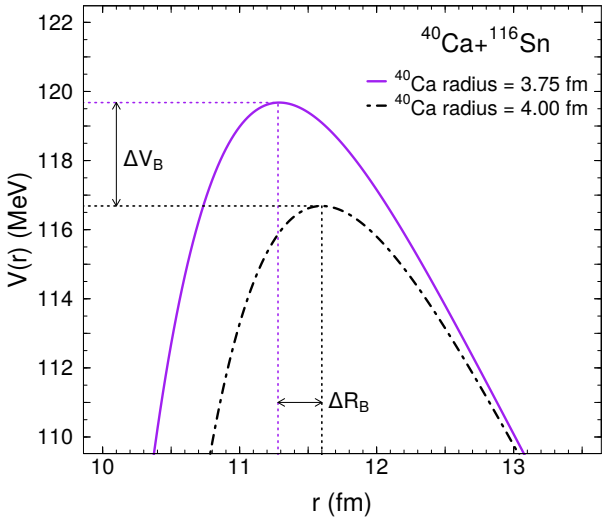

Fig. 4.3.: Barrier region of AW potential for ^{40}Ca+^{116}Sn with two different AW radius parameters for ^{40}Ca. The difference in V_B is 3.0 MeV and the difference in R_B is 0.3 fm.

various nuclear potentials for the different forms (dashed). The Coulomb contribution is taken from the frozen HF calculation, the difference between this and the Coulomb potential from point charges is smaller than the width of the line for the range of energy shown in the graph. The right panel is a zoom in of the left panel of the barrier region. The horizontal dotted lines at the turning point show the different barrier energies, V_B, (or interchangeably fusion barrier, barrier height) and the vertical dashed lines are the corresponding barrier radii, R_B. All three models, although different in approach, agree quite well in V_B, within 2 MeV and for R_B, within 0.3 fm.

The barrier position and energy is sensitive to small changes to basic nuclear structure properties, for example the radius of the interacting nuclei. If the radius of one of the nuclei is artificially increased by changing the radius parameter (R_i in Appendix D) in the AW potential, the barrier energy will reduce correspondingly since the nuclear potential will extend to larger distances. This effect is illustrated in Fig. 4.3.

The frozen HF, WS and AW potentials have different inner parts of the potential shape which is where the nuclear force starts playing a part in fusion, and in each case the nuclear force is treated differently. It is worth mentioning that the frozen HF potential in this thesis does not include Pauli blocking effects between nucleons of colliding nuclei. This effect has only been included recently in Ref. [186] with the density constrained frozen HF method. It mostly affects the inner part of the nucleus-nucleus potential, leading to a "Pauli repulsion". With the addition of Pauli repulsion the width of the peak region is increased significantly, which affects tunnelling. The main focus of this work is just around the barrier energy and not concerning the inner part of the nucleus-nucleus

potential. For ^{16}O+^{208}Pb, the barrier energy increases by almost 3 MeV. This amount is smaller (less than 1 MeV) for Ca+Ca systems. For systems with Ca+Sn, Pauli repulsion could then also affect the barrier energy. However, the main interest in this chapter is in the evolution of the barrier energy when going towards exotic systems. It is assumed that the impact of the Pauli repulsion does not affect the evolution with the neutron numbers of one nucleus, but only leads to a systematic shift of the barrier energies.

Systematic studies are a useful way of studying nuclear structure effects on barrier energies. Experimental data often exists with stable isotopes which can then be used to test the approach. In moving towards nuclei that are not well studied, namely ones that approach the neutron dripline, the predictive powers of HF methods can then be utilised.

4.2.3 Barrier energies

To study the systematics of fusion barriers, all groups I. $^{40-54}$Ca+^{116}Sn , II. $^{36-58}$Ca+^{132}Sn and III. ^{40}Ca+$^{124-136}$Sn will be considered. The systems in group II have the widest span of Ca isotopes on the heavier ^{132}Sn isotope (compared to group I). This group includes exotic nuclei colliding with exotic nuclei for which experimental measurements are not likely. Studies were then refined to group I with the stable ^{116}Sn so the progression of calcium isotopes moving from stable to exotic is more evident. Ca isotopes in this group were restricted to $A = 40$ to 54. Structure information about some of these isotopes is experimentally available. The chain of isotopes in group I still moves from stable calcium nuclei right through to neutron rich isotopes for which reactions experiments are not yet feasible. Group III contains the "inverse reactions" ^{40}Ca+$^{124-136}$Sn where only the ^{124}Sn isotope in the chain is stable. In each of the three chains, only even isotopes are considered in the following chapters, using the assumption of time reversal symmetry of the HF wavefunctions (more explanation on this in subsection 2.5.1).

For the systems in groups I, II and III, the Figs. 4.4 and 4.5 show the frozen HF barrier energy versus mass of the member of the chain in question. In each of the three groups, a general reduction of the barrier energy is observed with increasing mass. Also plotted alongside frozen HF barriers are the AW barriers as a comparison to a phenomenological model. The reduction for the frozen HF calculations is not a constant linear reduction, unlike for the phenomenological AW potential which bases the nuclear radii on just their mass number and does not account for quantum shell effects. In the systems with a calcium chain, there is a kink seen at ^{48}Ca. In the group III systems, there is a kink at ^{132}Sn. Frozen HF and other phenomenological barriers for a chain of isotones on a ^{208}Pb target is presented in Appendix E.1. Likewise, a kink appears in the frozen HF barriers

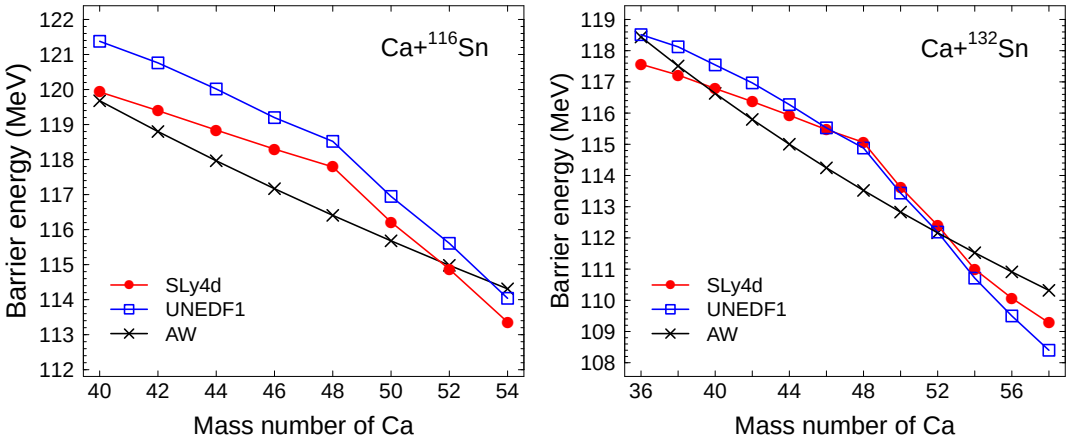

Fig. 4.4.: Frozen HF (red and blue) and AW (black) barrier energies for left: $^{40-54}$Ca+^{116}Sn and right: $^{36-58}$Ca+^{132}Sn. Both SLy4d [101] and UNEDF1 [104] parametrisations are shown.

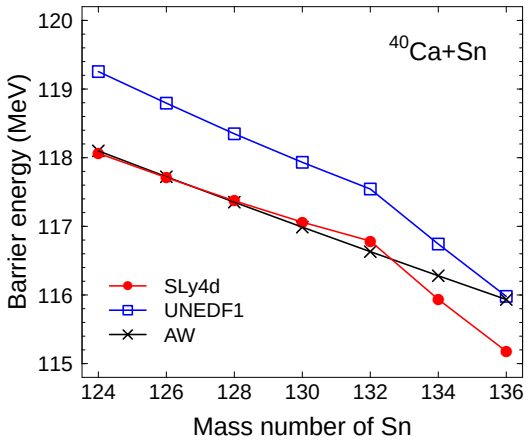

Fig. 4.5.: The same as Fig.4.4 but for systems ^{40}Ca+$^{124-136}$Sn.

but not for any of the barriers calculated with phenomenological models.

The change of gradient in barrier energies seen from the frozen HF results is an interesting feature which is explored in the next section through the shell structure of the isotopes.

4.2.4 Effect of ground state properties on barriers

The goal of this subsection is to explain trends seen in the frozen barrier energies for all groups of systems. For the static reactions in the previous section, all the nuclei remained in their ground state. The only properties of the nuclei that should be considered are those arising from ground states. It has already been established that in any model for the nucleus-nucleus potential, the size of the nucleus relates to the barrier radius and consequently the barrier energy, as shown in Fig. 4.3. Discussions will therefore start with nuclear radii. Then, consideration about what actually contributes to the nuclear

radius will ensue, for which the single particle shell structure will be explored.

All nuclei involved have at least one magic number and are to a good approximation spherical in their ground state. Deformation is not apparent in these calculations and is irrelevant in the following discussions.

Radii

In Fig. 4.3 it was shown how sensitive the phenomenological AW potential is to an artificial increase of the radius of just one nucleus. It is worth checking how the radius varies along an isotopic chain from the HF ground states. Before proceeding with any of this, a clear definition of the size of a nucleus, a quantum mechanical object with no clear boundary to its shape, is required. There are a few ways that a radius of a nucleus can be defined. One way is to characterise it by the root-mean-square (rms) radius. Both the proton and neutron rms radii can be found from

$$r_{p,n}^{\text{rms}} = \left(\int \rho_{p,n}(\mathbf{r}) r^2 d^3 r \right)^{\frac{1}{2}}, \tag{4.2.3}$$

where $\rho_{p,n}$ is the proton or neutron density.

The HF rms radius is plotted in Fig. 4.6 for the calcium isotopes (left) and tin isotopes (right). As the mass increases for both the calcium and tin isotopes, it is no surprise that the neutron rms radius increases. The increase in proton radius, though the proton number remains constant, accounts for the increasing symmetry energy. If there was no N and Z symmetry preference in a nucleus then the addition of neutrons would essentially leave the proton configuration unchanged since the Coulomb energy remains the same. The effect of increasing symmetry energy is more obviously seen through the calcium chain which starts with the symmetric ^{40}Ca nucleus (in N and Z) and ends with a the very neutron rich ^{58}Ca. As tin isotopes have more protons, more neutrons are required for stable isotopes to balance the Coulomb repulsion. The change in proportion of neutrons to protons between ^{124}Sn and ^{136}Sn isotopes is smaller than between the ^{40}Ca and ^{58}Ca isotopes.

Also included in Fig. 4.6 are the experimental charge rms radii for $^{40-50}$Ca [220, 230] and $^{124-132}$Sn [17, 204]. These values are relatively close to the calculated proton radii, especially for the doubly magic nuclei ^{48}Ca and ^{132}Sn. The deviations are larger for mid-shell nuclei due to correlations not accounted for at the mean field level [36].

Even though the proton rms radius is indeed changing, the neutron radius is larger in magnitude, increases more rapidly and is the more significant contributor to the nuclear

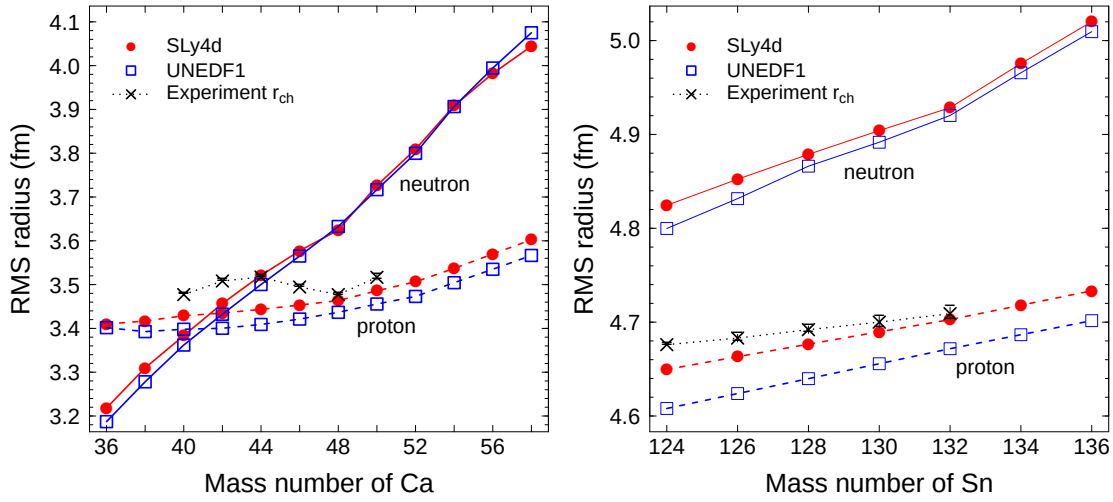

Fig. 4.6.: Neutron (solid) and proton (dashed) RMS radii of calcium isotopes (left) and tin isotopes (right). Experimental rms charge radii are included for comparison for $^{40-50}$Ca [220, 230] and $^{124-132}$Sn [17, 204] isotopes.

radius as a whole (with the exception for $^{36-40}$Ca). Furthermore, the neutron rms radius grows more rapidly after ^{48}Ca in the calcium chain and ^{132}Sn in the tin chain. The fact that these are both magic nuclei is not a coincidence, but nor should it be assumed that this particular trend only occurs at magic nuclei. For example, in the calcium chain (Fig. 4.6 (left)), there is no change in gradient of the neutron rms radius at ^{40}Ca but there is around the non-neutron magic ^{54}Ca. However, these kinks in the neutron rms radius at ^{48}Ca and ^{132}Sn match where there are kinks in the fusion barrier energies in Figs. 4.4 and 4.5.

To relate this definition of nuclear size to the increased barrier reduction seen in Figs. 4.4 and 4.5, consider simply the separation distance at which the nuclei experience the greatest potential, the barrier radius. When a nucleus increases in size, the barrier radius increases thereby lowering the Coulomb contribution to the nucleus-nucleus potential. It follows that along a chain of nuclei that increase more rapidly in size, the fusion barrier will decrease more rapidly.

The rms radius behaviour and development of a neutron skin fits well with the fusion barrier behaviour, but this alone is not satisfactory. The rms radius is a bulk property from the microscopic HF method which affords the luxury of exploring nuclear properties at a microscopic level. The nuclear rms radius is dependent on the radial part of the wavefunction for the entire nucleus, which comprises the wavefunctions for each nucleon. Examination into the single particle structure and configuration is now necessary.

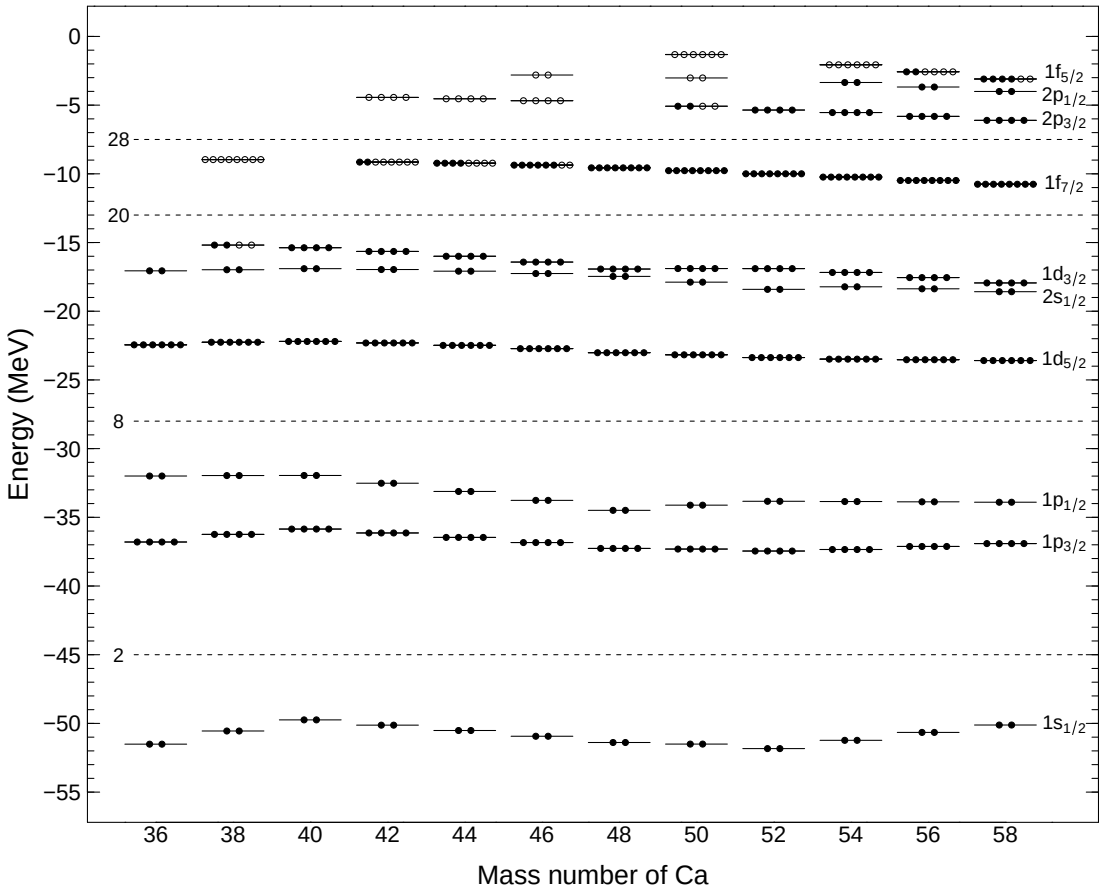

Fig. 4.7.: Neutron single particle shell configuration for calcium isotopes (calculated using the SLy4d parametrisation). Closed circles indicate the lowest energy configuration for N neutrons, open circles are shown on levels with partially occupied states. States appearing at energies above 0 MeV are omitted.

Single particle shell levels

The HF shell levels and energies provides insight into the internal microscopic structure of each nucleus in their ground state. The focus will be on neutrons following from the results seen from the neutron rms radii. The single particle neutron configuration for $^{36-58}$Ca is shown in Fig. 4.7 and that for $^{124-136}$Sn in Fig. 4.8. Some levels near the Fermi surface, shown in Figs. 4.7 and 4.8, are partially occupied (open circles) due to pairing interactions between neutrons in non-magic nuclei which accounts for noninteger occupation numbers of the outermost shells. For this reason, there are more states shown than required for the number of neutrons in many of the isotopes, if all levels were fully occupied.

Where the magic numbers occur, the energy gaps between the levels are at least 5 MeV. For example, in Fig. 4.7 between ^{48}Ca and ^{50}Ca (magic number 28 for neutrons moving to 30 neutrons) the neutrons have filled up the $1f_{7/2}$ shell and start to fill the $2p_{3/2}$ shell; the energy gap between these two shells is approximately 5 MeV. While the

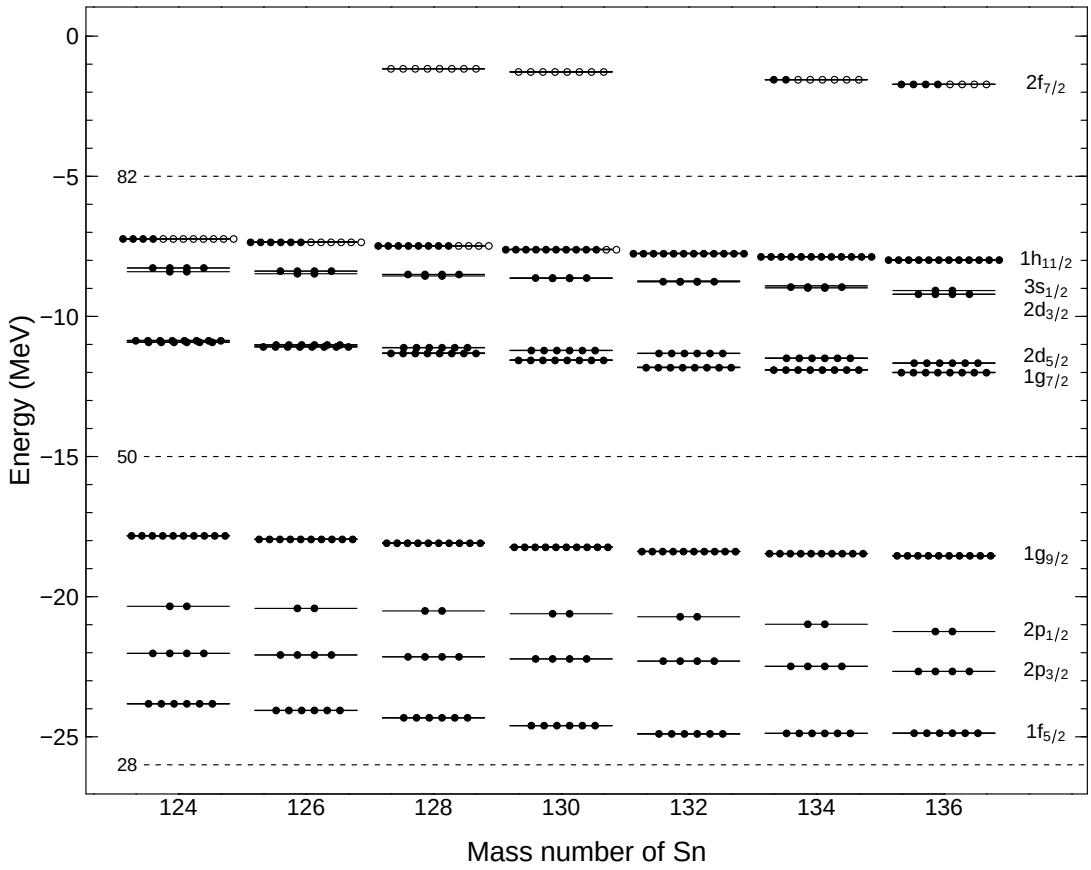

Fig. 4.8.: Same as for Fig. 4.7 but for $^{124-136}$Sn isotopes. The neutron shells preceding the $1f_{5/2}$ shell are omitted.

focus naturally is on the least bound shells as these nucleons are likely to interact with the target first, the particles in the inner shells should not be completely ignored in discussions.

In Fig. 4.4 on the right there are two kinks at $A = 48$ and 54. For $^{40-48}$Ca this corresponds to the filling of the $1f_{7/2}$ neutron shell in calcium. Between $^{48-54}$Ca this corresponds to the filling of both $2p$ shells and for ^{56,58}Ca this is the filling of $1f_{5/2}$ shell. The filling of the $1f_{7/2}$ and $1f_{5/2}$ shells produce a similar gradient in barrier energies, which could be attributed to the two shells having the same angular momentum. The filling of the $2p$ shells produce a steeper gradient, owing to the additional node in the wavefunctions of neutrons lying in the $2p$ shells.

Single particle radial wavefunctions

To verify that the neutrons in the outermost shells do have radial wavefunctions that extend further than those of the more bound shells, the single particle radial wavefunctions for neutrons in these shells are calculated, using the DENS code in NuShellX@MSU [32]. These are shell model calculations of ground states using the Hartree–Fock potential with

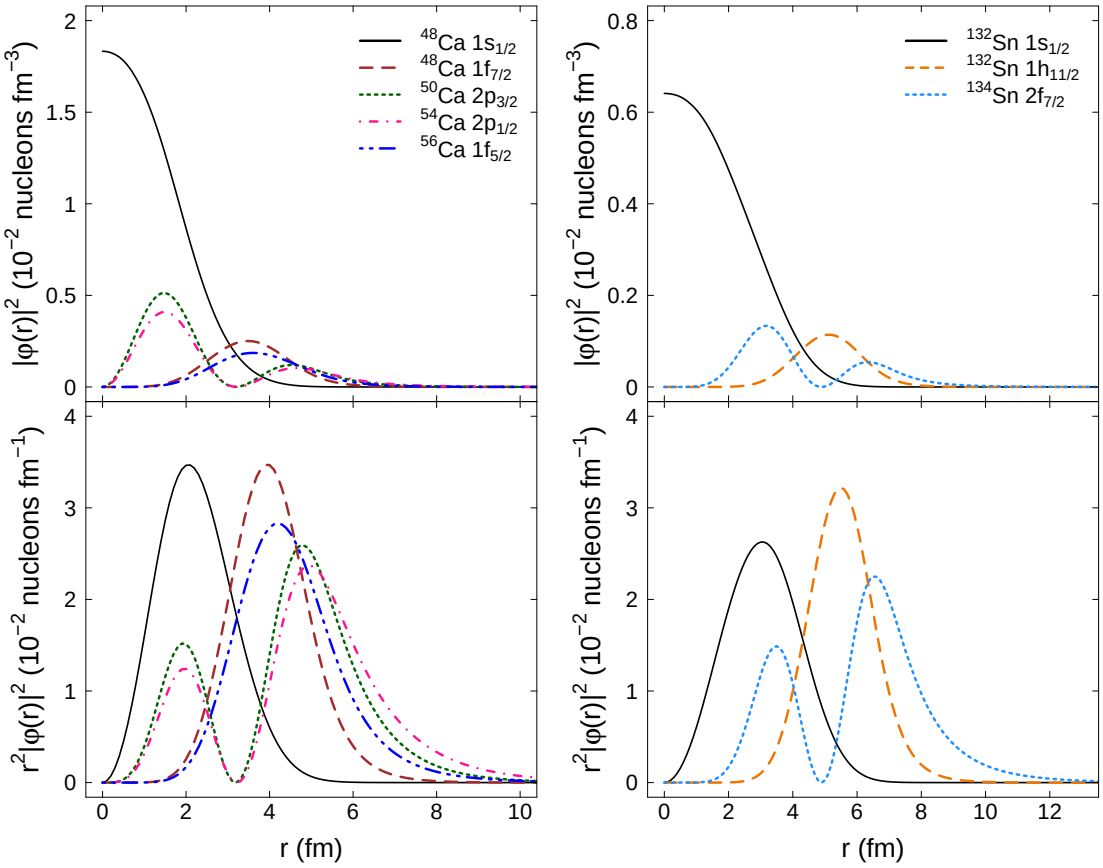

Fig. 4.9.: Probability density of single particle neutron radial wavefunctions (top panels) and multiplied by r^2 (bottom panels) for the least bound neutron in ^{48,50,54,56}Ca (left) and ^{132,134}Sn (right).

Sly4d parametrisation of the Skyrme interaction however with no BCS pairing functional included. It has been checked that the shell level energies agree well with the original EV8 calculations of the calcium and tin ground states seen in Fig. 4.7 and 4.8.

Shown in Fig. 4.9 are the the single particle wavefunction density functions (top panels) and the density functions multiplied with the square of the radial distance r^2 (bottom panels) for some neutron single particle shells in calcium and tin isotopes. On the left panels in Fig. 4.9, the wavefunctions shown are of the least bound neutrons in the isotopes ^{48,50,54,46}Ca, corresponding to the $1f_{7/2}, 2p_{3/2}, 2p_{1,2}$ and $1f_{5/2}$ shells respectively. The $1s_{1/2}$ shell wavefunction is included as a reference. On the right panels are the neutron wavefunctions for ^{132,134}Sn corresponding to the $1h_{11/2}$ and $2f_{7/2}$ shells respectively. These isotopes are shown because the rms neutron radius for the chain of calciums and tins in Fig. 4.6 shows kinks at ^{48,54}Ca and at ^{132}Sn. The bottom panels of Fig. 4.9 is included as a more direct comparison to the expression for rms radius (4.2.3) and also to magnify difference between the wavefunctions at their tail or at larger distances.

First, comparing the least bound neutrons of ^{48,50}Ca, it can be seen that the probability

density of $2p_{3/2}$ radial wavefunction in ^{50}Ca (green, dotted line) is higher than that of the ^{48}Ca $1f_{7/2}$ radial wavefunction (brown, dashed) at larger distances. This is because of the extra node in the $2p$ shells. Similarly, comparing the least bound neutrons of ^{54,56}Ca, it is the probability density of the $2p_{1/2}$ radial wavefunction in ^{54}Ca (pink, dot-dashed) that exceeds that of the $1f_{5/2}$ wavefunction in ^{56}Ca (blue, dot-dot-dashed), the former having an extra node. For the tin isotopes, it is also the case that the probability density of the $2f_{7/2}$ radial wavefunction (light blue, dotted) which has two nodes is larger than that of the $1h_{11/2}$ (orange, dashed) at larger distances.

The behaviour of the neutron single particle wavefunctions for these calcium isotopes is consistent to the occurrence of the kinks of the rms radii seen in Fig. 4.6.

The single particle wavefunctions sheds more light on the internal (static) structure of the chain of nuclides than just considering the shell level energies. They factor into the nuclear radius and in turn the fusion barriers.

4.3 Introducing dynamic effects

While considering fusion reactions by using frozen ground state densities is a useful starting point, most of the time it is not representative of how a fusion reaction should evolve, especially for heavy-ion collisions. A more realistic picture of a reaction naturally should include the dynamics of the nuclei as they approach each other during the collision. Dynamics in this chapter includes the internal excitations, for example vibrations and rotations that either the projectile or target undergoes as they approach each other, and also mass transfer between projectile and target. Rotational excitations will play a role when one or both of the nuclei are statically deformed, for example any of the actinides. None of the nuclei as calculated by HF in this chapter are other than spherical in their ground state so rotational modes are not considered. Fully 3D TDHF codes without any spatial symmetries assumed exist so triaxial nuclei or rotations in any axis can be considered [112, 212].

Excitational modes of vibrational and rotational nature and their effect on fusion reactions are often studied with the coupled-channel (CC) formalism and are known to have an effect on fusion reactions [46]. Mass transfer also plays an important role in heavy-ion reactions, however, currently no complete model for studying how transfer modes affect fusion reactions exists. The time-dependent HF (TDHF) approach can be used, both on its own and also in tandem with CC, for studying the effects of dynamics on reactions.

The TDHF approach has been shown to give different fusion thresholds than the corresponding frozen HF bare potential computed with the same energy density functional, indicating an important role of dynamics on the fusion mechanism [180, 182, 184, 217, 225]. Examples of this will materialise in the following section.

In addition to those cases already studied in the static fusion section, some other systems that have been studied in this work include:

- ^{92}Zr $+^{12}$C, ^{16}O, ^{35}Cl,
- ^{40,48}Ca$+^{40,48}$Ca.

The main motivation for including these particular systems is to check how reasonable the TDHF calculation of the fusion threshold is compared with experimental fusion barriers extracted from fusion measurements [119, 133, 193, 208]. The nucleus ^{35}Cl is odd-even but calculations will still be presented, assuming partial filling of shells and time reversal symmetry in the single particle wavefunctions. Discussions of this aspect were included in subsection 2.5.1.

4.3.1 Barrier thresholds from TDHF

The TDHF method described in Chapter 2 means that there is evolution of the density of the entire system that in turn recreates its mean field at each time step. Because of this, a nucleus-nucleus potential cannot be extracted in the same way as for the frozen HF method as the two nuclei are not considered as separate densities in the system. Extracting a nucleus-nucleus potential can be done by instead using the density-constrained TDHF method [211] which has not been used in this thesis, so the fusion barrier energy must be obtained differently. The semi-classical nature of TDHF makes this an easier task because at a given energy, a system will either fuse or separate after some particular time as there is no tunnelling of the many-body wavefunction taken into account. No probabilities of different outgoing trajectories are produced, merely the average trajectory. The success or failure of fusion occurring is judged entirely by this single, outgoing trajectory.

In this chapter, the extraction of a fusion barrier energy from the TDHF method used the distance between centre of masses of the two interacting nuclei. The notion of having separate centres of mass in this single mean field defined for the whole system is addressed by defining a neck plane perpendicular to the collision axis. At each time, its purpose is to separate the entire density of the system into two fragments [225]. Using this, the centres of masses of these two fragments and the distance between them can then be calculated at each time step. Fusion for the system was deemed successful if, at a given

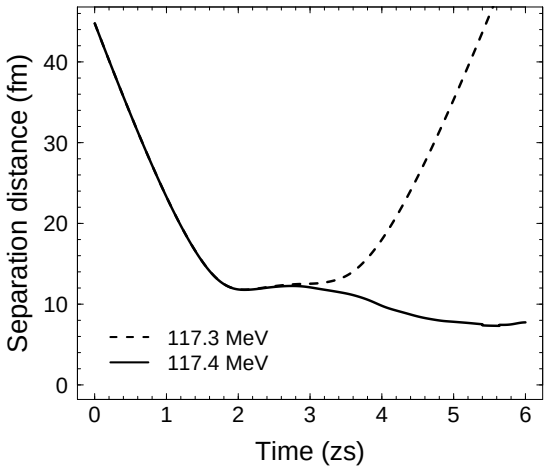

Fig. 4.10.: Distance between the centres of masses for the fragments in the ^{40}Ca+^{116}Sn reaction as a function of time. Two energies are shown, 117.3 MeV does not lead to fusion and increasing to 117.4 MeV leads to fusion. The TDHF fusion threshold for this system is taken as 117.35±0.05 MeV.

centre of mass energy $E_{\rm cm}$, the distance between the centres of masses remained below approximately 10 fm after a certain amount of time which will be defined.

Depending on how heavy the system is, the time limit will change and is adjusted until a compact nucleus (CN) is observed in the final fragment. The distance between the centres of masses is also dependent on the system and is not the only possibility to judge fusion by. For calcium on tin systems, a CN sticking time of 6 zs is enough to conclude that fusion has occurred. This is relatively short even in timescales of fusion, but examination of the final fragment justifies the time limit. On a more practical note fusion success can also be limited by computational time and patience. For heavier systems, a much longer time is likely to be necessary though still in the zeptosecond regime, which will be discussed in greater detail in Chapter 5.

An example of the distance between centre of mass with respect to time is presented in Fig. 4.10 for the system ^{40}Ca+^{116}Sn. The solid line is associated with a trajectory where fusion occurred and the dashed line is where reseparation occurred. Note that the system has decided whether it will fuse or not within approximately 1 zs, between 2 zs and 3 zs. In TDHF calculations, the fusion barrier energy is really then a fusion threshold which is found by varying $E_{\rm cm}$ in small steps. Typically steps of 0.1 MeV are used, meaning TDHF fusion threshold energies have a numerical uncertainties of ±0.05 MeV. All TDHF barriers presented henceforth will have this same uncertainty unless specified otherwise.

The TDHF fusion thresholds (dashed lines) for several systems are plotted with the corresponding frozen HF fusion barriers (solid lines) in Figs. 4.11, 4.12 and 4.13. The fusion barriers for the $^{40-54}$Ca+^{116}Sn reactions are shown in Fig. 4.11 on the left with

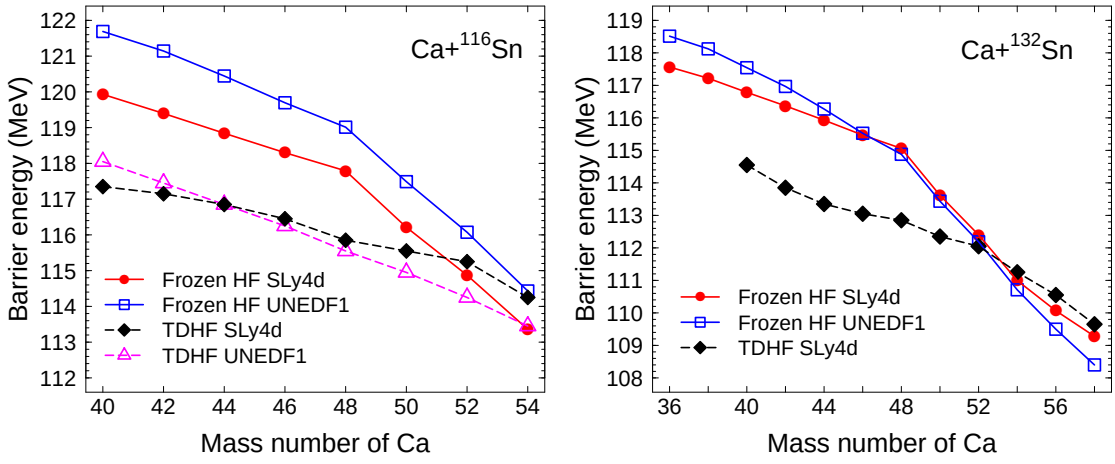

Fig. 4.11.: Barrier thresholds from TDHF (dashed) and frozen HF (solid). Left: for systems $^{40-54}$Ca+^{116}Sn. Right: for systems $^{40-58}$Ca+^{132}Sn.

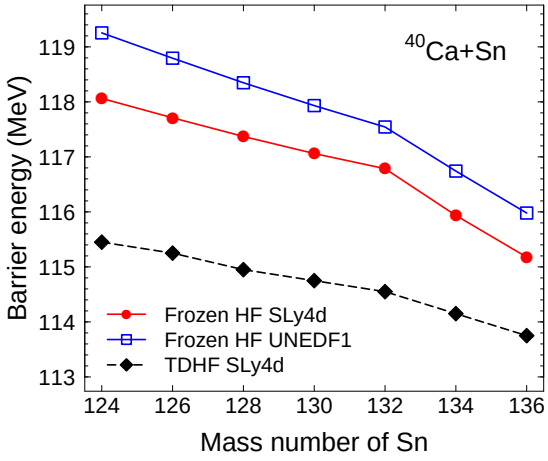

Fig. 4.12.: The same as Fig. 4.11 for the reactions ^{40}Ca+$^{124-136}$Sn .

two parametrisations of the Skyrme functional, SLy4d and UNEDF1. The lines which include the dynamics are, with few exceptions, lower than the static barriers. What happens for the chain of systems as a whole is that the dynamic effects (with TDHF) have overriden the static structure effects which characterised the static barrier, that is, the TDHF barriers no longer show a change of gradient around the ^{48}Ca+^{116}Sn system that was present in the frozen HF barriers. This means that the sub-barrier fusion enhancement expected from the neutron skin in a static picture is in fact not evident when dynamic processes are included. For the SLy4d parametrisation the fusion barrier is actually increased, relative to the frozen HF barrier, with the inclusion of dynamics for reactions with ^{52,54}Ca. This is surprising, as it is expected that dynamics should in general lower the fusion barrier [74]. For the UNEDF1 parametrisation the fusion barrier has been lowered in all cases, though with a much smaller magnitude for the most neutron rich calcium isotopes. Both parametrisations predict that for the most neutron

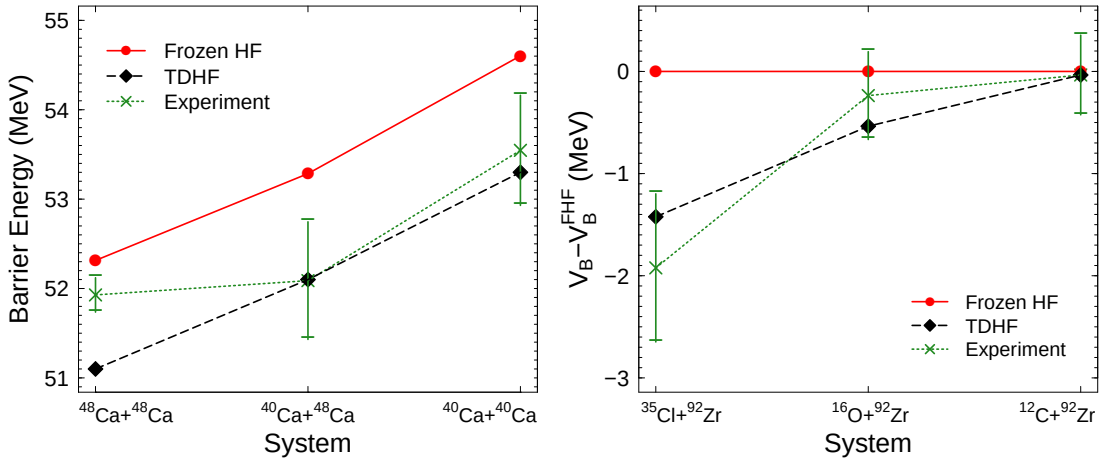

Fig. 4.13.: Left: Barrier thresholds from TDHF and frozen HF (calculated with the SLy4d parametrisation) compared with experimental barriers for Ca+Ca systems. Right: The difference between HF and experimental barriers to the frozen HF barriers for systems with a ^{92}Zr target.

rich isotopes a dynamical mechanism, due to couplings, occurs which counterbalances the lowering of fusion thresholds expected from the increasing neutron skin.

To check the results for the $^{40-54}$Ca+^{116}Sn reactions seen in Fig. 4.11 (left) are not unique to a particular isotope of the heavy fragment, it is compared with the same calcium chain but colliding with ^{132}Sn instead as was done for the static case in section 4.2.3. A similar trend occurs in the losing of the static structure effects for the SLy4d parametrisation. The crossover where the dynamic barrier becomes higher than the static barrier occurs now at ^{54}Ca+^{132}Sn and continues for the heavier systems. Using a different target altogether can be seen in the Appendix E.2 for systems $^{44-58}$Ca+^{208}Pb.

Calculations for the systems ^{40}Ca+$^{124-136}$Sn are presented in Fig. 4.12 and again show that the TDHF barriers wash out the static structure effect, but no crossover is seen in these particular systems. This result will be discussed in the coming sections, though it can already be seen that the gradient of frozen HF barriers after ^{132}Sn is larger (in magnitude) than the TDHF line.

To compare the TDHF predictions of fusion barriers to experimental values, the systems ^{40,48}Ca+^{40,48}Ca and ^{92}Zr +^{12}C, ^{16}O, ^{35}Cl as in Refs. [119, 133, 193, 208] were calculated and are presented in Fig. 4.13. In each of these systems the TDHF barrier again falls below the frozen HF barrier and matches quite well (in most cases within 0.5 MeV) with the experimental value. All these systems are lighter in mass region and consist of stable nuclei, so if TDHF matches stable systems well then one can hope it is a good predictive power for exotic systems.

TDHF calculations intrinsically incorporate a wide variety of dynamical effects, such

as couplings to vibration and transfer channels. What would be especially helpful is to be able to unravel these dynamic effects to see how they individually affect the fusion process. This is attempted in the following subsections.

4.3.2 Incorporating vibrations using Coupled-Channels method

It has just been checked that TDHF barriers are comparable to stable, experimental systems and also that the systematic results do not depend on choice of target. This calls for a refinement of the systems to focus on in the next subsections to just $^{40-54}$Ca+^{116}Sn.

The Coupled Channels (CC) method will be used to calculate fusion cross sections for the listed systems, using the CCFULL code [73] with TDHF inputs [182] using the TDHF results from Chapter 3 and fits to the frozen HF nucleus-nucleus potential in subsection 4.2.2. The calculations will first be done with no couplings and the barriers produced from these should match the frozen HF results. Then, the number of excitational modes will be increased, progressively including more vibrational excitations. Using the coupled channels approach alongside TDHF, the effects of certain excitations on a fusion reaction can be seen separately rather than all at once in a TDHF description [182]. Up to two excited states for the target nucleus and one excited state for the projectile can be included in the CCFULL calculations which are not dependent on the choice of projectile or target labelling. Using the calculated fusion cross sections, an average barrier can be found by taking the centroid of the barrier distribution. This will be compared to the fusion threshold found with TDHF. While this ignores the detailed structure of the barrier distribution obtained from the CC method, using the centroid is the fairest comparison since the whole premise of the TDHF method is based upon the average trajectory of a system.

The CCFULL code computes fusion reactions assuming the nuclear potential to be of the Woods–Saxon form (4.2.2) with the usual three parameters of potential depth V_0, diffuseness a and radius R_0. In all calculations these parameters were taken from fitting the WS potential to the frozen HF bare potential obtained with the SLy4d interaction to reproduce the barrier energy within a 1 keV error. The fitting region is only around the barrier because the frozen barrier needs to match well with CCFULL with no included excitations. The inner part of the HF potential should not be included in the fit, as was discussed in subsection 4.2.2, it does not include Pauli repulsion effects. Extending the fit far out into the tail of the potential at large separation distances or purely Coulomb region brings negligible change to the fit parameters. It has been checked that when no couplings are included in the CCFULL calculations the resulting centroid of the barrier

distribution $D(E)$ matches the frozen HF barrier within 200 keV.

Cross section calculations that were made with excitational states included the excitational energy and deformation parameter from the vibration TDHF results in Tab. 3.1 in Chapter 3. It will be explicitly mentioned when these values were not taken from TDHF results. No transfer coupling was included in any of the CCFULL calculations.

Barrier distributions

The barrier distribution $D(E)$ at the energy E_n has been calculated from the CCFULL fusion cross-section σ by [46, 155]

$$D(E) = \frac{d^2(E\sigma)}{dE^2} = \frac{(E\sigma)_{n+1} - 2(E\sigma)_n + (E\sigma)_{n-1}}{\Delta E^2}.$$

The value used for ΔE was between 0.4 MeV and 0.8 MeV. The barrier distribution is positive for energies ranging from 0 MeV up until some particular energy E', above which it becomes negative, as the barrier radius for higher angular momentum is less than that for zero angular momentum [46]. The average fusion barrier is then calculated using the centroid of $D(E)$ with the upper integration limit of E being E' [44],

$$V_B = \frac{\int_0^{E'} ED(E)dE}{\int_0^{E'} D(E)dE}. \tag{4.3.1}$$

Shown in Fig. 4.14 are calculated barrier distributions from CCFULL for the reaction ^{44}Ca+^{116}Sn, with no excitation (solid red line) and combinations of vibrational excitations of both calcium and tin. The barrier distribution is seen to change when certain excited modes are included and it follows that the centroid or average barrier also changes because of these particular excitations. All other barrier distributions for systems in $^{40-54}$Ca+^{116}Sn are presented in Appendix F.

The vibrational 3_1^- state of both the calcium and the tin shifts the peak of $D(E)$ to a lower energy without any dramatic change of shape to the barrier distribution which is essentially a renormalisation effect [75]. It is the calcium 3_1^- state that has the largest shifting effect. This one in particular was purposely studied in Chapter 3 because it is known to have an effect on fusion reactions involving ^{40}Ca [46]. Low-lying quadrupole 2_1^+ vibrational states experimentally observed in many even-even nuclei should also have an affect on fusion reactions [10]. In Chapter 3, it was discussed how TDHF cannot produce this collective state in mid-shell nuclei, and that the first 2^+ state seen in TDHF vibrational spectra was labelled as 2^+_{low} instead. To see what results in the barrier

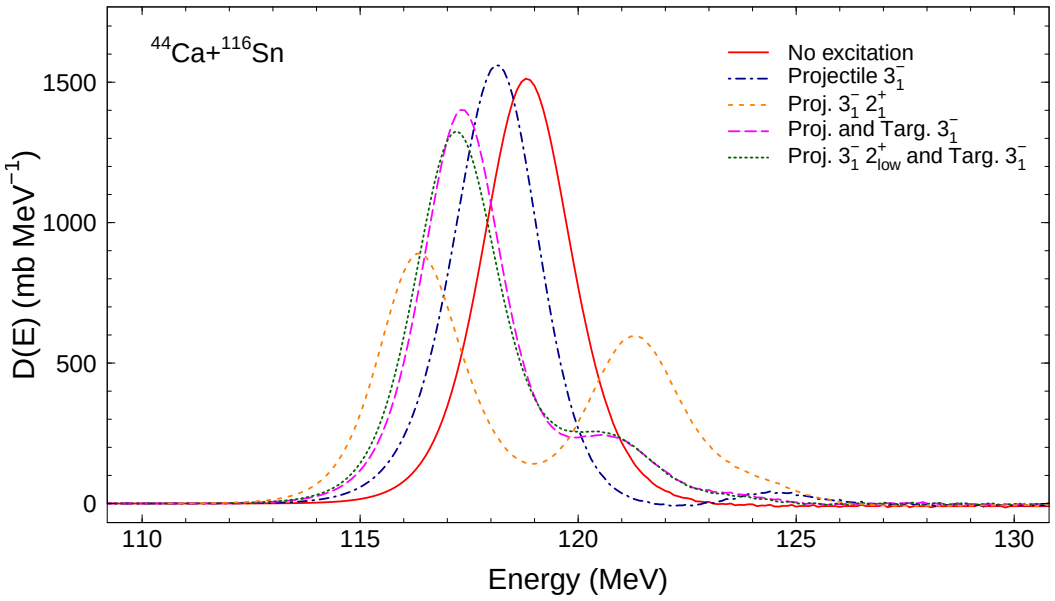

Fig. 4.14.: CCFULL barrier distributions for ^{44}Ca+^{116}Sn.

distribution by including the 2^+_1 state, the experimental values for excitation energy and deformation parameter have been used where the data exists. The 2^+_{low} state has almost an unobservable change in the barrier distribution and even less in the centroid, which was the case for every system.

Effect of vibrational excitations on average barrier energy

Inclusion of coupling to the first octupole phonon in the calcium isotopes in $^{40-54}$Ca+^{116}Sn systematically reduced the centroid of the barrier distribution with no coupling by up to about 1.5 MeV, as shown in Fig. 4.15 (blue diamonds).

The coupling to the experimental 2^+_1 state is actually seen to drastically modify the shape of the barrier distribution, producing a double peaked function seen in Fig. 4.14 for ^{44}Ca+^{116}Sn. The mid-shell nucleus ^{44}Ca is shown as the coupling to the 2^+_1 state would be strongest. Taking the centroid of such a clear double peaked function does not fairly represent what should be considered as the fusion barrier due to this particular excitation, and it so happens that the centroid lies very close to the other distributions produced under different excitational conditions. In any case, it should not be directly compared with a TDHF barrier since TDHF calculations do not take any vibrational experimental data as input. It would only be fair to compare the TDHF fusion threshold with barriers obtained from CCFULL with only TDHF inputs.

Vibrational states that have much higher excitation energies, such as giant quadrupole resonances, have only a small impact on the barrier [75, 182]. Coupling to the 3^-_1 state

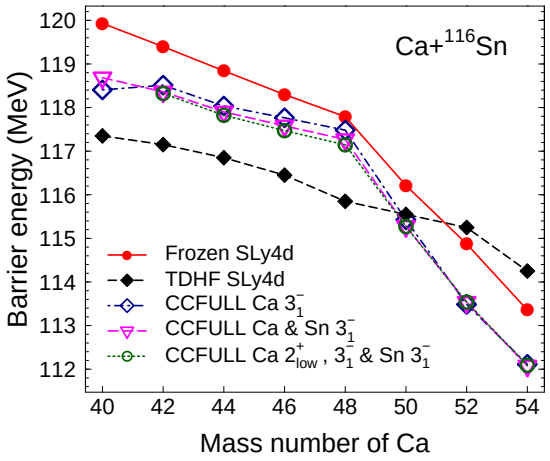

Fig. 4.15.: Barrier thresholds from TDHF, frozen HF and CCFULL calculations for reactions $^{40-54}$Ca+^{116}Sn .

in ^{116}Sn on top of the 3^-_1 in calcium reduces the barrier for the systems $^{42-54}$Ca+^{116}Sn by less than 0.2 MeV.

The CCFULL calculations confirm that the vibrational states included in the TDHF calculations lower the fusion threshold. This helps explain the lowering of the barrier due to dynamical effects as observed in Fig. 4.11 (left) for reactions with the non-exotic calcium isotopes. However, the vibrational couplings appear to reduce the fusion barrier too much for the most exotic systems (^{52,54}Ca+^{116}Sn in Fig. 4.15) and cannot explain the erosion of the static shell structure effects. Other dynamical effects must be important. Transfer effects are considered in the next section to try and understand this.

4.3.3 Transfer with TDHF

Vibrational couplings in fusion reactions lower the barrier energy for the $^{40-54}$Ca+^{116}Sn systems. The consideration of transfer in this fusion reactions study is motivated by the fact that the TDHF dynamic barrier does not consistently lower the static barrier in the case for the most neutron rich systems, particularly for ^{52,54}Ca+^{116}Sn and $^{52-58}$Ca+^{132}Sn. There have been several experimental investigations on transfer channels in reactions [11, 28, 56, 95, 96, 111, 192, 206, 209], notwithstanding, a clear interpretation of their effects on fusion is still lacking. When using the CC approach to study this, realistically incorporating transfer channels in CCFULL calculations is difficult [97, 147, 160, 205]. The TDHF approach can be used to study transfer reaction mechanisms in heavy-ion collisions [5, 103, 174, 219].

Equilibration of the N/Z ratio between two fragments in a reaction is a driving factor for nucleon transfer and this effect is accounted for in TDHF calculations [170, 176]. The N/Z ratio for $^{40-54}$Ca ranges from 1 to 1.70 and those of ^{116,132}Sn lie within this range,

at 1.32 and 1.64 respectively. The focus of this section will largely be on proton transfer for these systems. It is expected, from the argument of balancing the N/Z ratios, that proton transfer would happen in the direction from the light to heavy fragment for the lighter projectiles and from heavy to light fragments in neutron rich projectiles.

TDHF can be used to study transfer probabilities directly. First, the average N and Z number of a particular fragment at each time can be obtained, simply determined by integrating the proton and neutron densities around one fragment (in this subsection, it will be the heavy fragment) with the counting operator

$$\hat{N}_{\Omega}^{q} = \sum_{s} \int_{\Omega} \hat{a}^{\dagger}(\mathbf{r}sq)\hat{a}(\mathbf{r}sq)H(x - x_0)d^3r, \tag{4.3.2}$$

explained in subsection 2.5.2. Next, probabilities of transfer channels at the final time can be calculated using the particle number projection method [174], also explained in more detail in subsection 2.5.2. Due to the non-magic N number in many of the fragments, it is more difficult to understand probabilities of neutron transfer processes unless double projection techniques are used for systems with pairing [162].

The observation of nucleon transfer for these reactions is from the calculation of both these quantities from the final fragments. The average N and Z number and transfer probabilities are calculated at an energy just below the TDHF fusion threshold of a particular system, $E_{\mathrm{cm}} = 0.999V_B$. At this energy the system reseparates after the brief formation of a neck at half density, lasting less than 2 zs, through which transfer of nucleons can occur.

Average transfer numbers

Using the counting particle operator in (4.3.2), evolution of the N/Z value of the heavy fragment for an energy just below the TDHF fusion threshold ($0.999V_B$) is calculated. This is shown in Fig. 4.16 (left) for ^{54}Ca+^{116}Sn, as well as the evolution of the average N and Z numbers as a function of time (right). The shaded grey area is where a neck with density $\rho \geq 0.08$ nucleons fm^{-3} (half saturation density) occurs.

The values within and near the shaded region depend sensitively on the choice of neck plane and should not be analysed quantitatively for this reason. A spurious effect of the choice of neck plane is seen before the shaded region, where neutrons and protons are both seen to transfer to the calcium. Because of neck plane sensitivity, average transfer is quantified from the values of N and Z only at the final calculation time.

The average number of protons and neutrons in the final heavy fragment for $^{40-54}$Ca+^{116}Sn

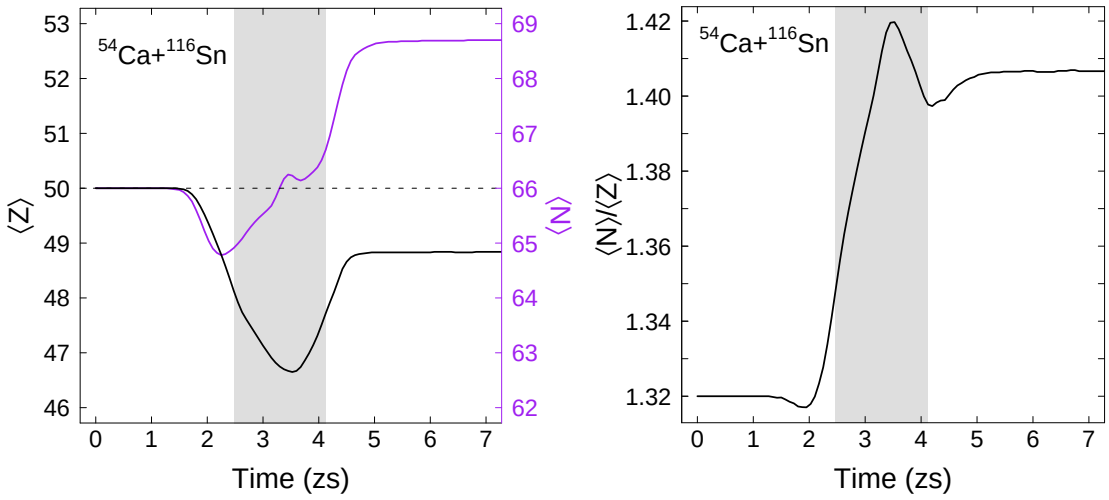

Fig. 4.16.: Left: average Z (black, left axis) and average N (purple, right axis) versus time, the original N and Z is shown with the horizontal dashed line. The shaded grey area is where the neck occurs. Right: average N/Z versus time for the heavy fragment in the reaction with ^{54}Ca.

are shown in Fig. 4.17. The average Z decreases while the average N increases with increasing calcium mass number. The transferred numbers of particles is not a smooth function with increasing calcium mass. The lack of smoothness may be due to the fact that these results are for energies only 0.1% below the fusion threshold and hence are very sensitive to small energy changes. Taking values for 1% below the fusion barrier, for example, will lead to much reduced transfer (less than 0.1 protons transferred in any of the reactions). Because the error in V_B is ± 0.05 MeV, the results in Fig. 4.17 should be taken as a general trend.

More neutrons are transferred than protons resulting in net mass transfer to the light calcium isotopes in almost every case. As shown in Fig. 4.6, the rms radii of the neutrons in the calcium isotopes are larger than those for the protons for isotopes heavier than ^{40}Ca. This neutron skin means there are neutrons in the outer shells of Ca which are more accessible to transfer at larger separation distances. The influence of neutron transfers on fusion is still not fully understood. Subbarrier fusion enhancement for the systems ^{40,48}Ca+^{132}Sn has been attributed to positive Q-values for neutron transfer, furthermore for ^{40}Ca+^{132}Sn subbarrier fusion is enhanced more than what can be accounted for by vibrational states [102]. It is not so clear that this enhancement appears at lower energies for the heavier system ^{48}Ca+^{132}Sn. In Ref. [65], the isovector contribution to the DC-TDHF fusion potentials for ^{40,48,54}Ca+^{132}Sn was shown to also be related to neutron transfer, compatible with the directions in Fig. 4.17 and the resulting TDHF fusion barriers in Fig. 4.11.

The direction of the average transfer in both groups of systems follows the charge

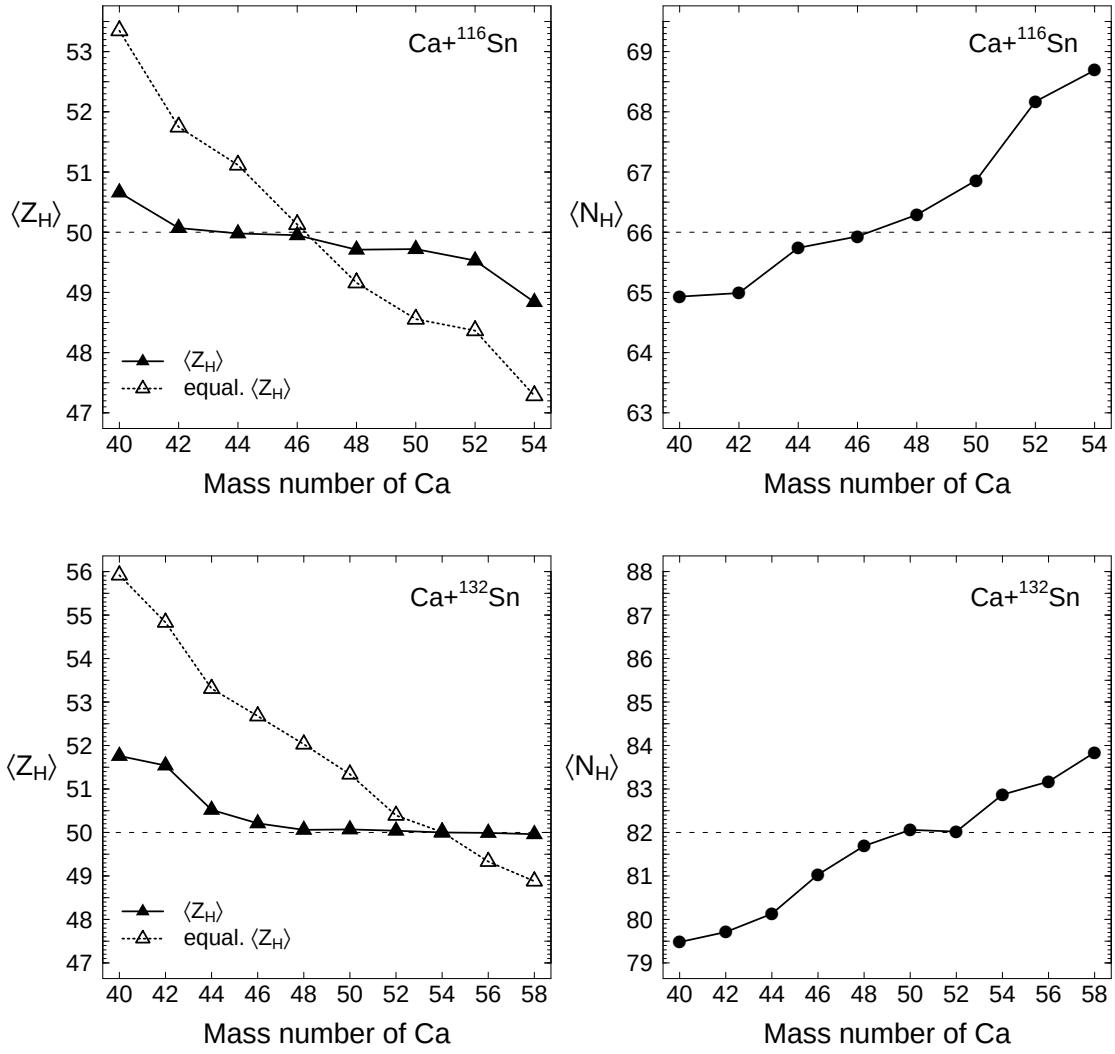

Fig. 4.17.: The average proton number (left) and neutron number (right) for the heavy fragment in $^{40-54}$Ca+^{116}Sn (top panels) and $^{40-58}$Ca+^{132}Sn (bottom panels). The dotted line and open triangles show the anticipated $\langle Z_H \rangle$ value assuming the heavy fragment has equalised its N/Z ratio with the compound system. The original Z_H and N_H (horizontal dashed lines) are also shown.

equilibration process where the initial neutron to proton ratio N/Z asymmetry between the fragments is reduced after contact. This is a manifestation of positive Q-values for transfer reactions induced by the symmetry energy, studied in detail with TDHF in transfer reactions [170, 183]. It results in protons being transferred from the calcium to the tin in ^{40}Ca+^{116}Sn and in the opposite direction for ^{54}Ca+^{116}Sn. Average neutron transfer occurs in the opposite direction to proton transfer. The dotted line in Fig. 4.17 shows the number of protons for the given $\langle N_H \rangle$, assuming that the projectile and target both have the same N/Z ratio as the compound system. Comparison of this line with the $\langle Z_H \rangle$ values indicates that, at this collision energy, the transfer reactions do not achieve the N/Z ratio of the compound system in the fragments. However, N/Z equivalence between fragments and compound system should be regarded as an upper limit since

N/Z equilibration acts to increase binding energies rather than to achieve equal N/Z ratios between the fragments.

For reactions involving ^{132}Sn, the same direction of average proton and neutron transfer happens as for ^{116}Sn but by different amounts. Very little average proton transfer occurs after ^{48}Ca+^{132}Sn in agreement with Ref. [65], perhaps because the N/Z ratio of ^{132}Sn is much higher and is a closer match to the heavier calcium nuclei.

Transfer probabilities

Now the corresponding probabilities of different transfer channels extracted from TDHF simulations (see subsection 2.5.2) will be presented. These can be used to see the average transfer results in the previous section in more detail. Transfer probabilities are computed using the particle number projection technique developed in Ref. [174] for systems without pairing, and extended in Ref. [162] for superfluid systems. This method has been used to study multi-nucleon transfer reactions [29, 162, 166, 170, 174, 191] and fission [167, 185]. Here it is used to determine only the proton transfer probabilities in $^{40-54}$Ca+^{116}Sn reactions as the fragments both have magic proton numbers. As a result the proton transfer probabilities are not affected by pairing correlations so just the single projection technique can be used [174].

The probability distribution of the final proton number in the heavy fragment is shown in Fig. 4.18 for $^{40-54}$Ca+^{116}Sn. As seen in Fig. 4.18, protons are transferred from the light fragment to the heavy fragment in ^{40}Ca+^{116}Sn with a probability for ^{116}Sn gaining 1 proton at around 40%. However, for projectiles of ^{48}Ca and heavier the transfer occurs preferentially from the heavy fragment to the light fragment. For the most neutron rich system ^{54}Ca+^{116}Sn there is a probability of just over 40% for one proton transfer from ^{116}Sn to ^{54}Ca. Note that even when the average proton transfer is near zero (for example ^{44}Ca+^{116}Sn in Fig. 4.17 for protons or ^{46}Ca+^{116}Sn for both neutrons and protons), non-zero probabilities for other transfer channels can still occur.

The proton transfer probability for ^{40,48}Ca+^{132}Sn is shown in Fig. 4.19, for the lighter system there are higher probabilities for proton pickup than for no proton transfer or proton stripping.

In addition to the isovector contribution to the potential mentioned above, proton transfer in either direction will change the Coulomb repulsion. In particular, one proton transfer from ^{54}Ca to ^{116}Sn increases the Coulomb potential, $V_C = e^2 Z_1 Z_2 / r$ by 2.7% and is expected to increase the fusion barrier. This is consistent with what is seen in the TDHF fusion barrier thresholds and is a possible explanation for why the dynamical

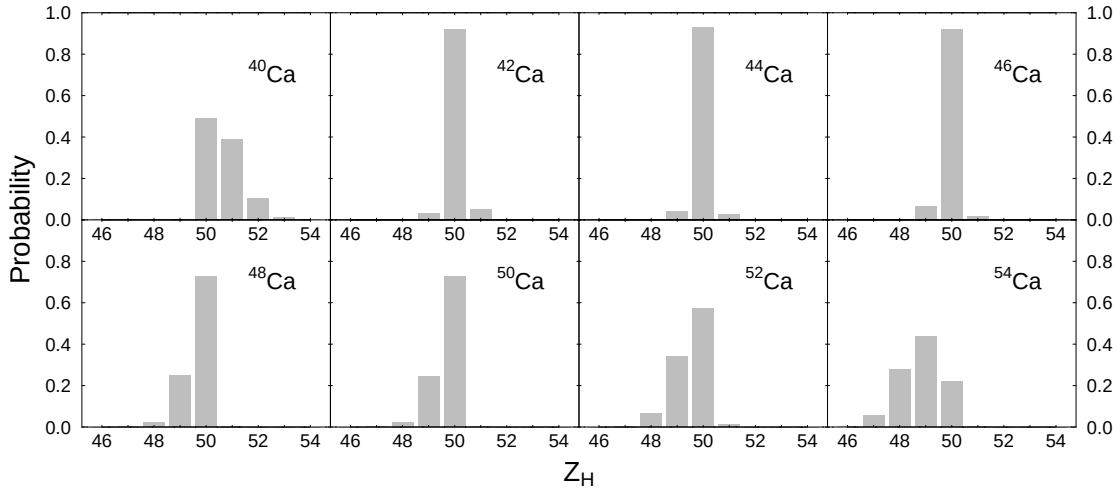

Fig. 4.18.: Proton number probabilities for the heavy fragment in the reactions $^{40-54}$Ca+^{116}Sn at $E_{\rm cm} = 0.999V_B$. The initial calcium projectile on ^{116}Sn is labelled on each panel.

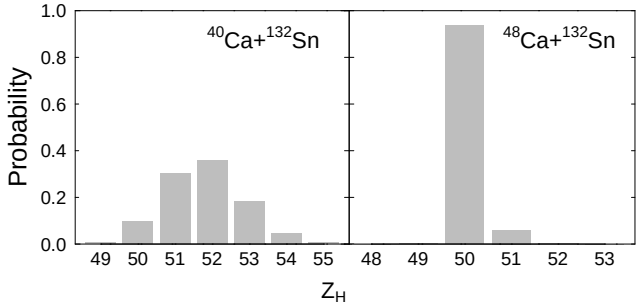

Fig. 4.19.: Proton number probabilities for ^{40,48}Ca+^{132}Sn at $E_{\rm cm} = 0.999V_B$.

TDHF fusion threshold is higher than the frozen HF barrier for this system.

An alternative explanation for the increase in fusion barriers seen for ^{52,54}Ca+^{116}Sn could be that the dissipation of the initial kinetic energy is faster (occurring at larger distances) with calcium isotopes heavier than ^{48}Ca due to a larger level density near the Fermi surface and weak neutron binding.

4.3.4 Energetics

The Q-values of nucleon transfer plays an important role in reactions at subbarrier energies [7, 102, 111]. Since calcium and tin both have magic proton numbers, the proton shells should be well bound and the Q-values of proton transfer should be calculated from HF to see if proton transfer is really energetically favoured within TDHF.

Transfer in a collision reaction is triggered to induce charge equilibration to balance the N/Z ratios of the colliding nuclei. It is a materialisation of the possible transfer channels with appropriate Q-values. If a particular transfer channel with a Q-value takes place,

this changes the kinetic energy of the system. The exit channel kinetic energy will be at a different relative position to the fusion threshold than the entrance channel kinetic energy.

In this subsection HF is used to understand these processes more clearly. First, finding out whether proton transfer is energetically favoured in the reactions $^{40-54}$Ca+^{116}Sn is done by calculating the corresponding Q-values, using the ground HF binding energies of the nuclei, and compared with the optimum Q-value. Second, the total kinetic energy loss (TKEL) is considered and calculated for a TDHF reaction. This quantity is related to what excitational modes have taken place. Optimum Q-values and TKEL values are again taken at reactions occurring at $E_{\rm cm} = 0.999V_B$.

Q-value and $Q_{\rm opt}$

Using TDHF, the ground state Q-value of a reaction can be calculated using the HF ground state binding energies (BE) of nuclei. For 1 proton pickup (transfer from heavy to light fragment), the ground state Q-value, $Q_{\rm g.s.}$, will be

$$Q_{\rm g.s.} = {\rm BE}(^{X}{\rm Ca}) + {\rm BE}(^{Y}{\rm Sn}) - {\rm BE}(^{X+1}{\rm Sc}) - {\rm BE}(^{Y-1}{\rm In}).$$

When $Q_{\rm g.s.}$ is positive, the reaction is energetically favoured. However, a positive $Q_{\rm g.s.}$ for charge transfer is not enough on its own to necessarily cause the reaction to occur. As charge transfer also changes the Coulomb potential between the reactants. This change in energy will also be a factor in deciding whether the transfer will be energetically favoured.

The energy difference between the incoming and outgoing Coulomb trajectories, known as the optimal Q-value ($Q_{\rm opt}$) is determined by requiring that trajectories are continuous. That is, when the transfer occurs, the two nuclei remain at the same distance of closest approach apart. The optimal Q-value is given by

$$Q_{\rm opt} = \frac{e^2}{R}\left(Z_{1f}Z_{2f} - Z_{1i}Z_{2i}\right), \tag{4.3.3}$$

where the subscript i (f) stands for initial (final) Z numbers and R is the radius of closest approach. Since $Z_{1f}Z_{2f} > Z_{1i}Z_{2i}$ for proton pickup, from (4.3.3), it can be seen that $Q_{\rm opt}$ is positive for proton pickup and negative for proton stripping. Since $Q_{\rm opt}$ relies on changing Z numbers, it is zero for purely neutron transfer.

For a central collision, when the reactant nuclei are initially far apart, the centre of mass energy for the system should be the same as the initial Coulomb potential as the

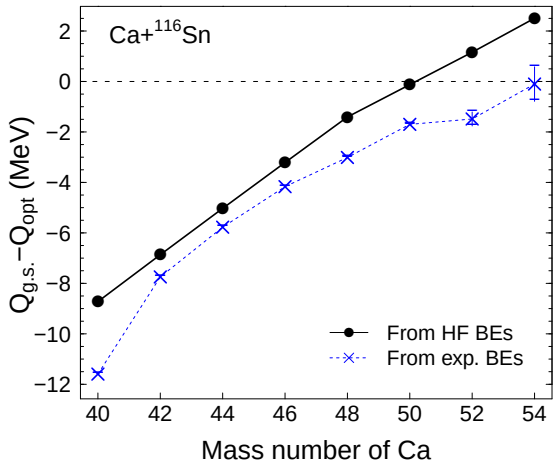

Fig. 4.20.: Difference between proton pickup $Q_{\text{g.s.}}$ and Q_{opt} for $^{40-54}$Ca+^{116}Sn. Both calculations from HF binding energies (black circles) and from experimental binding energies (blue crosses) are compared.

nuclear potential is zero at large distances. Therefore,

$$E_{\text{cm}} = \frac{Z_{1i}Z_{2i}}{R}e^2.$$

As continuity of the reaction trajectory is assumed, R can now be substituted into (4.3.3), giving

$$Q_{\text{opt}} = \left(\frac{Z_{1f}Z_{2f}}{Z_{1i}Z_{2i}} - 1\right)E_{\text{cm}}.$$

The Z numbers for 1 proton transfer are the same for each system in $^{40-54}$Ca+^{116}Sn, meaning Q_{opt} changes by the E_{cm} factor between system to system. How favourable charge transfer is for a particular reaction at a particular E_{cm} will now depend on both $Q_{\text{g.s.}}$ and Q_{opt} at E_{cm}. The difference between these two gives the net energy cost or gain and is shown in Fig. 4.20 for 1 proton pickup in $^{40-54}$Ca+^{116}Sn at $E_{\text{cm}} = 0.999V_B$. The resulting energy $Q_{\text{g.s.}} - Q_{\text{opt}}$ is, in principle, the energy loss or gain found in the exit channel of the system if 1 proton pickup were forced to occur. This energy can be used to populate other excited states in the exit channel of the system (e.g. vibrational states) which have an excitation energy less than or equal to $Q_{\text{g.s.}} - Q_{\text{opt}}$. If this value is negative, then the transfer is not energetically favoured and would be less likely to occur. In the event that $Q_{\text{g.s.}} - Q_{\text{opt}} = 0$, then this means the Q-value for the transfer has exactly matched the energy that is optimised for the final binding energies. For zero or positive values of $Q_{\text{g.s.}} - Q_{\text{opt}}$, the transfer is more likely to happen as the reaction would gain this amount of energy (or be neutral in energy in the case of zero $Q_{\text{g.s.}} - Q_{\text{opt}}$). In practice, the system in the exit channel can be in an excited state at an energy typically

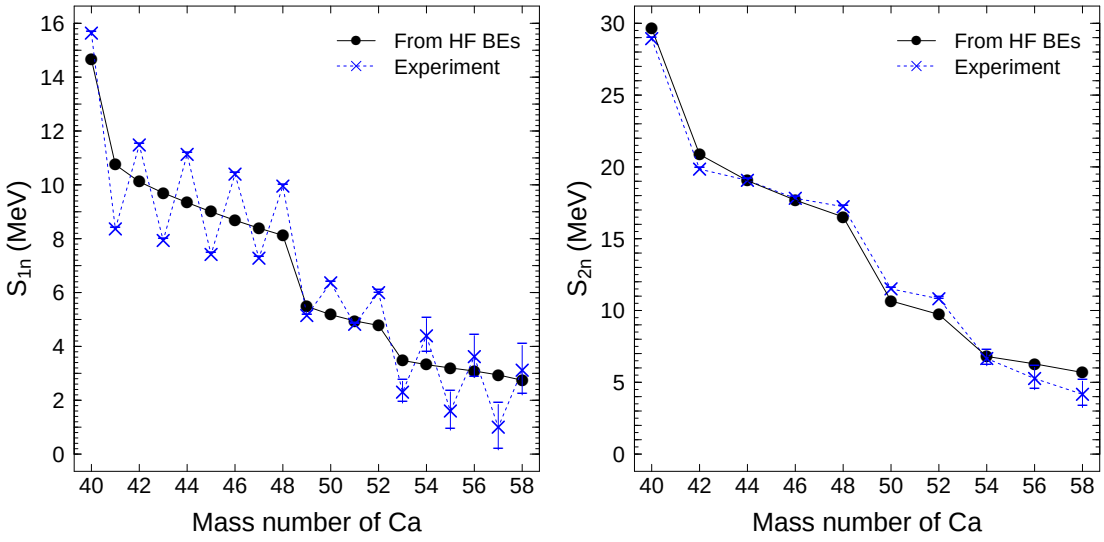

Fig. 4.21.: Separation energies of one neutron (left) and two neutrons (right) from calcium isotopes. Values are taken from HF BEs (black circles) and experiment (blue crosses).

falling in a normal distribution centered at $Q_{\text{g.s.}} - Q_{\text{opt}}$, for $Q_{\text{g.s.}} - Q_{\text{opt}} \geq 0$.

In Fig. 4.20 for the reaction ^{50}Ca+^{116}Sn, $Q_{\text{g.s.}} - Q_{\text{opt}}$ is almost 0 MeV and for ^{52,54}Ca+^{116}Sn, this value is positive. If 1 proton pickup does occur for reactions with a positive $Q_{\text{g.s.}} - Q_{\text{opt}}$ value, which is the case for ^{52,54}Ca+^{116}Sn, then this would be consistent with the increase of the dynamic TDHF barrier from the frozen HF barrier. This is because the Coulomb potential after the transfer increases, contributing overall to a higher fusion barrier. However, there is a gain of energy from the proton pickup process equal to $Q_{\text{g.s.}} - Q_{\text{opt}}$. This energy is likely to go into excitation energy. Nevertheless, this could also be converted to kinetic energy to possibly surpass the barrier energy. As such, it is not clear that this must necessarily lead to a larger barrier.

There are of course problems with Q-value interpretations using TDHF. First, the ground state Q-values of 1 proton transfer are calculated by taking the difference of masses between even and odd nuclei. It has been mentioned that in this thesis, calculations of nuclei from the HF method assume time reversal symmetry and partial filling of single particle states, so odd nuclei end up being only averages of the surrounding even isotopes. The separation energy of one nucleon would experimentally have a staggering effect due to pairing, which is not present in HF because of the incorrect binding energies for odd nuclei. This is illustrated in Fig. 4.21 where separation energies of one (left) and two (right) neutrons from calcium isotopes using HF binding energies are compared with experimental values. The separation of two neutrons bypasses the pairing staggering effect by skipping the odd nucleus and the HF values are in very good agreement with the experimental values.

Even if the HF ground state Q-value is taken to be correct from odd mass systems, the second problem is that the resulting HF value of $Q_{\text{g.s.}} - Q_{\text{opt}}$ would represent the "average value" of the Q-value distribution. There is no sensible concept of an average Q-value since Q-values in experimental data are at discrete values. The $Q_{\text{g.s.}} - Q_{\text{opt}}$ values using the experimental binding energies are shown in Fig. 4.20 for comparison; the HF values are within 2.5 MeV and are used in the next section to explore ideas of kinetic energy loss in a reaction.

Kinetic energy loss

The total mechanical energy of the reaction is defined as the sum of the following:

- the kinetic energy: the sum of the two separate kinetic energies of the fragments (in their centre of mass frames) done by calculating the centre of mass momentums of each fragment,
- the Coulomb energy: using the two separate fragments the Coulomb energy between the two can be found.

The kinetic, Coulomb and total mechanical energy taken at each time step are shown in Fig. 4.22 for ^{46}Ca+^{116}Sn at 99.9% of the fusion threshold. The shaded area indicates where a neck at half saturation density has formed. During this time, kinetic energy is zero as the compound system is stationary in the centre of mass frame, and the Coulomb energy reaches its maximum values since the separation distance between the nuclei is at a minimum.

As previously mentioned, the neck plane requires well established separation between the two fragments. When a neck forms, any meaningful physical interpretation to energies defined from the "two" fragments cannot be assigned. Instead, the total kinetic energy loss (TKEL) should be used. Though there is a kinetic energy component in Fig. 4.22, TKEL is the conventional name for the the difference between the total mechanical energy (solid black line) at initial and final time, this is indicated on the right of Fig. 4.22.

More formally, as presented in Ref. [170], using the centre of mass coordinates for the light (subscript L) and heavy (subscript H) fragment, the relative coordinate can be calculated

$$\mathbf{R}(t) := \mathbf{R}_H(t) - \mathbf{R}_L(t),$$

and used to find the relative velocity at any time,

$$\dot{\mathbf{R}}(t) = \frac{\mathbf{R}(t + \Delta t) - \mathbf{R}(t - \Delta t)}{2\Delta t}.$$

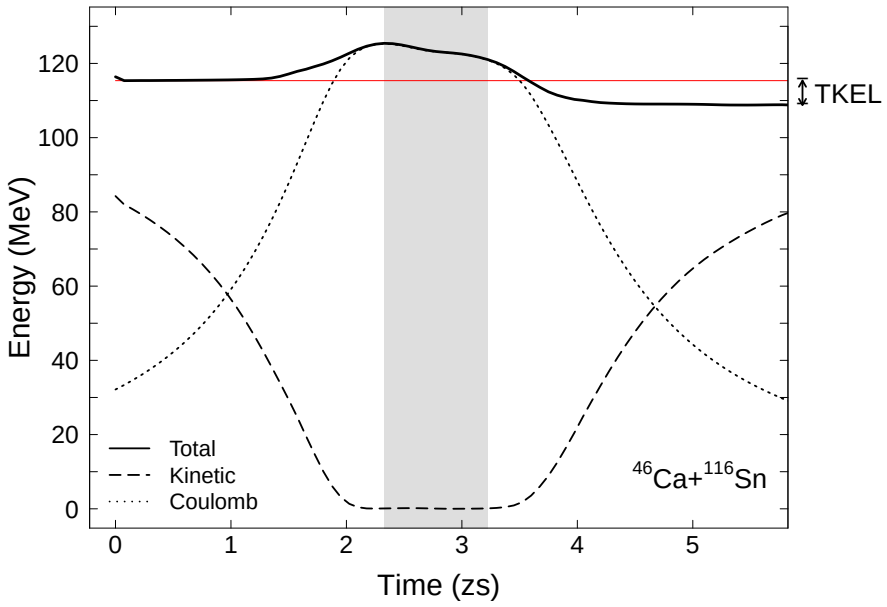

Fig. 4.22.: Total mechanical energy (solid) as a sum of kinetic energy (dashed) and Coulomb energy (dotted) evolution at $E_{\rm cm} = 0.999V_B$ for ^{46}Ca+^{116}Sn. The shaded area is where the half density neck forms for the system. The initial total mechanical energy is indicated by the horizontal red line. The difference between initial and final total mechanical energy is labelled as TKEL on the right.

The TKEL is

$$\mathrm{TKEL}(t) = E_{\rm cm} - \frac{\mu}{2}|\dot{\mathbf{R}}(t)|^2 - \frac{Z_H Z_L e^2}{|\mathbf{R}(t)|},$$

with $E_{\rm cm}$ and $Z_{H,L}$ being the initial energy for the whole system and Z numbers of the heavy or light fragments respectively.

For the system ^{46}Ca+^{116}Sn in Fig. 4.22, the TKEL at final time is 6.3 MeV. In this reaction, very little average transfer (fewer than 0.1 neutrons or protons, refer to Fig. 4.17) happens, so such a large energy loss cannot be owed to net transfer of either protons or neutrons. The energy loss is related to what excitation modes have been activated at the end of a reaction. Internal excitations would contribute to the energy loss, such as the 3^-_1 vibrational state of ^{46}Ca, as well as if there are any nucleons emitted in this reaction. Whilst the TDHF value of total kinetic energy loss cannot be fully quantified in this study, it can still be used to qualitatively see it is systematic in the reactions $^{40-54}$Ca+^{116}Sn.

Collisions at zero impact parameter at an energy just below the TDHF fusion threshold are expected to give maximum energy loss at this configuration [170, 176, 196]. The TKEL at final time for each system is shown in Fig. 4.23, on top of the half density neck times. There is not much correlation between the two quantities, although usually longer neck times would be associated with more transferred nucleons and thus more

energy loss. If anything, the plot shows that the relative movement of TKEL value from one calcium isotope to the next happens in almost the opposite direction to the neck times. The lightest system has the largest TKEL and the TKEL of all other systems lie between 5 and 7.5 MeV. There are expected to be more dynamics other than number of neutrons, neck formation and nucleon transfer between fragments that contribute more to the TKEL of each system. More quantitative analysis is necessary to fully understand energy dissipation in these reactions.

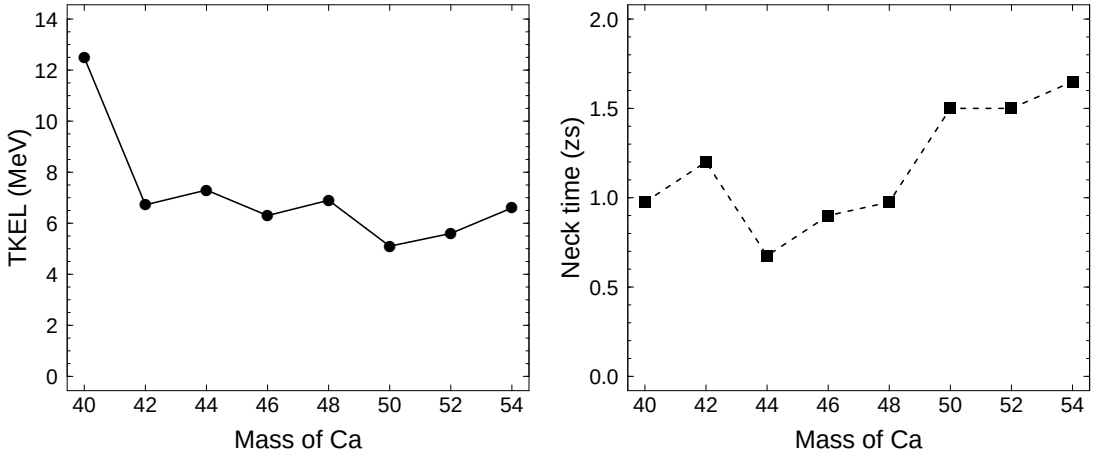

Fig. 4.23.: Left: TKEL at the end of $^{40-54}$Ca+^{116}Sn reactions at $E_{\rm cm} = 0.999V_B$. Right: half saturation density neck time for the same reactions.

4.4 Summary

Presented in this chapter were systematic studies of fusion barrier energies, looking at fusion reactions in a static picture and also with added dynamical effects. The three groups of systems $^{40-54}$Ca+^{116}Sn , $^{38-58}$Ca+^{132}Sn and $^{40-54}$Ca+^{116}Sn were studied.

Within the static picture, there were obvious differences between the HF method of calculating the fusion energy and the phenomenological fusion barrier models. The conventional models showed a near linear decrease of V_B with increasing mass of one of the nuclei, whereas the HF method showed some kinks at certain isotopes in the chain of reactions. To help explain this, the ground state properties as calculated by HF of each of the nuclei in the isotopic chains were studied more closely. The properties included rms radius and single particle shell levels, energies and radial wavefunctions. As a global property, the increased rate of neutron skin development along the chain causes more rapid decrease of the barrier, consistent in each of the groups of systems. The contribution of the radius increase was considered by the single particle levels and radial wavefunctions. The levels showed a significant energy increase whenever a kink occurred and the clearest

extension of the radial wavefunction was found when the quantum number n or node increased from 1 to 2. It is expected that for heavier isotopes these trends would continue.

The development of a neutron skin in exotic calcium and tin isotopes significantly lowers the barrier of the bare potential. This phenomenon is due to quantum shell effects and is not accounted for in standard parametrisations of the nucleus-nucleus potential, the latter are then only valid close to the valley of stability. The lowering of the barrier due to the neutron skin is purely a static effect.

Dynamics were incorporated into the reactions using TDHF and also the CC aproach. In many cases, adding dynamics (with TDHF) reduces the fusion barrier from the bare potential. What was most surprising was that the dynamics washed out static structure effects seen to characterise frozen barriers. A thicker neutron skin does not necessarily mean fusion is more easily achieved. This is especially apparent in the neutron rich reactions ^{52,54}Ca+^{116}Sn, with the SLy4d parametrisation of the Skyrme interaction, the TDHF fusion threshold was actually higher than the corresponding frozen HF barrier.

As TDHF incorporates several dynamical effects at once, they need to be unravelled. The focus was first on vibrational modes. Vibrational modes as calculated by TDHF (see Chapter 3) of calcium isotopes and the tin target were incorporated into the reactions separately using the CC approach. The largest contributor in reducing the frozen HF barrier was the 3_1^- state from the calcium isotopes. Other vibrational modes that are present in the TDHF reactions further reduce the barrier. This helps explain what is seen in the difference between the frozen HF barrier and TDHF fusion threshold in many cases but not for very exotic cases such as ^{52,54}Ca+^{116}Sn, where the addition of dynamical effects increase the barrier. In an attempt to understand this, transfer channels in $^{40-54}$Ca+^{116}Sn were explored.

Transfer in TDHF reactions was observed at energies just below the TDHF fusion threshold. The average number of neutrons and protons were counted at the end of a reaction, as well as the probability for proton transfer using the particle number projection method. Both transfer of protons and neutrons occurred. Charge transfer (pickup) in the heaviest reactions was first correlated with an increase in Coulomb barrier and therefore an increase in fusion barrier. Upon further exploration of energetics of these transfer channels, although they are compatible with the corresponding experimental Q-values, it is not obvious as to why proton pickup must necessarily lead to higher fusion barriers. Studies involving energy loss and Q-values with TDHF in this chapter can only be considered on a qualitative level.

There is a lot of scope for future work following on from the results presented in this

chapter, particularly in understanding dynamical effects seen in TDHF and how this affects the fusion barrier or threshold. A proper quantitative description of the transfer effects on the fusion barrier is undeniably desirable. This would be aided by employing the double particle number projection method [162] (for non-magic numbers in neutrons), and would be able to be extended to exotic systems with little or no magicity as well. Additional studies could be done on kinetic energy dissipation in TDHF, for example by a macroscopic reduction procedure [226] or using the density-constrained TDHF approach [213], to investigate where it occurs and its consequences for reactions just below the fusion threshold. The incorporation of dynamical pairing [162] in these reactions would also be useful as this would influence the transfer of nucleons and possibly also the vibrational modes seen in each individual nucleus.

Quasifission reactions 5

5.1 Overview

Following on from the previous two chapters, this chapter applies the Hartree–Fock method to reactions forming compound nuclei that are heavier than Ca+Sn. For these reactions fusion is not inevitable even if the energy is well above the single barrier. Instead, quasifission can result, where the system reseparates before formation of a compact compound nucleus due to the Coulomb potential between the two fragments being too large. This is one of the competing processes to heavy-ion fusion [21, 158, 173, 207] in the pursuit of superheavy element (SHE) formation. Experimentally, such reactions have been performed and studied with mass angle distributions (MADs) [53, 207] and mass energy distributions [92, 93, 105, 207]. For collisions with a nonzero impact parameter, usually quasifission occurs before the compound nucleus (CN) has completed one revolution. The mass ratio of the fragments, which can be reconstructed from their velocities, is defined as

$$M_R = \frac{m_1}{m_1 + m_2},$$

for the two fragments m_1 and m_2. It depends on many factors including contact time, orientation, impact parameter and reactant structure properties. The mass ratio along with centre of mass angle are used to construct MADs [83, 150]. Mass and angle correlation is an indicator of quasifission [53, 207].

Experimental spectra such as MADs are time integrated over the whole reaction. An advantage of using a time-dependent theory to study the same reactions is the ability to see dynamical processes that occur zeptosecond by zeptosecond. In this chapter the TDHF method is used to probe how heavy-ion reactions, specifically quasifission-type reactions, unfold.

An understanding of the effects of many factors involved in the entrance channel of heavy-ion reactions, for example reactant combinations [15, 80, 105], reactant deformation and orientation [83, 117], shell structures [99, 118, 183] and more, reveals much about quasifission reactions. In SHE synthesis reactions, nuclear structure effects may play a strong role as both doubly magic nuclei (^{48}Ca, ^{208}Pb) and statically deformed nuclei (actinide nuclei such as ^{238}U, ^{244}Pu, ^{248}Cm, ^{249}Cf) are used. Of particular importance is the role of magic numbers in heavy-ion fusion. This is because to create new SHE,

projectile nuclei heavier than the doubly magic ^{48}Ca nucleus have to be used due to manufacturing and physical limitations of actinide targets with higher Z number than ^{249}Cf. With this in mind, this chapter will present a study of several heavy-ion reactions involving various magic numbers of projectile and target nuclei. The systems studied in this chapter are:

I. ^{48}Ca,^{50}Ti, ^{52}Cr, ^{54}Fe, ^{56}Ni, ^{58}Zn+^{208}Pb,

II. ^{64}Ni+^{208}Pb, ^{54}Cr+^{204}Pb,

III. ^{54,52}Cr+^{196,198}Pt, and ^{34}S+^{232}Th.

The study of systems in group I involving a ^{208}Pb target and isotones with $N = 28$ span in proton number from $Z = 20$ to $Z = 30$. These were chosen to investigate the systematics in reactions varying projectile charge and magicity. The systems ^{64}Ni+^{208}Pb and ^{54}Cr+^{204}Pb in group II were included in the study to serve as comparative systems to the $N = 28$ chain as they have been measured experimentally [54, 118] and have different neutron magicity. The systems in groups I and II are referred to as the main study henceforth. The systems in group III with ^{54,52}Cr+^{196,198}Pt and ^{34}S+^{232}Th are included as auxiliary systems for the purpose of comparison to the main study as systems with one or no magic numbers. Detailed analysis of these auxiliary reactions are not presented and were chosen in part as they have been experimentally measured [149, 227].

To fully appreciate the advantage of using a time-dependent approach, the sections in this chapter are arranged as a "time history" of a heavy-ion collision. It begins with the initial time right up until the point of contact or capture. Following this are the dynamic processes during the neck lifetime. Finally, the break of the neck and reseparation of the fragments is investigated.

For the main study, both head-on collisions and collisions with angular momentum of $10\hbar$ were calculated. Head-on collisions are always the preliminary calculations as they require the smallest calculation box configuration and therefore are the quickest to complete. Incorporating angular momentum $L(\hbar) = \sqrt{\ell(\ell+1)}$ with $\ell = 10\hbar$ in reactions was included to simulate a more realistic situation which is more comparable to experimental data. It requires a larger calculation box and therefore much longer calculation times. The centre of mass energies for all the reactions varied from $E_{\rm cm} = 1.0V_B$ to $1.3V_B$ where V_B is the static barrier energy for each system calculated using the frozen HF method as seen in subsection 4.2.2. With the exception of ^{54}Cr, all the projectiles involved in the reactions have at least one magic number and are to a good approximation spherical

in their ground state. The HF ^{54}Cr nucleus was calculated as having a near spherical ground state. This meant that deformation axis of projectile (or target) was irrelevant in the main study.

The three auxiliary reactions ^{52,54}Cr+^{198,196}Pt and ^{34}S+^{232}Th have prolate deformed targets and it will be specified which orientation they took in the text where relevant. The energy range and angular momenta for these reactions were chosen to correspond with experimental measurements. The results from these systems were with centre of mass energies between $1.0V_B$ and $1.2V_B$ and values of ℓ ranging from $20\hbar$ to $55\hbar$.

The purpose of this study is not to compare TDHF results to experimental results. There are many existing studies involving this and it is verified that TDHF produces reasonable results in comparison to experiment [76, 82, 135, 170, 172, 214, 223]. Rather, the goal is to pull apart the quasifission reaction in zeptosecond timescales and use the results to help understand the role of magic numbers in these kinds of reactions.

5.2 Reaction classification

The definition of what is considered as quasifission and what is considered as fusion in TDHF calculations is necessary as a reference for the entire study presented in this chapter. Results and discussions in later sections are generally categorised into systems that reseparate and systems that fuse. Defining what is fusion in TDHF is simple: any system that remains as a compound system after an appropriate time limit. In lighter systems, such as Ca+Sn (see section 4.3), the limit is typically around 10–20 zs. The time limit is determined by the trends of the system evolution and will vary depending on how heavy the system is.

Systems that reseparate can be of quasifission-type as well as inelastic (quasielastic) and deep inelastic collisions. The definition specifically for quasifission reactions, within TDHF, needs to be addressed. Before the explanation of this, more details about the setup of the main study along with the divide between fused and reseparated systems are explained.

5.2.1 Defining fusion

Calculations for the main study (groups I and II) reactions were first done as central collisions. It is a good starting point to compare to reactions with other values of ℓ, or to see if there is an ℓ dependence of a particular property. The ℓ value was then increased to $10\hbar$, although for many systems the outcome of these reactions were short neck times and consequently scattering at very backward angles occurred. Increasing to $\ell = 20\hbar$ would

have likely prevented this and therefore served as a better comparison to experimental data as the ANU CUBE [83] detector placement for experiments measuring MADs are not usually placed at very backward angles (e.g. in recent Refs. [54, 149, 223, 228]). For the auxiliary systems, calculations were performed for even higher angular momentum values.

All systems started at a distance of 44.8 fm between the centres of mass of the nuclei and the maximum reaction time was 24 zs. Extending this time limit in some heavy systems would cause numerical fluctuations which change the system's centre of mass coordinates or move the compound system or fragments too close to the edge of the calculation box (with hard boundary conditions). There are configurations of the initial box that have been used to calculate a longer reaction time, for example in Refs. [135, 223] for the ^{40}Ca+^{238}U system where contact time reached up to 20 zs, although such calculations demand heavy computational time. The upper limits of a TDHF calculation in contact time (assuming an appropriately large box size for the system is used) is dictated by the mean field approximation. Certainly, TDHF calculations do not properly account for two-body collisions that are necessary for an excited compound nucleus to reach thermal equilibrium. During a low energy collision, two-body collisions are not significant within the time scale of a reaction, so TDHF calculations of quasifission reactions which happen in time scales of the order of 1×10^{-20} s [207] are within reason. On the other hand, fusion-fission reactions time scales are on the order of 1×10^{-18} s [53], which is well beyond the limit of a TDHF calculation.

To characterise the results into systems that fused and systems that reseparated, the appearance of a half saturation density (0.08 nucleons fm^{-3}) neck in each system was essential. Their corresponding times between creation and disappearance of a neck of this density or more are shown in Fig. 5.1 for $\ell = 0\hbar$ (left) and $\ell = 10\hbar$ (right) with respect to reaction energy in the centre of mass frame. Changing from a central collision configuration to including 10 units of angular momentum produced very similar results in the main study systems. Points that lie at 24 zs with an upward pointing arrow represent systems that remained together at this final calculation time and are deemed fusion reactions. Because the systems are much heavier than in Chapter 4, a longer time for defining fusion is appropriate as some neck lifetimes are longer than the fusion time limit of 6 zs used in section 4.3.

The system ^{48}Ca+^{208}Pb has an observed TDHF fusion threshold at an energy less than $1.0V_B$ (a reminder that V_B is the static barrier energy calculated with the frozen HF method), as presented in Appendix E.2. This means that this system does not exhibit

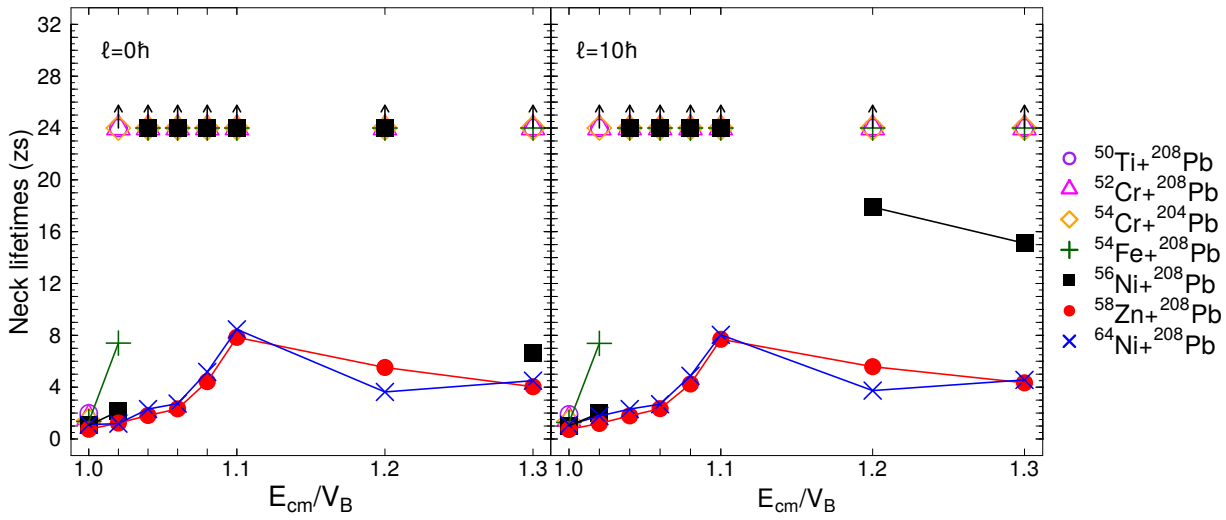

Fig. 5.1.: Half saturation density neck lifetimes in the systems for the main study.

any significant quasifission. As such, it has been omitted from any further results and analysis. On the other end of the scale, the two systems ^{58}Zn,^{64}Ni+^{208}Pb have a neck time of less than 24 zs over the entire energy range; there is essentially no TDHF fusion threshold in these cases.

Different definitions of fusion or contact time may also be used. In Ref. [178], the system ^{70}Zn+^{208}Pb is seen to never fuse at energies just below and up to 30% above the barrier, using the proximity barrier [20] as a reference. Instead of using the half saturation density neck to define contact time, the distance between the centres of mass staying below a value of 15 fm was used. This distance condition for fusion is was what was used in Chapter 4. Since Ca+Sn systems involve lighter and therefore smaller nuclei, a distance of 10 fm is sufficient. For ^{70}Zn+^{208}Pb, 15 fm is a large enough distance to accommodate for their sizes when they form a compound system. Also in this chapter the frozen HF barrier was chosen for the reference barrier for consistency in using the HF approach between static and dynamic calculations, as was done in Chapter 4.

As seen in Fig. 5.1, the systems ^{50}Ti, ^{52}Cr+^{208}Pb and ^{54}Cr+^{204}Pb reseparate at the frozen HF barrier energy then fuse from energies at and higher than 2% above the barrier. If there was a finer division of energies between $1.0V_B$ and $1.02V_B$ there would be a gentler slope of neck times leading up to their observed fusion at $1.02V_B$, as seen for ^{48}Ti+^{208}Pb in Ref. [178]. Increasing the frozen HF barrier energy by 2% increments proves to be very coarse energy steps for the lighter systems. This increment was chosen because of computational time limits. For ^{54}Fe+^{208}Pb, the system fuses from energies 4% above the barrier. In the case of ^{56}Ni+^{208}Pb, the system has a neck lifetime of less than 24 zs for energies at and up to 2% above the barrier, fuses for greater energies, then has

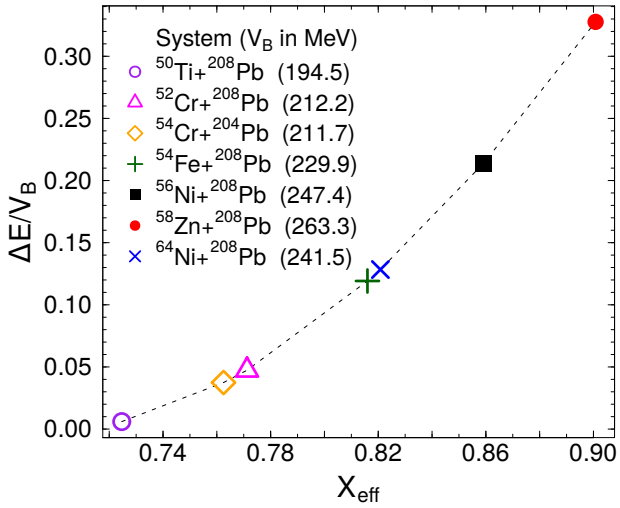

Fig. 5.2.: Extra push energy [16, 198, 199] as a ratio of frozen HF barrier energy, V_B, versus effective fissility of the main study systems. The dotted line is to guide the eye.

a neck lifetime less than 24 zs again for 20% ($\ell = 10\hbar$ only) and 30% above the barrier. If the fusion threshold time was increased to 40 zs for example, this system may appear to not reach fusion for the energy range $1.04V_B$–$1.1V_B$. Increasing the threshold time becomes computationally impractical, so the commitment to a time threshold of 24 zs for this study is required. Additionally, the interest of this study is in the trends between the systems rather than being quantitative for each specific system.

For the systems that reseparate at or just above their respective frozen HF barrier, V_B, then fuse from 2% or more above V_B, this difference in energy between reseparation and fusion is compared to the extra push energy (ΔE) [198, 199] and is presented in Fig. 5.2. The extra push energy is plotted as a ratio of the frozen HF barrier of each system, the latter which is indicated on the plot for reference, and as a function of entrance channel effective fissility as defined in Ref. [16]. Systems that reseparated at all energies between $1.0V_B$–$1.3V_B$ are also included in the figure. Comparing this to Fig. 5.1, the extra push energy as a ratio of each system's V_B is close to the TDHF results for the systems ^{50}Ti,^{52}Cr+^{208}Pb and ^{54}Cr+^{208}Pb. However, it overestimates the amount of energy needed for the systems ^{54}Fe,^{56}Ni+^{208}Pb and underestimates the energy for ^{64}Ni+^{208}Pb to fuse (which did not happen for 30% above V_B for this system). Finally, the system ^{58}Zn+^{208}Pb which did not fuse in the TDHF calculations had an extra push energy predicted at 34% above the barrier which extends further than the energy range used for TDHF calculations.

The neck times for the auxiliary systems (^{52,54}Cr+^{198,196}Pt and ^{34}S+^{232}Th) are presented in Fig. 5.3. All systems have neck durations exceeding 10 zs and reseparate before

24 zs across all angular momenta shown. Although the total mass for the system in these reactions is similar to those in the main study, there are fewer magic numbers and more angular momentum in these auxiliary systems. For ^{34}S+^{232}Th, there is also more initial mass asymmetry. All these factors may contribute to longer neck times and no observation of fusion.

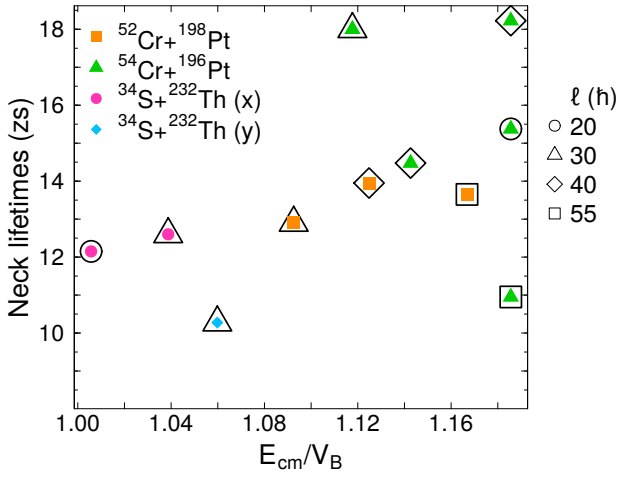

Fig. 5.3.: Same as Fig. 5.1 but for the auxiliary systems. Tip collisions of ^{34}S+^{232}Th are labelled with (x) and the side collision is labelled with (y). All Cr+Pt reactions were tip collisions.

5.2.2 Defining quasifission

To return to the discussion of which reseparated systems really can be labelled as quasifission in TDHF, definitions arising from experiment should provide an initial guide as to what to search for. In experiment, a system undergoing quasifission must be fully damped, exhibit some mass drift, and show angular anisotropy in the angular distribution of fragments [173, 207]. Reseparation also must occur before a compact CN shape has been achieved so that there is some memory of incoming nuclei, unlike in fusion-fission events where initial memory of reactants is completely lost and hence effects from the entrance channel are less significant.

In the TDHF calculations, quasifission is defined using the calculated total kinetic energy (TKE) and mass ratio of reseparated systems, then comparing these quantities to Viola systematics of fission fragments [81, 221] where

$$\mathrm{TKE}_{\mathrm{Viola}} = \frac{0.755 Z_1 Z_2}{A_1^{1/3} + A_2^{1/3}} + 7.3, \tag{5.2.1}$$

and Z_i and A_i, $i = 1, 2$ are the Z number and mass of the outgoing fragments respectively. The comparison between TDHF results and (5.2.1) is presented in Fig. 5.4 for the system

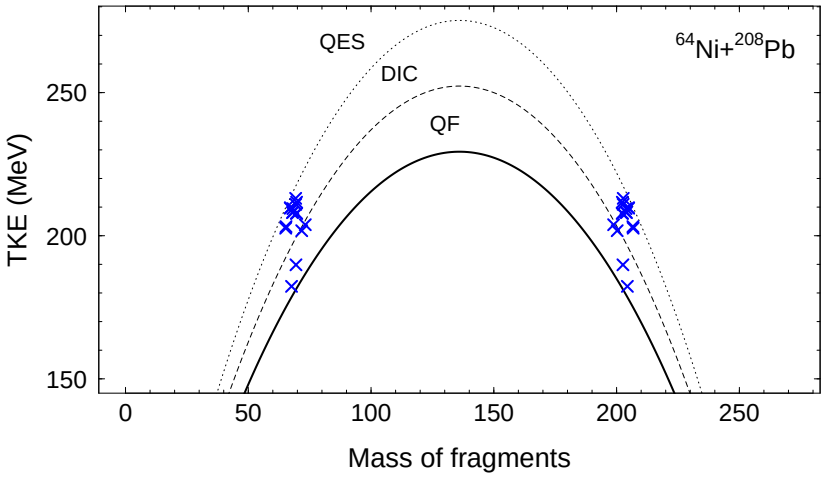

Fig. 5.4.: Total kinetic energy versus fragment mass for ^{64}Ni+^{208}Pb at $E_{\rm cm} = 1.0$–$1.3V_B$ and $\ell = 0\hbar, 10\hbar$ (blue crosses) compared to the Viola systematics (solid line). The upper limit of quasifission is indicated by the dashed line (at 10% above the solid line) and the upper limit of deep inelastic collisions is indicated by the dotted line (at 20% above the solid line). The regions of quasifission (QF), deep inelastic collisions (DIC) and quasielastic scattering (QES) are labelled on the plot.

^{64}Ni+^{208}Pb for energies between $1.0V_B$–$1.3V_B$ and $\ell = 0\hbar, 10\hbar$.

If the TDHF points lie within 10% of the Viola systematics (between solid and dashed lines) then the reaction is defined as quasifission. If the points lie between 10–20% of the Viola systematics (between dashed and dotted lines) then the reaction is defined as a deep inelastic collision. Points lying outside 20% of the Viola systematics are deemed quasielastic scattering reactions.

Using this criteria, the classification of all reactions from the main study in the TDHF picture are summarised in Tab. 5.1. Because of the short contact time and high mass asymmetry of the outgoing fragments (with masses close to the entrance channel), what is labelled as quasifission reactions are in fact fast quasifission reactions. It is certain that when separation is observed these are not fusion-fission reactions. This is because of the short time scale of the entire reaction. For systems with non-zero angular momentum that reseparate, there is less than a full revolution of the compound system before reseparation. In all systems that reseparate, during the contact time the compound system is not compact, there is often some strong identification of the two fragments.

Many of the reactions fall within the deep inelastic collision region. Even at $E_{\rm cm} = 1.0V_B$ where the contact time is very short (within 3 zs) for all reactions, and led to small amounts of nucleon transfer, the energy loss is sufficient enough for the reactions to be deep inelastic collisions with the exception of ^{50}Ti+^{208}Pb. Reactions that are labelled as quasifission are mostly from those reactions with angular momentum $\ell = 10\hbar$.

Now that the setup and classification of quasifission in TDHF has been discussed, the

System	E_{cm}/V_B															
	1.0		1.02		1.04		1.06		1.08		1.1		1.2		1.3	
	ℓ ($\hbar$)															
	0	10	0	10	0	10	0	10	0	10	0	10	0	10	0	10
^{50}Ti+^{208}Pb	QES	DIC	F	F	F	F	F	F	F	F	F	F	F	F	F	F
^{52}Cr+^{208}Pb	DIC	DIC	F	F	F	F	F	F	F	F	F	F	F	F	F	F
^{54}Cr+^{204}Pb	DIC	DIC	F	F	F	F	F	F	F	F	F	F	F	F	F	F
^{54}Fe+^{208}Pb	DIC	DIC	DIC	**QF**	F	F	F	F	F	F	F	F	F	F	F	F
^{56}Ni+^{208}Pb	DIC	DIC	DIC	DIC	F	F	F	F	F	F	F	F	F	**QF**	DIC	**QF**
^{64}Ni+^{208}Pb	DIC	DIC	DIC	DIC	DIC	DIC	DIC	DIC	DIC	**QF**	DIC	**QF**	DIC	DIC	**QF**	**QF**
^{58}Zn+^{208}Pb	DIC	DIC	DIC	DIC	DIC	DIC	QES	DIC	DIC	**QF**	DIC	**QF**	DIC	**QF**	**QF**	**QF**

Tab. 5.1.: Classification of reactions in the main study at all energies and angular momenta. Includes quasielastic scattering (QES), deep inelastic collisions (DIC), quasifission (**QF**) and fusion (F).

deconstruction of how these reactions unfold is addressed in chronological order in the following sections.

5.3 First contact

The formation of a neck at half saturation density and the moments immediately after this neck formation (up to 2 zs in total evolution time from initial separation of 44.8 fm) is what is considered as the first contact in a reaction. A neck forms for every system at the energy range presented in this study, whether they fused or reseparated. Discussed first is the configuration of a system soon after the nuclei have made contact and dissipation of total kinetic energy has been achieved, as well as the role of Pauli blocking in the energy region. Then, nucleon emission upon first neck formation is presented.

5.3.1 Formation of compound system

For systems with the same starting distance, increasing E_{cm} will hasten the formation of a half saturation density neck. In this section, instead of exploring the time at which the neck forms, the time near where the nuclei have stopped moving (when dissipation of the total kinetic energy has occurred) is taken. This time would be more of a direct comparison to the time of capture for a heavy-ion collision rather than the time of neck formation, which is more useful for modelling potential energy surfaces.

In selecting the time to identify where capture occurs, the first idea was to choose the first minimum of the distance between the centres of masses, r_{cm}, of the collision partners. Note that this is a neck plane (see subsection 4.3.1 and Ref. [225] for a description of this)

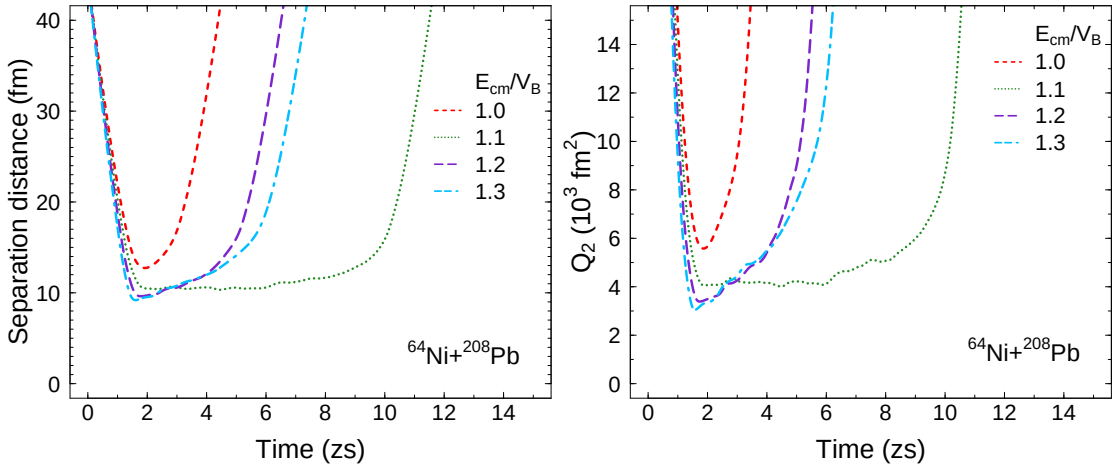

Fig. 5.5.: The separation distance (left) and Q_2 (right) for ^{64}Ni+^{208}Pb central collision at four different energies.

dependent quantity and for small values of $r_{\rm cm}$ where there is a large overlap between the two fragments, it is not reliable. The quadrupole moment is used in this section instead, taking the first minimum seen for every system at each energy. This is a reliable quantity as it depends on the density of the entire system. These two versions of minima are shown in Fig. 5.5 for ^{64}Ni+^{208}Pb as a central collision at various energies. The times at where the first minima occur are actually very similar between the two quantities.

The snapshot of the system density surface of at least 0.08 nucleons fm^{-3} at the time of the first minimum of Q_2 is shown on left of Fig. 5.6. The barrier energy, V_B, is not enough to lead the system to a more compact shape and there is a clear identification of the two fragments. As the energy increases, the identification weakens.

Now taking the $r_{\rm cm}$ values from the snapshots on the left of Fig. 5.6, these along with the corresponding energies are plotted on top of the frozen HF bare nucleus-nucleus potential for the same system on the right of Fig. 5.6. At the barrier energy (red square), the corresponding $r_{\rm cm}$ of the minimum Q_2 value is within 0.2 fm of the frozen barrier radius. As the energy increases, the distance where the first minimum of Q_2 occurs decreases and these points fall inside the frozen HF potential pocket.

The frozen HF potential shown in Fig. 5.6, as for Chapter 4, does not include the Pauli blocking effect. This effect would have a more significant role in these reactions involving ^{204,208}Pb compared to the Ca+Sn systems in Chapter 4. Relative to the frozen barrier radius, the onset of Pauli repulsion would be apparent at larger distances inside the pocket in heavy systems compared to lighter systems as there is more overlap of the nuclei in the former.

In the case of ^{64}Ni+^{208}Pb where a TDHF fusion threshold is not apparent, a corre-

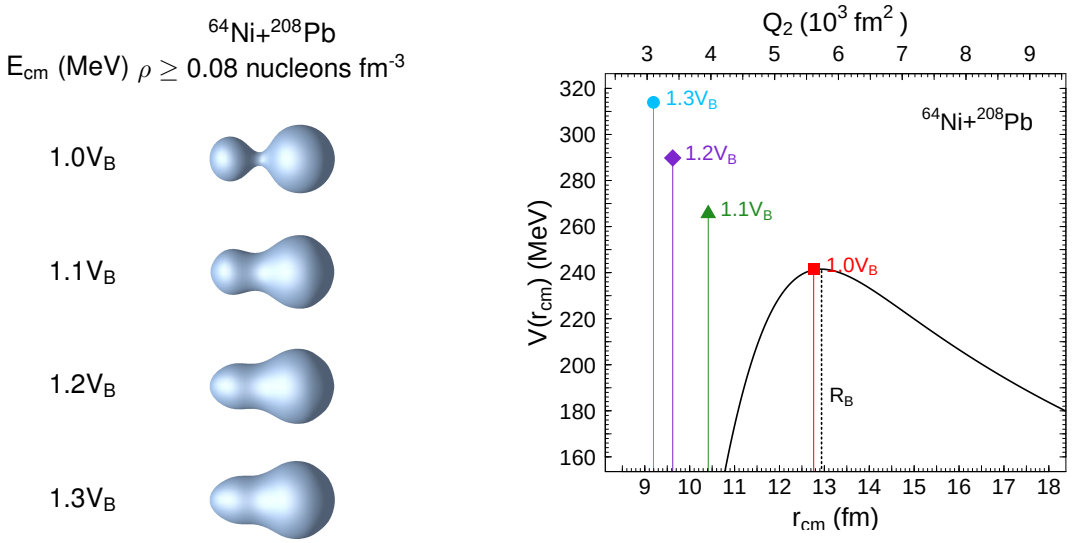

Fig. 5.6.: Left: half-density isosurface of central collisions of ^{64}Ni+^{208}Pb at $E_{\rm cm} = 1.0V_B$ MeV (top) through to $E_{\rm cm} = 1.3V_B$ MeV (bottom) at the first minimum of Q_2. Right: barrier top region of the frozen nucleus-nucleus potential for the same system. The coloured points show the distance between the centres of masses of the fragments to the left, at their respective energies. The position of the barrier radius is shown by the vertical dotted line.

sponding hypothetical one dimensional TDHF potential would have a very shallow pocket or a complete absence of one. The Pauli blocking effect would bring an addition to the frozen HF potential inside the barrier in Fig. 5.6 (right) [186], a shallowing of the pocket and from this a resulting increase of the barrier energy that is shifted to a lower barrier radius.

5.3.2 Particle emission

Soon after a neck has formed many systems experience particle emission, especially if the fragments have a lot of neutron or proton excess and also particularly at high energies such as 30% above the barrier. Appearing in Ref. [98] is a technique to count the number of emitted particles a system produces. The same technique is used in this section to count the particle emissions over the reaction time. At each time step, the number of neutrons and protons is counted by integrating the neutron and proton densities that lie above a small threshold for the total density for which the nucleons are considered to belong to a fragment. The difference between these numbers and the number at initial time is then the number of emitted neutrons or protons. If the number of emitted nucleons at time t is given by $EN(t)$, the threshold density is $\rho_{\rm th}$ and U is the calculation box then

$$EN(t) = \int_U \rho(\mathbf{r}, t_0) - \rho(\mathbf{r}, t)\Big|_{\rho > \rho_{\rm th}} dV.$$

The threshold density used for the systems in the calculation box sizes used is taken to be 0.0003 nucleons fm^{-3}, a cross section slice of the density at the final time was inspected to guide this number which is dependent on box size. If the threshold is too high (at or above 0.0005 nucleons fm^{-3} in all systems, energies and angular momenta) then the number of emitted particles is overestimated since a significant portion of the main nuclear mass lies under the threshold density "blanket". If the threshold is lower than 0.0003 nucleons fm^{-3}, the density of the emitted particles is likely to exceed this and would be included in the integration of the main nuclear mass at every time step. The threshold density in relation to the density slice $\rho_{y=0}$ at $y = z = 0$ ($x-$axis is the collision axis) of a system is shown in Fig. 5.7 for the central collision of ^{64}Ni+^{208}Pb with $E_{\rm cm} = 1.3V_B$.

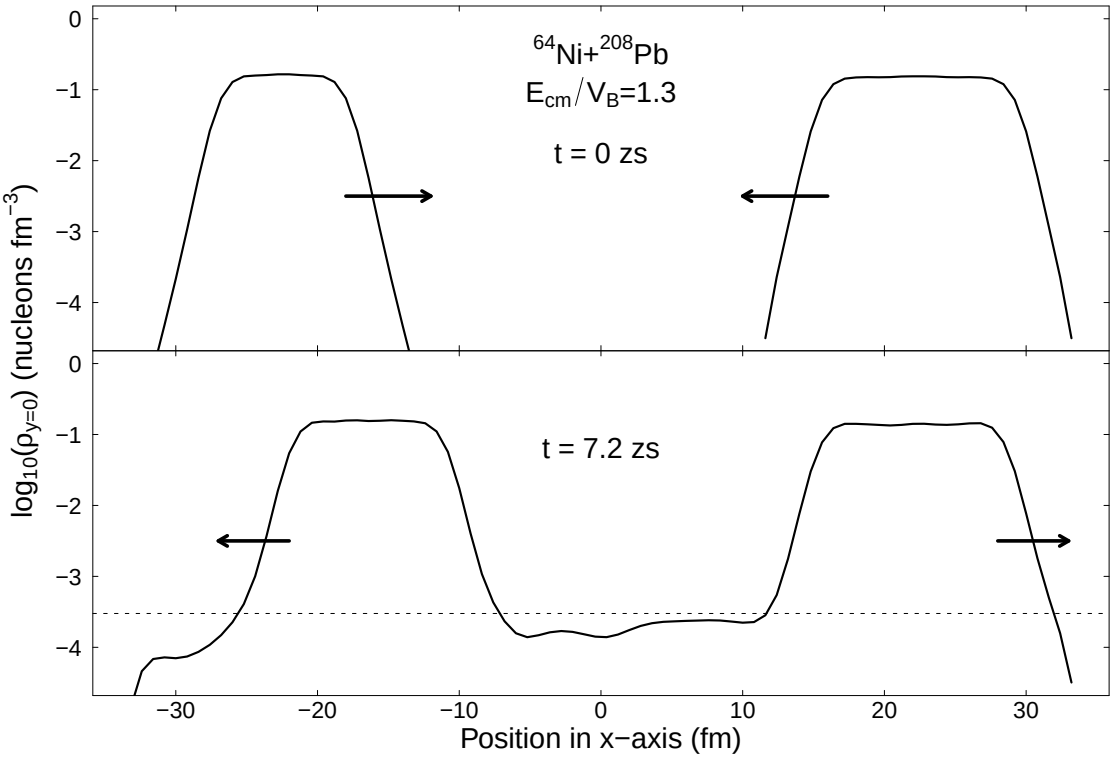

Fig. 5.7.: Logarithmic plot of the density profile at $y = 0$ of the central collision of ^{64}Ni+^{208}Pb with $E_{\rm cm} = 1.2V_B$ at initial time (top) and final time (bottom). The threshold density is indicated by the dashed line at 0.0003 nucleons fm^{-3}. The arrows indicate the direction of the motion of the fragments.

Proton and neutron emission over reaction time is presented in Fig. 5.8 for ^{58}Zn+^{208}Pb (left panels) and ^{56}Ni+^{208}Pb (right panels) for $\ell = 0\hbar$ at $E_{\rm cm} = 1.0V_B$ (top row) and $1.3V_B$ (bottom row). The same plots for systems in the main study at all energies and angular momenta are presented in Appendix G. The shaded regions in the plots indicates the time where the half saturation density neck existed. The relevant part of the plot for this section is the area at and directly after the start of the shaded region. For the

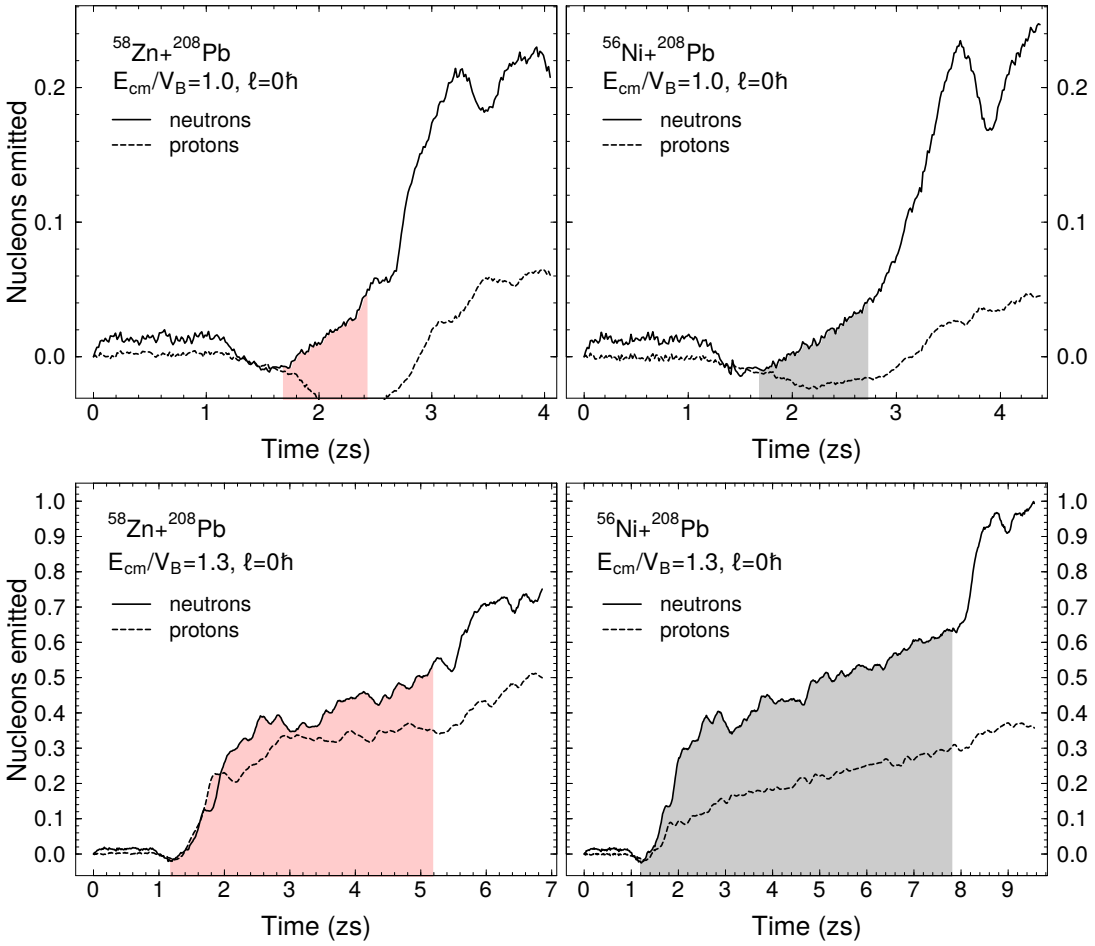

Fig. 5.8.: Particle emissions versus time for ^{56}Ni+^{208}Pb (top) and ^{58}Zn+^{208}Pb with $\ell = 0\hbar$ for $E_{\rm cm} = 1.0V_B$ (left) and $E_{\rm cm} = 1.3V_B$ (right). The shaded area indicates the times when the half saturation density neck existed in the reaction.

reaction at the barrier energy, almost as soon as the neck forms the neutron emissions start to increase gradually. At the highest energy the surge of both particle emissions at neck formation time is much more pronounced. This surge is common for all systems that reseparate, especially those which do at higher energies (^{64}Ni,^{58}Zn+^{208}Pb). For the systems that reseparate with $\ell = 10\hbar$, the resulting emission versus time plots look globally the same with surges appearing after the neck break at higher energies. The total number of emitted particles for the non-central collisions is slightly higher and is presented in a later section.

Spurious negative values appear for emissions because at 0 zs, the total number of integrated neutrons and protons is less than the true value, from integrating above the threshold density. This offset is accounted for in the number of nucleons emitted at each time step which means that the first time step should properly have zero emissions. The cutoff time is either when the fragments are back to being approximately 44.8 fm apart between the centre of mass coordinates if $\ell = 0\hbar$ or before they hit the side of the box for

$\ell = 10\hbar$.

Both proton and neutron emissions are present although neutron emission is significantly higher in all systems as protons undergoing emission must tunnel through the Coulomb barrier. The system with most proton emission was ^{58}Zn+^{208}Pb, the maximum being just under 0.7 protons at the highest energy. This is probably owed to the ^{58}Zn projectile having an excess of protons, some of which are likely to be less well bound and more susceptible to emission, as all other systems had less than 0.5 proton emission for all energies and angular momenta.

Neck formation, especially at $E_{\text{cm}} = 1.2V_B$ and $1.3V_B$, is traumatic enough for the system to prompt ejection of particles. Future work arising from these emission results would be a deeper investigation of what role different dynamical effects play in nucleon emission, for example transfer and magicity. Also, determining where emissions are coming from in the compound system would be useful, for example in ^{58}Zn+^{208}Pb one would expect proton emission to come from the zinc nucleus. This can be sourced from TDHF calculations by using the momentum distribution from the wavefunction of the system.

5.4 During contact time

Dynamical processes continue to take place while the neck of the system exists. As well as further particle emissions, the remaining contact time allows for nucleon transfer. Calculating the average transfer numbers in TDHF is detailed in subsection 2.5.2 and the results are presented for all systems that reseparate. Systems that have fused of course will have no separate fragments to observe final masses and charges. Whether a neck of a system looks like it will remain at a time less than 24 zs is also addressed in this section.

5.4.1 Particle transfer

Average transfer numbers

If transfer channels are favoured for a system then the process will begin when a neck forms. For systems that reseparate, the average N and Z numbers of the fragments versus time can be calculated. Recall that these average quantities are dependent on the choice of neck plane, so when there is an overlap between the two fragments, they are unreliable. As average N and Z numbers are calculated by integrating all the density that lies to one side of the neck plane (refer to subsection 2.5.2), it will also include emitted particles. This is not ideal since the goal is to see what mass is left in each of the two the

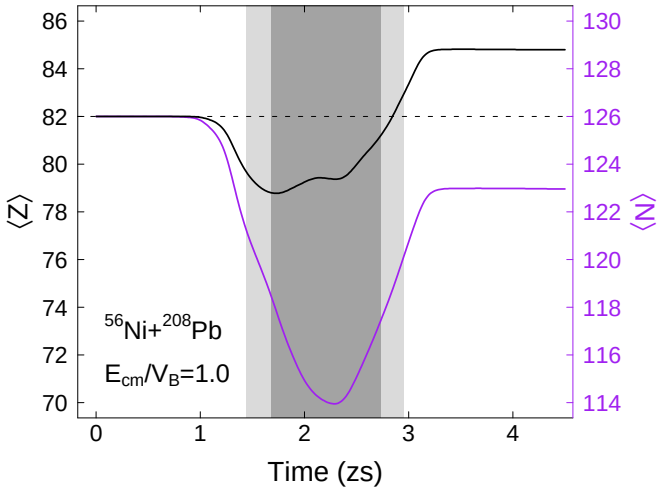

Fig. 5.9.: Average N and Z number of the heavy fragment for central collision of ^{56}Ni+^{208}Pb at $E_{\rm cm} = 1.0V_B$. The light shaded area is the neck duration at $\rho \geq 0.01$ nucleons fm^{-3} and the dark shaded area is neck duration at $\rho \geq 0.08$ nucleons fm^{-3}.

final fragments. However, as will be shown later, the largest number of emitted particles in any of the reactions that reseparate is less than two neutrons. As a percentage of the whole system, or in particular the heavy fragment which is the fragment used to determine transfer amounts here, this is small enough to ignore for the purposes of the following discussions.

The average N and Z numbers with respect to time for the heavy fragment in the system ^{56}Ni+^{208}Pb at the barrier energy for $\ell = 0\hbar$ is presented in Fig. 5.9. The dark grey shaded area is where the half saturation density neck occurs and the lighter shaded area is where the neck density at 0.01 nucleons fm^{-3} occurs. In the shaded region, the values for average N and Z are neck plane dependent. The useful part is when these numbers stabilise towards the end of the reaction where the fragments are well separated again. In this case the heavy fragment has gained protons and lost neutrons on average.

The difference between initial (dashed line) and final (solid lines) average N and Z numbers of the heavy fragment in Fig. 5.9 and all other reseparated systems is seen in Fig. 5.10 for the entire energy range and both angular momenta. With a handful of exceptions, the results between the two angular momentum values are rather similar. In every case the intial ^{204,208}Pb loses neutrons by the end of the reaction, shown in the top two panels. In many cases it gains protons, shown in the bottom panels. This direction of transfer is in favour of balancing out the N/Z ratios between the fragments.

By just considering the N/Z values of the two initial nuclei in each system, it is expected that the ^{204,208}Pb would lose neutrons and or gain protons as the N/Z ratio for these two isotopes is higher than any of the listed projectiles. For the systems with

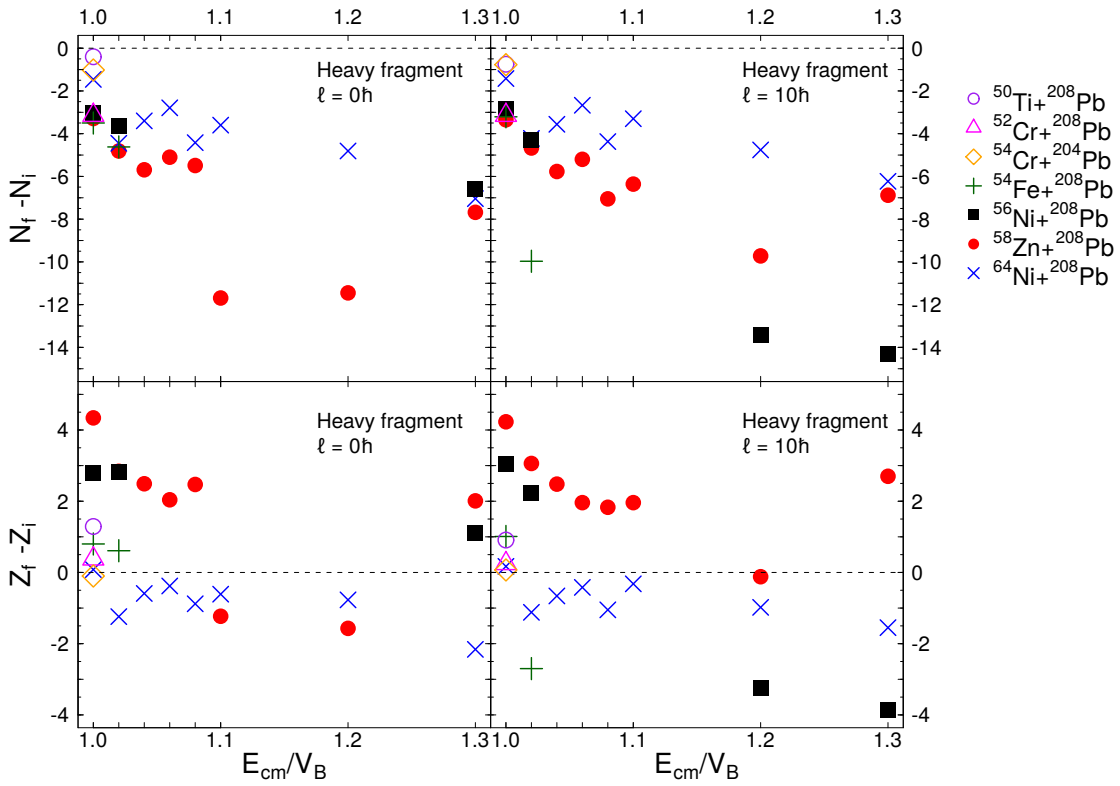

Fig. 5.10.: Difference between final and initial average N (top panels) and Z (bottom panels) numbers of the heavy fragment in the separated systems. Central collisions are the left panels and $\ell = 10\hbar$ are the right panels.

^{56,64}Ni projectiles, all proton numbers involved are magic. In the ^{64}Ni case, this may contribute to the fact that there is very little proton transfer (often less than one) as well as the fact that ^{64}Ni has the closest N/Z to ^{208}Pb of all projectiles considered for this target. The comparatively smaller N/Z factor for ^{56}Ni isotope means it could be more energetically favourable for proton transfer to occur rather than the preservation of all the magic numbers.

There is virtually no proton transfer for ^{54}Cr+^{204}Pb and at most one neutron transfer at the barrier energy. The neck time for this reaction is very short and the N/Z ratio between these two initial nuclei is more closely matched than any other combination in the main study. Introducing two extra neutrons in total to the system to make ^{52}Cr+^{208}Pb, which has a similar neck lifetime, increases the number of neutron transferred by approximately two and proton transfer remains insignificant at the barrier energy. Comparing this to the pair of systems ^{56,64}Ni+^{208}Pb where the difference in neutron number is 8, the transfer results of the two systems differ much more suggesting that a more drastic increase of number of neutrons in the system is needed to generate very different amounts of transfer.

There are some outliers seen in Fig. 5.10, including ^{58}Zn+^{208}Pb at energies 10% and

20% above the barrier for $\ell = 0\hbar$, ^{56}Ni+^{208}Pb at 20% and 30% above the barrier for $\ell = 10\hbar$ and ^{54}Fe+^{208}Pb at 2% above the barrier for $\ell = 10\hbar$. For reactions occurring at 10% or more above the barrier, it is worth mentioning that a head-on collision is the configuration for a reaction leading to maximum total kinetic energy loss [170, 176, 196]. With increasing energy, dynamics arising from this configuration such as a "density backsplash" may happen [27, 109]. Although this is more likely for energies from 2 MeV per nucleon or higher [109], it could be a contributing factor to these unusual transfer results in this study.

Q-values

The N/Z equilibration between fragments is driven by a manifestation of Q-values for the different transfer channels and was previously discussed in subsection 4.3.4. A compilation of ground state Q-values (experimental) of some of the possible outgoing trajectories of the systems is presented in Tab. 5.2. In order to make this table, emitted particles had to be ignored and just the changes of N and Z appearing in Fig. 5.10 were considered. Some values in Fig. 5.10 sit between integer values and not every single combination of ingoing and outgoing system is shown. For some systems only the extreme cases are shown, an example being for ^{64}Ni+^{208}Pb where proton transfer is mostly not apparent but the case of $1p$ and $2p$ pickup is listed on the table. As discussed in subsection 4.3.4, for proton transfer a positive ground state Q-value ($Q_{\text{g.s.}}$) alone is not enough to determine how likely a particular transfer reaction is to occur. Rather, the difference between ingoing and outgoing Coulomb trajectories, essentially the optimum Q-value (Q_{opt}), must be taken into account [30]. The difference $Q_{\text{g.s.}} - Q_{\text{opt}}$ is also listed in the table for this purpose. Recalling the expression for Q_{opt} from subsection 4.3.4,

$$Q_{\text{opt}} = \left(\frac{Z_{1f} Z_{2f}}{Z_{1i} Z_{2i}} - 1 \right) E_{\text{cm}}, \tag{5.4.1}$$

the E_{cm} value in (5.4.1) is taken to be the centre of mass energy used in the TDHF calculation for each reaction. Proton pickup will result in a greater Coulomb barrier in the exit channel, taken into account by Q_{opt}, and the resulting Q-value for the transfer is not always positive even if $Q_{\text{g.s.}}$ is.

In most cases, the difference $Q_{\text{g.s.}} - Q_{\text{opt}}$ is positive which indicates that the associated average transfer channel seen from TDHF is energetically favourable. The most positive values are for the ^{56}Ni,^{58}Zn+^{208}Pb reactions which have the most proton rich projectiles out of all the systems, making the N/Z ratios between initial fragments very mismatched.

Ingoing	Transfer channel		Outgoing	$Q_{\text{g.s.}}$ (MeV)	$Q_{\text{g.s.}} - Q_{\text{opt}}$ (MeV)
^{50}Ti+^{208}Pb	−1p		^{49}Sc+^{209}Bi	−8.360	−1.782
^{54}Fe+^{208}Pb	−1p	+3n	^{56}Mn+^{206}Bi	−1.063	5.082
	+3p	+10n	^{67}Cu+^{195}Au	21.883	4.398
^{56}Ni+^{208}Pb	−3p	+3n	^{56}Mn+^{208}At	−6.275	12.152
	−2p	+4n	^{58}Fe+^{202}Po	4.688	16.999
	−1p	+7n	^{62}Co+^{202}Bi	6.510	14.215
	+4p	+14n	^{74}Ge+^{190}Pt	35.072	7.054
^{64}Ni+^{208}Pb	+1p	+5n	^{69}Cu+^{203}Tl	2.650	−3.371
	+2p	+6n	^{72}Zn+^{200}Hg	8.801	−5.420
^{58}Zn+^{208}Pb	−4p	+3n	^{57}Fe+^{209}Rn	5.076	29.053
	−3p	+5n	^{60}Co+^{206}At	10.033	28.048
	−2p	+6n	^{62}Ni+^{204}Po	21.040	36.069
		+6n	^{68}Zn+^{198}Pb	32.027	32.027
	+1p	+12n	^{71}Ga+^{195}Tl	34.247	27.696

Tab. 5.2.: Some listed possibilities for outgoing systems according to transfer amounts (with respect to the projectile) shown in Fig. 5.10. Both experimental ground state Q-value and the difference with Q_{opt} are listed.

In the case of ^{64}Ni+^{208}Pb, where the N/Z ratio between fragments is closer than for the previous two reactions, negative values are apparent for proton pickup which supports the fact that for this system, proton transfer is often not seen referring to Fig. 5.9.

To compare transfer in this study to heavy systems with no magicity, the auxiliary systems ^{52,54}Cr+^{198,196}Pt and ^{34}S+^{232}Th are used as examples. Each of these systems have much longer neck times than those in the main study, all in excess of 10 zs and much more mass transfer happens as a result.

The auxiliary reactions at some of the energies are selected to appear in Tab. 5.3 to show the amounts of transfer and their respective $Q_{\text{g.s.}} - Q_{\text{opt}}$ differences. The numbers of protons and neutrons transferred is vastly higher than for the systems in the main study, with at least 16 neutrons and 8 protons transferred. This results in a much more mass equilibrated system. The most mass transfer seen was for the Cr+Pt systems when Pd+Ba was the exit channel. Increasing the angular momentum for the same system at one energy (as listed for ^{54}Cr+^{196}Pt) has decreased the amount of transfer and the final Q-value.

For the ^{34}S+^{232}Th systems, the difference in V_B between the tip (x) and side (y) configurations, at 144.96 MeV and 157.48 MeV respectively, is just over 12.5 MeV. In the lowest energy and angular momentum for the tip collision, the outgoing system favoured

System	E_{cm}/V_B	ℓ ($\hbar$)	Transfer channel		Outgoing	$Q_{\mathrm{g.s.}} - Q_{\mathrm{opt}}$ (MeV)
^{52}Cr+^{198}Pt	1.09	30	+22p	+38n	^{112}Pd+^{138}Ba	10.376
^{54}Cr+^{196}Pt	1.19	20	+22p	+36n	^{110}Pd+^{140}Ba	−3.091
		55	+19p	+31n	^{104}Tc+^{146}Pr	−10.792
^{34}S+^{232}Th (x)	1.01	20	+8p	+16n	^{58}Cr+^{208}Pb	25.800
(x)	1.03	30	+9p	+16n	^{59}Mn+^{207}Tl	20.902
(y)	1.03	30	+16p	+27n	^{77}Ge+^{189}W	8.204

Tab. 5.3.: Auxiliary systems transfer amounts (with respect to projectile). The tip orientation of ^{232}Th is denoted by (x) and the side orientation by (y). The Cr+Pt systems are tip collisions.

the doubly magic ^{208}Pb nucleus. Similar mass transfer resulted for the same system with an increase in energy and angular momentum. For the side collision the exit channel is a more mass equilibrated system. Although due to the higher Coulomb potential in the exit channel, the resulting Q-value is lower than for the tip collisions.

Numbers of transferred nucleons are somewhat dependent on the contact time, using the main and auxiliary systems as comparisons to each other. In the systems with no magicity, in particular ^{34}S+^{232}Th, it is seen that transfer leading to outgoing fragments with or near magic numbers were favoured. In the main study, it may not only be the short neck time that leads to much smaller transfer numbers in comparison but also the fact that the systems begin with many magic numbers, and it could be the case that being near shell closure is more favourable than mass equilibration. Conversely, as most of the systems start with three magic numbers, this may lead to much smaller transfer numbers and consequently a shorter contact time.

To improve the discussions of transfer seen in the TDHF reactions the emitted particles should be removed from the counting of the average N and Z in a fragment. This can be achieved by defining a more restricted region to integrate proton and neutron densities over rather than selecting an entire side of the calculation box for the integration limits in equation (4.3.2).

So far, only reseparated systems have been shown in results such as final transfer numbers. However, if a system has shown a neck existence after some time, it is sometimes difficult to ascertain whether the neck actually will break or whether it will continue and lead to being classified as a fusion reaction. This is addressed in the next subsection.

5.4.2 Will the neck break?

There are a few approaches in deciding if a system is likely to remain as a compound nucleus at a reaction time less than or at 24 zs which is the threshold time for fusion in this chapter. Previously in Chapter 4, the distance between the centres of masses, $r_{\rm cm}$, of the fragments was used instead. If the distance reached and remained below 10 fm by 6 zs then it was classified as fusion. This definition of fusion is sufficient for lighter systems such as Ca+Sn. For heavy systems, this is not definitive enough of a value to use as the size of the nuclei involved in heavy systems are large enough to remain as a compound system with $r_{\rm cm}$ greater than 10 fm and still be classified as a fusion reaction. In Ref. [178] for ^{70}Zn+^{208}Pb the $r_{\rm cm}$ requirement is 15 fm which accounts for the increasing size of the nuclei, however the proxy used in this chapter to decide whether a system had fused is the quadrupole moment of the total system instead. As mentioned in subsection 5.3.1, quadrupole moment is independent of the neck plane and therefore a suitable measure to use. If the quadrupole moment remained fairly constant or within a small range over a large time, and was not increasing overall at 24 zs, then it was decided that this would be defined as fusion and calculations need not continue past 24 zs.

A zero valued quadrupole moment means the total system is in a perfect spherical configuration. As the systems in this chapter study are heavy and do not exhibit a compact CN shape, the expected resulting quadrupole moment would be positive indicating a prolate shape even for systems that are labelled as fused.

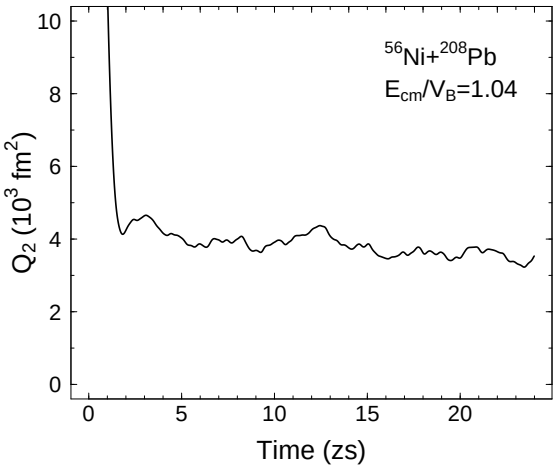

Fig. 5.11.: Quadrupole moment for composite system from a central collision of ^{56}Ni+^{208}Pb at $E_{\rm cm} = 1.04V_B$.

The system ^{56}Ni+^{208}Pb at $E_{\rm cm} = 1.04V_B$ is used as an example where the quadrupole moment test would be useful. This system reseparated at $E_{\rm cm} = 1.0V_B$ and $1.02V_B$ with neck times less than 2 zs each so the same system seemed a promising candidate to

reseparate again at $E_{\rm cm} = 1.04V_B$. The quadrupole moment for this system, presented in Fig. 5.11, remains between $3.5 \times 10^3 - 4.5 \times 10^3$ fm^2 from 2 zs onwards and is not globally increasing at final time. This indicates the system is not likely to reseparate soon after 24 zs.

The quadrupole moment was one of the quantities contributing to the decision of the reaction time threshold of 24 zs, as any system that had not reseparated had a stable quadrupole moment at this maximum time.

5.5 Reseparation of fragments

Systems that remain fused have now been well identified. The dynamics that occur as soon as a neck forms and during the observed lifetime of the neck have been discussed thus far. The discussion in this section moves on to the ongoing dynamics that happen near the end of a reaction for a system that reseparates. Included as part of the dynamics associated with reseparation is further particle emission and whether N/Z equilibration between outgoing fragments has been achieved.

5.5.1 Final particle emission

It was seen in Fig. 5.8 that almost as soon as a neck forms, particle emissions started to gradually increase and for the highest energies there was a surge of particle emission. During the rest of the neck lifetime, the emissions rose steadily. Now when the neck breaks, corresponding to the end of the shaded regions in Fig. 5.8, there is another clear surge of emitted neutrons in the case of ^{56}Ni,^{58}Zn+^{208}Pb. This is also true for other systems and over the whole energy range. The surge is not so prominent for protons.

A study of where nucleons are being emitted from at this point in the reaction would be beneficial, in particular to check if they are being released from around the neck region and concurrently check whether the neck density mainly consists of protons or neutrons.

The final emission at the cutoff time in Fig. 5.8 is seen for every system at both $\ell = 0\hbar$ and $10\hbar$ in Fig. 5.12. The cutoff time where these emissions are calculated is different for every system. The fragments must be well separated but have not yet hit any sides of the box. In most cases, it is unlikely for an emitted particle to rejoin the fragments after it has been released, as the volume occupied by the fragments as a percentage of the total box size is only about 5% in the heaviest case of ^{64}Ni+^{208}Pb. Where it could occur is if the system reseparates close to the edge of the box. This was only the case for ^{56}Ni+^{208}Pb at $E_{\rm cm} = 1.2V_B$ and $1.3V_B$ with $\ell = 10\hbar$.

The number of particles emitted increases as the energy increases, and neutron emission

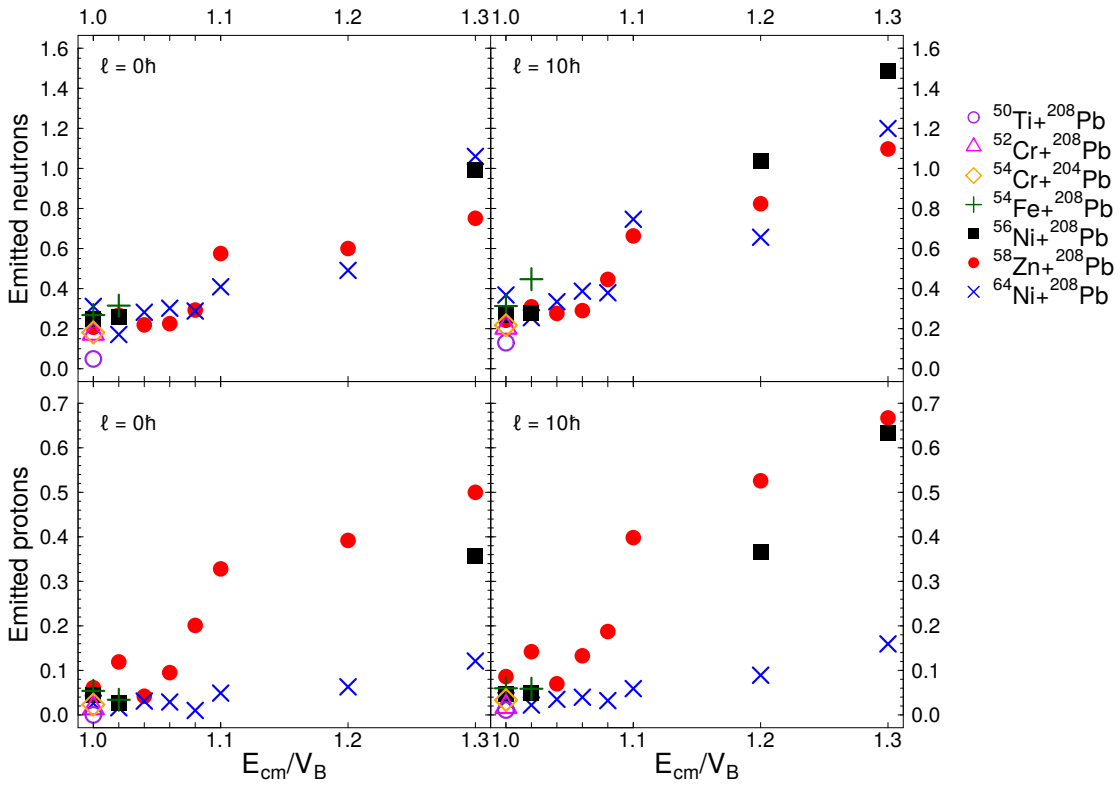

Fig. 5.12.: Final numbers of emitted neutrons (top row) and protons (bottom row) in the main systems. Central collisions on the left and $\ell = 10\hbar$ on the right.

is overall more abundant than proton emission as previously mentioned, as a result of the Coulomb barrier for protons. Since the only two systems that reseparated over the entire energy region were ^{58}Zn,^{64}Ni+^{208}Pb, overall trends relating to centre of mass energy and neck times can only be made for these systems. Even though the system ^{56}Ni+^{208}Pb fused for many energies, it nonetheless falls within the upwards trend of emission seen in ^{58}Zn,^{64}Ni+^{208}Pb. As mentioned before, the proton emission for ^{64}Ni is very low as the N/Z ratio for this projectile is higher than any of the other projectiles for this target. By contrast, ^{58}Zn emits at least 0.3 protons from 10% above the barrier onwards.

To compare the emission of reseparated systems to a system that fused, in Fig. 5.13 is the emission versus time (same as Fig. 5.8) for the system ^{56}Ni+^{208}Pb as a central collision at an energy $E_{\rm cm} = 1.04V_B$. Emissions are seen to steadily increase over reaction time with final emission being just less than 0.4 and just over 0.1 for neutrons and protons respectively. Fig. 5.13 lacks the characteristic surge of emissions that is seen in Fig. 5.8 at the end of the neck lifetime, confirming that the surge is instigated by the breaking of the neck in a system.

Overall, for this study the final numbers of emitted particles are relatively small in comparison to Ref. [98] where TDHF calculations of actinide on actinide collisions at

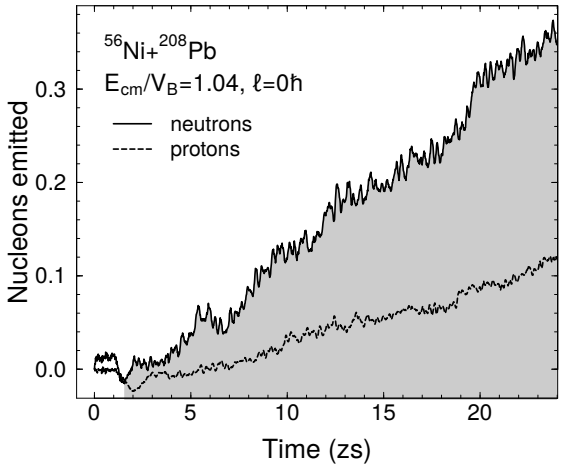

Fig. 5.13.: Emission versus time for the central collision of ^{56}Ni+^{208}Pb at $E_{\rm cm} = 1.04V_B$. This system fused.

and above barrier energies lead to observed emission of at least two two neutrons.

5.5.2 Outgoing fragments

In identifying the outgoing fragments' mass and charge, the fact that emitted particles are included must again be ignored as was done for section 5.4.1. Although, the maximum number of protons that has been emitted from any case is 0.7 protons, meaning the charge of one of the outgoing fragments is at most off by 1. For neutrons, the final fragment N number could change by 1 or 2 in the most extreme cases as the maximum emitted number is 1.5 neutrons over all systems. Because of the emissions, the uncertainty in final Z and N number would affect the associated $Q_{\rm g.s.}$ for the transfer reaction and also $Q_{\rm opt}$ for proton transfer.

To see whether N/Z equilibration has been achieved through the process of relatively fast inelastic collisions or quasifission (less than 10 zs total for the main study), the change in N/Z of the heavy fragment appears with respect to energy for all systems is plotted in Fig. 5.14. The change in N/Z is not dependent on system energy or on the observed neck lifetime of which most are less than 10 zs. This is consistent with the findings that N/Z equilibration is a fast process that can happen within 1 zs [62], which was approximately the shortest neck time of all systems in the main study. It is therefore apparent that N/Z equilibration is the most desirable configuration for these systems, even more so than preservation of magic numbers. It also suggests in the case of a very exotic "projectile" like ^{58}Zn, transfer is motivated to happen and finalise quite rapidly, since the difference in N/Z for the longest neck time for this system (at $1.1V_B$) is approximately the same as for $1.0V_B$.

In Fig. 5.14 the dashed lines are the difference between the composite system's N/Z

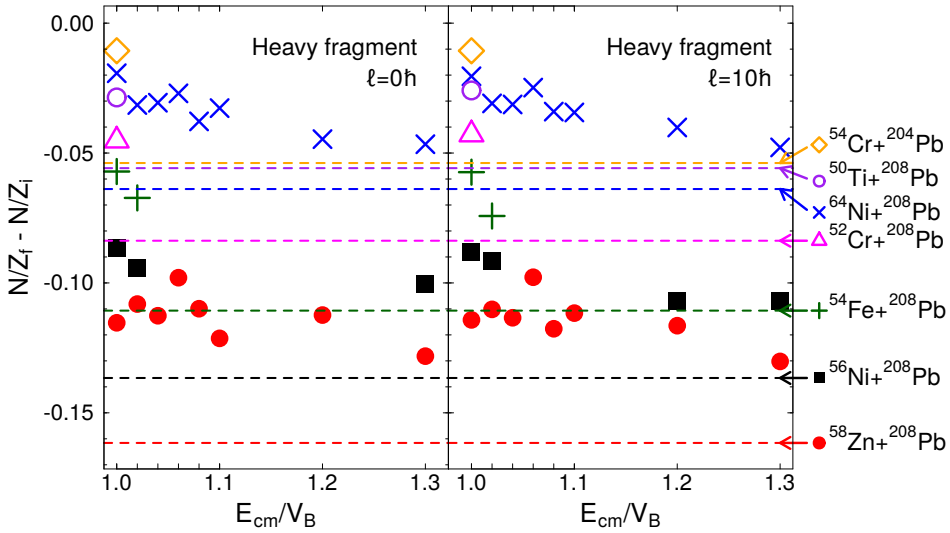

Fig. 5.14.: Difference between final and initial N/Z ratio of the heavy fragment for $\ell = 0\hbar$ (left) and $\ell = 10\hbar$ (right). The dashed lines indicate the N/Z ratio for the composite system, labelled on the right.

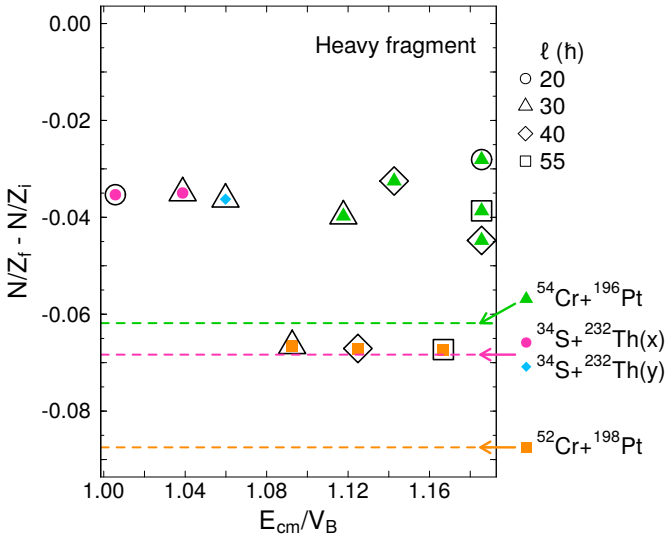

Fig. 5.15.: Same as Fig. 5.14 but for the auxiliary systems.

ratio and initial heavy fragment N/Z, they are labelled accordingly with arrows on the right. The final N/Z ratios of the fragments do not reach this for the composite system as if they had then the points in Fig. 5.14 would lie directly on their corresponding dashed line. They have, however, moved in the direction towards the dashed line and may have reached equilibrium nonetheless. As mentioned previously in subsection 5.4.1, transfer occurs not to equalise the N/Z ratio but to optimise binding energies of the collision partners.

To see whether the N/Z equilibration of fragments comes closer in value to the N/Z of the compound system with longer necktimes, less magicity and more mass transfer, the results from the auxiliary systems will serve this purpose. The N/Z ratios of the heavy

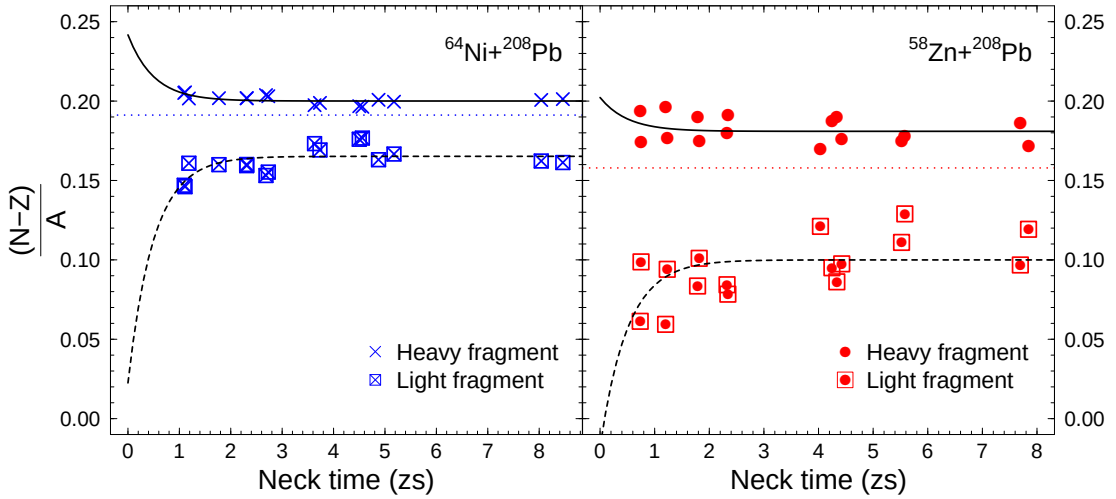

Fig. 5.16.: The quantity $(N-Z)/A$ versus neck time for each fragment of the systems ^{64}Ni+^{208}Pb (left) and ^{58}Zn+^{208}Pb (right). Horizontal dotted lines indicate the value for the composite system. Black solid and dashed lines are fits to the function $\alpha + \beta e^{-t/\tau}$.

fragment in the auxiliary systems is presented in Fig. 5.15. These N/Z ratios for the exit channel fragments in these systems on average have not reached significantly closer to the N/Z of the compound system compared to the main study.

The fast process of charge equilibration is illustrated further in Fig. 5.16 which shows the N and Z asymmetry of both outgoing fragments as a function of neck time for ^{64}Ni,^{58}Zn+^{208}Pb. These systems are shown as they had the largest range of neck or contact time over the energy range of the calculations. Each of the fragments are fitted to the function $\alpha + \beta e^{-t/\tau}$ for parameters α and β that are different for each fragment in each system. The relaxation time τ parameter was set to 0.5 zs in all cases as an example relaxation time. The initial N/Z asymmetry and $(N-Z)/A$ values between fragments is quite different between these two systems (initially, ^{58}Zn has a negative $(N-Z)/A$ value). By the end of the reaction, the difference in $(N-Z)/A$ values for the fragments between the systems is much reduced. Furthermore, it is evident that the charge equilibration was achieved within 2 zs for both systems.

5.6 Summary

The dynamics associated with heavy-ion collisions, some of which classify as quasifission, along the reaction timescale has been presented in this chapter using the TDHF approach. Discussions about heavy-ion collisions in this chapter were illustrated through reactions with a chain of $N = 28$ isotope projectiles (ranging from Ti to Zn) on a ^{208}Pb target, including the two extra systems ^{64}Ni+^{208}Pb and ^{54}Cr+^{204}Pb as a comparison to vary in the neutron magicity of the system. The reason the $N = 28$ chain was chosen was to

explore the effect of proton magicity between the shell closures at $Z = 20, 28$. Mentioned in Chapter 4 and appearing in Appendix E.2, was that the system ^{48}Ca+^{208}Pb had a TDHF fusion threshold below the static barrier. Because of this, this system was omitted from further study as many results relied on the system reseparating. The energy range for these reactions was between $1.0V_B$–$1.3V_B$ where V_B was the frozen HF barrier energy.

It turned out in this study that ^{58}Zn+^{208}Pb was the only system along the $N = 28$ chain that did not fuse at any energy. The system ^{64}Ni+^{208}Pb also did not fuse at any energy while ^{56}Ni+^{208}Pb only fused at some energies. Comparing ^{56,64}Ni+^{208}Pb was a similar test to the systems $^{40-54}$Ca+^{116}Sn in Chapter 4 where the neutron number of projectile was increased. In this chapter, ^{56}Ni+^{208}Pb showed to have a TDHF fusion threshold at an energy 4% above the static barrier, whereas ^{64}Ni+^{208}Pb does not appear to have a TDHF fusion threshold at all. The addition of neutrons in the projectile here has decreased the contact time and brought some hindrance to fusion. With the systems $^{40-54}$Ca+^{116}Sn, the similar result was seen in that the addition of neutrons actually unexpectedly increased the TDHF fusion threshold (relative to the static barrier).

The systems from ^{50}Ti,^{52}Cr,^{54}Fe,^{56}Ni,^{58}Zn,^{64}Ni+^{208}Pb and ^{54}Cr+^{208}Pb (the "main study") that reseparated in this chapter were not necessarily quasifission reactions. Quasifission in TDHF was defined by the final total kinetic energy of the system with respect to the mass ratio of the fragments in the exit channel and comparing this to the Viola systematics [81, 221]. If the TKE of the system was within 10% of the Viola systematics then it was deemed a quasifission reaction; if it was in the range 10%-20% above the Viola systematics then it was a deep inelastic collision; and reactions lying outside 20% were deemed as quasielastic scattering. Many of the systems that reseparated were actually deep inelastic collisions rather than quasifission reactions.

In the main study, a noticeable surge of emission of particles were observed at the time of the neck breaking (in systems that reseparated). In the high energies for ^{56}Ni,^{58}Zn,^{64}Ni+^{208}Pb, a surge in emissions was also apparent at the time when the half saturation density neck was seen to appear. The number of emitted particles increased with increasing energy and was mostly neutron emission. Systems that fused emitted particles constantly over 24 zs but the final emitted number of particles was much smaller (less than half) than for the reseparated systems. This means that a dramatic shape change in the nuclear density of the compound system, that is, either at scission or at contact, has noticeable effects on the dynamics of the system.

All transfer that was observed in the reactions happened in the direction to equilibrate the N/Z factors between the reactant nuclei. For the main study, an attempt at this

equilibration happens very quickly (within 2 zs) and can even be achieved in what was defined as a quasielastic collision rather than deep inelastic collisions or quasifission reactions that had long contact times. Because of this short timescale for N/Z equilibration, it was not an energy nor angular momentum dependent process.

To compare systems in the main study to systems far from magic numbers, three auxiliary systems ^{52,54}Cr+^{198,196}Pt and ^{34}S+^{232}Th, all which have been measured experimentally, were used. These three systems resulted in quasifission, had longer neck times and much more mass equilibration. Transfer in the direction of N/Z equilibration between reactant nuclei was also apparent for these systems, but the longer neck times in comparison to the main study did not lead to the exit channel fragments having significantly closer N/Z ratios to the compound system.

The aim of the main study was to explore systems that result in quasifission. Most of the time, the systems, energies and angular momentum values that were chosen in the main study did not lead to a quasifission result; many of the reactions ended up fusing or defined as a deep inelastic collision. This in itself was not overly problematic as discussion and conclusions did not vary between a particular system that was a deep inelasic collision for one energy and quasifission for another. However, to improve the main study, calculating collisions with higher angular momentum values (for example $\ell = 20\hbar$ or above) may have led to more reactions that properly qualify as TDHF quasifission as seen in the auxiliary study, instead of fusion. Fusion is a more likely outcome for low angular momentum values. Increasing the angular momentum would also have simulated a more realistic situation in terms of angular coverage accessible with experimental setups such as the CUBE detector [83].

Alongside higher angular momentum, selecting a chain of systems with fewer magic numbers or with at least more variation also would have been beneficial to examine the role of magicity in detail. When there are already three magic numbers for the most part in the system, the effects of additional magic numbers are somewhat diluted. Quasifission, or reseparation in general, may have been more apparent at above barrier energies in TDHF for systems with less magicity. Another key factor of the main study to improve is the energy range, focussing on above barrier energies between $1.0V_B$ and $1.1V_B$ would have been sufficient.

Other specific future work was mentioned in relevant sections in this chapter, in particular there is capacity for more investigation into the emission of particles in reactions. This would be worthwhile in reactions leading to SHE formation since deexcitation of compound nuclei is through neutron emission. Emission during a reaction may also may

affect the probability of survival of the CN, and hence the probability of fast quasifission in heavy-ion reactions. Sourcing where in the system emitted particles emerge from would also be interesting. For example, in the ^{58}Zn+^{208}Pb reactions, the observed emitted protons would be expected to come from the ^{58}Zn-like fragment. However, for systems involving a projectile and target that have similar initial N/Z ratios or that are well bound in both protons and neutrons, it would not be so obvious and it may be that the neck is the source of emissions in either case since a surge in emissions were seen after its break in almost every case in the main study. Being able to check this could also shed light on the neck dynamics. This leads to further study into the dynamics of the neck of a system and their effects on not only emission but also energy dissipation and transfer. Lastly, the removal of emitted particles from counting average numbers of nucleons in a fragment is necessary to improve quantitative characterisation of transfer, and this would be increasingly important for systems that emit large numbers of nucleons.

Conclusion 6

The motivation of this thesis was to better understand the dynamics associated with heavy-ion reactions, as part of the ongoing pursuit of superheavy element (SHE) studies. A comprehensive theoretical understanding of heavy-ion reactions can be useful for experimental programs aimed at synthesising SHEs from hot fusion reactions [137, 139], serving as a predictive tool into suitable projectile and target combinations amongst other things. The approach to studying this topic was self-consistent mean field theory (Hartree–Fock (HF) theory). The reasons and specifics for studying nuclear systems with HF and time-dependent HF (TDHF) theory were discussed in Chapter 2. In short, because of the nature of nuclear systems being a many body problem with a nucleon-nucleon interaction that is not well known, HF methods based on phenomenological energy density functionals are able to address both of these issues, being a suitable candidate for studying problems in nuclear physics.

Understanding the dynamics present in nuclear systems and their significance in heavy-ion reactions was the goal of this work. Application of the (TD)HF theory for this work was done in stages, separated by the chapters appearing in this thesis. Each chapter brought with it more complex dynamics than the previous, with the systems and reaction types that were presented therein. The applications started with vibrational modes, then moved to to fusion reactions and finally quasifission reactions. As TDHF incorporates at once all the dynamics at mean field level in a single calculation, this increase of complexity in stages allowed us to progressively study the different resulting dynamical effects characteristic to reaction types.

6.1 What we learnt

First of all, the (TD)HF method proved indispensable in understanding different structure and dynamics in a range of nuclear systems. For nuclear structure, the access to single particle states led to more detailed understanding of vibrational modes and also neutron skins. In reactions, the ability to follow a collision with respect to time revealed when certain processes start to occur, for example neck formation, emission and nucleon transfer. This was helpful in examining what dynamics contributes to observables such as the fusion barrier or contact time between two nuclei. A microscopic approach to reaction studies uncovers many physical phenomena and from its use in the present work we

have also encountered drawbacks from the TDHF approach in our understanding of the resulting dynamics.

Vibrations

The TDHF method in the small amplitude limit (corresponding to the random phase approximation method) was first applied to a systematic study of vibrational modes in Chapter 3, in particular to the low-lying octupole and quadrupole vibrations. The focus of this study was on the isotopes $^{40-54}$Ca. The setup of the calculations meant that the only dynamics present were the one phonon vibrations of one multipole moment of one nucleus in a single calculation. This makes a close study of the nature of specific vibrational modes in different nuclei possible.

The objective of this chapter within the scope of the thesis was twofold: to check that TDHF reproduces experimental data of vibrational modes (such as excitation energy and deformation parameter) reasonably for stable isotopes, then predicting results for exotic nuclei with neutron excess. The effects of adding neutrons were seen to systematically change vibrational spectra. The collective nature of low-lying octupole vibrational states was observed with TDHF. Low-lying quadrupole vibrations were also present in TDHF. However, the observed quadrupole modes are associated to 2_1^+ states in doubly magic nuclei only. For mid shell nuclei, a dynamical or perhaps even beyond mean field treatment of pairing is needed to reproduce and study the known collectivity of low-lying quadrupole vibrations in many even-even nuclei.

Near barrier collisions

The HF and TDHF method was next applied to reactions, largely focussing on $^{40-54}$Ca+^{116}Sn systems near the fusion barrier energy. The calculations presented in Chapter 4 were split into reactions without dynamics (with the frozen HF method) and then TDHF reactions with dynamics. The resulting fusion barriers from the static and dynamic calculations were compared with the goal of dismantling the different dynamical effects present in fusion reactions.

Dynamic reactions introduce couplings that include the vibrational modes that were studied in Chapter 3. In comparing the fusion barriers between static and dynamic calculations, a major result was that the inclusion of dynamics and neutron excess did not always decrease the fusion barrier as would be expected from calculations using other phenomenological models. This has direct implications to heavy-ion fusion or synthesis of SHEs.

For systems involving stable nuclei where the fusion barrier energy did decrease with the inclusion of dynamics, the vibrational couplings were the main contributor to this decrease. For the systems with the most neutron rich projectiles, transfer channels play a significant role and possibly contributed to the observed increase in the dynamical fusion barrier. There is a lot of scope to take transfer studies further within TDHF to better interpret its role in near barrier reactions as it is not fully understood.

Above barrier heavy-ion collisions

Continuing the application of TDHF to reactions, Chapter 5 was a study of reactions of yet heavier systems focussing on ^{48}Ca,^{50}Ti,^{52}Cr,^{54}Fe,^{56}Ni, ^{64}Ni,^{58}Zn+^{208}Pb and ^{54}Cr+^{204}Pb at above (static HF) barrier energies. The dynamics from these reactions that were studied included mass transfer and nucleon emission. As well as understanding these processes, investigating the role of magic numbers in initial projectile and target combinations was also a goal of this chapter.

Heavy systems, unlike those studied in Chapter 4, do not always lead to fusion at increasing energies. Systems that effectively did not have a fusion barrier showed that N/Z equilibration was more desirable than the preservation of initial magic numbers after reseparating. Conversely, systems starting with no magic numbers showed outgoing fragments that were near shell closure. The amount of mass transfer increases with increasing contact time for systems that reseparate. However, the final N/Z ratios in the outgoing fragments did not show to be energy or contact time dependent.

In many cases, TDHF predicted fusion for the above listed systems including those that are experimentally known to not fuse at and above barrier energies. Following from this, magic numbers in the entrance channel were not found to have a large influence in the success of fusion in systems with significant initial N/Z asymmetry. Choosing systems with fewer initial magic numbers may have resulted in a larger sensitivity to an addition or reduction of magic numbers to the outcome of the reaction. The setup of the study in this chapter did not lead to the observation of many reactions that qualified as quasifission nor a real test of the significance of magic numbers. Future studies in quasifission dynamics around this mass and energy region can now be refined to better choice of systems, energies and angular momenta used in calculations to test these ideas.

6.2 Applications to SHE research

The accumulation of systems studied in Chapters 4 and 5 has brought about some interesting results in low energy ($E_{\rm cm} = 0.999V_B - 1.3V_B$, where V_B is the static HF fusion barrier) heavy-ion collisions. The two major factors that were explored in projectile and target combinations were neutron excess in the projectile (and subsequently, its N/Z ratio) and also the number of magic numbers in the system.

Neutron excess in projectile was not found to lead to an expected lowering of the fusion barrier as per phenomenological model predictions. This happened for $^{40-54}$Ca+^{116}Sn systems where the ^{52,54}Ca projectiles led to a higher dynamic fusion barrier. It was also apparent in ^{56,64}Ni+^{208}Pb systems, which are reminiscent of cold fusion type reactions for SHE formation, where fusion was not achieved at all for the ^{64}Ni projectile at above barrier energies. The system ^{64}Ni+^{238}U, that leads to the SHE $Z = 120$, has been studied experimentally [40] and with TDHF [172]. If the next shell closure is at $N = 172$ as predicted by self-consistent field theories, and compound nuclei from hot fusion reactions deexcite by $3n$ or $4n$, then systematic studies with ^{58,60}Ni beams that have fewer neutrons may also be useful.

Another factor playing a role in heavy-ion collisions is magicity in the projectile or target. Magic proton numbers in Chapter 4 were constant although its role in collisions was not fully tested in application to SHE formation as the Ca+Sn systems are too light. The proton magicity for these systems served as a basis for studying the effects of adding more neutrons into the system. The role of magic numbers in heavy-ion collisions was explored in more depth in Chapter 5. In general, systems with a Pb target usually had a total of 3 or 4 magic numbers and the main observation was that fusion was quite successful in the systems with light projectiles ranging from ^{48}Ca to ^{56}Ni (along an $N = 28$ chain). Magic numbers could be attributed to the fusion outcomes although as mentioned, the role of magicity may have been washed out due to the presence of too many magic numbers. Calculations of hot fusion reactions with Ni+^{238}U could extend to the exotic doubly magic ^{78}Ni to further explore effects from both magic numbers and neutron excess.

6.3 Future perspectives

Specific points of interest for future work are discussed at the end of every chapter in this thesis, relevant to the material presented in each chapter. Here, a general future direction of this project will be discussed instead. Studying even heavier systems than

those presented in this thesis is a logical next step in order to learn more about dynamics associated with heavy-ion collision studies possibly leading to SHE formation. Specific reactions to study theoretically could include (in order of heaviness):

- Very neutron rich projectiles ranging from for example ^{56}Ca to ^{80}Zn colliding with a stable targets ^{204,208}Pb as a direct extension to systems studied in Chapter 5. It may confirm the consistency of neutron excess not necessarily leading to fusion. If that is the case, quasifission reactions can be further studied.

- The systems $^{58,60,70-78}$Ni+^{238}U, which can reach the next SHE $Z = 120$ encompassing also the next predicted neutron magic numbers $N = 172, 184$, in order understand more about neutron excess and magicity in hot fusion type reactions.

- Stable Pb or Bi projectiles on actinide targets ^{238}U, ^{244}Pu, ^{248}Cm, and ^{252}Cf. This could continue to explore the role of magicity of projectiles in extreme heavy-ion reaction situations for which the reactants are not near the neutron dripline and have more similar initial N/Z ratios.

- Switching the Pb and Bi projectiles from above to another actinide, providing superfluidity in both colliding nuclei and would also be in touch with recent actinide collision studies [4, 69, 98].

- Studying fission and quasifission modes of SHEs $Z \geq 104$, which is necessary to understand competing processes to compound nucleus formation or decay of superheavy nuclei.

As far as choosing a theoretical approach for studying these heavy-ion reactions, mean field methods are definitely still worthwhile at this stage even though there are important physical phenomena in reactions, relevant to exotic nuclei, that are not well described by the TDHF approach. Its biggest weakness is the inability to account for quantum tunnelling due to its deterministic nature. Other dynamics that are either neglected or underestimated include pair and alpha clustering which can effect transfer and breakup dynamics and also fluctuation of observables [177].

Updated extensions to the HF setup used in this thesis and suggested future work would be beneficial, especially for collisions involving actinides. The first modification would be to use time-dependent BCS pairing with TDHF [55, 164] as a compromise to the heavy computation times needed from using the TDHF-Bogoliubov method.

In addition, the semi-classical nature of TDHF severely limits the studies of transfer channels and their effects on reactions. This includes studies on multinucleon transfer

or quasifission reactions. Because of the deterministic nature of TDHF, only an average transfer channel (the average trajectory of all possible transfer channels) will ever be an output of a TDHF calculation. Studying various transfer channels in the time-dependent microscopic approach can be achieved by using the generator coordinate method [71, 79] and would improve understanding of hindrance of fusion due to transfer.

For TDHF reactions leading to a highly excited compound nucleus, its deexcitation over longer time scales cannot be described properly within the current approach where two-body collisions are neglected. These collisions are significant in such a process, and are accounted for in the Extended TDHF method [232].

In a slightly different direction, testing more fundamental approaches to the nucleon-nucleon effective interaction for example the quark meson coupling parametrisation of the Skyrme energy density functional [72, 115] should in principle provide a better description of nuclear structure, in particular exotic nuclei, and consequently its effects on reactions.

Variational calculus problem

A

The basic, one dimensional varational calculus problem is finding functions $y : V \to \mathbb{F}$ for a vector space V that are extrema for a functional $J : X \to \mathbb{R}$ of the form

$$J[y] = \int_{x_0}^{x_1} f(x, y(x), y'(x))dx, \tag{A.1}$$

where $y \in X$ and y' being the derivative of y with respect to x. As $J[y] \in \mathbb{R}$ the integral must be definite, and space the $X \subseteq C^k[V]$ is a function space with $k \geq 1$. Problems of type (A.1) can be extended to more general cases where $f = f(x, y, y', y'', ..., y^{(m)})$ for finite m in which X must be at least C^m, also for functions y of more than one independent or dependent variables in an n-dimensional vector space V.

To find extrema of J in $S \subseteq X$, as for usual functions of one or several variables, a derivative (if it exists) of J will be zero. Or, if $y \in S$ is a stationary point of J then the derivative of J with respect to y is zero. Derivatives of J can be found by taking a function $y \in S, \tilde{y} = y + \varepsilon\eta$ where $\varepsilon > 0$ is small (and real) and $\eta \in X$ such that $\|\tilde{y} - y\| < \varepsilon$ using the norm in X (so it should be a normed vector space too). Evaluating $J[\tilde{y}] - J[y]$, it can be shown that

$$J[\tilde{y}] - J[y] = \varepsilon \int_{x_0}^{x_1} \eta \left[\frac{\partial f}{\partial y} - \frac{d}{dx}\left(\frac{\partial f}{\partial y'}\right)\right] dx + O(\varepsilon^2). \tag{A.2}$$

If only considering extrema (saddle points of J are not of interest), then if y is a local maximum then $J[\tilde{y}] - J[y] \leq 0$ and if it is a local minimum then $J[\tilde{y}] - J[y] \geq 0$. The integral term in (A.2) is called the first variation of J and is denoted by $\delta J(\eta, y)$. The sign of $J[\tilde{y}] - J[y]$ depends on the sign of $\delta J(\eta, y)$. It also must not change for any $\tilde{y}$ whether it is a minimum or maximum, requiring $\delta J = 0$. This is where the Euler–Lagrange equation is born and the definition of the functional derivative of J with respect to y is

$$\frac{\delta J}{\delta y} := \frac{\partial f}{\partial y} - \frac{d}{dx}\left(\frac{\partial f}{\partial y'}\right) = 0. \tag{A.3}$$

The functional differential is

$$\delta J = \int_{x_0}^{x_1} \frac{\delta J[y]}{\delta y(x)} \delta y(x) dx, \tag{A.4}$$

with $\delta y = \varepsilon\eta$. If J depends on a function $K = K[y]$ which is also a functional of y, the

functional derivative of J with respect to y can be found by using the chain rule

$$\frac{\delta J[y]}{\delta y(x)} = \int \frac{\delta J[K[y]]}{\delta K[y](x')} \frac{\delta K[y](x')}{\delta y(x)} dx'. \tag{A.5}$$

For functionals or functions (g) that are not of type (A.1), the functional derivative can still be obtained by converting said function into a functional of type (A.1), by writing it as

$$g(u) = L[g] = \int g(v)\delta(u - v)dv, \tag{A.6}$$

for $u, v \in V$ and $L : X \to \mathbb{R}$. The functional derivative of L can now be found with (A.3).

Finally, the problem (A.1) can be extended to include constraints. When (A.1) is subject to the additional constraint

$$I[y] = \int_{x_0}^{x_1} h(x, y(x), y'(x))dx = C,$$

where C is a constant, finding extrema of J now requires

$$\delta(J - \lambda I) = 0, \tag{A.7}$$

where λ is a (constant) Lagrange multiplier.

B Skyrme EDF parametrisation

B.1 General parameters

The relationship between Skyrme parameters $(x_i, t_i, W_0, W_0', \gamma), i = 0, ..., 3$ to the $(b_j, B_j), j = 0, ..., 7$ parameters is given by the following equations [24]:

$$
\begin{aligned}
b_0 &= \frac{t_0}{2}\left(1 + \frac{x_0}{2}\right), & B_0 &= \frac{t_0}{2}\left(\frac{1}{2} + x_0\right),\\
b_1 &= \frac{1}{4}\left[t_1\left(1 + \frac{x_1}{2}\right) + t_2\left(1 + \frac{x_2}{2}\right)\right], & B_1 &= \frac{1}{4}\left[t_1\left(\frac{1}{2} + x_1\right) - t_2\left(\frac{1}{2} + x_2\right)\right],\\
b_2 &= \frac{1}{16}\left[3t_1\left(1 + \frac{x_1}{2}\right) - t_2\left(1 + \frac{x_2}{2}\right)\right], & B_2 &= \frac{1}{16}\left[3t_1\left(\frac{1}{2} + x_1\right) - t_2\left(\frac{1}{2} + x_2\right)\right],\\
b_3 &= \frac{t_3}{12}\left(1 + \frac{x_3}{2}\right), & B_3 &= \frac{t_3}{12}\left(\frac{1}{2} + x_3\right),\\
b_4 &= \frac{W_0}{2}, & B_4 &= \frac{W_0'}{2},\\
b_5 &= \frac{1}{8}(t_1 x_1 + t_2 x_2), & B_5 &= \frac{1}{8}(t_1 - t_2),\\
b_6 &= \frac{t_0 x_0}{4}, & B_6 &= \frac{t_0}{4},\\
b_7 &= \frac{t_3 x_3}{24}, & B_7 &= \frac{t_3}{24}.
\end{aligned}
$$

In the present HF calculations, the time odd terms are not used and in the TDHF calculations, the condition $b_5 = B_5 = 0$ is imposed. In addition, the SLy4d parametrisation imposes $b_4 = B_4$.

The relationships between the functional derivatives used in deriving the single particle Hamiltonian and the (b_i, B_i) parameters are given by:

$$
\begin{aligned}
\frac{\delta E}{\delta \tau_q} &= \frac{\hbar^2}{2m} + b_1\rho - B_1\rho_q,\\
\frac{\delta E}{\delta \rho_q} &= 2b_0\rho + b_1\tau - 2b_2\nabla\rho + b_3(\gamma+2)\rho^{\gamma+1} - 2B_0\rho_q + B_1\tau_q - 2B_2\Delta\rho_q\\
&\quad - B_3\left(\gamma\rho^{\gamma-1}\sum_q \rho_q^2 + 2\rho_q\rho^\gamma\right) + b_7\gamma\rho^{\gamma-1} - B_7\sum_q \gamma\rho^{\gamma-1}\mathbf{S}_q^2\\
&\quad + \left[\frac{1}{2}V_C - e^2\left(\frac{3\rho_p}{\pi}\right)^{\frac{1}{3}}\right]\delta_{qp},
\end{aligned}
$$

$$\frac{\delta E}{\delta \mathbf{J}_q} = -b_4 \nabla \rho - 2b_5 \mathbf{J} - B_4 \nabla \rho_q - 2B_5 \mathbf{J}_q,$$
$$\frac{\delta E}{\delta \mathbf{j}_q} = -2b_1 \mathbf{j} - 2B_1 \mathbf{j}_q + b_4 \nabla \times \mathbf{S} + B_4 \nabla \times \mathbf{S}_q,$$
$$\frac{\delta E}{\delta \mathbf{S}_q} = 2b_6 \mathbf{S} + 2b_7 \rho^\gamma \mathbf{S} - 2B_6 \mathbf{S} - 2B_7 \rho^\gamma \mathbf{S}_q + b_4 \nabla \times \mathbf{j} + B_4 \nabla \times \mathbf{j}_q.$$

B.2 The asym28 and asym36 parametrisations

Two extra Skyrme parametrisations labelled as asym28 and asym36 were tested in section 2.5.3 for frozen HF barrier energies for the systems $^{40-54}$Ca+^{116}Sn. These two parametrisations were created using the same fitting procedure [179] as for the SLy4d [101] parametrisation but the symmetry energy is instead set to 28 MeV and 36 MeV respectively. The $(x_i, t_i, W_0, W_0', \gamma), i = 0, ..., 3$ values of each parametrisation are listed below in Tab. B.1.

	asym28	asym36
x_0	0.9487	0.9043
x_1	-0.9742	-0.4225
x_2	-1.0000	-1.0000
x_3	1.7311	1.3756
t_0	-2384.4444	-2496.6853
t_1	431.6545	427.8275
t_2	-176.9374	-417.7702
t_3	12716.1311	13898.8659
W_0	117.8201	119.5835
γ	0.1667	0.1667

Tab. B.1.: Parameter values for asym28 and asym36. Similarly to the Sly4d parametrisation, $W_0 = W_0'$.

C Vibrational spectra for Sn isotopes

The strength functions for the single phonon octupole and quadrupole moments of $^{124-136}$Sn isotopes are presented in Figs. C.1 and C.2 respectively. The spectra were calculated from taking a scaled imaginary Fourier transformation of the multipole moment functions of each type. Multipole moment functions were produced from calculations using linear response theory within the TDHF framework using with the SLy4d [101] parametrisation of the Skyrme interaction, as described in section 3.3.

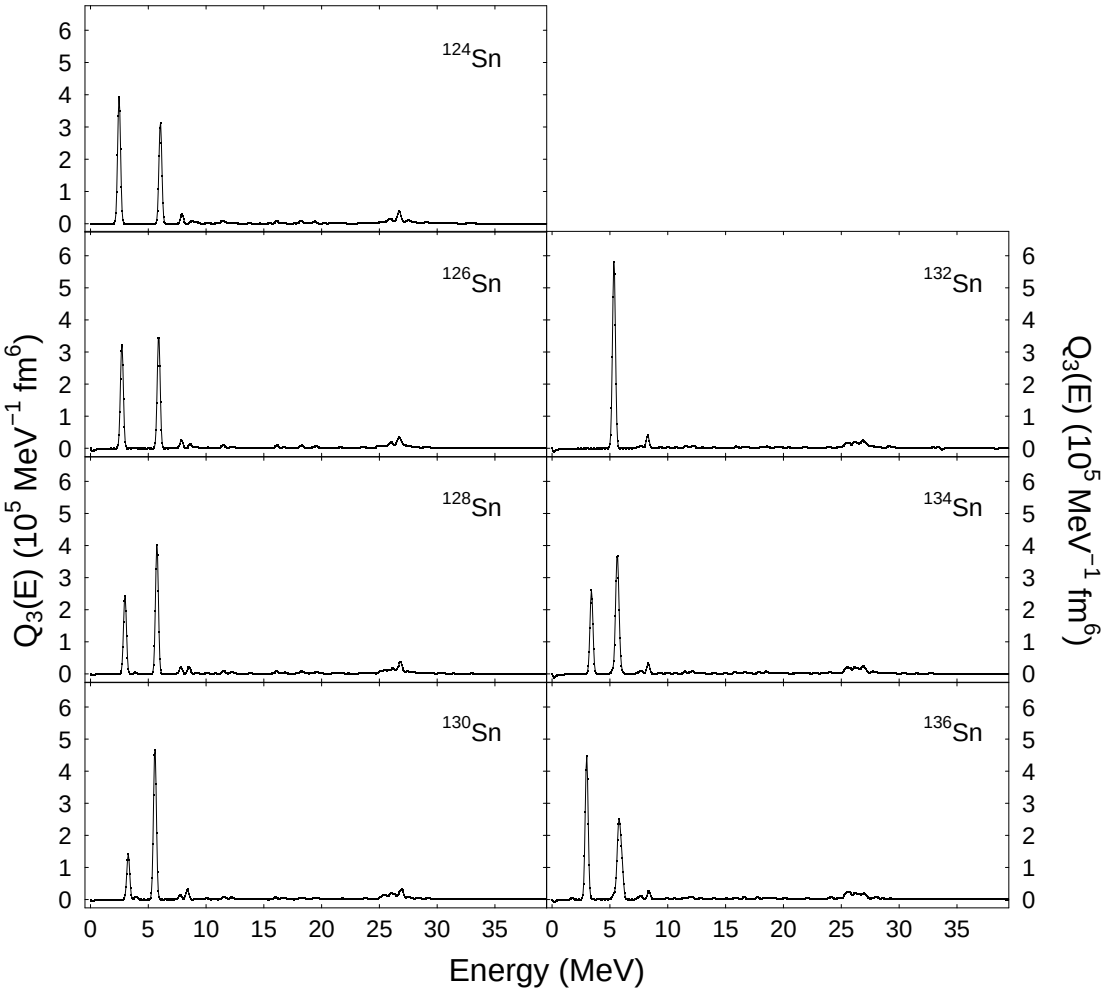

Fig. C.1.: Octupole strength functions for $^{124-136}$Sn.

In the octupole vibrations spectra, the strong peak appearing at approximately 2.5–3 MeV in the $^{124-130}$Sn isotopes that decreases in intensity is associated with the neutrons filling the $1h_{11/2}$ shell. This shell is completely filled in ^{132}Sn which is why there is no

longer this low-lying peak for that isotope, as neutron excitations would have to cross a magic shell gap. The peak reappears for ^{134,136}Sn as neutrons are filling the next $2f_{7/2}$ shell which can be excited to other single particle levels. The first intensive peak seen for all $^{124-136}$Sn isotopes is associated with their respective 3^-_1 states. The spread of small peaks between 25–28 MeV is associated with the high energy octupole resonance. In the

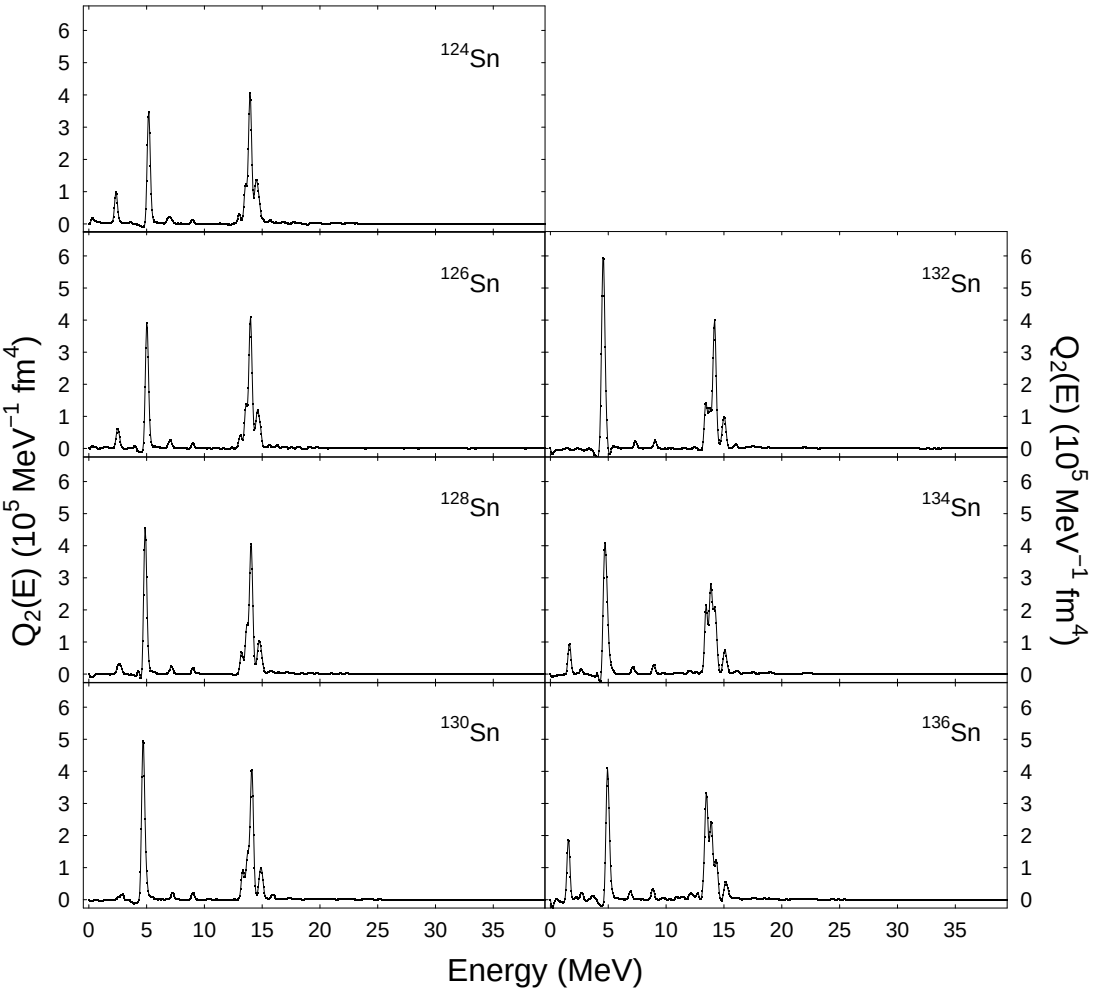

Fig. C.2.: Quadrupole strength functions for $^{124-136}$Sn.

quadrupole excitations spectra, there are strong peaks at approximately 5 MeV and 14 MeV, the latter which is associated with the giant quadrupole resonance (GQR). The strong 5 MeV peak is associated with the 2^+_1 for the doubly magic ^{132}Sn, but experimental low-lying 2^+_1 states for $^{124-136}$Sn are expected to have excitation energies at less than 2 MeV. There is a small peak between 2–3 MeV for all of the isotopes except ^{132}Sn, however due to the relative low strength of the peak (as compared with the GQR) it is not likely to be collective.

Akyüz–Winther ion-ion potential

D

As in Ref. [31], the nuclear part of the Akyüz–Winther ion-ion potential uses an exponential form

$$V_{\mathrm{AW}}(r) = -S_0 \bar{R}_{12} \exp\left(\frac{R-r}{a}\right).$$

The parameters are given by

$$\begin{aligned}
S_0 &= 65.4 \text{ MeV fm}^{-1}, \\
R_i &= 1.20 A_i^{\frac{1}{3}} - 0.35 \text{ fm}, \\
\bar{R}_{12} &= \frac{R_1 R_2}{R_1 + R_2} \text{ fm}, \\
R &= R_1 + R_2 \text{ fm}, \\
\frac{1}{a} &= 1.16 \left(1 + 0.48 \left(A_1^{-\frac{1}{3}} + A_2^{-\frac{1}{3}}\right)\right) \text{ fm}^{-1}.
\end{aligned}$$

The Akyüz–Winther parameter fits to the Woods–Saxon potential

$$V_{\mathrm{WS}} = \frac{-V_0}{1 + \exp\left[(r - R_0)/a\right]},$$

are given by

$$\begin{aligned}
V_0 &= 16\pi\gamma \bar{R}_{12} a \text{ MeV}, \\
\gamma &= 0.95 \left[1 - 1.8 \left(\frac{N_1 - Z_1}{A_1}\right)\left(\frac{N_2 - Z_2}{A_2}\right)\right] \text{ MeV fm}^{-2}, \\
R_0 &= R_1 + R_2 + 0.29 \text{ fm}, \\
a &= 0.63 \text{ fm}.
\end{aligned}$$

Extra HF barriers

E

E.1 $^{31\text{-}46}XX_{20}+^{208}Pb$

The difference between frozen HF barriers (circles) and the Akyüz–Winther barriers (crosses) are presented in Fig. E.1 for the systems $^{31-46}XX_{20}+^{208}Pb$. The phenomenological Bass [9] (triangles) and São Paolo [39] (squares) potentials are shown as a comparison.

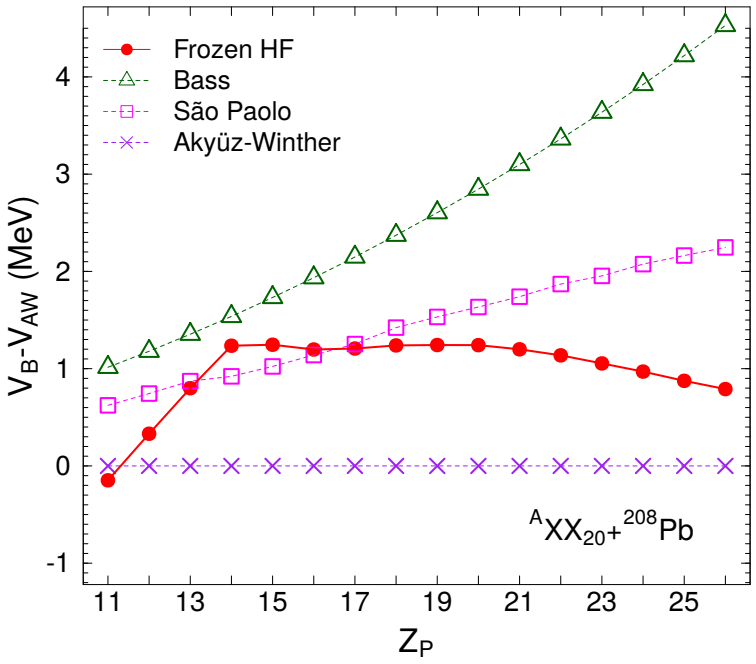

Fig. E.1.: Difference of barrier energies with AW barrier energies (crosses) for systems $^{31-46}XX_{20}+^{208}Pb$. The frozen HF (circles), Bass (triangles) and São Paolo (squares) potentials are included. HF calculations were done with the SLy4d [101] parametrisation of the Skyrme energy density functional.

The three phenomenological potentials predict almost linear increase of the barrier with increasing projectile charge. The HF barriers change gradient after $Z_p = 14$, corresponding to the $^{34}Si+^{208}Pb$ reaction. This is similar to what happens with an isotope chain (see section 4.2) and in this case, may be due to the protons beginning to fill the $2s_{1/2}$ and $1d_{3/2}$ shells. Alternatively, the light projectiles with $Z = 11 - 14$ are very asymmetric in N and Z and the lack of protons may leave these isotones weakly bound and with a proportionally larger radius than the projectiles with $Z > 14$ resulting in a lower fusion barrier.

E.2 $^{44\text{-}58}$Ca+^{208}Pb

The barrier energies for the systems $^{44-58}$Ca+^{208}Pb are presented in Fig. E.2 from both frozen HF (red circles) and TDHF (black diamonds) calculations. As a comparison, the Bass (triangles), Akyüz–Winther (crosses) and São Paolo (open diamonds) phenomenological potentials are also included. Similarly to the Ca+Sn systems (Chapter 4), there are kinks in the frozen HF barriers at ^{48,54}Ca. Only even-even calcium projectiles were used in TDHF calculations to reduce computational time.

The dynamic TDHF threshold is vastly different from the frozen HF barriers. For projectiles up to ^{48}Ca, the addition of dynamics decreases the barrier but for heavier projectiles the barrier is increased substantially, by more than 5 MeV in the heaviest systems. This may be due to the onset of quasifission processes hindering fusion at near (frozen) barrier energies. It may also be from proton pickup channels as was found for ^{52,54}Ca+^{116}Sn, possibly contributing to the increase of their fusion barriers.

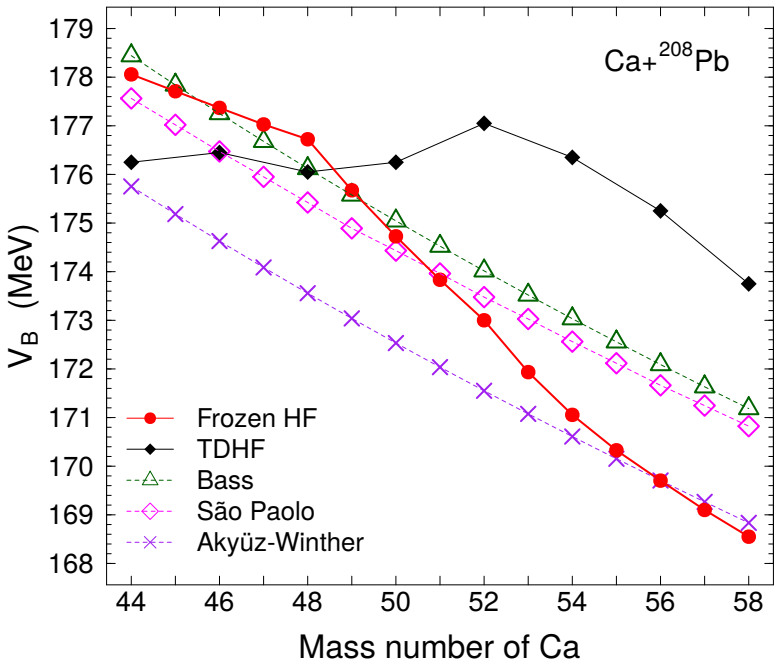

Fig. E.2.: Barrier energies for $^{44-58}$Ca+^{208}Pb with frozen HF (circles) and TDHF (diamonds) methods. Included for comparison are the AW potential (crosses), Bass (triangles) and São Paolo (open diamonds) barriers. HF calculations were done with the SLy4d parametrisation.

Barrier distributions with CCFULL

F

Barrier distributions for $^{40-54}$Ca+^{116}Sn were calculated using the CCFULL code and are presented in Fig. F.1. The barrier distribution plot for the system ^{44}Ca+^{116}Sn is enlarged in Chapter 4, Fig. 4.14.

The barrier distributions were first calculated with no couplings (solid red line), then with the $^{40-54}$Ca 3^-_1 state (blue dot dashed), $^{40-54}$Ca and ^{116}Sn 3^-_1 states (pink long dashed) and $^{40-54}$Ca $3^-_1, 2^+_{\text{low}}$ states with the ^{116}Sn 3^-_1 state (green dotted). The excitation energy and deformation parameter inputs for these vibrational states were taken from TDHF vibrational calculations, listed in Chapter 3 Tabs. 3.1 and 3.2. Additionally, for the projectiles where the data exists, the experimental 2^+_1 state (orange dashed) was also included into the CCFULL calculations as a comparison. This low-lying collective state changes the shape of the barrier distribution which is most apparent mid-shell projectiles ($^{42-46}$Ca), compared with the 3^-_1 state of the projectile which essentially renormalises the peak [74].

The resulting barriers for the $^{40-54}$Ca+^{116}Sn systems can be seen in Chapter 4, Fig. 4.15. Not including the experimental 2^+_1 state of calcium, all vibrational modes that were included into the CCFULL calculations reduced the static barrier (centroid of the solid red line).

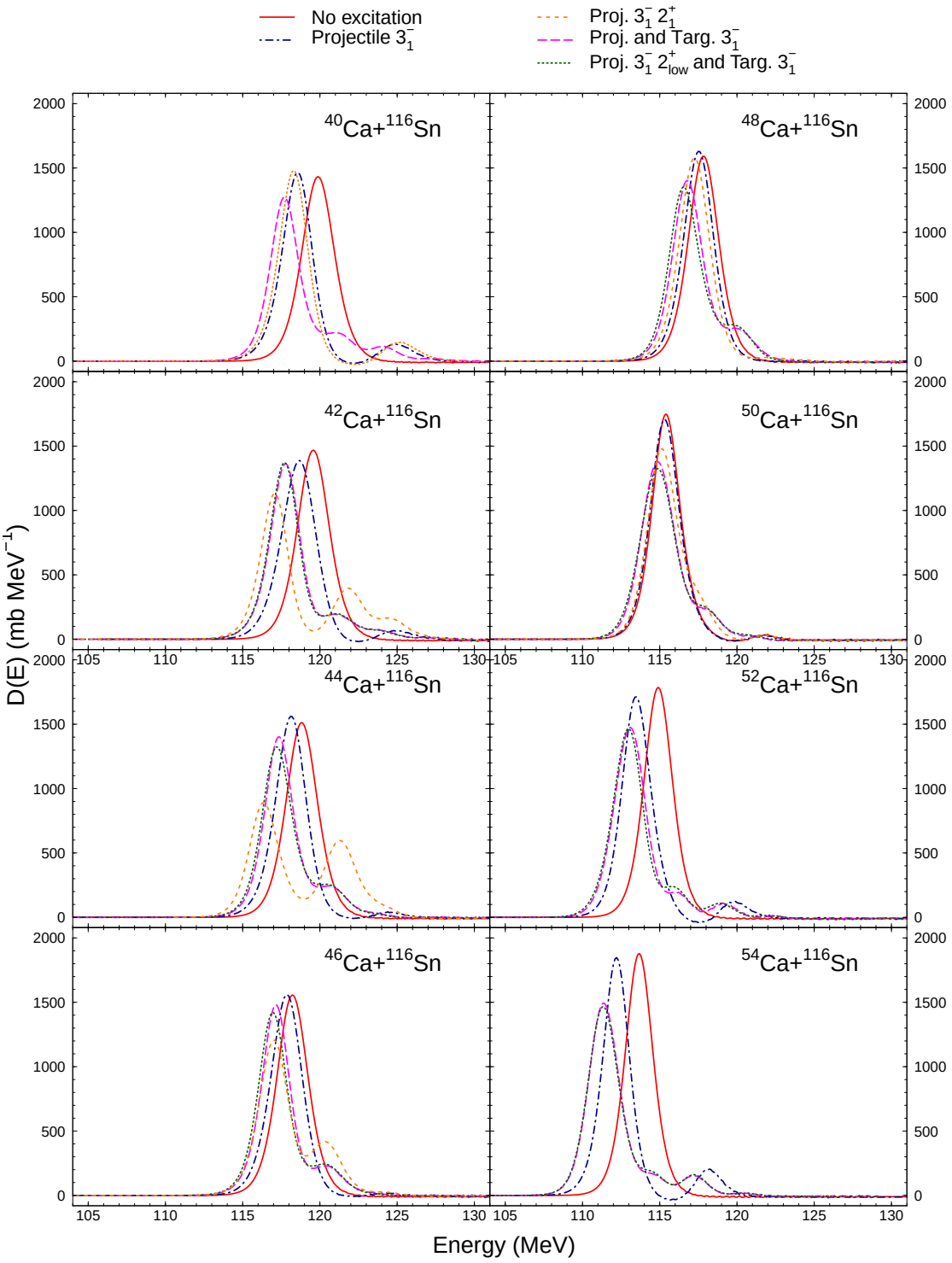

Fig. F.1.: Barrier distributions for several target and projectile vibrational excitation combinations for $^{40-54}$Ca+^{116}Sn. Calculations made with CCFULL using HF inputs.

Particle emission G

Particle emission over time is presented in Figs. G.1, G.2, G.3 and G.4 for various systems calculated with TDHF that reseparate at and above frozen HF barrier energies. In Fig. G.1, which is the same as Fig. 5.8 in Chapter 5 but for $\ell = 10\hbar$, similar features occur to the $\ell = 0\hbar$ case in that when the neck breaks, a surge in emission of particles is seen.

For ^{56}Ni+^{208}Pb at $1.3V_B$ (bottom right panel), there is no characteristic surge seen at the break of the neck. This system was close to the edge of the calculation box at scission point. This may result in an inaccurate calculation of emitted particles which could rejoin the compound system quickly if emissions occurred near the edge of the box. For this system, the calculation beyond 18 zs (after the compound system hits the edge of the box with hard boundary conditions) would lead to unphysical results of emissions and total kinetic energy. Results presented within Chapter 5 for this system are taken before this happens.

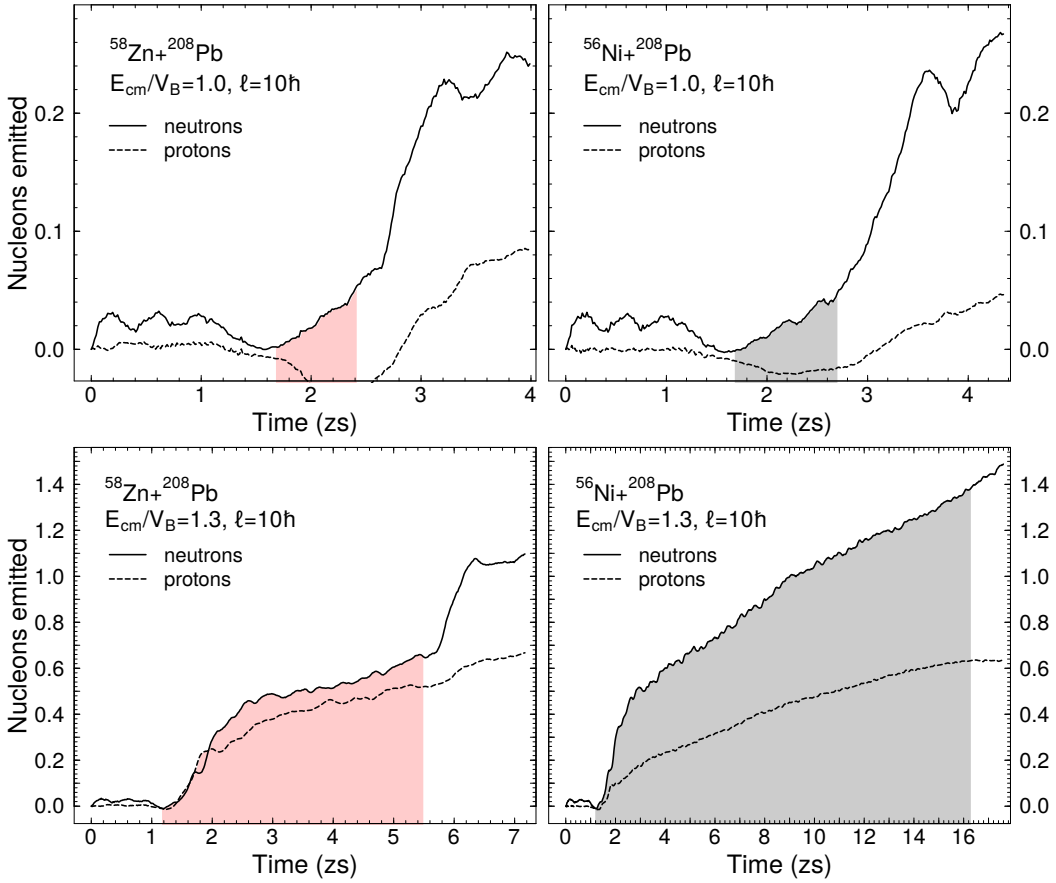

Fig. G.1.: Particle emission versus time for ^{58}Zn+^{208}Pb (left panels) and ^{56}Ni+^{208}Pb (right panels) at $E_{\rm cm} = 1.0V_B, 1.3V_B$ and $\ell = 10\hbar$. The shaded region indicates where the neck at half saturation density occurred.

The emissions for the system ^{58}Zn+^{208}Pb at $E_{\rm cm} = 1.1V_B$ and $1.2V_B$ for $\ell = 0\hbar$ and $10\hbar$ is presented in Fig. G.2. Protons and neutrons are emitted in roughly equal numbers over the reaction time until the break of the neck (end of the shaded region). At and after this point, more neutrons are emitted than protons.

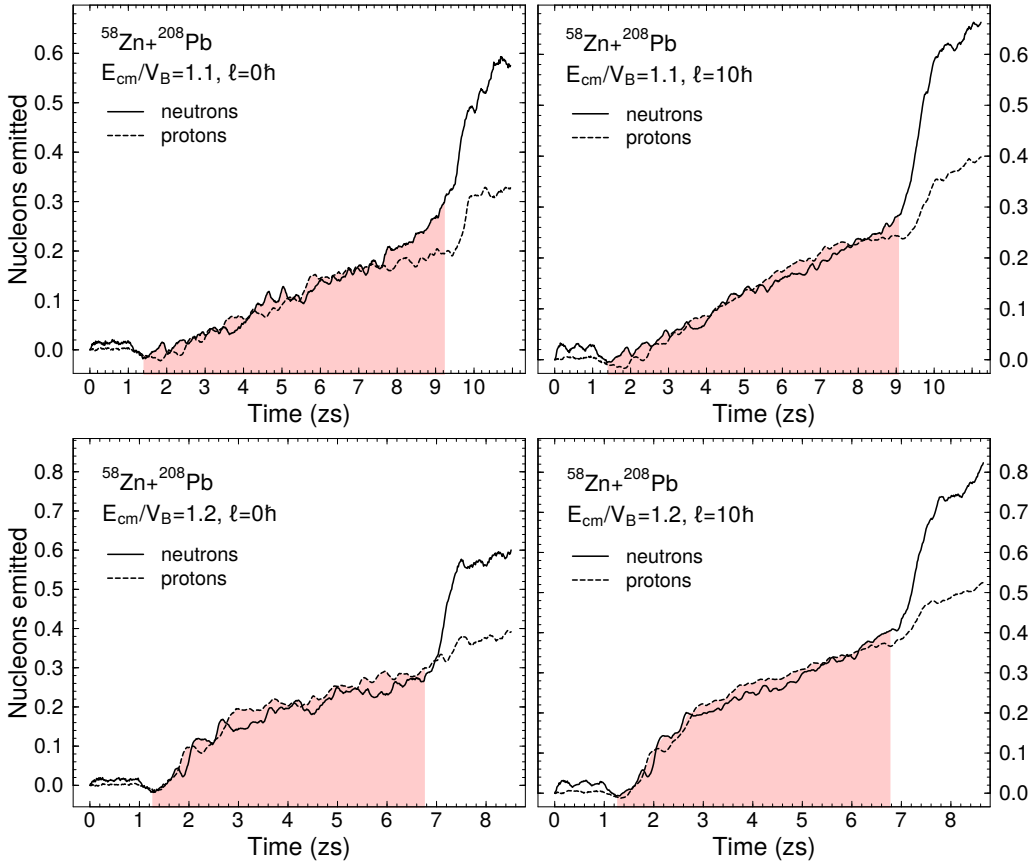

Fig. G.2.: Particle emission versus time for ^{58}Zn+^{208}Pb at $E_{\rm cm} = 1.1V_B$ (top row) and $1.2V_B$ (bottom row) with $\ell = 0\hbar$ (left panels) and $10\hbar$ (right panels). The shaded region indicates where the neck at half saturation density occurred.

The systems ^{64}Ni+^{208}Pb at $E_{\rm cm} = 1.0V_B - 1.3V_B$ are seen in Fig. G.3 for $\ell = 0\hbar$ (left panels) and $\ell = 10\hbar$ (right panels). There are much smaller amounts of proton emission as compared with the ^{56}Ni,^{58}Zn+^{208}Pb systems in Figs. 5.8, G.1 and G.2. This is due to the ^{64}Ni projectile having a higher initial N/Z ratio as compared with the other two projectiles, meaning the protons are more well bound and less susceptible for emission. The surge of neutron emissions is apparent over the entire energy range and at both values of angular momentum (noting the changing scale on the vertical axis).

Finally, emission versus time plots for ^{54}Fe,^{54}Cr,^{52}Cr,^{50}Ti+^{208}Pb are presented in Fig. G.4, all at $E_{\rm cm} = 1.0V_B$ for $\ell = 0\hbar, 10\hbar$. Contact times for these systems are very short (less than 2 zs) resulting in the total emission amount being small compared to the ^{56,64}Ni,^{58}Zn+^{208}Pb systems. Although there is a surge of neutron emission upon the break of the neck, this does not exceed 0.2 neutrons which is rather small.

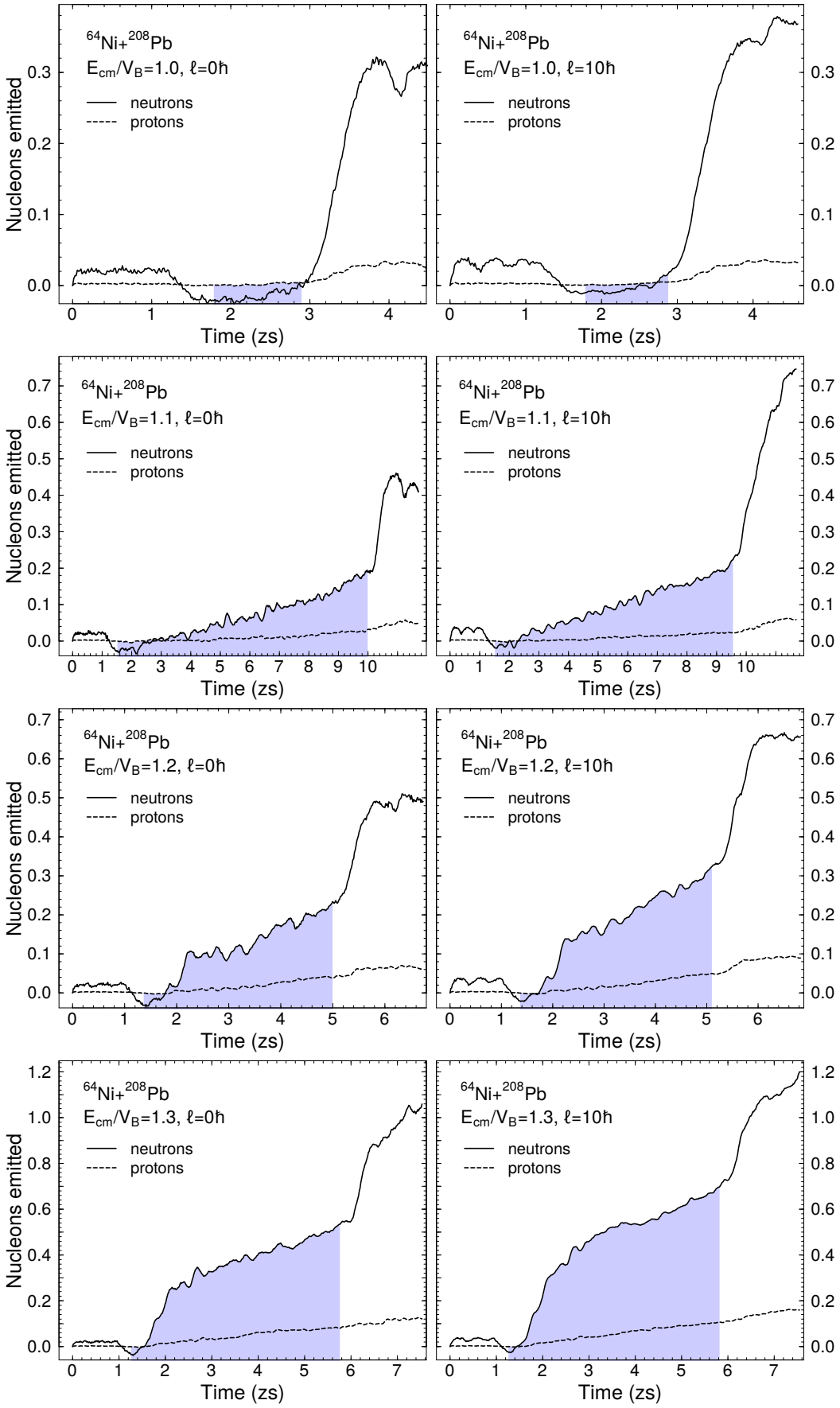

Fig. G.3.: Particle emission versus time for ^{64}Ni+^{208}Pb at $E_{\rm cm} = 1.0V_B - 1.3V_B$ with $\ell = 0\hbar$ (left panels) and $10\hbar$ (right panels). The shaded region indicates where the neck at half saturation density occurred.

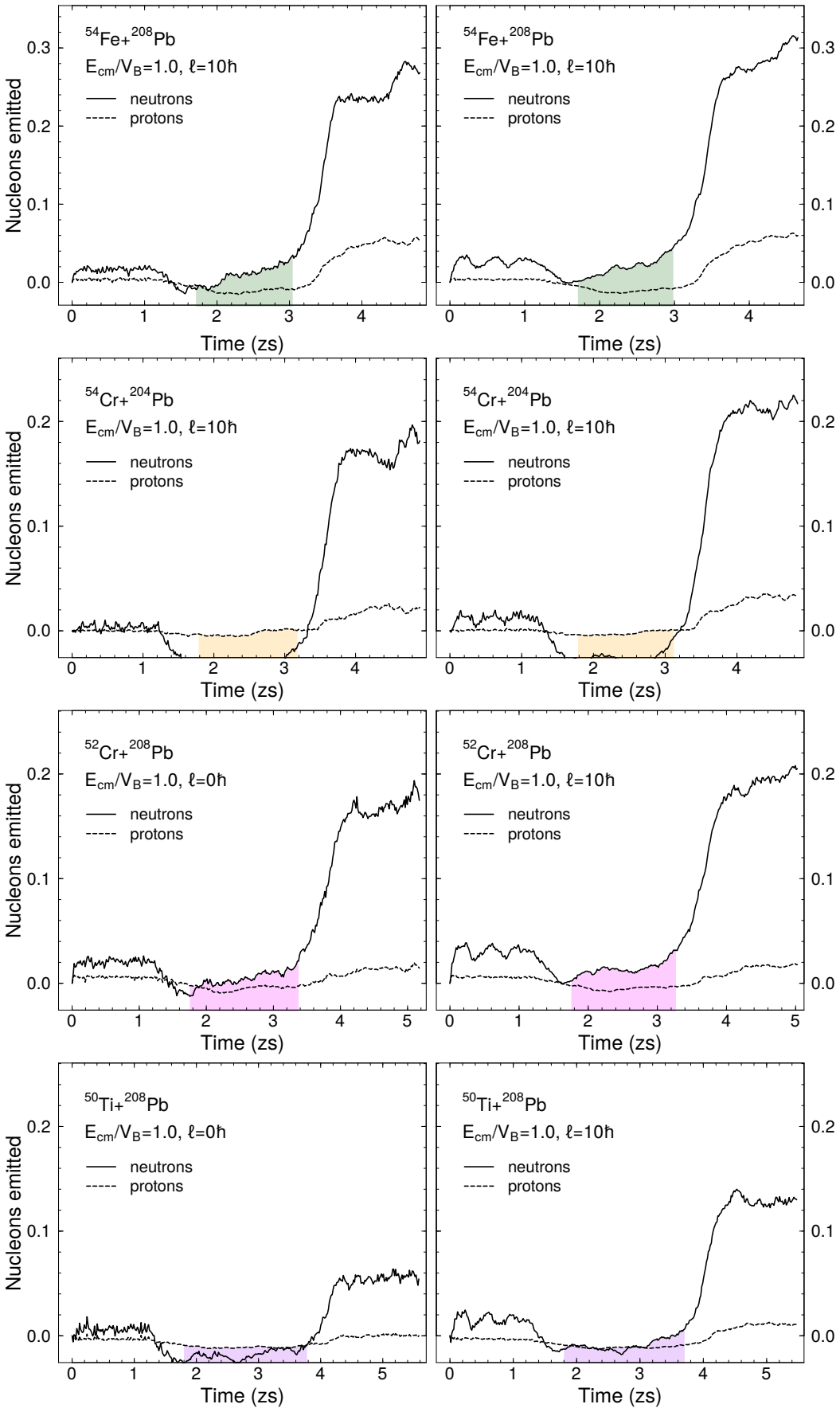

Fig. G.4.: Particle emission versus time for ^{54}Fe,^{54}Cr,^{52}Cr,^{50}Ti+^{208}Pb systems (from top to bottom) at $E_{\rm cm} = 1.0V_B$ and $\ell = 0\hbar, 10\hbar$.

Bibliography

[1] Ait-Tahar, S. and Brink, D.: 1993, *Nuclear Physics A* **560(3)**, 765

[2] Avez, B., Simenel, C., and Chomaz, P.: 2008, *Phys. Rev. C* **78**, 044318

[3] Avez, B. and Simenel, C.: 2013, *Eur. Phys. J. A* **49(6)**, 76

[4] Ayik, S., Yilmaz, B., Yilmaz, O., Umar, A. S., and Turan, G.: 2017, *Phys. Rev. C* **96**, 024611

[5] Ayik, S., Yilmaz, O., Yilmaz, B., Umar, A. S., Gokalp, A., Turan, G., and Lacroix, D.: 2015, *Phys. Rev. C* **91**, 054601

[6] Back, B. B.: 1985, *Phys. Rev. C* **31**, 2104

[7] Back, B. B., Esbensen, H., Jiang, C. L., and Rehm, K. E.: 2014, *Rev. Mod. Phys.* **86**, 317

[8] Bardeen, J., Cooper, L. N., and Schrieffer, J. R.: 1957, *Phys. Rev.* **106**, 162

[9] Bass, R.: 1977, *Phys. Rev. Lett.* **39**, 265

[10] Beckerman, M.: 1988, *Reports on Progress in Physics* **51(8)**, 1047

[11] Beckerman, M., Salomaa, M., Sperduto, A., Enge, H., Ball, J., DiRienzo, A., Gazes, S., Chen, Y., Molitoris, J. D., and Nai-feng, M.: 1980, *Phys. Rev. Lett.* **45**, 1472

[12] Bender, M., Heenen, P.-H., and Reinhard, P.-G.: 2003, *Rev. Mod. Phys.* **75**, 121

[13] Bender, M., Rutz, K., Reinhard, P.-G., Maruhn, J. A., and Greiner, W.: 1999, *Phys. Rev. C* **60**, 034304

[14] Bennaceur, K., Bonche, P., and Meyer, J.: 2003, *Comptes Rendus Physique* **4(4)**, 555

[15] Berriman, A. C., Hinde, D. J., Dasgupta, M., Morton, C. R., Butt, R. D., and Newton, J. O.: 2001, *Nature* **413**, 144–147

[16] Bjørnholm, S. and Świątecki, W.: 1982, *Nuclear Physics A* **391(2)**, 471

[17] Blanc, F. L., Cabaret, L., Cottereau, E., Crawford, J. E., Essabaa, S., Genevey, J., Horn, R., Huber, G., Lassen, J., Lee, J. K. P., Scornet, G. L., Lettry, J., Obert, J., Oms, J., Ouchrif, A., Pinard, J., Ravn, H., Roussière, B., Sauvage, J., and Verney, D.: 2005, *Phys. Rev. C* **72**, 034305

[18] Blatt, J. M. and Weisskopf, V. F.: 1952, *Theoretical Nuclear Physics*, John Wiley and Sons, New York

[19] Błocki, J. and Flocard, H.: 1979, *Physics Letters B* **85(2)**, 163

[20] Błocki, J., Randrup, J., Świątecki, W., and Tsang, C.: 1977, *Annals of Physics* **105(2)**, 427

[21] Bock, R., Chu, Y., Dakowski, M., Gobbi, A., Grosse, E., Olmi, A., Sann, H., Schwalm, D., Lynen, U., Müller, W., Bjørnholm, S., Esbensen, H., Wölfli, W., and Morenzoni, E.: 1982, *Nuclear Physics A* **388(2)**, 334

[22] Bohm, D. and Pines, D.: 1953, *Phys. Rev.* **92**, 609

[23] Bohr, A. and Mottelson, B. R.: 1975, *Nuclear Structure*, Vol. 1, W. A. Benjamin, Reading, MA

[24] Bonche, P., Flocard, H., and Heenen, P.: 1987, *Nuclear Physics A* **467(1)**, 115

[25] Bonche, P., Flocard, H., and Heenen, P.: 2005, *Computer Physics Communications* **171(1)**, 49

[26] Bonche, P., Flocard, H., Heenen, P., Krieger, S., and Weiss, M.: 1985, *Nuclear Physics A* **443(1)**, 39

[27] Bonche, P., Koonin, S., and Negele, J. W.: 1976, *Phys. Rev. C* **13**, 1226

[28] Bourgin, D., Courtin, S., Haas, F., Stefanini, A. M., Montagnoli, G., Goasduff, A., Montanari, D., Corradi, L., Fioretto, E., Huiming, J., Scarlassara, F., Rowley, N., Szilner, S., and Mijatović, T.: 2014, *Phys. Rev. C* **90**, 044610

[29] Bourgin, D., Simenel, C., Courtin, S., and Haas, F.: 2016, *Phys. Rev. C* **93**, 034604

[30] Broglia, R. A., Dasso, C. H., Landowne, S., and Winther, A.: 1983, *Phys. Rev. C* **27**, 2433

[31] Broglia, R. A. and Winther, A.: 1981, *Heavy Ion Reactions Lecure Notes, Vol. I: Elastic and Inelastic Reactions*, Benjamin/Cummings, Reading, MA

[32] Brown, B. A., Rae, W. D. M., McDonald, E., and Horoi, M.: *NuShellX@MSU*, `https://people.nscl.msu.edu/~brown/resources/resources.html`

[33] Brueckner, K. A., Buchler, J. R., and Kelly, M. M.: 1968, *Phys. Rev.* **173**, 944

[34] Bulgac, A., Magierski, P., Roche, K. J., and Stetcu, I.: 2016, *Phys. Rev. Lett.* **116**, 122504

[35] Carey, T. A., Cornelius, W. D., DiGiacomo, N. J., Moss, J. M., Adams, G. S., McClelland, J. B., Pauletta, G., Whitten, C., Gazzaly, M., Hintz, N., and Glashausser, C.: 1980, *Phys. Rev. Lett.* **45**, 239

[36] Caurier, E., Langanke, K., Martínez-Pinedo, G., Nowacki, F., and Vogel, P.: 2001, *Physics Letters B* **522(3–4)**, 240

[37] Chabanat, E., Bonche, P., Haensel, P., Meyer, J., and Schaeffer, R.: 1997, *Nuclear Physics A* **627(4)**, 710

[38] Chabanat, E., Bonche, P., Haensel, P., Meyer, J., and Schaeffer, R.: 1998, *Nuclear Physics A* **635(1)**, 231

[39] Chamon, L. C., Carlson, B. V., Gasques, L. R., Pereira, D., De Conti, C., Alvarez, M. A. G., Hussein, M. S., Cândido Ribeiro, M. A., Rossi, E. S., and Silva, C. P.: 2002, *Phys. Rev. C* **66**, 014610

[40] Corradi, L., Stefanini, A. M., Lin, C. J., Beghini, S., Montagnoli, G., Scarlassara, F., Pollarolo, G., and Winther, A.: 1999, *Phys. Rev. C* **59**, 261

[41] Cusson, R. Y., Smith, R. K., and Maruhn, J. A.: 1976, *Phys. Rev. Lett.* **36**, 1166

[42] Ćwiok, S., Dobaczewski, J., Heenen, P.-H., Magierski, P., and Nazarewicz, W.: 1996, *Nuclear Physics A* **611(2)**, 211

[43] Dai, G.-F., Guo, L., Zhao, E.-G., and Zhou, S.-G.: 2014, *Phys. Rev. C* **90**, 044609

[44] Dasgupta, M., Gomes, P. R. S., Hinde, D. J., Moraes, S. B., Anjos, R. M., Berriman, A. C., Butt, R. D., Carlin, N., Lubian, J., Morton, C. R., Newton, J. O., and Szanto de Toledo, A.: 2004, *Phys. Rev. C* **70**, 024606

[45] Dasgupta, M., Hinde, D. J., Diaz-Torres, A., Bouriquet, B., Low, C. I., Milburn, G. J., and Newton, J. O.: 2007, *Phys. Rev. Lett.* **99**, 192701

[46] Dasgupta, M., Hinde, D. J., Rowley, N., and Stefanini, A. M.: 1998, *Annual Review of Nuclear and Particle Science* **48(1)**, 401

[47] Dasso, C., Landowne, S., and Winther, A.: 1983, *Nuclear Physics A* **405(2)**, 381

[48] Davies, K., Flocard, H., Krieger, S., and Weiss, M.: 1980, *Nuclear Physics A* **342(1)**, 111

[49] Dirac, P. A. M.: 1930, *Mathematical Proceedings of the Cambridge Philosophical Society* **26(3)**, 376–385

[50] Dobaczewski, J., Flocard, H., and Treiner, J.: 1984, *Nuclear Physics A* **422(1)**, 103

[51] Dobaczewski, J., Nazarewicz, W., and Reinhard, P.-G.: 2001, *Nuclear Physics A* **693(1)**, 361 , Radioactive Nuclear Beams

[52] Dobaczewski, J., Nazarewicz, W., Werner, T. R., Berger, J. F., Chinn, C. R., and Dechargé, J.: 1996, *Phys. Rev. C* **53**, 2809

[53] du Rietz, R., Hinde, D. J., Dasgupta, M., Thomas, R. G., Gasques, L. R., Evers, M., Lobanov, N., and Wakhle, A.: 2011, *Phys. Rev. Lett.* **106**, 052701

[54] du Rietz, R., Williams, E., Hinde, D. J., Dasgupta, M., Evers, M., Lin, C. J., Luong, D. H., Simenel, C., and Wakhle, A.: 2013, *Phys. Rev. C* **88**, 054618

[55] Ebata, S., Nakatsukasa, T., Inakura, T., Yoshida, K., Hashimoto, Y., and Yabana, K.: 2010, *Phys. Rev. C* **82**, 034306

[56] Evers, M., Dasgupta, M., Hinde, D. J., Luong, D. H., Rafiei, R., du Rietz, R., and Simenel, C.: 2011, *Phys. Rev. C* **84**, 054614

[57] Ferrell, R. A.: 1957, *Phys. Rev.* **107**, 1631

[58] Flocard, H., Koonin, S. E., and Weiss, M. S.: 1978, *Phys. Rev. C* **17**, 1682

[59] Fock, V.: 1930, *Zeitschrift für Physik* **61(1-2)**, 126–148

[60] Fracasso, S., Suckling, E. B., and Stevenson, P. D.: 2012, *Phys. Rev. C* **86**, 044303

[61] Freeman, W. S., Ernst, H., Geesaman, D. F., Henning, W., Humanic, T. J., Kühn, W., Rosner, G., Schiffer, J. P., Zeidman, B., and Prosser, F. W.: 1983, *Phys. Rev. Lett.* **50**, 1563

[62] Freiesleben, H. and Kratz, J.: 1984, *Physics Reports* **106(1)**, 1

[63] Ghiorso, A.: 2003, *Chem. Eng. News* **81**, 174

[64] Giannoni, M. J. and Quentin, P.: 1980, *Phys. Rev. C* **21**, 2076

[65] Godbey, K., Umar, A. S., and Simenel, C.: 2017, *Phys. Rev. C* **95**, 011601

[66] Goddard, P., Stevenson, P., and Rios, A.: 2015, *Phys. Rev. C* **92**, 054610

[67] Goddard, P., Stevenson, P., and Rios, A.: 2016, *Phys. Rev. C* **93**, 014620

[68] Gogny, D.: 1973, in J. de Boer and H. Mang (eds.), *Proceedings of the International Conference on Nuclear Physics, Munich*, Vol. 1, p. 48, North Holland Pub. Co., Amsterdam

[69] Golabek, C. and Simenel, C.: 2009, *Phys. Rev. Lett.* **103**, 042701

[70] Gombás, P.: 1952, *Annalen der Physik* **445(4-5)**, 253

[71] Griffin, J. J. and Wheeler, J. A.: 1957, *Phys. Rev.* **108**, 311

[72] Guichon, P. A., Saito, K., Rodionov, E., and Thomas, A. W.: 1996, *Nuclear Physics A* **601(3)**, 349

[73] Hagino, K., Rowley, N., and Kruppa, A.: 1999, *Computer Physics Communications* **123(1)**, 143

[74] Hagino, K. and Takigawa, N.: 2012, *Progress of Theoretical Physics* **128(6)**, 1061

[75] Hagino, K., Takigawa, N., Dasgupta, M., Hinde, D. J., and Leigh, J. R.: 1997, *Phys. Rev. Lett.* **79**, 2014

[76] Hammerton, K., Kohley, Z., Hinde, D. J., Dasgupta, M., Wakhle, A., Williams, E., Oberacker, V. E., Umar, A. S., Carter, I. P., Cook, K. J., Greene, J., Jeung, D. Y., Luong, D. H., McNeil, S. D., Palshetkar, C. S., Rafferty, D. C., Simenel, C., and Stiefel, K.: 2015, *Phys. Rev. C* **91**, 041602

[77] Hartree, D. R.: 1928, *Mathematical Proceedings of the Cambridge Philosophical Society* **24(1)**, 89–110

[78] Hergert, H., Papakonstantinou, P., and Roth, R.: 2011, *Phys. Rev. C* **83**, 064317

[79] Hill, D. L. and Wheeler, J. A.: 1953, *Phys. Rev.* **89**, 1102

[80] Hinde, D. and Dasgupta, M.: 2005, *Physics Letters B* **622(1)**, 23

[81] Hinde, D., Leigh, J., Bokhorst, J., Newton, J., Walsh, R., and Boldeman, J.: 1987, *Nuclear Physics A* **472(2)**, 318

[82] Hinde, D., Williams, E., Mohanto, G., Simenel, C., Jeung, D. Y., Dasgupta, M., Prasad, E., Wakhle, A., Vo-Phuoc, K., Carter, I. P., Cook, K. J., Luong, D. H., Palshetkar, C. S., Rafferty, D. C., and Simpson, E. C.: 2016, *EPJ Web Conf.* **123**, 03005

[83] Hinde, D. J., Dasgupta, M., Leigh, J. R., Mein, J. C., Morton, C. R., Newton, J. O., and Timmers, H.: 1996, *Phys. Rev. C* **53**, 1290

[84] Hinde, D. J., Jeung, D. Y., Prasad, E., Wakhle, A., Dasgupta, M., Evers, M., Luong, D. H., du Rietz, R., Simenel, C., Simpson, E. C., and Williams, E.: 2018, *Phys. Rev. C* **97**, 024616

[85] Hoffman, D. C., Lawrence, F. O., Mewherter, J. L., and Rourke, F. M.: 1971, *Nature* **234**, 132

[86] Hofmann, S.: 1998, *Reports on Progress in Physics* **61(6)**, 639

[87] Hofmann, S. and Münzenberg, G.: 2000, *Rev. Mod. Phys.* **72**, 733

[88] Hofmann, S., Ninov, V., Heßberger, F. P., Armbruster, P., Folger, H., Münzenberg, G., Schött, H. J., Popeko, A. G., Yeremin, A. V., Andreyev, A. N., Saro, S., Janik, R., and Leino, M.: 1995a, *Zeitschrift für Physik A Hadrons and Nuclei* **350(4)**, 281

[89] Hofmann, S., Ninov, V., Heßberger, F. P., Armbruster, P., Folger, H., Münzenberg, G., Schött, H. J., Popeko, A. G., Yeremin, A. V., Andreyev, A. N., Saro, S., Janik, R., and Leino, M.: 1995b, *Zeitschrift für Physik A Hadrons and Nuclei* **350(4)**, 277

[90] Hofmann, S., Ninov, V., Heßberger, F. P., Armbruster, P., Folger, H., Münzenberg, G., Schött, H. J., Popeko, A. G., Yeremin, A. V., Saro, S., Janik, R., and Leino, M.: 1996, *Zeitschrift für Physik A Hadrons and Nuclei* **354(3)**, 229

[91] Ichikawa, T., Hagino, K., and Iwamoto, A.: 2007, *Phys. Rev. C* **75**, 057603

[92] Itkis, I. M., Kozulin, E. M., Itkis, M. G., Knyazheva, G. N., Bogachev, A. A., Chernysheva, E. V., Krupa, L., Oganessian, Y. T., Zagrebaev, V. I., Rusanov, A. Y., Goennenwein, F., Dorvaux, O., Stuttgé, L., Hanappe, F., Vardaci, E., and de Goés Brennand, E.: 2011, *Phys. Rev. C* **83**, 064613

[93] Itkis, M., Aÿstö, J., Beghini, S., Bogachev, A., Corradi, L., Dorvaux, O., Gadea, A., Giardina, G., Hanappe, F., Itkis, I., Jandel, M., Kliman, J., Khlebnikov, S., Kniajeva, G., Kondratiev, N., Kozulin, E., Krupa, L., Latina, A., Materna, T., Montagnoli, G., Oganessian, Y., Pokrovsky, I., Prokhorova, E., Rowley, N., Rubchenya, V., Rusanov, A., Sagaidak, R., Scarlassara, F., Stefanini, A., Stuttge, L., Szilner, S., Trotta, M., Trzaska, W., Vakhtin, D., Vinodkumar, A., Voskressenski, V., and Zagrebaev, V.: 2004, *Nuclear Physics A* **734(Supplement C)**, 136

[94] Jiang, C. L., Esbensen, H., Rehm, K. E., Back, B. B., Janssens, R. V. F., Caggiano, J. A., Collon, P., Greene, J., Heinz, A. M., Henderson, D. J., Nishinaka, I., Pennington, T. O., and Seweryniak, D.: 2002, *Phys. Rev. Lett.* **89**, 052701

[95] Jiang, C. L., Rehm, K. E., Back, B. B., Esbensen, H., Janssens, R. V. F., Stefanini, A. M., and Montagnoli, G.: 2014, *Phys. Rev. C* **89**, 051603

[96] Jiang, C. L., Stefanini, A. M., Esbensen, H., Rehm, K. E., Almaraz-Calderon, S., Avila, M. L., Back, B. B., Bourgin, D., Corradi, L., Courtin, S., Fioretto, E., Galtarossa, F., Goasduff, A., Haas, F., Mazzocco, M. M., Montanari, D., Montagnoli, G., Mijatovic, T., Sagaidak, R., Santiago-Gonzalez, D., Scarlassara, F., Strano, E. E., and Szilner, S.: 2015, *Phys. Rev. C* **91**, 044602

[97] Karpov, A. V., Rachkov, V. A., and Samarin, V. V.: 2015, *Phys. Rev. C* **92**, 064603

[98] Kedziora, D. J. and Simenel, C.: 2010, *Phys. Rev. C* **81**, 044613

[99] Khuyagbaatar, J., David, H. M., Hinde, D. J., Carter, I. P., Cook, K. J., Dasgupta, M., Düllmann, C. E., Jeung, D. Y., Kindler, B., Lommel, B., Luong, D. H., Prasad, E., Rafferty, D. C., Sengupta, C., Simenel, C., Simpson, E. C., Smith, J. F., Vo-Phuoc, K., Walshe, J., Wakhle, A., Williams, E., and Yakushev, A.: 2018, *Phys. Rev. C* **97**, 064618

[100] Kibedi, T. and Spear, R.: 2002, *Atomic Data and Nuclear Data Tables* **80(1)**, 35

[101] Kim, K.-H., Otsuka, T., and Bonche, P.: 1997, *Journal of Physics G: Nuclear and Particle Physics* **23(10)**, 1267

[102] Kolata, J. J., Roberts, A., Howard, A. M., Shapira, D., Liang, J. F., Gross, C. J., Varner, R. L., Kohley, Z., Villano, A. N., Amro, H., Loveland, W., and Chavez, E.: 2012, *Phys. Rev. C* **85**, 054603

[103] Koonin, S. E., Davies, K. T. R., Maruhn-Rezwani, V., Feldmeier, H., Krieger, S. J., and Negele, J. W.: 1977, *Phys. Rev. C* **15**, 1359

[104] Kortelainen, M., McDonnell, J., Nazarewicz, W., Reinhard, P.-G., Sarich, J., Schunck, N., Stoitsov, M. V., and Wild, S. M.: 2012, *Phys. Rev. C* **85**, 024304

[105] Kozulin, E. M., Knyazheva, G. N., Itkis, I. M., Itkis, M. G., Bogachev, A. A., Chernysheva, E. V., Krupa, L., Hanappe, F., Dorvaux, O., Stuttgé, L., Trzaska, W. H., Schmitt, C., and Chubarian, G.: 2014, *Phys. Rev. C* **90**, 054608

[106] Krieger, S., Bonche, P., Flocard, H., Quentin, P., and Weiss, M.: 1990, *Nuclear Physics A* **517(2)**, 275

[107] Kruppa, A. T., Bender, M., Nazarewicz, W., Reinhard, P.-G., Vertse, T., and Ćwiok, S.: 2000, *Phys. Rev. C* **61**, 034313

[108] Kruppa, A. T., Heenen, P. H., and Liotta, R. J.: 2001, *Phys. Rev. C* **63**, 044324

[109] Köhler, H. and Flocard, H.: 1979, *Nuclear Physics A* **323(1)**, 189

[110] Leigh, J. R., Dasgupta, M., Hinde, D. J., Mein, J. C., Morton, C. R., Lemmon, R. C., Lestone, J. P., Newton, J. O., Timmers, H., Wei, J. X., and Rowley, N.: 1995, *Phys. Rev. C* **52**, 3151

[111] Liang, J. F., Allmond, J. M., Gross, C. J., Mueller, P. E., Shapira, D., Varner, R. L., Dasgupta, M., Hinde, D. J., Simenel, C., Williams, E., Vo-Phuoc, K., Brown, M. L., Carter, I. P., Evers, M., Luong, D. H., Ebadi, T., and Wakhle, A.: 2016, *Phys. Rev. C* **94**, 024616

[112] Maruhn, J., Reinhard, P.-G., Stevenson, P., and Umar, A.: 2014, *Computer Physics Communications* **185(7)**, 2195

[113] Maruhn, J. A., Reinhard, P. G., Stevenson, P. D., Stone, J. R., and Strayer, M. R.: 2005, *Phys. Rev. C* **71**, 064328

[114] Maruhn, J. A., Reinhard, P.-G., Stevenson, P. D., and Strayer, M. R.: 2006, *Phys. Rev. C* **74**, 027601

[115] McRae, E., Simenel, C., Simpson, E. C., and Thomas, A. W.: 2017, *ArXiv e-prints*, `https://arxiv.org/abs/1704.07991`

[116] Mişicu, Ş. and Esbensen, H.: 2006, *Phys. Rev. Lett.* **96**, 112701

[117] Mitsuoka, S., Ikezoe, H., Nishio, K., Satou, K., and Lu, J.: 2002, *Phys. Rev. C* **65**, 054608

[118] Mohanto, G., Hinde, D. J., Banerjee, K., Dasgupta, M., Jeung, D. Y., Simenel, C., Simpson, E. C., Wakhle, A., Williams, E., Carter, I. P., Cook, K. J., Luong, D. H., Palshetkar, C. S., and Rafferty, D. C.: 2018, *Phys. Rev. C* **97**, 054603

[119] Montagnoli, G., Stefanini, A. M., Jiang, C. L., Esbensen, H., Corradi, L., Courtin, S., Fioretto, E., Goasduff, A., Haas, F., Kifle, A. F., Michelagnoli, C., Montanari, D., Mijatović, T., Rehm, K. E., Silvestri, R., Singh, P. P., Scarlassara, F., Szilner, S., Tang, X. D., and Ur, C. A.: 2012, *Phys. Rev. C* **85**, 024607

[120] Morita, K., Morimoto, K., Kaji, D., Akiyama, T., ichi Goto, S., Haba, H., Ideguchi, E., Kanungo, R., Katori, K., Koura, H., Kudo, H., Ohnishi, T., Ozawa, A., Suda, T., Sueki, K., Xu, H., Yamaguchi, T., Yoneda, A., Yoshida, A., and Zhao, Y.: 2004, *Journal of the Physical Society of Japan* **73(10)**, 2593

[121] Morton, C. R., Berriman, A. C., Dasgupta, M., Hinde, D. J., Newton, J. O., Hagino, K., and Thompson, I. J.: 1999, *Phys. Rev. C* **60**, 044608

[122] Mosel, U. and Greiner, W.: 1969, *Zeitschrift für Physik A Hadrons and nuclei* **222(3)**, 261

[123] Münzenberg, G.: 1988, *Reports on Progress in Physics* **51(1)**, 57

[124] Münzenberg, G., Armbruster, P., Folger, H., Heßberger, P. F., Hofmann, S., Keller, J., Poppensieker, K., Reisdorf, W., Schmidt, K. H., Schött, H. J., Leino, M. E., and Hingmann, R.: 1984, *Zeitschrift für Physik A Atoms and Nuclei* **317(2)**, 235

[125] Münzenberg, G., Armbruster, P., Heßberger, F. P., Hofmann, S., Poppensieker, K., Reisdorf, W., Schneider, J. H. R., Schneider, W. F. W., Schmidt, K. H., Sahm, C. C., and Vermeulen, D.: 1982, *Zeitschrift für Physik A Atoms and Nuclei* **309(1)**, 89

[126] Münzenberg, G., Hofmann, S., Heßberger, F. P., Reisdorf, W., Schmidt, K. H., Schneider, J. H. R., Armbruster, P., Sahm, C. C., and Thuma, B.: 1981, *Zeitschrift für Physik A Atoms and Nuclei* **300(1)**, 107

[127] Nakatsukasa, T., Matsuyanagi, K., Matsuo, M., and Yabana, K.: 2016, *Rev. Mod. Phys.* **88**, 045004

[128] Nakatsukasa, T. and Yabana, K.: 2005, *Phys. Rev. C* **71**, 024301

[129] Negele, J. W.: 1982, *Rev. Mod. Phys.* **54**, 913

[130] Negele, J. W., Koonin, S. E., Möller, P., Nix, J. R., and Sierk, A. J.: 1978, *Phys. Rev. C* **17**, 1098

[131] Negele, J. W. and Vautherin, D.: 1972, *Phys. Rev. C* **5**, 1472

[132] Newton, J. O., Butt, R. D., Dasgupta, M., Hinde, D. J., Gontchar, I. I., Morton, C. R., and Hagino, K.: 2004, *Phys. Rev. C* **70**, 024605

[133] Newton, J. O., Morton, C. R., Dasgupta, M., Leigh, J. R., Mein, J. C., Hinde, D. J., Timmers, H., and Hagino, K.: 2001, *Phys. Rev. C* **64**, 064608

[134] Nilsson, S. G., Tsang, C. F., Sobiczewski, A., Szymański, Z., Wycech, S., Gustafson, C., Lamm, I.-L., Möller, P., and Nilsson, B.: 1969, *Nuclear Physics A* **131(1)**, 1

[135] Oberacker, V. E., Umar, A. S., and Simenel, C.: 2014, *Phys. Rev. C* **90**, 054605

[136] Oganessian, Y. T.: 1975, in H. H. Ludwig, B.-M. Peter, and G. C. Konrad (eds.), *Classical and Quantum Mechanical Aspects of Heavy Ion Collisions*, pp 221–252, Springer Berlin Heidelberg, Berlin Heidelberg

[137] Oganessian, Y. T.: 2007, *Journal of Physics G: Nuclear and Particle Physics* **34(4)**, R165

[138] Oganessian, Y. T., Abdullin, F. S., Bailey, P. D., Benker, D. E., Bennett, M. E., Dmitriev, S. N., Ezold, J. G., Hamilton, J. H., Henderson, R. A., Itkis, M. G., Lobanov, Y. V., Mezentsev, A. N., Moody, K. J., Nelson, S. L., Polyakov, A. N., Porter, C. E., Ramayya, A. V., Riley, F. D., Roberto, J. B., Ryabinin, M. A., Rykaczewski, K. P., Sagaidak, R. N., Shaughnessy, D. A., Shirokovsky, I. V., Stoyer, M. A., Subbotin, V. G., Sudowe, R., Sukhov, A. M., Tsyganov, Y. S., Utyonkov, V. K., Voinov, A. A., Vostokin, G. K., and Wilk, P. A.: 2010, *Phys. Rev. Lett.* **104**, 142502

[139] Oganessian, Y. T., Abdullin, F. S., Bailey, P. D., Benker, D. E., Bennett, M. E., Dmitriev, S. N., Ezold, J. G., Hamilton, J. H., Henderson, R. A., Itkis, M. G., Lobanov, Y. V., Mezentsev, A. N., Moody, K. J., Nelson, S. L., Polyakov, A. N., Porter, C. E., Ramayya, A. V., Riley, F. D., Roberto, J. B., Ryabinin, M. A., Rykaczewski, K. P., Sagaidak, R. N., Shaughnessy, D. A., Shirokovsky, I. V., Stoyer, M. A., Subbotin, V. G., Sudowe, R., Sukhov, A. M., Taylor, R., Tsyganov, Y. S., Utyonkov, V. K., Voinov, A. A., Vostokin, G. K., and Wilk, P. A.: 2011, *Phys. Rev. C* **83**, 054315

[140] Oganessian, Y. T., Tret'yakov, Y. P., Iljinov, A. S., Demin, A. G., Pleve, A. A., Tret'yakov, S. P., Plotko, V. M., Ivanov, M. P., Danilov, N. A., Korotkin, Y. S., and Flerov, G. N.: 1974, *JETP Letters* **20**, 265

[141] Oganessian, Y. T., Utyonkov, V. K., Lobanov, Y. V., Abdullin, F. S., Polyakov, A. N., Sagaidak, R. N., Shirokovsky, I. V., Tsyganov, Y. S., Voinov, A. A., Gulbekian, G. G., Bogomolov, S. L., Gikal, B. N., Mezentsev, A. N., Iliev, S., Subbotin, V. G., Sukhov, A. M., Subotic, K., Zagrebaev, V. I., Vostokin, G. K., Itkis, M. G., Moody, K. J., Patin, J. B., Shaughnessy, D. A., Stoyer, M. A., Stoyer, N. J., Wilk, P. A., Kenneally, J. M., Landrum, J. H., Wild, J. F., and Lougheed, R. W.: 2006, *Phys. Rev. C* **74**, 044602

[142] Oganessian, Y. T., Utyonkov, V. K., Lobanov, Y. V., Abdullin, F. S., Polyakov, A. N., Shirokovsky, I. V., Tsyganov, Y. S., Gulbekian, G. G., Bogomolov, S. L., Gikal, B. N., Mezentsev, A. N., Iliev, S., Subbotin, V. G., Sukhov, A. M., Buklanov, G. V., Subotic, K.,

Itkis, M. G., Moody, K. J., Wild, J. F., Stoyer, N. J., Stoyer, M. A., and Lougheed, R. W.: 1999, *Phys. Rev. Lett.* **83**, 3154

[143] Oganessian, Y. T., Utyonkov, V. K., Lobanov, Y. V., Abdullin, F. S., Polyakov, A. N., Shirokovsky, I. V., Tsyganov, Y. S., Gulbekian, G. G., Bogomolov, S. L., Gikal, B. N., Mezentsev, A. N., Iliev, S., Subbotin, V. G., Sukhov, A. M., Ivanov, O. V., Buklanov, G. V., Subotic, K., Itkis, M. G., Moody, K. J., Wild, J. F., Stoyer, N. J., Stoyer, M. A., Lougheed, R. W., Laue, C. A., Karelin, Y. A., and Tatarinov, A. N.: 2000, *Phys. Rev. C* **63**, 011301

[144] Oganessian, Y. T., Utyonkoy, V. K., Lobanov, Y. V., Abdullin, F. S., Polyakov, A. N., Shirokovsky, I. V., Tsyganov, Y. S., Gulbekian, G. G., Bogomolov, S. L., Mezentsev, A. N., Iliev, S., Subbotin, V. G., Sukhov, A. M., Voinov, A. A., Buklanov, G. V., Subotic, K., Zagrebaev, V. I., Itkis, M. G., Patin, J. B., Moody, K. J., Wild, J. F., Stoyer, M. A., Stoyer, N. J., Shaughnessy, D. A., Kenneally, J. M., and Lougheed, R. W.: 2004, *Phys. Rev. C* **69**, 021601

[145] Öhrström, L. and Jan, R.: 2016, *Pure and Applied Chemistry* **88**, 1225

[146] Pardi, C. I. and Stevenson, P. D.: 2013, *Phys. Rev. C* **87**, 014330

[147] Pollarolo, G.: 2013, *Acta Phys. Pol. B* **44**, 407

[148] Prasad, E., Hinde, D. J., Williams, E., Dasgupta, M., Carter, I. P., Cook, K. J., Jeung, D. Y., Luong, D. H., Palshetkar, C. S., Rafferty, D. C., Ramachandran, K., Simenel, C., and Wakhle, A.: 2017, *Phys. Rev. C* **96**, 034608

[149] Prasad, E., Wakhle, A., Hinde, D. J., Williams, E., Dasgupta, M., Evers, M., Luong, D. H., Mohanto, G., Simenel, C., and Vo-Phuoc, K.: 2016, *Phys. Rev. C* **93**, 024607

[150] Rafiei, R., Thomas, R. G., Hinde, D. J., Dasgupta, M., Morton, C. R., Gasques, L. R., Brown, M. L., and Rodriguez, M. D.: 2008, *Phys. Rev. C* **77**, 024606

[151] Raman, S., Nestor, C., and Tikkanen, P.: 2001, *Atomic Data and Nuclear Data Tables* **78(1)**, 1

[152] Reinhard, P.-G. and Flocard, H.: 1995, *Nuclear Physics A* **584(3)**, 467

[153] Reinhard, P.-G., Stevenson, P. D., Almehed, D., Maruhn, J. A., and Strayer, M. R.: 2006, *Phys. Rev. E* **73**, 036709

[154] Ring, P. and Schuck, P.: 1980, *The Nuclear Many-body Problem*, Texts and monographs in physics, Springer-Verlag

[155] Rowley, N., Satchler, G., and Stelson, P.: 1991, *Physics Letters B* **254(1)**, 25

[156] Rutz, K., Bender, M., Bürvenich, T., Schilling, T., Reinhard, P.-G., Maruhn, J. A., and Greiner, W.: 1997, *Phys. Rev. C* **56**, 238

[157] Ryssens, W., Hellemans, V., Bender, M., and Heenen, P.-H.: 2015, *Computer Physics Communications* **187(Supplement C)**, 175

[158] Sahm, C.-C., Clerc, H.-H., Schmidt, K.-H., Reisdorf, W., Armbruster, P., Heßberger, F. P., Keller, J. G., Münzenberg, G., and Vermeulen, D.: 1984, *Z. Phys. A* **319**, 113

[159] Sandulescu, N., Liotta, R., and Wyss, R.: 1997, *Physics Letters B* **394(1)**, 6

[160] Scamps, G. and Hagino, K.: 2015, *Phys. Rev. C* **92**, 054614

[161] Scamps, G. and Hashimoto, Y.: 2017, *Phys. Rev. C* **96**, 031602

[162] Scamps, G. and Lacroix, D.: 2013a, *Phys. Rev. C* **87**, 014605

[163] Scamps, G. and Lacroix, D.: 2013b, *Phys. Rev. C* **88**, 044310

[164] Scamps, G., Lacroix, D., Bertsch, G. F., and Washiyama, K.: 2012, *Phys. Rev. C* **85**, 034328

[165] Scamps, G., Rodríguez-Tajes, C., Lacroix, D., and Farget, F.: 2017, *Phys. Rev. C* **95**, 024613

[166] Scamps, G., Sargsyan, V. V., Adamian, G. G., Antonenko, N. V., and Lacroix, D.: 2015a, *Phys. Rev. C* **91**, 024601

[167] Scamps, G., Simenel, C., and Lacroix, D.: 2015b, *Phys. Rev. C* **92**, 011602

[168] Scarlassara, F., Beghini, S., Montagnoli, G., Segato, G., Ackermann, D., Corradi, L., Lin, C., Stefanini, A., and Zheng, L.: 2000, *Nuclear Physics A* **672(1)**, 99

[169] Sekizawa, K.: 2017, *Phys. Rev. C* **96**, 041601

[170] Sekizawa, K. and Yabana, K.: 2013, *Phys. Rev. C* **88**, 014614

[171] Sekizawa, K. and Yabana, K.: 2014, *Phys. Rev. C* **90**, 064614

[172] Sekizawa, K. and Yabana, K.: 2016, *Phys. Rev. C* **93**, 054616

[173] Shen, W. Q., Albinski, J., Gobbi, A., Gralla, S., Hildenbrand, K. D., Herrmann, N., Kuzminski, J., Müller, W. F. J., Stelzer, H., Tke, J., Back, B. B., Bjrnholm, S., and Srensen, S. P.: 1987, *Phys. Rev. C* **36**, 115

[174] Simenel, C.: 2010, *Phys. Rev. Lett.* **105**, 192701

[175] Simenel, C.: 2011, *Phys. Rev. Lett.* **106**, 112502

[176] Simenel, C.: 2012, *Eur. Phys. J. A* **48(11)**, 152

[177] Simenel, C.: 2014a, *Journal of Physics G: Nuclear and Particle Physics* **41(9)**, 094007

[178] Simenel, C.: 2014b, *Clusters in Nuclei*, Vol. 3, Chapt. 4, pp 95–145, Springer, Switzerland

[179] Simenel, C.: 2015, private communication.

[180] Simenel, C. and Avez, B.: 2008, *International Journal of Modern Physics E* **17(01)**, 31

[181] Simenel, C. and Chomaz, P.: 2009, *Phys. Rev. C* **80**, 064309

[182] Simenel, C., Dasgupta, M., Hinde, D. J., and Williams, E.: 2013a, *Phys. Rev. C* **88**, 064604

[183] Simenel, C., Hinde, D., du Rietz, R., Dasgupta, M., Evers, M., Lin, C., Luong, D., and Wakhle, A.: 2012, *Physics Letters B* **710(4)**, 607

[184] Simenel, C., Keser, R., Umar, A. S., and Oberacker, V. E.: 2013b, *Phys. Rev. C* **88**, 024617

[185] Simenel, C. and Umar, A. S.: 2014, *Phys. Rev. C* **89**, 031601

[186] Simenel, C., Umar, A. S., Godbey, K., Dasgupta, M., and Hinde, D. J.: 2017, *Phys. Rev. C* **95**, 031601

[187] Simenel, C., Buete, J., and Vo-Phuoc, K.: 2016, *EPJ Web Conf.* **123**, 01004

[188] Simenel, C., Dasgupta, M., Hinde, D. J., Kheifets, A., and Wakhle, A.: 2013, *EPJ Web of Conferences* **63**, 02001

[189] Skyrme, T. H. R.: 1956, *The Philosophical Magazine: A Journal of Theoretical Experimental and Applied Physics* **1(11)**, 1043

[190] Sobiczewski, A., Gareev, F., and Kalinkin, B.: 1966, *Physics Letters* **22(4)**, 500

[191] Sonika, Roy, B. J., Parmar, A., Pal, U. K., Kumawat, H., Jha, V., Pandit, S. K., Parkar, V. V., Ramachandran, K., Mahata, K., Pal, A., Santra, S., Mohanty, A. K., and Sekizawa, K.: 2015, *Phys. Rev. C* **92**, 024603

[192] Stefanini, A., Fortuna, G., Pengo, R., Meczynski, W., Montagnoli, G., Corradi, L., Tivelli, A., Beghini, S., Signorini, C., Lunardi, S., Morando, M., and Soramel, F.: 1986, *Nucl. Phys. A* **456(3)**, 509

[193] Stefanini, A., Montagnoli, G., Silvestri, R., Corradi, L., Courtin, S., Fioretto, E., Guiot, B., Haas, F., Lebhertz, D., Mason, P., Scarlassara, F., and Szilner, S.: 2009, *Physics Letters B* **679(2)**, 95

[194] Stetcu, I., Bulgac, A., Magierski, P., and Roche, K. J.: 2011, *Phys. Rev. C* **84**, 051309

[195] Stokstad, R. G., Eisen, Y., Kaplanis, S., Pelte, D., Smilansky, U., and Tserruya, I.: 1978, *Phys. Rev. Lett.* **41**, 465

[196] Strayer, M. R., Cusson, R. Y., Stoecker, H., Maruhn, J. A., and Greiner, W.: 1983, *Phys. Rev. C* **28**, 228

[197] Suzuki, M.: 1993, *Proceedings of the Japan Academy Series B* **69(7)**, 161

[198] Swiatecki, W.: 1982, *Nuclear Physics A* **376(2)**, 275

[199] Swiatecki, W. J.: 1981, *Physica Scripta* **24(1B)**, 113

[200] Tamura, T.: 1969, *Annual Review of Nuclear Science* **19(1)**, 99

[201] Tamura, T. and Udagawa, T.: 1964, *Nuclear Physics* **53**, 33

[202] Tanimura, Y., Lacroix, D., and Ayik, S.: 2017, *Phys. Rev. Lett.* **118**, 152501

[203] Terasaki, J., Engel, J., and Bertsch, G. F.: 2008, *Phys. Rev. C* **78**, 044311

[204] Terashima, S., Sakaguchi, H., Takeda, H., Ishikawa, T., Itoh, M., Kawabata, T., Murakami, T., Uchida, M., Yasuda, Y., Yosoi, M., Zenihiro, J., Yoshida, H. P., Noro, T., Ishida, T., Asaji, S., and Yonemura, T.: 2008, *Phys. Rev. C* **77**, 024317

[205] Thompson, I., Nagarajan, M., Lilley, J., and Fulton, B.: 1985, *Phys. Lett. B* **157(4)**, 250

[206] Timmers, H., Corradi, L., Stefanini, A., Ackermann, D., He, J., Beghini, S., Montagnoli, G., Scarlassara, F., Segato, G., and Rowley, N.: 1997, *Phys. Lett. B* **399(1–2)**, 35

[207] Tōke, J., Bock, R., Dai, G., Gobbi, A., Gralla, S., Hildenbrand, K., Kuzminski, J., Müller, W., Olmi, A., Stelzer, H., Back, B., and Bjørnholm, S.: 1985, *Nuclear Physics A* **440(2)**, 327

[208] Trotta, M., Stefanini, A. M., Corradi, L., Gadea, A., Scarlassara, F., Beghini, S., and Montagnoli, G.: 2001, *Phys. Rev. C* **65**, 011601

[209] Trzcińska, A., Piasecki, E., Amar, A., Czarnacki, W., Keeley, N., Kisieliński, M., Kliczewski, S., Kowalczyk, M., Lommel, B., Mutterer, M., Siudak, R., Stolarz, A., Strojek, I., Tiourin, G., and Trzaska, W. H.: 2016, *Phys. Rev. C* **93**, 054604

[210] Umar, A. S. and Oberacker, V. E.: 2005, *Phys. Rev. C* **71**, 034314

[211] Umar, A. S. and Oberacker, V. E.: 2006a, *Phys. Rev. C* **74**, 021601

[212] Umar, A. S. and Oberacker, V. E.: 2006b, *Phys. Rev. C* **73**, 054607

[213] Umar, A. S., Oberacker, V. E., Maruhn, J. A., and Reinhard, P. G.: 2009, *Phys. Rev. C* **80**, 041601

[214] Umar, A. S., Oberacker, V. E., Maruhn, J. A., and Reinhard, P.-G.: 2010, *Phys. Rev. C* **81**, 064607

[215] Umar, A. S., Oberacker, V. E., and Simenel, C.: 2015, *Phys. Rev. C* **92**, 024621

[216] Umar, A. S., Oberacker, V. E., and Simenel, C.: 2016, *Phys. Rev. C* **94**, 024605

[217] Umar, A. S., Simenel, C., and Oberacker, V. E.: 2014, *Phys. Rev. C* **89**, 034611

[218] Umar, A. S., Strayer, M. R., and Reinhard, P. G.: 1986, *Phys. Rev. Lett.* **56**, 2793

[219] Umar, A. S., Oberacker, V. E., and Maruhn, J. A.: 2008, *Eur. Phys. J. A* **37(2)**, 245

[220] Vermeeren, L., Silverans, R. E., Lievens, P., Klein, A., Neugart, R., Schulz, C., and Buchinger, F.: 1992, *Phys. Rev. Lett.* **68**, 1679

[221] Viola, V. E., Kwiatkowski, K., and Walker, M.: 1985, *Phys. Rev. C* **31**, 1550

[222] Vo-Phuoc, K., Simenel, C., and Simpson, E. C.: 2016, *Phys. Rev. C* **94**, 024612

[223] Wakhle, A., Simenel, C., Hinde, D. J., Dasgupta, M., Evers, M., Luong, D. H., du Rietz, R., and Williams, E.: 2014, *Phys. Rev. Lett.* **113**, 182502

[224] Washiyama, K.: 2015, *Phys. Rev. C* **91**, 064607

[225] Washiyama, K. and Lacroix, D.: 2008, *Phys. Rev. C* **78**, 024610

[226] Washiyama, K., Lacroix, D., and Ayik, S.: 2009, *Phys. Rev. C* **79**, 024609

[227] Williams, E.:, in preparation.

[228] Williams, E., Hinde, D. J., Dasgupta, M., du Rietz, R., Carter, I. P., Evers, M., Luong, D. H., McNeil, S. D., Rafferty, D. C., Ramachandran, K., and Wakhle, A.: 2013, *Phys. Rev. C* **88**, 034611

[229] Williams, E., Sekizawa, K., Hinde, D. J., Simenel, C., Dasgupta, M., Carter, I. P., Cook, K. J., Jeung, D. Y., McNeil, S. D., Palshetkar, C. S., Rafferty, D. C., Ramachandran, K., and Wakhle, A.: 2018, *Phys. Rev. Lett.* **120**, 022501

[230] Wohlfahrt, H. D., Shera, E. B., Hoehn, M. V., Yamazaki, Y., and Steffen, R. M.: 1981, *Phys. Rev. C* **23**, 533

[231] Wong, C. Y.: 1973, *Phys. Rev. Lett.* **31**, 766

[232] Wong, C.-Y. and Tang, H. H. K.: 1978, *Phys. Rev. Lett.* **40**, 1070

[233] Woods, R. D. and Saxon, D. S.: 1954, *Phys. Rev.* **95**, 577

[234] Yannouleas, C., Dworzecka, M., and Griffin, J.: 1983, *Nuclear Physics A* **397(2)**, 239

[235] Yao, J. M. and Hagino, K.: 2016, *Phys. Rev. C* **94**, 011303